Pharmaceutical formulation strategies for novel antibiotic substances utilizing salt formation and two- and three-dimensional printing techniques

Dissertation zur Erlangung des naturwissenschaftlichen Doktorgrades der

Julius-Maximilians-Universität Würzburg

vorgelegt von

Marco Saedtler

aus Lich

Würzburg 2020

Eingereicht bei der Fakultät für Chemie und Pharmazie am

Gutachter der schriftlichen Arbeit

1. Gutachter:

2. Gutachter:

Prüfer des öffentlichen Promotionskolloquiums

1. Prüfer:

2. Prüfer:

3. Prüfer:

Datum des öffentlichen Promotionskolloquiums

Doktorurkunde ausgehändigt am

Die vorliegende Arbeit wurde in der Zeit von April 2015 bis Oktober 2020 am Institut für Pharmazie und Lebensmittelchemie der Bayerischen Julius-Maximilians-Universität Würzburg unter der Anleitung von Herrn Prof. Dr. Dr. Lorenz Meinel angefertigt.

Table of contents

Summary

Salt formation is a routinely used strategy for poorly water-soluble drugs and traditionally performed with small inorganic counterions. High energy crystal lattices as well as effects on the local pH within the aqueous boundary layer during dissolution drive the increased dissolution rate and apparent solubility. Ionic liquids however, by definition low melting ionic salts with often large organic counterions, combine an increased dissolution rate with solubilization of the drug by the counterion itself. Long lasting supersaturation profiles of increased kinetic solubility were reported for several drugs formulated as ionic liquids increasing their overall bioavailability. Furthermore, aggregation and micellization between highly lipophilic compounds and amphiphilic bile acids was described before, demonstrating the capabilities of the human body itself to utilize solubilization of poorly water-soluble compounds. Development of novel counterions not only tailoring the desired physicochemical properties e.g. dissolution rate of the parent drug but adding – in a best-case scenario synergistic – pharmacological activity has been driven forward in the last years. However, salt formation can only be applied for ionizable i.e. acidic or basic compounds. While co-crystals can be used as a nonionized alternative, their formation is not always successful leading to an urgent need for other formulation strategies. In these lines, development of 2D and 3D printing techniques has been ongoing for the last decades and their pharmaceutical application has been demonstrated. The versatile nature and commercial availability allow a decentralized production further elaborating this technique for a highly flexible and patient-oriented supply with medication.

This thesis focuses on the theoretical background and potential application of salt formation in the pharmaceutical development of a drug candidate. The first section presents the current knowledge and state of the art in preparation of low melting ionic liquids i.e. salts and is translated to the *in vitro* investigation of molecular interaction between the poorly water-soluble drug imatinib and components of the human intestinal fluid in the second section. Development of novel antibiotic counterions and assessment of their potential use in pharmaceutical formulations with fluoroquinolones is described in the last two sections.

Chapter I describes the application of low melting ionic liquids in pharmaceutical formulation and details their development in the last two decades from versatile organic solvents in chemical synthesis towards amorphous strategies for drug delivery. The chapter

gives a general overview on molecular structure and physicochemical properties of several drug containing ionic liquids and details the mechanisms which attribute to a typically fast dissolution, increased aqueous solubility as well as enhanced permeation which was reported in several publications.

Chapter II translates the increased aqueous solubility of drugs by an organic counterion to the human gastrointestinal tract with taurocholate and lecithin as main drivers for the solubilization of highly lipophilic and poorly water-soluble drugs. Investigation of the interaction of imatinib – a poorly water-soluble weak base – with fasted- and fed state simulated intestinal fluids revealed a complex interplay between the components of the intestinal fluid and the drug. Mixed vesicles and micelles were observed in concentration dependent aggregation assays and revealed differences in their size, molecular arrangement as well as composition, depending on the tested drug concentration. Overall, the study outlines the effective interaction of weakly basic drugs with taurocholate and lecithin to minimize recrystallization during intestine passage finally leading to favorable supersaturation profiles.

Chapter III focuses on the development of novel antibiotic counterions which potentially move the evolution of ionic liquids from a pharmaceutical salt with tailored physicochemical properties to a synergistic combination of two active pharmaceutical ingredients. The natural occurring anacardic acid derived from the cashew nut shell inspired a series of antibacterial active acidic compounds with increasing alkyl chain length. Their physicochemical properties, antibacterial activity, bacterial biofilm inhibition and cytotoxicity were detailed and *in vivo* activity in a *Galleria mellonella* model was assessed. This group of anacardic acid derivatives is synthetically accessible, easily modifiable and yielded two compounds with favorable activity and physicochemical profile for further drug development.

Chapter IV outlines the potential application of anacardic acid derivatives in pharmaceutical formulations by salt formation with fluoroquinolone antibiotics as well as novel techniques such as 2D/3D printing for preparation of drug imprinted products. Despite anacardic acid derivatives demonstrated promising physicochemical properties, salt formation with fluoroquinolone antibiotics was not feasible. However, 2D/3D printed samples with anacardic acid derivative alone or in combination with ciprofloxacin demonstrated physical compatibility between drug and matrix as well as antibacterial activity against three *S. aureus* strains in an agar diffusion assay. Conclusively, drug printing

can be applied for the herein tested compounds, but further process development is necessary.

In summary, preparation of low melting ionic liquids, salts or co-crystals is an appropriate strategy to increase the aqueous solubility of poorly water-soluble drugs and tailor physicochemical properties. The counterion itself solubilizes the drug and furthermore potentially interferes with the complex micellar environment in the human intestine. However, salt formation as routinely used formulation strategy is not feasible in every case and development of alternative techniques is crucial to hurdle challenges related to unfavorable physicochemical properties. The outlined techniques for 2D/3D drug printing provide versatile production of drug products while extending the design space for novel drug development.

Zusammenfassung

Die Salzbildung mit pharmazeutischen Wirkstoffen – als routinemäßig durchgeführte Strategie für schlecht wasserlösliche Substanzen – wird traditionell mit kleinen, anorganischen Gegenionen durchgeführt. Eine tragende Rolle spielen hierbei ein hochenergetisches Kristallgitter sowie die Beeinflussung des pH-Wertes in der ruhenden Grenzschicht während des Auflösungsprozesses. Diese treiben eine beschleunigte Auflösungsrate sowie eine Erhöhung der scheinbaren Löslichkeit an. Ionische Flüssigkeiten stellen per Definition niederschmelzende ionische Salze mit oftmals großen, organischen Gegenionen dar. Sie kombinieren, aufgrund ihrer hohen Gitterenergie, eine beschleunigte Auflösungsratemit der Solubilisierung des Wirkstoffs durch das Gegenion. Langanhaltende Übersättigungen mit erhöhter kinetischer Löslichkeit und eine damit einhergehende, verbesserte Bioverfügbarkeit, wurden bereits bei verschiedenen Wirkstoffen beobachtet, die als ionische Flüssigkeiten formuliert wurden. Auch der menschliche Körper nutzt diesen Effekt und solubilisiert schlecht wasserlösliche Substanzen durch Aggregation und Mizellisierung lipophiler Substanzen mit amphiphilen Gallensäuren. Die Entwicklung neuartiger – meist kationischer – Gegenionen wurde in den letzten Jahren vorangetrieben. Vor allem Gegenionen, die nicht nur die gewünschten physikochemischen Eigenschaften (z.B. Auflösungsrate) hervorbringen, sondern einen eigenen – im besten Fall synergistischen – pharmakologischen Effekt aufweisen. Jedoch kommt eine Salzbildung nur für ionisierbare Substanzen respektive Säuren und Basen in Frage. Während Co-Kristalle als Alternative für nicht-ionisierbare Substanzen dienen können, ist deren Herstellung nicht immer erfolgreich und neue Formulierungsstrategien werden notwendig. Deshalb wurde unter anderem die Entwicklung von 2D- und 3D-Druckverfahren in den letzten Jahrzehnten vorangetrieben und deren Relevanz für pharmazeutische Fragestellungen aufgezeigt. Die vielseitige Natur und kommerzielle Verfügbarkeit des 2D/3D-Drucks erlaubt eine dezentrale Produktion und ermöglicht eine flexible und patientenorientierte Medikamentenversorgung.

Diese Dissertation beschäftigt sich vorrangig mit den theoretischen Hintergründen und den praktischen Anwendungsmöglichkeiten der Salzbildung in der pharmazeutischen Entwicklung eines potenziellen Wirkstoffes. Das erste Kapitel präsentiert den gegenwärtigen Stand der Technik zur Verwendung von niederschmelzenden ionischen Flüssigkeiten. Diese Erkenntnisse werden im Anschluss auf eine Untersuchung der Interaktionen des schlecht wasserlöslichen Wirkstoffs Imatinib und den Bestandteilen der

menschlichen Verdauungssäfte übertragen. Die Entwicklung neuartiger, antibiotisch wirksamer Gegenionen und deren potenzielle Verwendung in pharmazeutischen Formulierungen mit Fluorchinolonen ist Gegenstand der letzten zwei Kapitel.

Kapitel I beschreibt niederschmelzende ionische Flüssigkeiten in pharmazeutischen Formulierungen und führt deren Entwicklung in den letzten drei Jahrzehnten aus: Vom vielfältig anwendbaren, organischen Lösemittel für die chemische Synthese hin zur amorphen Darreichungsform. Das Kapitel gibt einen Überblick über die molekularen Strukturen und physikochemischen Eigenschaften verschiedener wirkstoffbeinhaltender, ionischer Flüssigkeiten. Hierbei werden die zugrundeliegenden Mechanismen dargelegt, was im Besonderen die rasche Auflösung, eine erhöhte Löslichkeit in wässrigen Medien sowie eine Beeinflussung der Permeation meint.

Kapitel II überträgt die Beobachtung einer erhöhten Löslichkeit in Gegenwart eines organischen Gegenions auf den menschlichen Verdauungstrakt, in dem Taurocholat und Lecithin hauptverantworlich für die Solubilisierung von liphilen und schlecht wasserlöslichen Substanzen sind. Untersuchungen der Interaktion von Imatinib, einer schlecht wasserlöslichen, schwachen Base, mit simulierten, intestinalen Flüssigkeiten zeigten ein komplexes System aus Bestandteilen der intestinalen Flüssigkeit und dem Wirkstoff. Gemische aus Vesikel und Mizellen, die mithilfeeines Aggregationsassays untersucht wurden, zeigten, in Abhängigkeit von momentanen Wirkstoffkonzentrationen, Unterschiede in ihrer Größe sowie der molekularen Anordnung und Zusammensetzung. Zusammenfassend beschreibt dieses Kapitel die effektive Interaktion von schwachen Basen mit Taurocholat und Lecithin sowie eine Möglichkeit zur Minimierung von Rekristallisation und damit der Aufrechterhaltung von übersättigten Zuständen während der Wirkstoff den Verdauungstrakt passiert.

Kapitel III befasst sich mit der Entwicklung neuartiger antibiotischer Gegenionen. Diese treiben möglicherweise die Weiterentwicklung von ionischen Flüssigkeiten mit optimierten physikochemischen Eigenschaften zu synergistischen Kombinationen aus zwei pharmakologisch aktiven Substanzen voran. Die natürlich vorkommende Anacardsäure, welche sich aus der Schale der Cashewnuss gewinnen lässt, hat eine Reihe von antibakteriellen, sauren Substanzen inspiriert, die sich allein in der Länge ihrer Alkylkette unterschieden. Physikochemische Eigenschaften, antibakterielle Aktivität, Inhibition des bakteriellen Biofilms sowie Zytotoxizität wurden untersucht und anschließend *in vivo*

mittels *Galleria mellonella*-Modell beleuchtet. Diese Gruppe aus Anacardsäurederivaten ist synthetisch zugänglich, einfach chemisch modifizierbar und brachte zwei Substanzen mit vorteilhafter Aktivität und physikochemischen Eigenschaften zur weiteren Entwicklung hervor.

Kapitel IV beschreibt die potenzielle Anwendung der Anacardsäurederivate in pharmazeutischen Formulierungen. Durch Salzbildung mit Fluorchinolon-Antibiotika sowie Nutzung neuerer Techniken, wie dem 2D/3D-Druck, wurden wirkstoffbedruckte Darreichungsformen hergestellt. Obwohl die Anacardsäurederivate vielversprechende physikochemische Eigenschaften zeigten, eigneten sie sich nicht für eine Salzbildung mit Fluorchinolonen. Trotzdem war es möglich Anacardsäurederivate allein oder in Kombination mit Ciprofloxacin auf Oberflächen zu drucken, wobei keine physische Inkompatibilität zwischen Wirkstoff und Matrix erkennbar war jedoch eine antibakterielle Wirkung gegen drei *S. aureus* Stämme gezeigt werden konnte. Abschließend stellte sich der Druck von Wirkstoffen, mit den untersuchten Techniken, als machbar heraus, wobei eine Weiterentwicklung des Prozesses sicherlich notwendig ist.

Zusammenfassend stellt die Herstellung von niederschmelzenden, ionischen Flüssigkeiten, Salzen oder Co-Kristallen eine geeignete Strategie dar, die Löslichkeit schlecht wasserlöslicher Substanzen zu verbessern und deren physikochemische Eigenschaften zu optimieren. Das Gegenion kann dabei dazu beitragen den Wirkstoff zu solubilisieren, wobei es sehr wahrscheinlich ist, dass er auch mit dem komplexen mizellaren System des menschlichen Verdauungstrakts interagiert. Trotzdem ist eine routinemäßige Salzbildung nicht in allen Fällen zielführend und alternative Technologien müssen entwickelt werden, um die Herrausforderungen mit unvorteilhaften physikochemischen Eigenschaften zu meistern. Die beschriebenen 2D/3D-Druckverfahren bieten hierbei eine Produktion variabler und vielfältiger Darreichungsformen und erweitern den Gestaltungsraum für neuartige Wirkstoffentwicklungen.

Chapter I: Amorphous ionic liquid strategies for pharmaceutical application

Marco Saedtler[1] and Lorenz Meinel[1]*

[1]Institute of Pharmacy and Food Chemistry, University of Würzburg,
Am Hubland, DE-97074 Würzburg, Germany

Introduction

Ionic liquids (IL) are salts with a melting point (T_m) or a glass transition (T_g) temperature below 100 °C.[1] Since the first description of air- and water stable imidazolium ILs in 1992, the field has diverged into different applications. The 1st generation of ILs are solvents with tunable physical properties in chemical synthesis deploying their non-volatile nature and thermal stability. The 2nd generation are IL-solvents tailoring chemical reactivity and solvation, thereby expanding chemical synthesis into liquid crystal development, biotechnology, analytics, extraction and other applications. The 3rd generation has been introduced as impacting biological properties for active pharmaceutical ingredients (API), e.g. when profiling APIs as IL through counterion design in an effort to control physical-chemical and pharmaceutical properties (e.g. dissolution rate) or providing additional functionality by using biologically active counterions (**Figure 1**). ILs are fully ionized with various transition states including co-crystal salts or deep eutectic mixtures. To this end, effective salt formation generally requires pK_a differences as of $\Delta pK_a \geq 3$, to ensure ionization. Otherwise, the formation of co-crystals may occur resulting in mixed crystals within which the API crystallizes with one or more of what is referred to as co-former. In contrast to ILs, the interaction in these systems is non-ionic and by hydrogen bonding and/or van-der-Waals interaction.
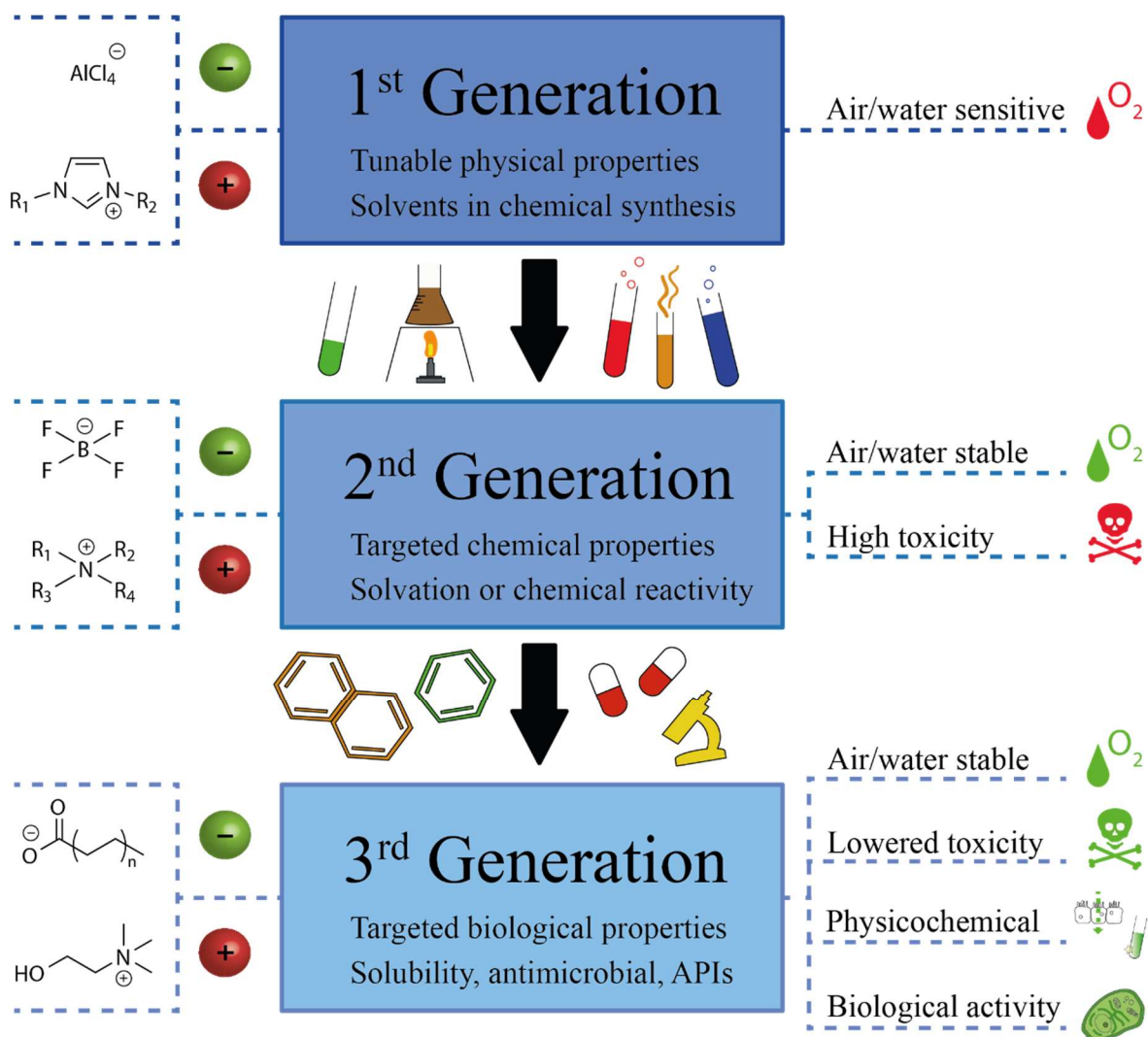
Figure 1 Categorization into three generations of Ionic Liquids in the development over the last decades. Adapted from Ref. [1].

Here, we focus on pharmaceutical application. The first IL with a bioactive molecule was reported in 1998, starting off from miconazole, an antifungal drug, being chemically modified into an imidazolium ion by alkylation, thereby introducing a permanent positive charge, which in return was paired with hexafluorophosphate resulting in an ionic liquid.[2] This study sparked an enormous interest in pharmaceutical application, leading to steadily increasing numbers of contributions in the upcoming years (**Figure 2**).
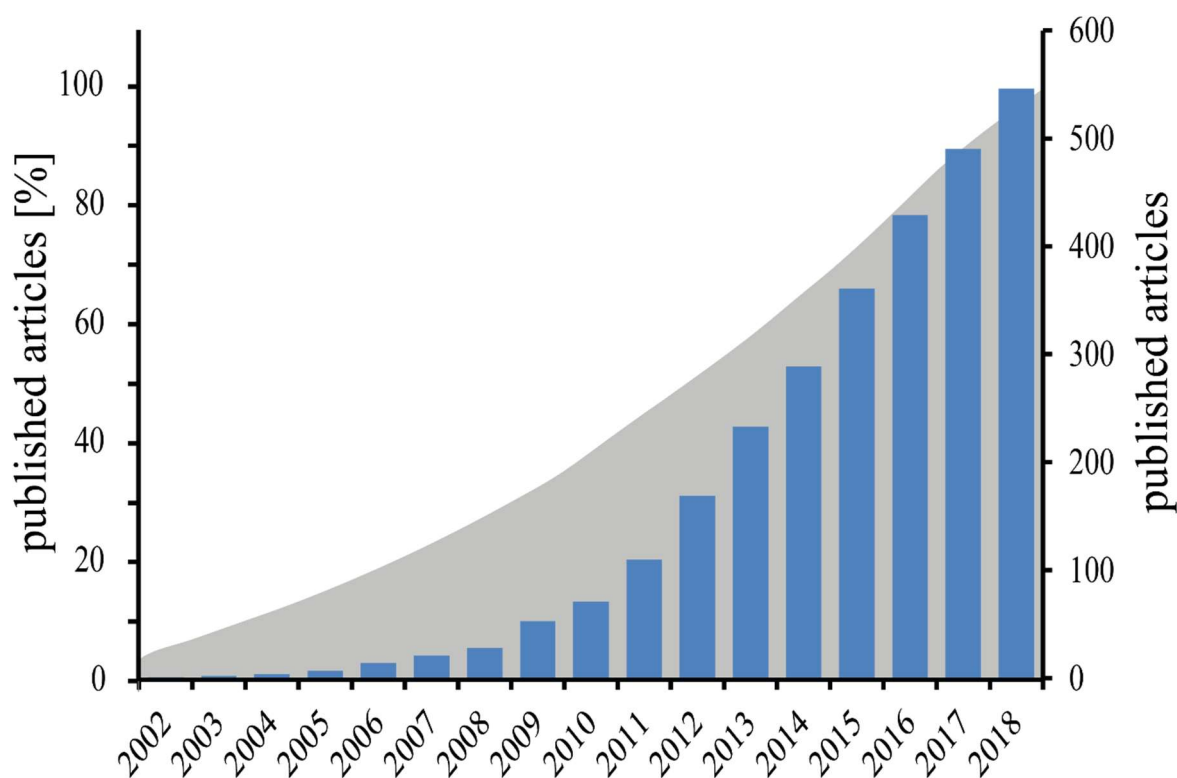
Figure 2 Blue columns represent articles published combining drugs and Ionic Liquids. Grey area represents articles dealing with drug formulations in the same time frame. Analysis performed on PubMed.gov (https://www.ncbi.nlm.nih.gov/pubmed/) using "Ionic Liquid(s) AND drug(s) or API(s)" and "pharmaceutical AND formulation".

Many of these studies detail rational counterion design addressing pharmaceutical challenges of APIs including poor water solubility and/or low permeability in an ultimate effort to improve bioavailability. Commonly used counterions are summarized (**Figure 3**). These API-ionic liquids (API-IL) were previously classified into those wherein (i) the counterion and the API are covalently attached to each other, those wherein (ii) a basic API forms ILs with acidic counterions or those wherein (iii) an acidic API forms ILs with basic counterions.[3] The pharmaceutical translation also benefits from recent regulatory guidelines such as issued by the Food and Drug Administration (FDA) detailing salt and co-crystals forms of APIs as present in ILs but also related images such as cocrystals. This article details the use of ILs to tune API physicochemical properties and highlights the aspects governing these properties. Excellent review articles are available covering related topics including cytotoxicity or environmental impact of ILs.[4-6]
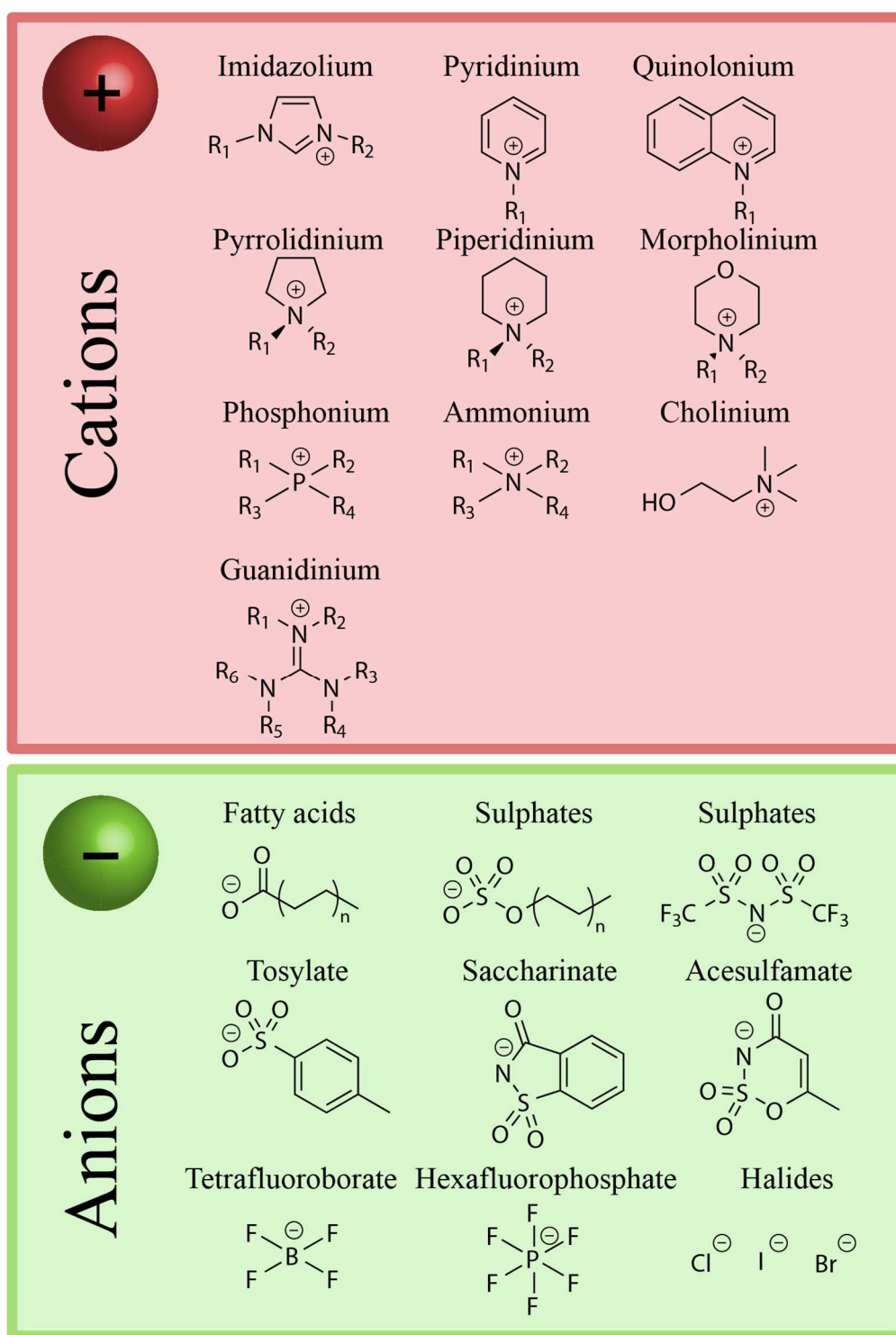
Figure 3 Commonly used cations and anions in the preparation of Ionic Liquids.

Physicochemical properties

The search for new drug candidates in high-throughput screenings principally favors the selection of poorly water-soluble compounds. Up to 70% of new APIs are poorly water-soluble and 40% of the marketed immediate release drugs are practically insoluble in water.[7] Of all APIs, approximately 50% are marketed as salts.[8] These salts often show favorable dissolution rates mainly as of the fact that the API's counterion originates from a strong base or acid. When exposed to water, a favorable pH is established by the counterion within the aqueous boundary layer (ABL) favoring the dissociation of the API in water and thereby its ability to interact with water molecules. Another strategy is to maximize the free enthalpy of the crystal to an extent that other pharmaceutical properties such as storage stability are still met, thereby facilitating the exit of molecules from the solid crystal into the aqueous surrounding phase leading into a faster dissolution rate and possibly exploitable supersaturation phenomena. It is at this interface at which ionic liquid strategies provide an interesting leverage in balancing the pH gradients within the ABL on the one hand and the free enthalpy within the crystal on the other hand (*vide infra*). The solubility of a compound as outlined by Yalkowsky et al. is critically impacted by its lipophilicity (logP) and melting point.[9] The resulting mathematic correlation is known as the General Solubility Equation (GSE) was developed for organic nonelectrolytes and it remains to be shown to which extent similar correlations on the melting point and lipophilicity and possibly more parameters are required to adequately predict the pharmaceutical performances of APIs as a function of counterion structure when presented as salts in ILs The actual extend in which assumptions from the GSE are valid for ILs has to be evaluated from the literature. For example, while the melting point of Flurbiprofen salts – a nonsteroidal anti-inflammatory drug (NSAID) – controlled by different ammonium counterions correlated with its aqueous solubility, no significant correlation was found between logP of the cation and the solubility of the resulting Flurbiprofen salt.[10] Contrasting these findings, Ampicillin – an antibiotic drug – was converted to ILs with different organic cations including ammonium-, phosphonium-, pyridinium- and imidazolium salts.[11] In these cases, the lipophilicity of the counterion inversely correlated with its solubility. While these results are contrary to each other regarding the lipophilicity of a salt, the impact of the melting point tends to be comparable to nonelectrolytes. Both of these aspects will be discussed in the following section, detailing their effects on dissolution and solubility. In general, a lower melting point correlates with

lower lattice forces within the crystalline structure hence more free enthalpy as compared to salts with higher melting points. Less interaction, less force drives the dissolution rate. In organic compounds these forces consist of Coulombic forces, van der Waals forces and hydrogen bonding dictating the lattice structure and the Gibbs-Energy or free enthalpy (G) required for phase transition (solid$_1$ → solid$_2$ or solid → solution) all of which typically being reflected by the melting point. Briefly, the free enthalpy is a reaction's thermodynamic potential and a process will be spontaneous if the difference (ΔG) between the free enthalpy of its final (G$_2$) and initial state (G$_1$) is negative (ΔG = G$_2$ – G$_1$ < 0). Judged from the Gibbs-Helmholtz Equation solubility is, therefore, driven by the transfer of enthalpy (ΔH) from the system to its environment and/or gain of entropy (ΔS) at a given temperature.

The change in enthalpy during dissolution (ΔH$_{diss}$) is the sum of three separate processes, namely the breaking of solute-solute interactions and solvent-solvent (ΔH$_{lattice}$) interactions (both endothermic) and the solvation of the solute (ΔH$_{solv}$) (exothermic). When converting a compound into an IL the solute-solute interactions (ΔH$_{lattice}$) as well as the entropy are affected. While the change in entropy (ΔS) decreases when dissolving an amorphous IL (due to higher disorder in an amorphous state e.g. as of the dissociation of the IL or disorder of surrounding water molecules), the spontaneous dissolution can be addressed to massive increase in ΔH which is contributed to a decrease in lattice free enthalpy ΔH$_{lattice}$ – which is the major hurdle during dissolution – and the solvation of the drug molecules by water ΔH$_{solv}$. This decrease in lattice forces leading to increased lattice energy can be achieved by using bulky counterions, disturbing the formation of an ordered crystalline lattice typically reflected by a decreased melting point.[12,13] However, in addition to these thermodynamic considerations, kinetic ones apply focusing on the diffusion of drug molecules from the surface of the compound into the bulk solution. In detail, when a compound dissolves from a solid matrix, a static aqueous boundary layer (ABL) is formed around it. This ABL is separating the solid phase from the bulk solution (**Figure 4**). Within this ABL a concentration gradient of the API is present, stretching from the saturated concentration of the compound at the crystal surface to the measured concentration (C) in the bulk solution. While the thickness (h) of this ABL is governed by viscosity and shear by the liquid medium, diffusion within this layer is the driving force for the drug molecules to move towards the bulk solution and as reflected in the Nernst-Brunner diffusion layer model (**Eq. 1**) with the dissolution rate (J) being a function of the diffusion coefficient (D) of the drug, the surface area (A), the thickness of the diffusion layer (h) as well as the drugs saturated concentration

in solution (C_s) and the measured bulk concentration (C).[14] This simplified equation reveals possibilities to influence the dissolution of a compound by increasing its overall exposed surface or reducing the thickness of the ABL e.g. by stirring. The Stokes-Einstein-Equation (**Eq. 2**) details the diffusion coefficient (D) using the Boltzmann-Constant (k_B), the absolute temperature (T), the dynamic viscosity of the medium (η) and the hydrodynamic radius of diffusing particles or molecules (r). Following this equation, the diffusion increases at higher temperatures, lower viscosity and smaller particle size.

$$J = \frac{dm}{dt} = \frac{DA}{h}(c_s - c) \tag{1}$$

$$D = \frac{k_B T}{6\eta\pi r} \tag{2}$$

While these aspects – governing the diffusion and thereby the dissolution of a drug – can hardly be controlled during the dissolution of an orally administered drug, salt formation with strong acids or bases was identified to positively influence the pH value within the ABL what is driving the dissolution rate. Along these lines, the salt of a basic drug, e.g. hydrochloride, will result in an acidic pH within the ABL, thereby favoring the protonation hence thermodynamic solubility of the basic API and vice versa for acidic APIs when salt formation was e.g. with sodium hydroxide. Therefore, a counterion from a strong base or strong acid impacts the pH in the ABL more effectively driving the dissolution rate, as compared to the bulky and typically less strong counterions which are used for ILs. Thereby, the aforementioned positive impact of the ILs on the dissolution rate by increasing the free enthalpy within the crystal are in part counteracted by their less effective pH control in the ABL– two sides of the same coin which need to be balanced during development. In addition, other parameters possibly impact the performances in the ABL, including precipitation of the API in its free form resulting in insoluble layers limiting diffusion from the API crystal or supersaturation within the API of the free form.[15]
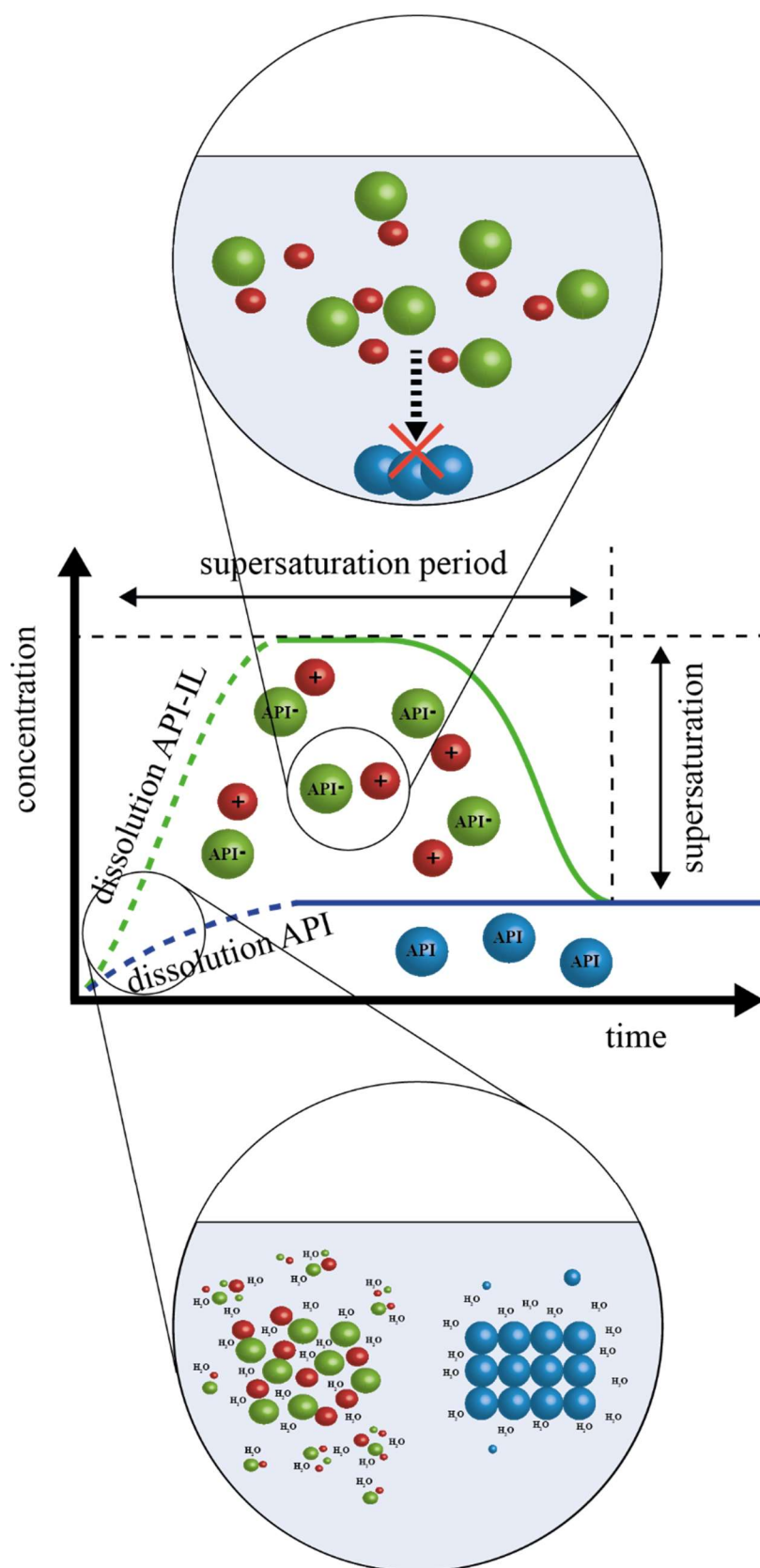
Figure 4 Overview of dissolution and kinetic solubility of active pharmaceutical ingredients in neutral form and formulated as Ionic Liquid.

Once the API diffuses from the ABL into the surrounding bulk solution, aggregation phenomena critically impact supersaturation phenomena. Along these lines, we are using the following terms to detail API solubility within bulk. Solubility is used for the thermodynamic / equilibrium solubility covering ionized and non-ionized species of a base or acid. Intrinsic solubility is the equilibrium solubility of the non-ionized form and kinetic solubility is the solubility measured at visible precipitation which can be metastable and reflect e.g. supersaturation. Particularly for ionic liquids the formation of soluble API/counterion aggregates has been reported in the ABL and it is this aspect which provides another leverage accessible by the IL strategy.[16,17] The goal is to impact the kinetic solubility in solution by mediating metastable supersaturation throughout pharmaceutically relevant time frames thereby increasing API bioavailability. Some interesting studies point in this direction. For example, supramolecular structures in solution have been reported for 1-dodecyl-3-methylimidazolium Ibuprofenate.[16] While in higher concentrations smaller micelles (1-5 nm) were formed, larger aggregates (100-400 nm) were observed during dilution. ^{1}H NMR studies revealed the role of π-π, cation-π and H-bonding interactions. This complexed / aggregated but soluble state showed to transiently keep the API in solution, a process confirmed by others who assigned the increase in kinetic solubility to cation and API supramolecular assemblies in solution. Furthermore, the authors demonstrated a "self-stabilizing mechanism" in that the aggregating API increased the cation/API ratio over time (the counterion was soluble in water) while at the same time showing that an increase in this ratio increased the kinetic solubility and stability of the API complexes in solution.[17] In fact, that mechanism might be particularly interesting when it comes to stabilizing the supersaturated state for longer time frames. In another study, this mechanism was corroborated for five nonsteroidal anti-inflammatory drugs (NSAIDs) and tetrabutylphosphonium yielding ILs and room-temperature Ionic Liquids (RT-IL) with up to 130-fold and 1000-fold improvement for the kinetic solubility and dissolution rates, respectively, and as compared to the neutral form.[18] Sometimes, such aggregates might lead to misinterpretation of increased thermodynamic solubility whereas in fact this resulted from dissolution of invisible aggregates e.g. when acetonitrile is used in preparing the samples for HPLC analysis. Thereby water-insoluble aggregates dissolve and are interpreted as water soluble. Most studies have been conducted in aqueous buffer systems. However, a recent study on the solubilization of the basic drug Imatinib in simulated intestinal fluids exhibited a complex system of biological colloids and aggregation within these bio relevant media.[19]

These findings suggest the importance of studies in presence of biologically relevant media including media mimicking the human intestinal fluid (**Figure 5**). The impact of the Ionic Liquid strategy on the intestinal absorption and its bio relevance was confirmed *in vivo* when studying the pharmacokinetics of API-ILs after oral application to rats.[20] Briefly, a library consisting of 36 ammonium and phosphonium cations was paired with an acidic poorly water-soluble drug (PWSD) Selurampanel. Experimentally determined dissolution rates and time spans with supersaturation were successfully predicted from algorithms built off these data sets. Furthermore, the study reported a proof of concept to build different release profiles through counterion design and these sustained release profiles were confirmed in rats after oral dosage of the API-IL. The extent to which pharmacokinetics can be tailored through - excipient free - IL / API complexes arguably needs more studies to discuss a design space for this aspect which in addition might be very specific to the respective API. Several studies investigated the impact of the hydrophilic-lipophilic balance of an IL on its water solubility and highlight the tuneability of ILs to challenge specific tasks of delivery.[20,21] The recently rising interest in choline – a natural occurring quaternary ammonium ion – is based on its favorable toxicological profile and the possibility to formulate ILs and RT-ILs with acidic drugs resulting in improved solubility compared to their neutral form.[22,23] While natural or generally recognized as safe (GRAS) counterions are considered to be non-toxic and straightforward in a potential drug approval, ILs from these still need a full toxicological assessment as the impact of aggregation and thereby distribution and accumulation within the body have to be examined. The investigation for such anionic candidates is not yet complete and reviewing studies on ILs in the last two decades revealed that most effort is put into the development of different cations. Nonetheless, it has been shown that water interaction of ILs is of course influenced by the anion and has to be considered when tailoring for example IL solvents in which the API is dissolved.[24] Several studies used such ILs as drug reservoir resulting in sustained release or longer analgesic effects.[1,12,25] Regarding a possible usage for API-free ILs as solvents for APIs or combination of cationic APIs with anions, more studies are necessary to detail the role of the anion in these formulations and to identify potential non-toxic candidates for counterion development.
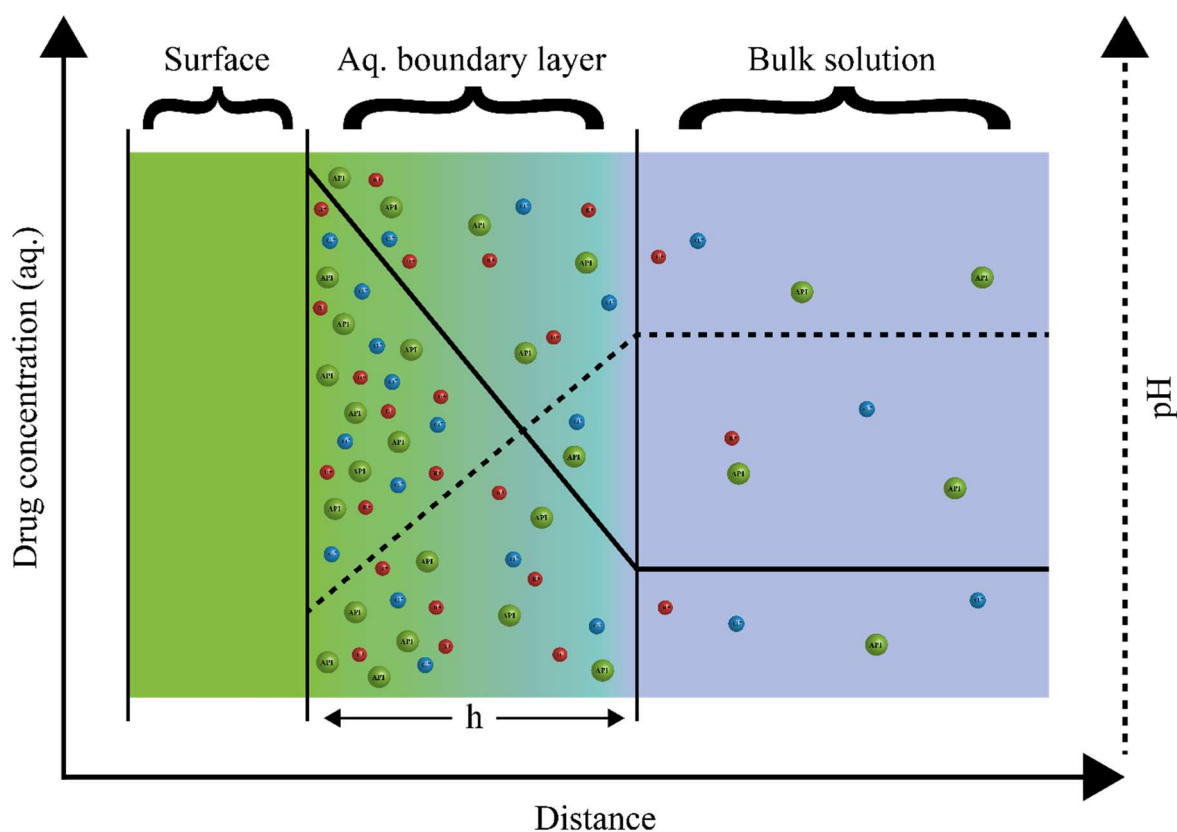
Figure 5 Aqueous Boundary Layer as observed on the surface of dissolving drugs. The solid line represents drug concentration and the dashed line the theoretical pH.

Besides dissolution rate and solubility of salt entities, stability as one of the major concerns during API development and affected by salt selection. For example, physical instability as of polymorphism may challenge the pharmaceutical quality of a drug, potentially yielding crystal forms with different dissolution rates and biopharmaceutical performances. It is for this reason, that the polymorph with the lowest crystal energy is typically selected for pharmaceutical development.[26] A prominent example, Ranitidine hydrochloride was patented as Polymorph 1. Subsequent production batches, however, yielded another, more stable Polymorph 2 which was not covered by the original patent.[27] When Ranitidine, Lidocaine and Ibuprofen were prepared as ILs yielding three room temperature Ionic Liquids, an advantage of these RT-ILs within the context of Ranitidine's patenting history was the absence of polymorphs resulting from their liquid state at room temperature.[1] While liquid IL formulations can be a potential solution for polymorphism, hygroscopicity is another aspect of particular interest when studying the long-term storage of solid drug entities. Following this consideration it was shown that hygroscopic procaininium acetate IL with a T_g = -25 °C was observed to form a dihydrate in the presence of water with a

T_m = 52 °C.[28] Therefore, one potential caveat with IL salts might result from their hygroscopic nature compared to their free form, that can lead to deliquescence during storage and formation of hydrates.[29] However, this is not always the case. For example, lower water sorption was observed for a series of 36 different ammonium- and phosphonium ILs.[18,20] Some of these ILs were reported stable for up to 6 months when stored at 25 ± 1 °C and 50 ± 5% relative humidity.[20] Keeping in mind that solubility and therefore bioavailability might be changing between different polymorphs of an IL, highlights the importance of studies on storage stability. Furthermore, these findings demonstrated that hygroscopicity is a property that is "tailored".

Permeation

The impact of ILs on permeation enhancement of APIs by complex formation and simultaneous transport through biological barriers has been previously reported.[30,31] Several studies reported higher lipophilic partitioning or permeation of ILs through artificial and cellular membranes, while others did not observe this effect. For example, Tetracycline was paired with docusate to tailor its hydrophilicity and the resulting IL was compared to the hydrochloride salt for water solubility as well as octanol-water and liposome-water partitioning.[32] The tetracycline IL had a reduced solubility as compared to the chloride salt but tetracycline released form the IL partitioned more strongly into the lipophilic phase. Similarly, when the counterion decreases the lipophilicity of a salt aggregate - as observed for the basic API Imatinib formulated, as co-crystal and co-crystal salt with Syringic acid - an increase in kinetic solubility was observed but in this case no impact on permeation through artificial membranes or Caco-2 cell monolayers was reported.[33] Another study reported similar outcome with an entirely different approach. The study used ionic liquids as a formulation base within which compounds were diluted and tested on silicone membranes and tissue culture.[30] Extending these observations to tissue culture, the model compounds Mannitol and Cefadroxil were delivered deeper into and more effectively through porcine skin when spiked into and co-administered with tetraalkylphosphonium oleat, hexanoate or geranate as well as cholinium geranate ILs.[34] Particularly cholinium geranate showed a 16-fold increased delivery of Cefadroxil into deep tissue, while no skin irritation was observed. A comparable observation was shown when ILs derived from aliphatic carboxylic acids and aliphatic amines showed enhanced skin permeation of the model drug phenol red on abdominal skin of rats.[35] Another interesting approach combined

two APIs to enhance their mutual permeation. In this study simultaneous transport was shown for a "deep eutectic liquid co-crystal" prepared from Lidocaine and Ibuprofen. The authors claimed that the mechanism was by complexation through strong hydrogen bonding between the two entities and that this interaction at least in part lasted in solution. The permeation of the complex was higher, but lower as observed for the respective neutral forms.[31] The above mentioned studies reveal the role of hydrogen bonded complexes formed between the API and its counterion or co-former in solution. Though the results considering permeability of these complexes through artificial membranes, skin or *in vitro* Caco-2 monolayers are inconsistent, their formation in solution was well studied by ^{1}H-NMR in a recent study.[33]

Although no IL formulation has reached the point of regulatory approval yet, an IL formed from Lidocaine and Etodolac has already been tested in clinical trials. This formulation showed significantly higher *in vitro* skin permeation for Etodolac when applied to the skin in the complex with Lidocaine. Lidocaine permeation, however, was not affected, leading the authors to the assumption that lidocaine "self-sacrificially improves the skin permeation of Etodolac".[36] The Phase I trial studying the pharmacokinetics and safety of Etodolac-Lidocaine IL patches yielded promising results with 6-fold enhanced exposure while no serious adverse events were observed.[37] In November 2016 the project was terminated by the sponsor MEDRx.[6,38]

Conclusion

Ionic Liquids offer tailored physicochemical properties without changing the chemical structure of the API (**Figure 6**). Release profiles of drugs can be controlled, lasting from immediate release to sustained release and without the necessity of drug dosage forms. Furthermore, the biopharmaceutical properties including permeation through epithelial barriers and skin can be effectively addressed by forming selected ILs. In addition, incomplete dissociation of the IL after dissolution substantially affect supersaturated states in solution, occasionally leading to increased kinetic solubility and to an extent, that new convenient routes of administration may become feasible for APIs when presented as ILs. It is for these supramolecular complexes in solution that exciting novel functionalities may be introduced to a given API and future studies will further link the dynamics in solution with bioavailability and perhaps the prediction of bioavailability from algorithms.
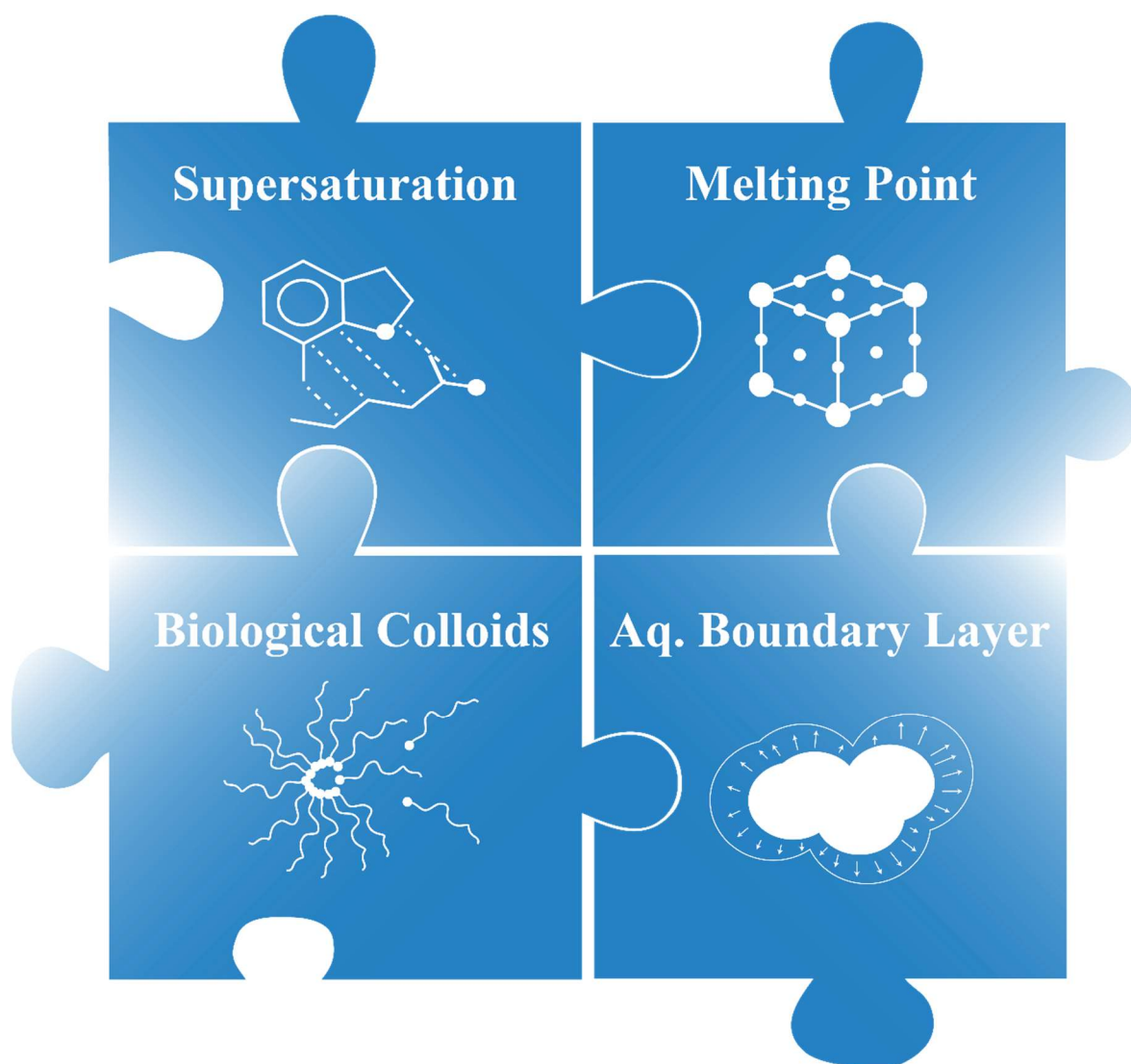
Figure 6 Summary of all four major aspects covered within this chapter. Supersaturation controls aggregation and kinetic solubility; Melting Point reflects the lattice structure and lattice forces; Aqueous Boundary Layer influences pH and dissolution rate; Biological Colloids affect drug aggregation and solubilization.

References

1. Hough, W.L., Smiglak, M., Rodríguez, H., Swatloski, R.P., Spear, S.K., Daly, D.T., Pernak, J., Grisel, J.E., Carliss, R.D., Soutullo, M.D., Davis, J.J.H.,Rogers, R.D.: The third evolution of ionic liquids: active pharmaceutical ingredients. New J. Chem. **31**, 1429 (2007)

2. Davis, J.H., Forrester, K.J.,Merrigan, T.: Novel organic ionic liquids (OILs) incorporating cations derived from the antifungal drug miconazole. Tetrahedron Lett. **39**, 8955-8958 (1998)

3. Egorova, K.S., Seitkalieva, M.M., Posvyatenko, A.V., Khrustalev, V.N.,Ananikov, V.P.: Cytotoxic Activity of Salicylic Acid-Containing Drug Models with Ionic and Covalent Binding. ACS Med. Chem. Lett. **6**, 1099-104 (2015)

4. Balk, A., Holzgrabe, U.,Meinel, L.: 'Pro et contra' ionic liquid drugs - Challenges and opportunities for pharmaceutical translation. Eur. J. Pharm. Biopharm. **94**, 291-304 (2015)

5. Marrucho, I.M., Branco, L.C.,Rebelo, L.P.: Ionic liquids in pharmaceutical applications. Annu. Rev. Chem. Biomol. Eng. **5**, 527-46 (2014)

6. Egorova, K.S., Gordeev, E.G.,Ananikov, V.P.: Biological Activity of Ionic Liquids and Their Application in Pharmaceutics and Medicine. Chem. Rev. **117**, 7132-7189 (2017)

7. Kawabata, Y., Wada, K., Nakatani, M., Yamada, S.,Onoue, S.: Formulation design for poorly water-soluble drugs based on biopharmaceutics classification system: basic approaches and practical applications. Int. J. Pharm. **420**, 1-10 (2011)

8. Stahl, P.H.,Wermuth, C.G.: Handbook of Pharmaceutical Salts: Properties, Selection, and Use. 2nd Ed. Zurich: Wiley-VCH, VHCA, Weinheim (2011)

9. Jain, N., Yang, G., Machatha, S.G.,Yalkowsky, S.H.: Estimation of the aqueous solubility of weak electrolytes. Int. J. Pharm. **319**, 169-71 (2006)

10. Anderson, B.D.,Conradi, R.A.: Predictive Relationships in the Water Solubility of Salts of a Nonsteroidal Anti-Inflammatory Drug. J. Pharm. Sci. **74**, 815-820 (1985)

11. Florindo, C., Araujo, J.M., Alves, F., Matos, C., Ferraz, R., Prudencio, C., Noronha, J.P., Petrovski, Z., Branco, L., Rebelo, L.P.,Marrucho, I.M.: Evaluation of solubility and partition properties of ampicillin-based ionic liquids. Int. J. Pharm. **456**, 553-9 (2013)

12. Stoimenovski, J., MacFarlane, D.R., Bica, K.,Rogers, R.D.: Crystalline vs. ionic liquid salt forms of active pharmaceutical ingredients: a position paper. Pharm. Res. **27**, 521-6 (2010)

13. Prakasha, A.S.: The counter ion: expanding excipient functionality. J. Excipients Food Chem. **2**, 28-40 (2011)

14. Higuchi, W.I.: Diffusional Models Useful in Biopharmaceutics. J. Pharm. Sci. **56**, 315-324 (1967)

15. Serajuddin, A.T.: Salt formation to improve drug solubility. Adv. Drug. Deliv. Rev. **59**, 603-16 (2007)

16. Sanan, R., Kaur, R.,Mahajan, R.K.: Micellar transitions in catanionic ionic liquid–ibuprofen aqueous mixtures; effects of composition and dilution. RSC Adv. **4**, 64877-64889 (2014)

17. Balk, A., Widmer, T., Wiest, J., Bruhn, H., Rybak, J.C., Matthes, P., Muller-Buschbaum, K., Sakalis, A., Luhmann, T., Berghausen, J., Holzgrabe, U., Galli, B.,Meinel, L.: Ionic liquid versus prodrug strategy to address formulation challenges. Pharm. Res. **32**, 2154-67 (2015)

18. Balk, A., Wiest, J., Widmer, T., Galli, B., Holzgrabe, U.,Meinel, L.: Transformation of acidic poorly water soluble drugs into ionic liquids. Eur. J. Pharm. Biopharm. **94**, 73-82 (2015)

19. Wiest, J., Saedtler, M., Bottcher, B., Grune, M., Reggane, M., Galli, B., Holzgrabe, U.,Meinel, L.: Geometrical and Structural Dynamics of Imatinib within Biorelevant Colloids. Mol. Pharm. **15**, 4470-4480 (2018)

20. Wiest, J., Saedtler, M., Balk, A., Merget, B., Widmer, T., Bruhn, H., Raccuglia, M., Walid, E., Picard, F., Stopper, H., Dekant, W., Luhmann, T., Sotriffer, C., Galli, B., Holzgrabe, U.,Meinel, L.: Mapping the pharmaceutical design space by amorphous ionic liquid strategies. J. Control. Release **268**, 314-322 (2017)

21. McCrary, P.D., Beasley, P.A., Gurau, G., Narita, A., Barber, P.S., Cojocaru, O.A.,Rogers, R.D.: Drug specific, tuning of an ionic liquid's hydrophilic–lipophilic balance to improve water solubility of poorly soluble active pharmaceutical ingredients. New J. Chem. **37**, 2196 (2013)

22. Shadid, M., Gurau, G., Shamshina, J.L., Chuang, B.C., Hailu, S., Guan, E., Chowdhury, S.K., Wu, J.T., Rizvi, S.A.A., Griffin, R.J.,Rogers, R.D.: Sulfasalazine in ionic liquid form with improved solubility and exposure. MedChemComm **6**, 1837-1841 (2015)

23. Araújo, J.M.M., Florindo, C., Pereiro, A.B., Vieira, N.S.M., Matias, A.A., Duarte, C.M.M., Rebelo, L.P.N.,Marrucho, I.M.: Cholinium-based ionic liquids with pharmaceutically active anions. RSC Adv. **4**, 28126-28132 (2014)

24. Khan, I., Kurnia, K.A., Mutelet, F., Pinho, S.P.,Coutinho, J.A.: Probing the interactions between ionic liquids and water: experimental and quantum chemical approach. J. Phys. Chem. B. **118**, 1848-60 (2014)

25. Jaitely, V., Karatas, A.,Florence, A.T.: Water-immiscible room temperature ionic liquids (RTILs) as drug reservoirs for controlled release. Int. J. Pharm. **354**, 168-73 (2008)

26. Singhal, D.,Curatolo, W.: Drug polymorphism and dosage form design: a practical perspective. Adv. Drug. Deliv. Rev. **56**, 335-47 (2004)

27. Bucar, D.K., Lancaster, R.W.,Bernstein, J.: Disappearing polymorphs revisited. Angew. Chem. Int. Ed. Engl. **54**, 6972-93 (2015)

28. Cojocaru, O.A., Kelley, S.P., Gurau, G.,Rogers, R.D.: Procainium Acetate Versus Procainium Acetate Dihydrate: Irreversible Crystallization of a Room-Temperature Active Pharmaceutical-Ingredient Ionic Liquid upon Hydration. Cryst. Growth Des. **13**, 3290-3293 (2013)

29. Newman, A.W., Reutzel-Edens, S.M.,Zografi, G.: Characterization of the "hygroscopic" properties of active pharmaceutical ingredients. J. Pharm. Sci. **97**, 1047-59 (2008)

30. Stoimenovski, J.,MacFarlane, D.R.: Enhanced membrane transport of pharmaceutically active protic ionic liquids. Chem. Commun. (Camb.) **47**, 11429-31 (2011)

31. Wang, H., Gurau, G., Shamshina, J., Cojocaru, O.A., Janikowski, J., MacFarlane, D.R., Davis, J.H.,Rogers, R.D.: Simultaneous membrane transport of two active pharmaceutical ingredients by charge assisted hydrogen bond complex formation. Chem. Sci. **5**, 3449 (2014)

32. Alves, F., Oliveira, F.S., Schroder, B., Matos, C.,Marrucho, I.M.: Synthesis, characterization, and liposome partition of a novel tetracycline derivative using the ionic liquids framework. J. Pharm. Sci. **102**, 1504-12 (2013)

33. Reggane, M., Wiest, J., Saedtler, M., Harlacher, C., Gutmann, M., Zottnick, S.H., Piechon, P., Dix, I., Muller-Buschbaum, K., Holzgrabe, U., Meinel, L.,Galli, B.: Bioinspired co-crystals of Imatinib providing enhanced kinetic solubility. Eur. J. Pharm. Biopharm. **128**, 290-299 (2018)

34. Zakrewsky, M., Lovejoy, K.S., Kern, T.L., Miller, T.E., Le, V., Nagy, A., Goumas, A.M., Iyer, R.S., Del Sesto, R.E., Koppisch, A.T., Fox, D.T.,Mitragotri, S.: Ionic liquids as a class

of materials for transdermal delivery and pathogen neutralization. Proc. Natl. Acad. Sci. U S A **111**, 13313-8 (2014)

35.   Kubota, K., Shibata, A.,Yamaguchi, T.: The molecular assembly of the ionic liquid/aliphatic carboxylic acid/aliphatic amine as effective and safety transdermal permeation enhancers. Eur. J. Pharm. Sci. **86**, 75-83 (2016)

36.   Miwa, Y., Hamamoto, H.,Ishida, T.: Lidocaine self-sacrificially improves the skin permeation of the acidic and poorly water-soluble drug etodolac via its transformation into an ionic liquid. Eur. J. Pharm. Biopharm. **102**, 92-100 (2016)

37.   Miwa, Y., Hamamoto, H., Hikake, S.,Kuwabara, Y.: A phase I, randomized, open-label, cross-over study of the pharmacokinetics, dermal tolerability, and safety of MRX-7EAT Etodolac-Lidocaine Topical Patch in healthy volunteers. The Journal of Pain **14**, S72 (2013)

38.   Kuwabara, Y., Hamamoto, H., Hikake, S.,Miwa, Y.: A randomized, multi-Center, double-blind, placebo-controlled phase II/III trial to evaluate the efficacy, tolerability and safety of MRX-7EAT Etodolac-Lidocaine Topical Patch in the treatment of pain. The Journal of Pain **14**, S73 (2013)

Chapter II: Geometrical and structural dynamics of Imatinib within biorelevant colloids

Johannes Wiest[1], Marco Saedtler[1], Bettina Böttcher[2], Marvin Grüne[3], Maude Reggane[4], Bruno Galli[4], Ulrike Holzgrabe[1] and Lorenz Meinel[1]*

[1]Institute of Pharmacy and Food Chemistry, University of Würzburg,

Am Hubland, DE-97074 Würzburg, Germany,

[2]Department of Biochemistry, Rudolf Virchow Center, University of Würzburg,

Josef-Schneider-Straße 2, DE-97080 Würzburg, Germany,

[3]Institute of Organic Chemistry, University of Würzburg,

Am Hubland, DE-97074 Würzburg, Germany,

[4]Novartis Pharma AG, Lichtstraße 35, CH-4002 Basel, Switzerland
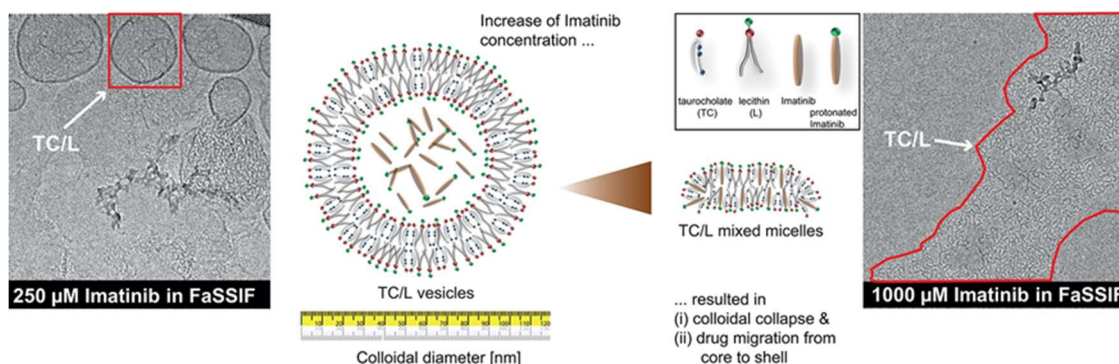
Abstract

Solubilization of lipophilic drugs is essential for efficient uptake. We detail the solubilization of imatinib in simulated gastrointestinal fluids containing taurocholate (TC) and lecithin (L) and reflecting fasted versus fed states using NMR spectroscopy, X-ray diffractometry, transmission electron microscopy, and dynamic light scattering analysis. Imatinib concentration impacted colloidal geometries and molecular dynamics in a fasted state. At drug substance concentrations up to 250 µM, imatinib was mainly engulfed within the core of >110 nm in diameter vesicles. At higher drug concentrations, the colloids collapsed to <40 nm, and imatinib migrated into the shell of the micelles, mainly being associated with the lipophilic face of TC but not with L. Simulating the fed state resulted in the formation of small micelles independent of the drug concentration. Furthermore, a hydrogel was formed, effectively keeping the drug substance in an amorphous state even when stressed by drying. In conclusion, this study detailed the fascinating dynamics of colloidal structures and molecular assembly as a function of imatinib concentration in biorelevant conditions. This approach may provide a blueprint for the rational development of future pharmaceutical formulations, taking the molecular interactions with bile salts/phospholipids into account.

Introduction

Drug absorption in the gastrointestinal tract is critically impacted by physiological solubilization.[1-3] In return, solubilization is impacted by bile, which is continuously formed by hepatic cells, stored and concentrated in the gallbladder, and secreted into the duodenum.[4-6] Along with a dynamic composition of electrolytes, organic anions, lipids (phospholipids, cholesterol), and water, bile contains bile acids, which are steroid acids conjugated with taurine and glycine.[5] About 90% of these bile acids are actively recycled through reabsorption by an ileal, apical sodium-dependent bile salt transporter. A smaller proportion is metabolized by bacteria to be more lipophilic, passively reabsorbing secondary bile acids.[6,7] The remarkable solubilization potential of bile salts is because of their amphipathic nature, driving the systemic availability of some vitamins or poorly water-soluble drugs.[8-10] Within the context of drug absorption, a recent study detailed the formation of mixed micelles between an amphiphilic drug and taurocholate (TC) in simulated intestinal fluid.[11] It is for their paramount role in solubilization, hence drug absorption for poorly water-soluble drugs, why a mechanistic understanding of interactions of bile salts with drugs

and/or lecithin (L) is desirable. It stands to reason to which extent such insight will fuel future formulation strategies for poorly water-soluble drugs, and to which extent a targeted exploitation of the biological solubilization processes will be efficient for pharmacokinetic improvement.[12-14] For that, we are presenting a study using the tyrosine-kinase inhibitor imatinib in an effort to detail its solubilization by bile salts and L on a molecular level amenable by nuclear magnetic resonance (NMR) spectroscopy but not more frequently used methods in this context, including scattering or imaging techniques. Imatinib is marketed as its mesylate salt, with a mean absolute bioavailability of 98% (capsule formulation) and high variability in AUC levels after oral dosing. When given with high fat meal (triggering the emptying of the gall bladder), the t_{max} value is prolonged by 1.5 h.[15] The fate of imatinib, in terms of aggregation, interaction with TC and/or L, as well as solubilization, was tested in buffers and biorelevant dissolution media simulating fasting conditions (FaSSIF) and fed conditions (FeSSIF) in the proximal small intestine, respectively,[16,17] using NMR spectroscopy, dynamic light scattering (DLS), and cryo-electron microscopy.
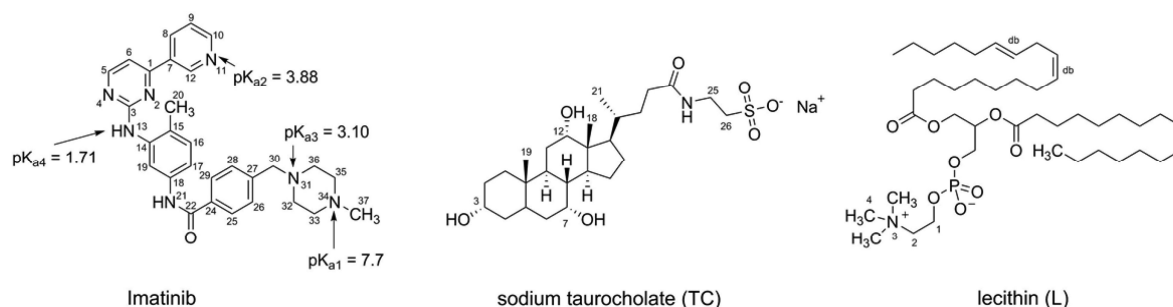

Figure 1 Chemical structure of imatinib, sodium taurocholate (TC), and lecithin (L). pK_a values of imatinib were previously reported.[24]

Materials

Imatinib mesylate was kindly provided from Novartis Pharma AG (Basel, Switzerland). FaSSIF/FeSSIF/ FaSSGF instant powder was purchased from biorelevant.com (London, UK). HPLC grade water was obtained by an inhouse Millipore system from Merck (Darmstadt, Germany). Deuterated water (D_2O, 99.9% D) and deuterated acetic acid$_4$ (99.5% D) were purchased from Deutero GmbH (Kastellaun, Germany). Sodium deuteroxide (40%) in deuterated water (NaOD, 99% D), 35% deuterium chloride in deuterated water (DCl, 99% D), 85% deuterated phosphoric acid-d$_3$ in deuterated water (D_3PO_4, 98% D), deuterated water (D_2O, 99.9% D) containing 0.05% 3-(trimethylsilyl)propionic2,2,3,3-d$_4$ sodium salt (TSP-d$_4$), sodium chloride (99%), and

monobasic sodium phosphate anhydrous (99%) were purchased from Sigma-Aldrich (Schnelldorf, Germany). Hexadeuteriodimethyl sulfoxide (DMSO-d$_6$, 99.8% D) was purchased from Euriso-top (Saarbrücken, Germany). Monobasic sodium phosphate monohydrate (99%) was purchased from Gruessing (Filsum, Germany). Dibasic sodium phosphate anhydrous (99%) was purchased from Acros Organics (Geel, Belgium). Tween 80 was purchased from Caelo (Hilden, Germany). Standard 5 mm NMR tubes (400 MHz/900 MHz) and coaxial insert tubes were purchased from Norell (Landisville, PA).

Methods

Preparation of Imatinib Free Base

The free base was prepared by addition of 2.5 mL of aqueous sodium hydroxide (1 M) to 1 g of imatinib mesylate dissolved in 10 mL of water. The precipitate was filtered and washed with water. The crude product was recrystallized in methanol, filtered, and dried in vacuo. The identity and purity of the product was confirmed by ^{1}H/^{13}C NMR spectroscopy, HPLC, and XRPD.

NMR Measurement

Concentration dependent ^{1}H NMR measurements were performed on a Bruker Avance 400 MHz spectrometer (Karlsruhe, Germany) operating at 400.13 MHz with a BBO BB-H 5 mm probe head, and data processing was done with the software TopSpin 3.0. The temperature was adjusted with a BCU-05 (Bruker) temperature control unit. For ^{1}H NMR, the acquisition parameters were applied as follows: 1024 scans, at a temperature of 300 K, flip angle of 30°, spectral width of 20.55 ppm, and transmitter offset of 6.175 ppm. The acquisition time was set to 3.985 s followed by a relaxation delay of 1.0 s with collection of 64 000 data points at a sample spinning frequency of 20 Hz. Processing parameters were set to an exponential line broadening window function of 0.3 Hz, an automatic baseline correction, and manual phasing. The spectra were referenced to the external standard of 0.05% 3-(trimethylsilyl)propionic-2,2,3,3-d$_4$ sodium salt (TSP-d$_4$) in D$_2$O filled in a coaxial insert tube.

The 2D NOESY spectra of 1000 µM and 250 µM imatinib in FaSSIF were recorded with a Bruker 600 MHz Avance III HD NMR spectrometer using a 5 mm cryo-probe and the pulse sequence noesygpphpr in the phase-sensitive mode with States-TPPI, presaturation of the

residual HDO signal during the relaxation delay and the mixing time, and with a pulsed magnetic field gradient in the mixing time. The spectra were recorded at 298 K with a spectral width of 9.43 ppm, 8K data points in the t2 time domain and 280 t1 increments, 24 transients for each t1 increment, and a relaxation delay of 3.0 s. Mixing times of 20, 40, 80, 200, and 500 ms were used for each sample to ensure discrimination between cross-relaxation and spin-diffusion. The data were processed using squared cosine window functions, zero-filling in both dimensions, and linear prediction in the t1 dimension prior to Fourier transformation. A manual phase correction and an automatic baseline correction in both dimensions were performed. DOSY NMR data were measured at 298 K with a Bruker Avance III HD 600 spectrometer and a 5 mm BBFO probe containing a z-axis gradient coil with a maximum gradient strength of 50 G cm^{-1}. To avoid the influence of convection effects on the results (due to temperature gradients in the coil of the probe), two different pulse sequences were used. On the one hand, the stimulated echo BPP-LED pulse sequence (longitudinal eddy current delay sequence with bipolar gradient pulse pairs for diffusion and additional spoil gradients after the second and fourth 90° pulse) was applied.[18] Therein, the convection in z-direction was suppressed by rotation of the sample.[19,20] On the other hand, experiments were performed using a corresponding double stimulated echo pulse sequence (without sample rotation and with spoil gradients after the second, fourth, and sixth 90° pulse) in which the convection compensation was achieved by the double stimulated echo pulse train.[21] The "smoothed square" diffusion gradients were linearly incremented from 2 to 98% in 16 steps. The eddy current delay was set to 5 ms. Diffusion times Δ of 50 or 150 ms and durations δ of a bipolar gradient pulse between 7.5 and 10 ms were used. The diffusion coefficients were obtained by Levenberg− Marquardt fittings (using the Bruker software Topspin 3.0) of the signal intensities versus the gradient strength. No differences between both pulse sequences were observed, the reported diffusion constants were obtained from the measurements with the BPP-LED pulse sequence.

Preparation of 50 mM Sodium Phosphate Buffer pH 2, 4, 7.4 in D$_2$O.

For pH 7.4, a 50 mM solution of dibasic sodium phosphate in D$_2$O was prepared, and the pH was adjusted with NaOD or D$_3$PO$_4$ to pD 7.81 (= pH 7.4).[22] For pH 2 and 4, a 50 mM solution of dibasic sodium phosphate in D$_2$O was prepared, and the pH was adjusted with D$_3$PO$_4$ to pD 2.41 (= pH 2) and 4.41 (= pH 4).

Aggregation Assay

The aggregation assay of LaPlante et al. was used for determination of the critical aggregation concentration (CAC).[23] For simulating biorelevant concentrations of imatinib, the concentration was increased up to the nominal concentration of 1000 μM. The standard dose of 400 mg per day of imatinib mesylate (M_r = 589.7 g/mol) would result in a maximum intestinal concentration of about 1400 μM using an estimated intestinal volume of 500 mL. The dilution series used here was to cover that concentration range and below in an effort to address natural absorption/dilution in the intestinal passage. Briefly, a 100 mM stock solution of imatinib free base in DMSO-d_6 was prepared, and 15 μL was added to 1500 μL of buffer (solvent switch method). According to the dilution scheme of LaPlante, six samples were obtained for each media (1000 μM − 1000 μM + tween 80−500 μM − 250 μM − 125 μM − 62.5 μM). Detailed information on the assay is provided in **Scheme S1**.

Preparation of FaSSIF and FeSSIF in Deuterated Water

FaSSIF and FeSSIF were prepared according to the protocol of biorelevance, except for using deuterated water and DCl/NaOD. The pD was adjusted to 6.91 for FaSSIF (pH 6.5) and 5.41 for FeSSIF (pH 5). A phosphate buffer analogous to FaSSIF and an acetate buffer analogous to FeSSIF, but without TC and L, were prepared.

DLS

The average particle size of different concentrations of imatinib (1000 μM − 1000 μM + tween 80 − 500 μM − 250 μM − 125 μM − 62.5 μM) in FaSSIF and FeSSIF was measured by DLS. Measurements were performed with unfiltered samples in disposable UV-cuvettes (1.5 mL) from Brand (Wertheim, Germany) using a DelsaNanoHC particle analyzer from Beckman Coulter (Brea, California) with backscattering at an angle of 165°. Measurements were performed in triplicate with an accumulation of 70 scans at 298 K, and the data were analyzed by the CONTIN algorithm. For FaSSIF and FeSSIF, the density was determined by the density meter DMA 35 from Anton Paar (Ostfildern, Germany) at 298 K, the refractive index by an Abbe refractometer from Carl Zeiss (Oberkochen, Germany) at 298 K, and the viscosity by an Ubbelohde viscometer from SI Analytics (Mainz, Germany) at 298 K. The average particle size in FaSSIF was evaluated with a refractive index of 1.334 and a viscosity

of 0.8559 cP. For pure FeSSIF, a refractive index of 1.337 and a viscosity of 0.9138 cP were used.

Preparation of FaSSIF and FeSSIF for DLS Measurements

FaSSIF and FeSSIF were prepared according to the protocol of biorelevance. Briefly, for FaSSIF, 42 mg of sodium hydroxide, 395 mg of monobasic sodium phosphate monohydrate, and 619 mg of sodium chloride were dissolved in about 90 mL of Millipore water, the pH was adjusted to 6.5 by 1 M NaOH and filled up to 100 mL with Millipore water. In 100 mL of buffer, 224 mg of SIF powder was dissolved and used 2 h after preparation. For FeSSIF, 404 mg of sodium hydroxide, 865 mg of glacial acetic acid, and 1.187 g of sodium chloride were dissolved in 90 mL of Millipore water, the pH was adjusted to 5 with either 1 M NaOH or HCl and filled up to 100 mL. In 100 mL of buffer, 1.12 g of SIF powder was dissolved.

Solubility Measurements

The solubility of the free base of imatinib was determined by the shake flask method. Briefly, 4−5 mg of imatinib free base was weighed into a 1.5 mL reaction vial, and 1 mL of FaSSIF, FeSSIF, or a FaSSIF or FeSSIF equivalent buffer, but without TC/L, respectively, was added. Each sample was shaken vigorously and checked for the presence of solid. If no solid was present, 1−2 mg of imatinib was further added, and this was repeated until a precipitate was observed. At this point, the pH was measured, and the vials were shaken with 800 rpm at 300 K for another 24 h, at which point the pH was rechecked. The samples were filtered with 0.2 μm PVDF syringe filters from Whatman (Maidstone, UK) and diluted 1:1 for FaSSIF, buffer pH 6.5 and 5, and 1:20 for FeSSIF with methanol HPLC grade to avoid precipitation. The measurements were performed in triplicate. The concentration was determined by using a LaChrom Elite HPLC from Hitachi with a binary pump, an autosampler, a column thermostat, a UV detector, and an Eclipse XDB-C18 column (4.6 mm × 150 mm, 5 μm) from Agilent (Waldbronn, Germany). The separation was carried out at 25 °C using a gradient of A (10 mM phosphate buffer pH 6.2 with 5% acetonitrile) and B (acetonitrile with 0.1% TFA) with a flow of 1 mL/min, starting at 90% A from 0 to 0.5 min, 90−10% A from 0.5 to 3.5 min, 10% A from 3.5 to 6.5 min, and 10− 90% A within 0.5 min, followed by equilibration for 0.5 min with 90% A. The injection volume was 20 μL, and for detection, a wavelength of 267 nm was used.

X-ray Powder Diffractometry (XRPD)

The residues collected after 24 h for the solubility measurements were centrifuged, and the deposit was subjected to diffractometric characterization. In those cases in which an amorphous hydrogel was formed, the samples were measured directly, and after, these were dried overnight in vacuum at room temperature in an effort to study imatinib crystallization within these gels. The residues of the solubility measurements were applied on a silicon single crystal holder in a wet and dried state and analyzed with a Bruker Discover D8 powder diffractometer (Karlsruhe, Germany) using Cu Kα radiation (unsplit $K_{\alpha 1}$ + $K_{\alpha 2}$ doublet, mean wavelength λ = 154.19 pm) at a power of 40 kV and 40 mA, a focusing Goebel mirror, and a 1.2 mm microfocus alignment. The scattered X-ray beam went through a receiving slit with a 7.5 mm opening, 2.5° axial Soller slit, and detection was performed with a LynxEye-1DDetector (Bruker AXS) using the full detector range of 192 channels. Measurements were done in reflection geometry in a coupled two theta/theta mode with a step size of 0.025° in 2θ and 0.25 s measurement time per step in the range of 5−60° (2θ). Data collection and processing were carried out with the software packages DIFFRAC.Suite and DIFFRAC.EVA 2.1 from Bruker (Karlsruhe, Germany).

Cryo-Electron Microscopy

Holey carbon coated copper grids Quantifoil R 1.2/1.3 (400 mesh) from Quantifoil Micro Tools GmbH (Jena, Germany) were glow discharged for 60 s with a plasma cleaner PDC-002 from Harrick Plasma (Ithaca, New York) on a medium setting and used within 1 h. Samples (3.5 µL) were applied on the glow discharged grids, incubated for 45 s at 25 °C with 100% humidity, blotted from both sides for 4 s with blot force 0, and plunged in liquid ethane using a Vitrobot IV from FEI (Eindhoven, The Netherlands). Samples were transferred into a Tecnai Spirit from FEI with a cryotransfer holder model 626 from Gatan GmbH (Munich, Germany). Images were taken manually under low dose conditions at 120 kV with a primary magnification of 26000− 30000 and a dose of 2000 e/nm^2 with an Eagle CCD-camera from FEI.

Results

Effect of pH in Phosphate Buffer

Imatinib selfaggregation was concentration dependent at both pH 7.4 and 4, resulting in ^{1}H signals shifts to a higher field, except for imatinib's H-19 (**Figure 1**). Supplementation of the surfactant tween 80 reverted the shifts (**Figures S1** and **S2**). The critical aggregation concentration (CAC) was between 25−50 µM at both pH 7.4 and 4, respectively (**Figures S3** and **S4**). In contrast to pH 4 or 7.4, the concentration dependent changes of chemical shifts were marginal at pH 2 (**Figure S5**). All signals were sharp at the three pH values.
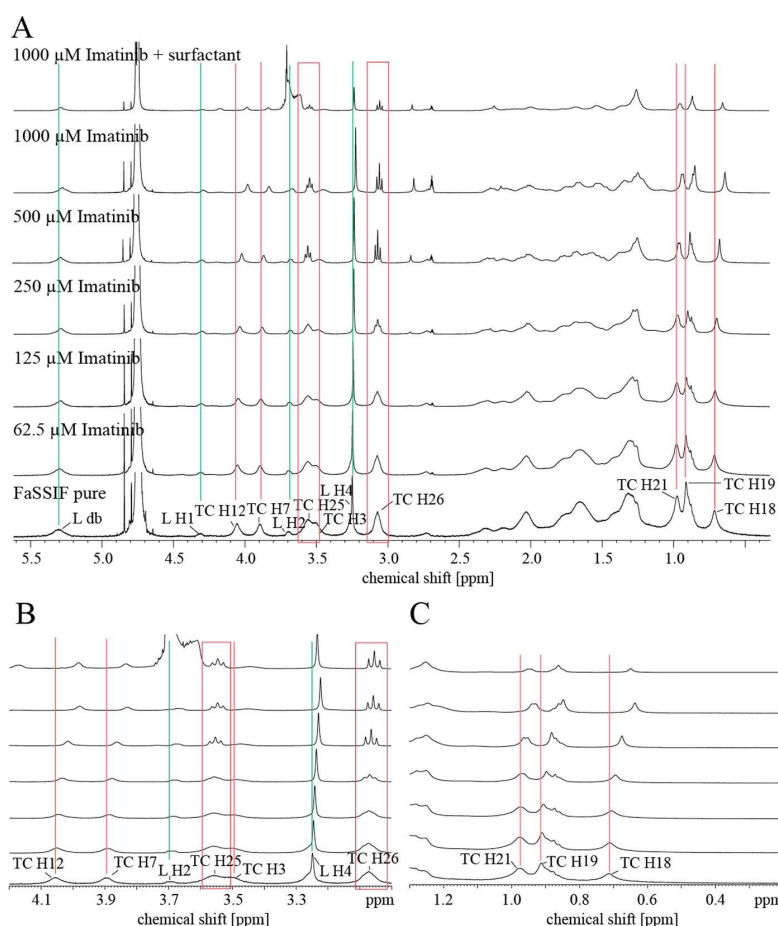

Figure 2 (A) Concentration dependent ^{1}H NMR spectra of pure FaSSIF (bottom) and FaSSIF with imatinib at concentrations as indicated. A high field shift was observed for the methyl signals TC H18/19/21 (between 0.5−1 ppm) and sharper methylene signals of TC H25/26 (red boxes) of TC at concentrations exceeding 250 µM imatinib. The L proton signals were less influenced by the presence of imatinib (green lines). (B, C) Excerpt of (A) detailing the chemicals shifts of TC and L as a function of imatinib concentration.

Effect of FaSSIF

FaSSIF is a phosphate buffer (pH 6.5; osmolality 270 mOsmol/kg) containing TC and L at concentrations of 3 and 0.75 mM, respectively. Similar to the observations in phosphate buffer (*vide supra*), concentration dependent chemical shifts were observed with broad signals at concentrations ≤125 μM and sharper signals at concentrations ≥250 μM (**Figure S6).** Interaction was observed for TC by high field shifts of TC H18, 19, 21, 7, and 12. Furthermore, the ^{1}H signals of TC H25/26 became sharper at an imatinib concentration ≥250 μM (**Figure 2**). Relatively weak shifts were observed for L's H1, 2, and 4 (phosphatidylcholine group) and olefinic protons L db of the lipophilic chain (**Figure 2**). Supplementation of surfactant shifted the signals back to lower field, and the signals became sharper for imatinib (**Figure S6**). Increasing the temperature from 298 K/25 °C to 313 K/40 °C did not change the spectra (data not shown). These experiments in FaSSIF were repeated without TC and L, leading to sharper signals (**Figure S7**) and resulting in the similar outcome as previously observed in plain buffer at pH 7.4 (**Figure S1**) and 4 (**Figure S2**). We further studied the impact of mesylate, the counterion used for the commercial drug product Gleevec. TC's signals H25/26 became sharper for the mesylate salt at lower imatinib concentrations (**Figure S8**) as compared to those of the imatinib free base under otherwise identical conditions (**Figure 2**). [1]H,[1]H-NOESY spectra at 1000 μM imatinib concentration revealed imatinib−imatinib, TC−TC, and L−L interactions and intermolecular interactions between imatinib−TC but not with L (**Figure 3**). At 250 μM imatinib, no intermolecular interactions between imatinib and L or TC were observed (**Figure S9**).
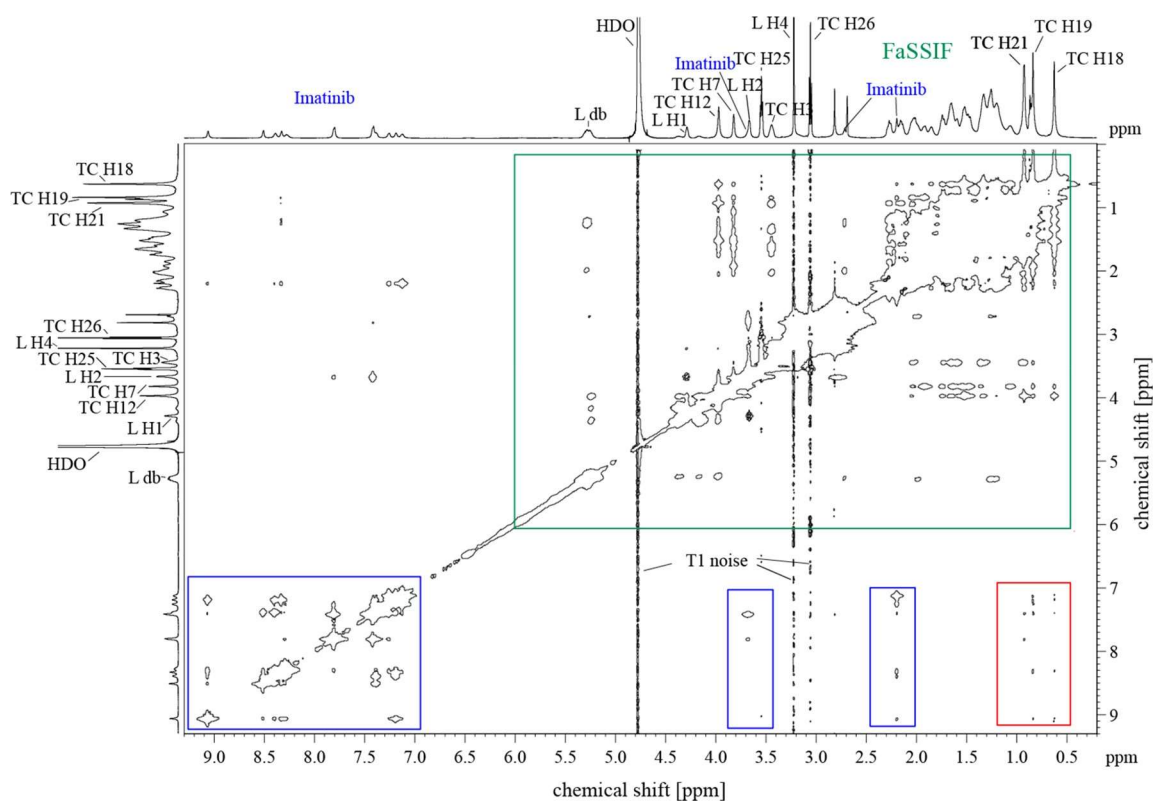
Figure 3 ^{1}H,^{1}H-NOESY spectrum of 1000 μM imatinib in FaSSIF recorded with a mixing time of 40 ms. Intermolecular NOEs of FaSSIF (green box), imatinib (blue box), and the intermolecular NOEs between TC and imatinib (red box) were observed. The cross peaks (red box) between the aromatic functions of imatinib and TC's methyl groups (TC H18/H19/H21) indicated the interaction of imatinib with the lipophilic plane of TC but not with L within the micelles.

The complex interaction between the molecules was also characterized by diffusion ordered nuclear magnetic resonance spectroscopy (DOSY NMR). In general, three main supramolecular species were observed throughout the experiments, (A) mixed micelles of TC and L and (B) pure TC micelles, as described before.[11,25] Furthermore, (C) pure imatinib aggregates were observed (**Figure 4**). Baseline experiments in FaSSIF not containing imatinib had four supramolecular species, with species A1 (2.47×10^{-11} m^2/s) and B1 (2.58×10^{-10} m^2/s) having a higher signal intensity than A2 (5.45×10^{-11} m^2/s) and B2 (1.56×10^{-10} m^2/s). Supplementation of 250 μM imatinib reduced the number of supramolecular to three, with diffusion constants for A (mixed micelles of TC and L) of 2.36×10^{-11} m^2/s, B (pure TC micelles) of 2.65×10^{-10} m^2/s, and C (pure imatinib aggregates) of 1.63×10^{-10} m^2/s (**Table 1**). At 1000 μM imatinib, the diffusion constants doubled for A to 4.11×10^{-11} m^2/s and decreased for B to 2.51×10^{-10} m^2/s and C to 1.51×10^{-10} m^2/s. Surfactant further increased the diffusion constant for A to 4.53×10^{-11} m^2/s and decreased B to 2.09×10^{-10}

m^2/s and C to 1.10×10^{-10} m^2/s (**Table 1**). The diffusion constant of the residual solvent signal water (HDO) was identical in all of the measurements.
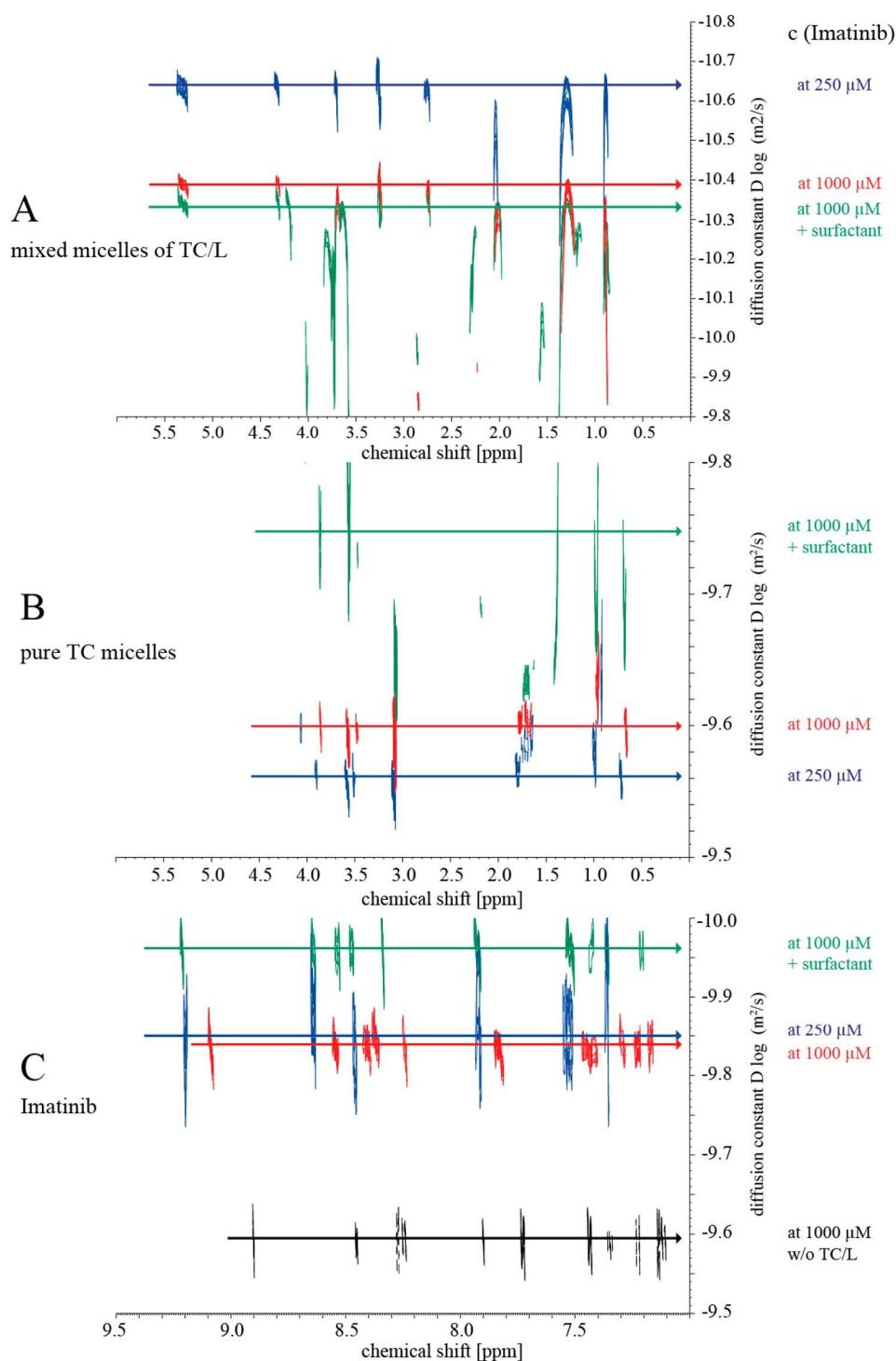

Figure 4 Excerpt of the DOSY spectra for the mixed vesicles of TC and L (A), the pure TC micelles (B), and for imatinib (C) with 250 μM imatinib (blue), 1000 μM imatinib (red), and 1000 μM and supplementation of surfactant (green) in FaSSIF. The DOSY measurement was repeated with 1000 μM imatinib in FaSSIF without TC and L (C, black).

Table 1 Diffusion Constants of the Supramolecular Species in FaSSIF Dependent on the Concentration of Imatinib.

	diffusion constant $[10^{-10}\,\text{m}^2/\text{s}]$ | $[-\log (\text{diffusion constant } [\text{m}^2/\text{s}])]$		
C of imatinib (µM)	mixed micelles of TC/L (A)	pure TC micelles (B)	pure imatinib aggregates (C)
0	1:0.25 [10.61]	1:2.58 [9.59]	
	2:0.55 [10.26]	2:1.56 [9.81]	
250	0.24 [10.63]	2.65 [9.58]	1.63 [9.79]
1000	0.41 [10.39]	2.51 [9.60]	1.51 [9.82]
supplementation of surfactant	0.45 [10.34]	2.09 [9.68]	1.10 [9.96]

We further analyzed the average colloidal size by DLS. Average sizes increased from 70 ± 1.8 nm (PDI 0.039 ± 0.024) as observed in pure FaSSIF to 84 ± 1.9 nm (PDI 0.055 ± 0.034), 116 ± 26.8 (PDI 0.158 ± 0.065), and 132 ± 20.6 nm (PDI 0.207 ± 0.056) at 62.5, 125, and 250 µM imatinib concentration, respectively (**Figure 5**). Average micelle sizes decreased from 70 ± 1.8 to 33 ± 3.6 nm (PDI 0.200 ± 0.040) at 1000 µM imatinib and to 22.3 ± 9.0 nm (PDI 0.205 ± 0.004) in the presence of surfactant. Reducing the imatinib concentrations to 500 µM had no impact on micelle size (34 ± 4.1 nm/PDI 0.287 ± 0.036).
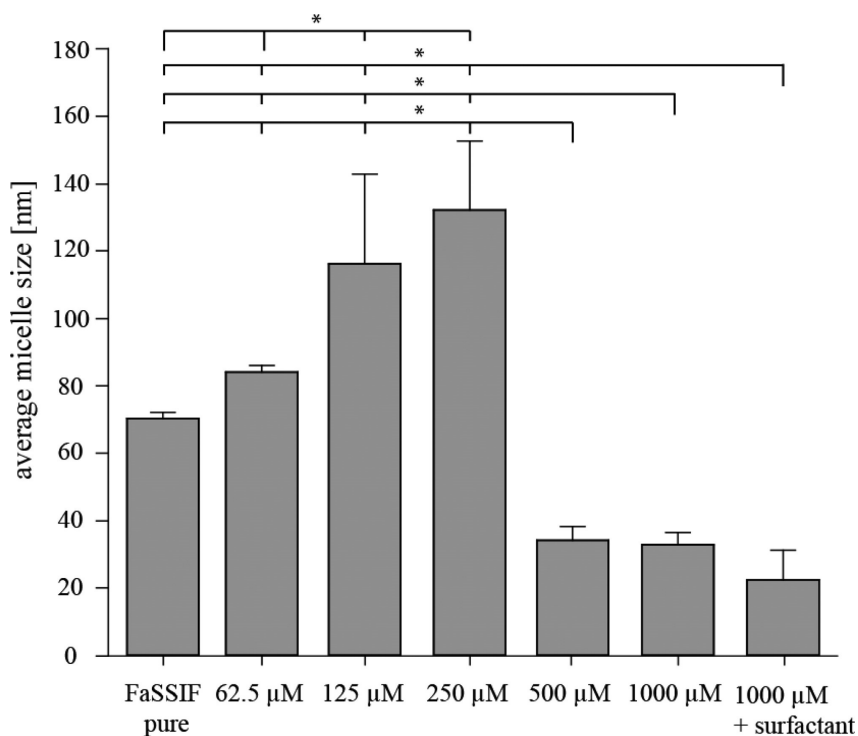
Figure 5 Average micelle size in FaSSIF after addition of different concentrations of imatinib free base and supplementation of surfactant after 2 h equilibration. Data are shown as mean ± SD, and ANOVA was used with the Tukey test for post hoc comparison; p ≤ 0.05 was considered statistically significant.

The data was corroborated by cryo-electron microscopy images. In pure FaSSIF, (**Figure 6A)** vesicles of TC and L (TC/L) were observed. At 250 μM imatinib, bigger globular vesicles of TC/L were visible (**Figure 6B**), and at 1000 μM imatinib, small thread-like micelles of TC/L were detected (**Figure 6C**). The red-outlined structures possibly represent mixed micelles of TC in **Figure 6A**, colloidal aggregates of imatinib, and mixed micelles of TC in **Figure 6B,C**.
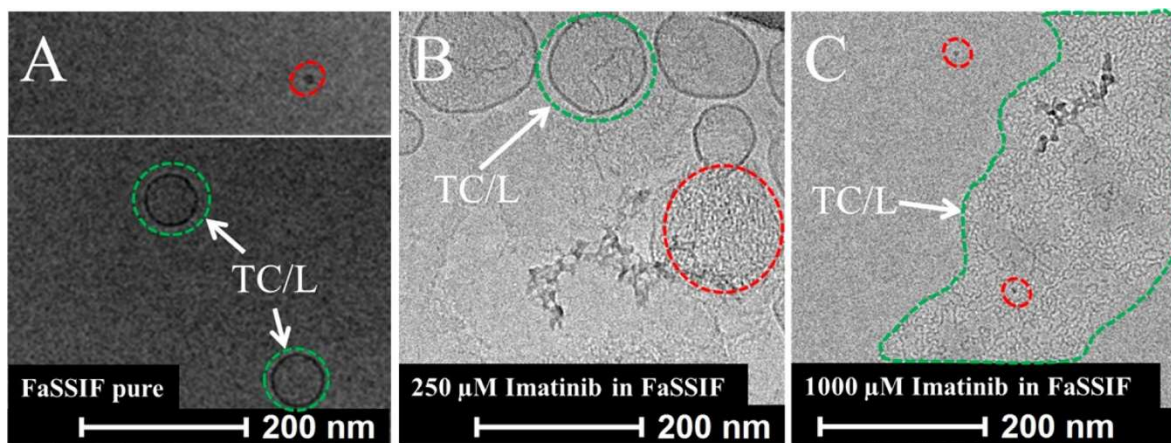

Figure 6 Cryo-electron microscopy images of (A) pure FaSSIF, (B) 250 μM imatinib, and (C) 1000 μM imatinib in FaSSIF. (A) In pure FaSSIF, vesicles of TC and L (TC/L) were observed (green). (B) Addition of 250 μM imatinib increased the TC/L vesicle size (green). (C) Increasing imatinib concentration to 1000 μM resulted into a colloidal collapse with mixed micelles of TC/L and imatinib (green).

Imatinib in FeSSIF

FeSSIF is an acetate buffer (pH 5; osmolality 670 mOsmol/kg) containing TC and L at concentrations of 15 and 3.75 mM, respectively. Imatinib concentration dependent chemical shifts were observed, which responded to the presence of surfactant (**Figure S10**) but to a lesser extent than that observed in FaSSIF (**Figure S6**). The TC ^{1}H signals TC H25 and H26 were sharp at all imatinib concentrations, while TC H18, 19, 21, 7, and 12 shifted with increasing concentration (**Figure 7**). Imatinib weakly influenced the L ^{1}H signals L db, L H1, 2, and 4 as a function of the imatinib concentration (**Figure 7**) and as observed for FaSSIF (**Figure 2**). ^{1}H NMR spectra in the acetate buffer (pH 5 without TC or L) of imatinib resulted in sharp and high-field shifted signals at concentrations exceeding 250 μM, other than for H19, which had a low field shift (**Figure S11**), and as observed for FaSSIF (**Figure 2).** ^{1}H NMR spectra in the acetate buffer (pH 5 without TC or L) of imatinib resulted in sharp and high-field shifted signals at concentrations exceeding 250 μM, other than for H19, which

had a low field shift (**Figure S11**), and as observed for pH 6.5 (**Figure S7**). Supplementation of surfactant broadened the signals and resulted in a low field shift of the proton resonances (**Figure S11**). These experiments with the free base were repeated with imatinib mesylate (**Figure S12**) in FeSSIF, resulting in a slight shift to a higher field compared to the imatinib free base (**Figure 7**). The average particle size in FeSSIF was not significantly impacted by the concentration of imatinib or surfactant (**Figure 8**).
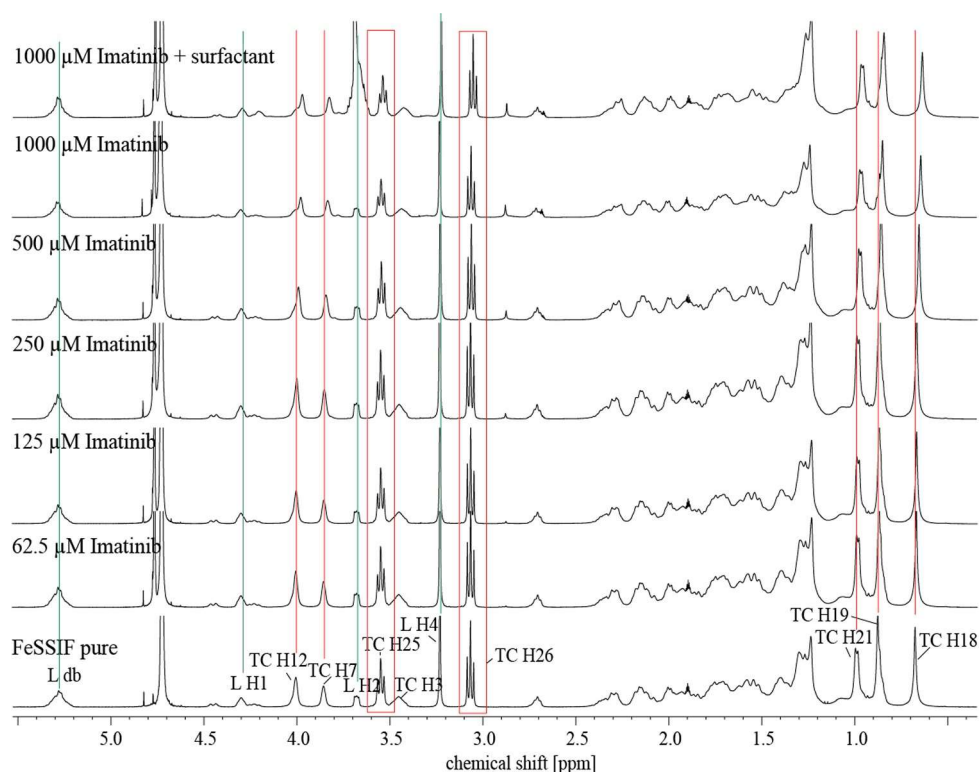
Figure 7 ^{1}H NMR spectra of pure FeSSIF (bottom) and FeSSIF with imatinib at concentrations as indicated. At imatinib concentrations of 250 μM or higher, the methyl signals of TC (TC H18/19/21) shifted to higher field at 0.5−1 ppm (red lines). The sharp ^{1}H signals of the TC H25/26 methylene groups indicated higher tumbling rates of TC within the smaller mixed micelles in FeSSIF as compared to the larger vesicular structures observed in FaSSIF.

Solubility

The solubility of imatinib free base in FaSSIF was about two times higher compared to that of the phosphate buffer pH 6.5 (FaSSIF without TC and L), and about 20-fold higher in FeSSIF compared to that of the acetate buffer pH 5 (FeSSIF without TC and L; **Table 2**). We also attempted measuring the thermodynamic solubility of the mesylate salt, the marketed form of imatinib. However, we were unable to find conditions resulting in sediment of the drug (as required to measure thermodynamic solubility) because of the instantaneous formation of an orange hydrogel preventing sedimentation.

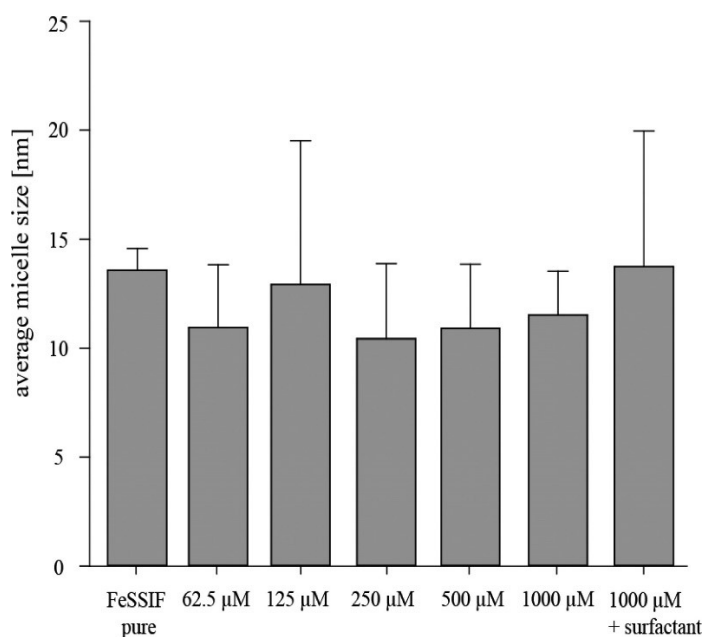**Figure 8** Average particle size of the micelles in FeSSIF after the addition of different concentrations of imatinib and supplementation of surfactant after 2 h equilibration. Data are shown as mean ± SD, no statistically significant differences were observed using ANOVA with a Tukey test and $p \leq 0.05$.

Crystallinity

No change of the crystal structure of imatinib free base was observed in FaSSIF and FaSSIF without TC and L after 24 h (**Figures S13** and **S14**). In contrast, FeSSIF exposure yielded an amorphous orange hydrogel consisting of imatinib, TC, and L at a ratio of 1:0.7:0.1, and water as determined by comparison of the integrals in the ^{1}H NMR spectrum (**Figure S15**). Following drying of the orange hydrogel overnight at room temperature in vacuum, an amorphous halo was recorded, and the reflexes from recrystallized sodium chloride and sodium acetate were observed (**Figure S16**). In contrast, the absence of TC and L (acetate buffer at pH 5) resulted in the precipitation of crystalline imatinib acetate following drying, as indicated by the diffractogram and the ^{1}H NMR spectrum (**Figures S17** and **S18**).

Discussion

Imatinib was aggregated in buffers at pH 4 and 7.4 but not at pH 2. When exposed to FaSSIF (phosphate buffer at pH 6.5 and containing TC/L at 3/0.75 mM; osmolality 270 mOsmol/kg), the imatinib concentration impacted both the molecular arrangement and the size of the colloidal structure. Larger (>110 nm diameter) vesicles dominated up to 125−250 μM imatinib with a very low signal shift for both, TC and L (**Figures 2** and **S9**). Imatinib signals

were broad at these low concentrations (**Figure S6**), whereas in absence of TC and L, sharp signals were recorded (**Figure S7**). This provided evidence that the majority of imatinib molecules were located within the vesicles. In summary, at low concentrations of imatinib, the drug was located within the core of the vesicles, whereas the vesicle's shell consisted mainly of TC/L or TC/ TC, and very little or no imatinib was in the shell. In contrast, higher imatinib concentrations resulted in a breakdown of vesicle structures into micelles with different molecular arrangements (**Table 1, Figures 2-6**). This illustrated the semiquantitative assessment possibility on drug localization and geometrical features of supramolecular structures as a function of drug concentration deploying NMR spectroscopy. Both TC and imatinib became more flexible as compared to lower imatinib concentrations and as indicated by sharper signals. A strong interaction was found between TC and imatinib and, to a lesser extent, between imatinib and the alkyl chains/double bonds of L (**Figure 2**). In summary, the data suggested that at higher concentrations of imatinib, the drug was positioned between TC molecules with the lipophilic side of TCs facing the imatinib aryl parts, and it is this complex which is embedded within the shell of the micelles (**Figure 3**). We found that the smaller radius of the micelles (**Figures 5** and **6**) observed at higher imatinib concentrations resulted in higher rotational freedom and sharper signals of the proton resonances of TC and imatinib. Overall, with increasing imatinib concentrations and in FaSSIF, larger vesicles, engulfing the drug in their cores, transitioned to small micelles containing the drug within the shell with a preferential association to TC. Imatinib−imatinib aggregates were in equilibrium with the micellar/vesicular structures at all concentrations (the transition is schematically shown in **Figure 9**).

Table 2 Results of Solubility Measurements of Imatinib Free Base in FaSSIF, FeSSIF, and Analogous Buffer without TC/L by the Shake Flask Method at 300 K (n = 3).

buffer	pH$_{before}$	pH$_{after 24h}$	solubility (µM)	wet residue characterized by XRPD
FaSSIF	6.5	6.6	450 ± 10	no change[a] or partly amorphous
buffer w/o TC/L	6.5	6.6	230 ± 10	no change
FeSSIF	5	5.5	4480 ± 180	amorphous
buffer w/o TC/L	5	6.5	210 ± 30	crystalline, acetate salt

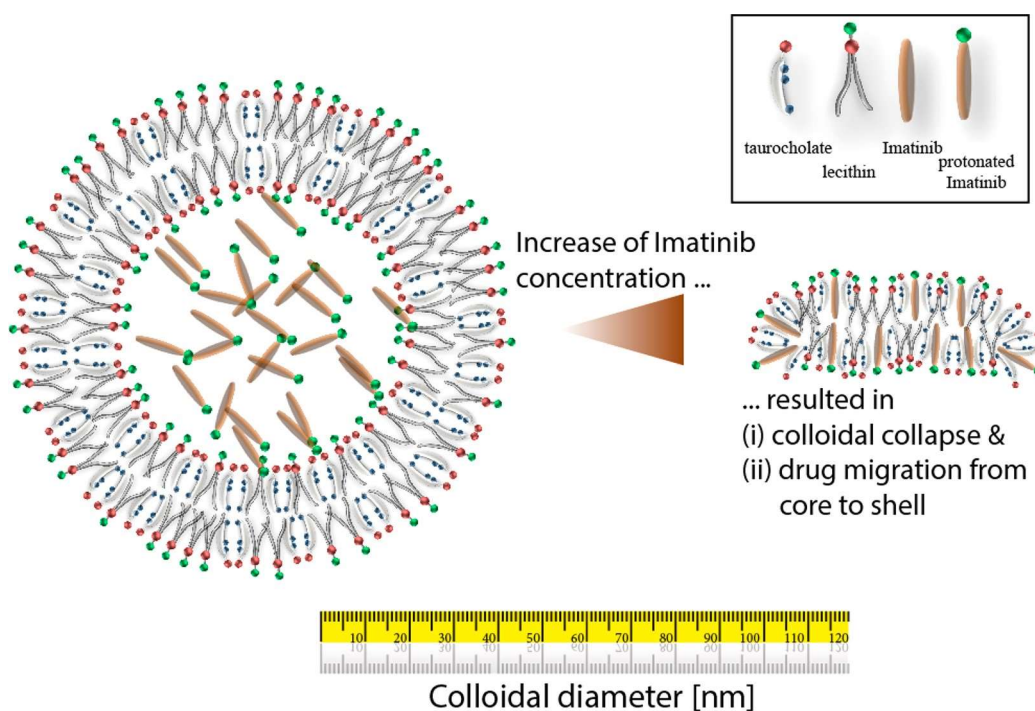[a] No change expresses identical crystal structure to the imatinib free base before dissolution.

Figure 9 Migration of TC/L vesicles at imatinib concentrations <250 µM (imatinib was engulfed within the core of the micelles) to smaller TC/L micelles at imatinib concentrations >250 µM (imatinib transitioned into the micelles' shell). Coexisting colloidal aggregates of imatinib, TC mixed micelles, and vesicles/micelles of pure TC/L are not shown.

We observed smaller micelles of TC/L or TC/TC, but no larger vesicles in FeSSIF (acetate buffer at pH 5 and containing TC/L at 15/3.75 mM; osmolality 670 mOsmol/kg), as compared to those of FaSSIF (**Figure 8**). The imatinib molecules interacted with TC and, to a lesser extent, with L (**Figure 7**), as observed for higher drug concentrations in FaSSIF. In conclusion and in contrast to FaSSIF, no transition from vesicles to micelles was observed in FeSSIF with increasing drug concentration. The molecular arrangement was similar within the micelles observed in FeSSIF compared to the micelles observed at high drug concentrations in FaSSIF. Nevertheless, the diameter of the micelles was further reduced (**Figures 5** and **8**). The solubility in FeSSIF was the highest compared to all other tested conditions, resulting from a complete transition from crystal to amorphous states, respectively. This was accompanied by the formation of an orange hydrogel within which imatinib remained amorphous even after stress through drying (**Figure S15**). Following protonation at the piperazine nitrogen (N34; **Figure 1**), imatinib becomes amphiphilic thereby triggering the interaction with TC through its acidic sulfonic group, while the lipophilic aspects of both molecules interact through hydrophobic interaction. These interactions are causal for the observed phase transitions leading to hydrogel formation in

the presence of imatinib, TC, and L, which was composed of the three constituents at a ratio of 1:0.7:0.1 (**Figure S18**). Neither in the wet state nor after drying of the hydrogel crystallization of imatinib was observed, again demonstrating the strong interaction of imatinib, TC, and L, even after drying. Future studies are required to link the information on micelle interaction in FaSSIF versus FeSSIF provided here to previously reported pharmacokinetic variabilities (t_{max}) in patients.[26,27] One hypothesis is that effective integration of imatinib into intestinal micelles, as shown here, is causal to delayed intestinal absorption because of efficient micelle entrapment.[28,29] Similarly, the observations in buffer may link our data sets to previous reports, indicating an enrichment of imatinib in acidic lysozymes, possibly reflecting nanoscale aggregates within the lysozymes thereby trapping the drug within the compartment (**Figure S2**).[30] Previous NMR studies using a poor water-soluble S1P1 agonist detailed that TC/TC micelles were impacted by drug concentrations and not the TC/L micelles in contrast to imatinib, for which both species were impacted (*vide supra*).[11] This illustrated that the geometrical and structural dynamics of the micelle/vesicle interplay with drugs are impacted by the drugs' structure, suggesting that studies like these need to be repeated for each new chemical entity. These studies may provide the necessary mechanistic insights why some drugs are better soluble in the presence of TC/L, whereas others are equally soluble in plain buffer.[31] We speculate that future formulation strategies may be deduced from such molecular insights for each new chemical entity. For example, drugs solubilizing within TC and/or L may benefit from formulations leading to high supersaturation profiles because recrystallization is minimized through effective interaction with the micelles/vesicles. Similarly, a need of prolonged supersaturation may be postulated from these mechanistic studies, thereby impacting formulation demands.

Future experiments are required to link the impact of the structural geometries and molecular interaction within the micelles/vesicles to imatinib stability, release, and bioavailability. Furthermore, moving from in vitro to in vivo settings will further complicate the interpretation because of the presence of many species of bile acids as well as the occurring metabolism of these bile salts due to the gut flora.[32]

Conclusion

In conclusion, this study provided insights into the performances of TC and/or L for imatinib solubilization. It further detailed the dynamics of geometrical changes and molecular assemblies as a function of drug concentrations. Future studies are needed to detail the biopharmaceutics of these dynamics. Another interesting research direction along these lines is to detail the differences of naturally occurring (and dynamically changing their composition due to degradation of their components, hence their solubilization capacity) micelles to micelles formed by synthetic excipients within pharmaceutical formulations (which are not degraded during transit) and the effects on drug binding within the micelles, drug release, and drug bioavailability. We expect that integration of such insights on molecular assembly of new entities with TC and/or L may provide another perspective leading to improved formulation performances.

Acknowledgments

References

1. Holm, R.; Mullertz, A.; Mu, H. Bile salts and their importance for drug absorption. Int. J. Pharm. 2013, 453 (1), 44−55.

2. Riethorst, D.; Baatsen, P.; Remijn, C.; Mitra, A.; Tack, J.; Brouwers, J.; Augustijns, P. An In-Depth View into Human Intestinal Fluid Colloids: Intersubject Variability in Relation to Composition. Mol. Pharmaceutics 2016, 13 (10), 3484−3493.

3. Enhsen, A.; Kramer, W.; Wess, G. Bile acids in drug discovery. Drug Discovery Today 1998, 3 (9), 409−418.

4. Boyer, J. L. Bile formation and secretion. Compr. Physiol. 2013, 3 (3), 1035−1078.

5. Riethorst, D.; Mols, R.; Duchateau, G.; Tack, J.; Brouwers, J.; Augustijns, P. Characterization of Human Duodenal Fluids in Fasted and Fed State Conditions. J. Pharm. Sci. 2016, 105 (2), 673−681.

6. Hofmann, A. F. Bile acids: trying to understand their chemistry and biology with the hope of helping patients. Hepatology 2009, 49 (5), 1403−1418.

7. Ashby, K.; Navarro Almario, E. E.; Tong, W.; Borlak, J.; Mehta, R.; Chen, M. Review article: therapeutic bile acids and the risks for hepatotoxicity. Aliment. Pharmacol. Ther. 2018, 47 (12), 1623−1638.

8.   Yano, K.; Masaoka, Y.; Kataoka, M.; Sakuma, S.; Yamashita, S. Mechanisms of membrane transport of poorly soluble drugs: role of micelles in oral absorption processes. J. Pharm. Sci. 2010, 99 (3), 1336−1345.

9.   Hofmann, A. F.; Hagey, L. R. Key discoveries in bile acid chemistry and biology and their clinical applications: history of the last eight decades. J. Lipid Res. 2014, 55 (8), 1553−1595.

10.   Hofmann, A. F. The Continuing Importance of Bile Acids in Liver and Intestinal Disease. Arch. Intern. Med. 1999, 159 (22), 2647 .

11.   Vogtherr, M.; Marx, A.; Mieden, A. C.; Saal, C. Investigation of solubilising effects of bile salts on an active pharmaceutical ingredient with unusual pH dependent solubility by NMR spectroscopy. Eur. J. Pharm. Biopharm. 2015, 92, 32−41.

12.   Pade, V.; Stavchansky, S. Link between drug absorption solubility and permeability measurements in Caco-2 cells. J. Pharm. Sci. 1998, 87 (12), 1604−1607.

13.   Dressman, J. B.; Amidon, G. L.; Reppas, C.; Shah, V. P. Dissolution testing as a prognostic tool for oral drug absorption: immediate release dosage forms. Pharm. Res. 1998, 15 (1), 11−22.

14.   Brouwers, J.; Brewster, M. E.; Augustijns, P. Supersaturating drug delivery systems: the answer to solubility-limited oral bioavailability? J. Pharm. Sci. 2009, 98 (8), 2549−2572.

15.   European Medicines Agency (EMA), Summary of Product Characteristics of Glivec. http://www.ema.europa.eu/docs/en_GB/document_library/EPAR_-_Product_Information/human/000406/ WC500022207.pdf.

16.   Klein, S. The use of biorelevant dissolution media to forecast the in vivo performance of a drug. AAPS J. 2010, 12 (3), 397−406.

17.   Galia, E.; Nicolaides, E.; Horter, D.; Lobenberg, R.; Reppas, C.; Dressman, J. B. Evaluation of various dissolution media for predicting in vivo performance of class I and II drugs. Pharm. Res. 1998, 15 (5), 698−705.

18.   Wu, D. H.; Chen, A. D.; Johnson, C. S. An Improved DiffusionOrdered Spectroscopy Experiment Incorporating Bipolar-Gradient Pulses. J. Magn. Reson., Ser. A 1995, 115 (2), 260−264.

19.   Lounila, J.; Oikarinen, K.; Ingman, P.; Jokisaari, J. Effects of Thermal Convection on NMR and Their Elimination by Sample Rotation. J. Magn. Reson., Ser. A 1996, 118 (1), 50−54.

20.   Esturau, N.; Sanchez-Ferrando, F.; Gavin, J. A.; Roumestand, C.; Delsuc, M. A.; Parella, T. The use of sample rotation for minimizing convection effects in self-diffusion NMR measurements. J. Magn. Reson. 2001, 153 (1), 48−55.

21.   Jerschow, A.; Müller, N. Suppression of Convection Artifacts in Stimulated-Echo Diffusion Experiments. Double-Stimulated-Echo Experiments. J. Magn. Reson. 1997, 125 (2), 372−375.

22.   Baucke, F. G. K. Further Insight into the Dissociation Mechanism of Glass Electrodes. The Response in Heavy Water. J. Phys. Chem. B 1998, 102 (24), 4835−4841.

23.   LaPlante, S. R.; Carson, R.; Gillard, J.; Aubry, N.; Coulombe, R.; Bordeleau, S.; Bonneau, P.; Little, M.; O'Meara, J.; Beaulieu, P. L. Compound Aggregation in Drug Discovery: Implementing a Practical NMR Assay for Medicinal Chemists. J. Med. Chem. 2013, 56 (12), 5142−5150.

24.   Szakacs, Z.; Beni, S.; Varga, Z.; Orfi, L.; Keri, G.; Noszal, B. Acid-base profiling of imatinib (gleevec) and its fragments. J. Med. Chem. 2005, 48 (1), 249−255.

25.   Schurtenberger, P.; Lindman, B. Coexistence of simple and mixed bile salt-lecithin micelles: an NMR self-diffusion study. Biochemistry 1985, 24 (25), 7161−7165.

26. Peng, B.; Dutreix, C.; Mehring, G.; Hayes, M. J.; Ben-Am, M.; Seiberling, M.; Pokorny, R.; Capdeville, R.; Lloyd, P. Absolute bioavailability of imatinib (Glivec) orally versus intravenous infusion. J. Clin. Pharmacol. 2004, 44 (2), 158−162.

27. Peng, B.; Hayes, M.; Resta, D.; Racine-Poon, A.; Druker, B. J.; Talpaz, M.; Sawyers, C. L.; Rosamilia, M.; Ford, J.; Lloyd, P.; Capdeville, R. Pharmacokinetics and pharmacodynamics of imatinib in a phase I trial with chronic myeloid leukemia patients. J. Clin. Oncol. 2004, 22 (5), 935−942.

28. Raina, S. A.; Zhang, G. G.; Alonzo, D. E.; Wu, J.; Zhu, D.; Catron, N. D.; Gao, Y.; Taylor, L. S. Impact of Solubilizing Additives on Supersaturation and Membrane Transport of Drugs. Pharm. Res. 2015, 32 (10), 3350−3364.

29. Taylor, L. S.; Zhang, G. G. Physical chemistry of supersaturated solutions and implications for oral absorption. Adv. Drug Delivery Rev. 2016, 101, 122−142.

30. Fu, D.; Zhou, J.; Zhu, W. S.; Manley, P. W.; Wang, Y. K.; Hood, T.; Wylie, A.; Xie, X. S. Imaging the intracellular distribution of tyrosine kinase inhibitors in living cells with quantitative hyperspectral stimulated Raman scattering. Nat. Chem. 2014, 6 (7), 614−622.

31. Ottaviani, G.; Gosling, D. J.; Patissier, C.; Rodde, S.; Zhou, L.; Faller, B. What is modulating solubility in simulated intestinal fluids? Eur. J. Pharm. Sci. 2010, 41 (3−4), 452−457.

32. Enright, E. F.; Joyce, S. A.; Gahan, C. G.; Griffin, B. T. Impact of Gut Microbiota-Mediated Bile Acid Metabolism on the Solubilization Capacity of Bile Salt Micelles and Drug Solubility. Mol. Pharmaceutics 2017, 14 (4), 1251−1263.

Supporting Information
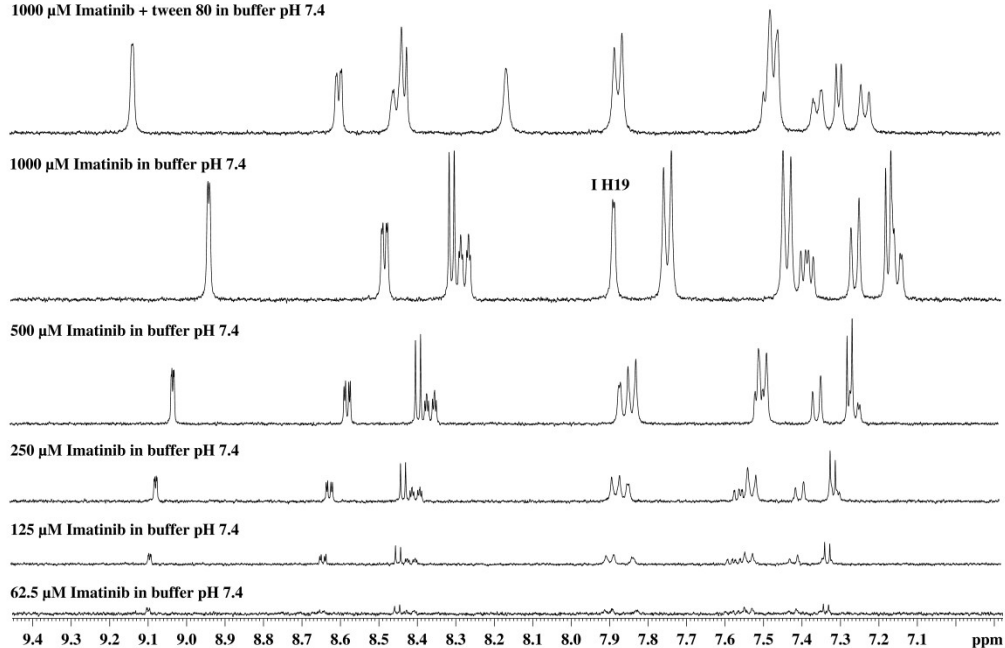
Figure S1: Concentration dependent ^{1}H NMR spectra of Imatinib (aromatic range) in buffer pH 7.4.
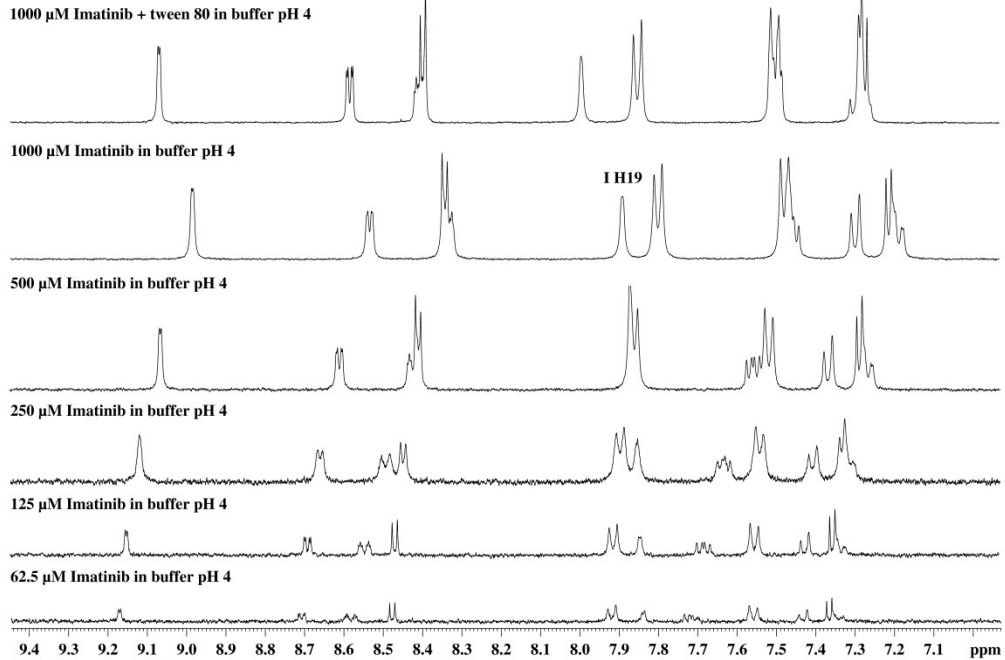
Figure S2: Concentration dependent ^{1}H NMR spectra of Imatinib (aromatic range) in buffer pH 4.
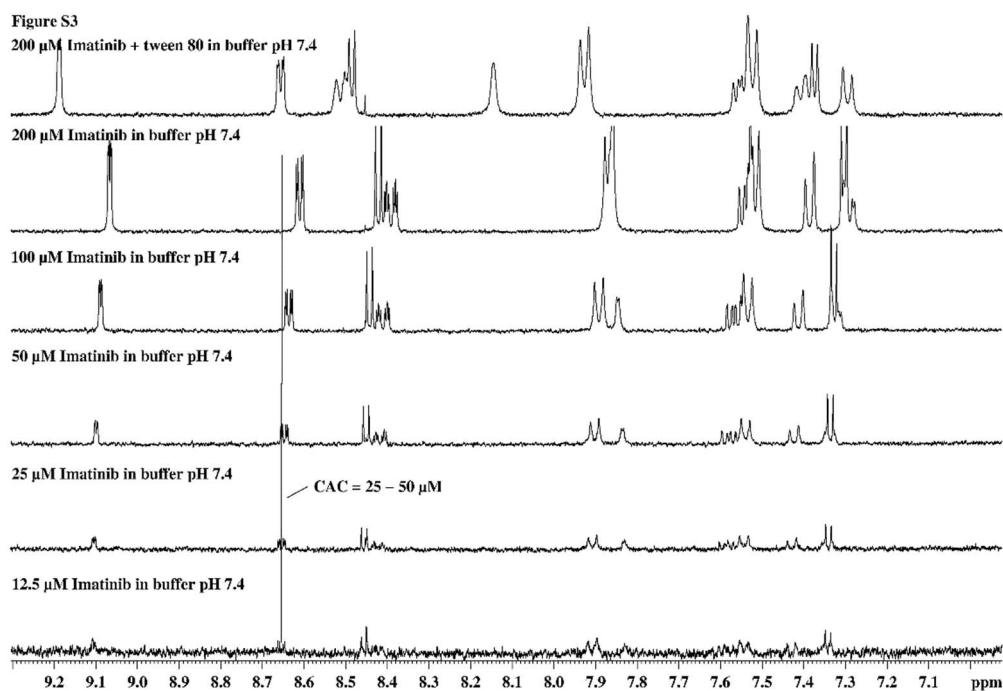
Figure S3: Determination of the critical aggregation concentration (CAC) by concentration dependent ^{1}H NMR spectroscopy of Imatinib at pH 7.4.
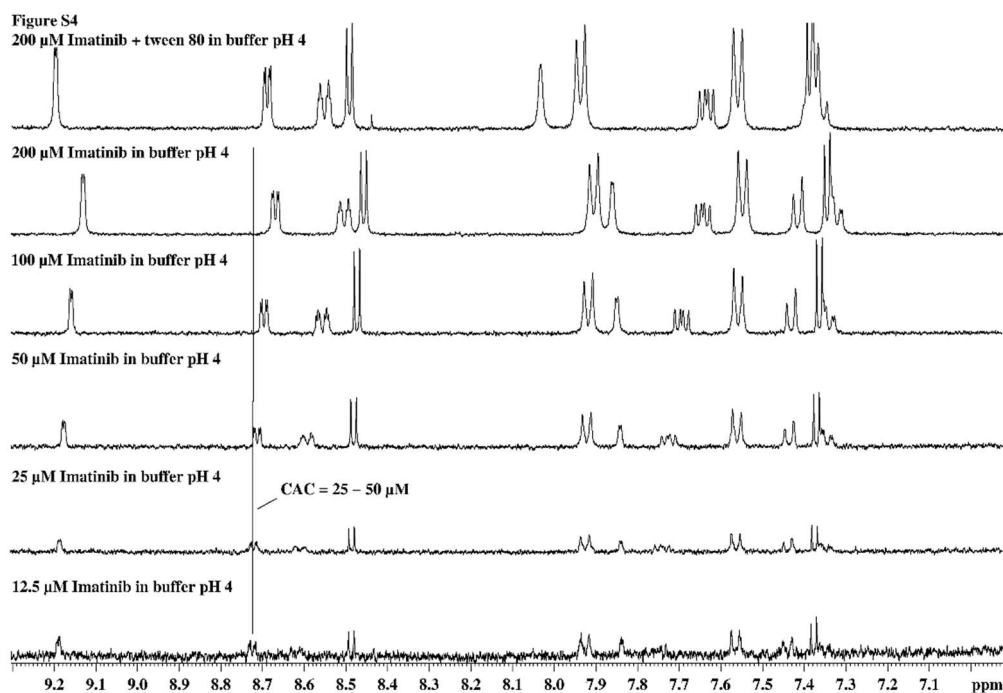
Figure S4: Determination of the critical aggregation concentration (CAC) by concentration dependent ^{1}H NMR spectroscopy of Imatinib at pH 4.
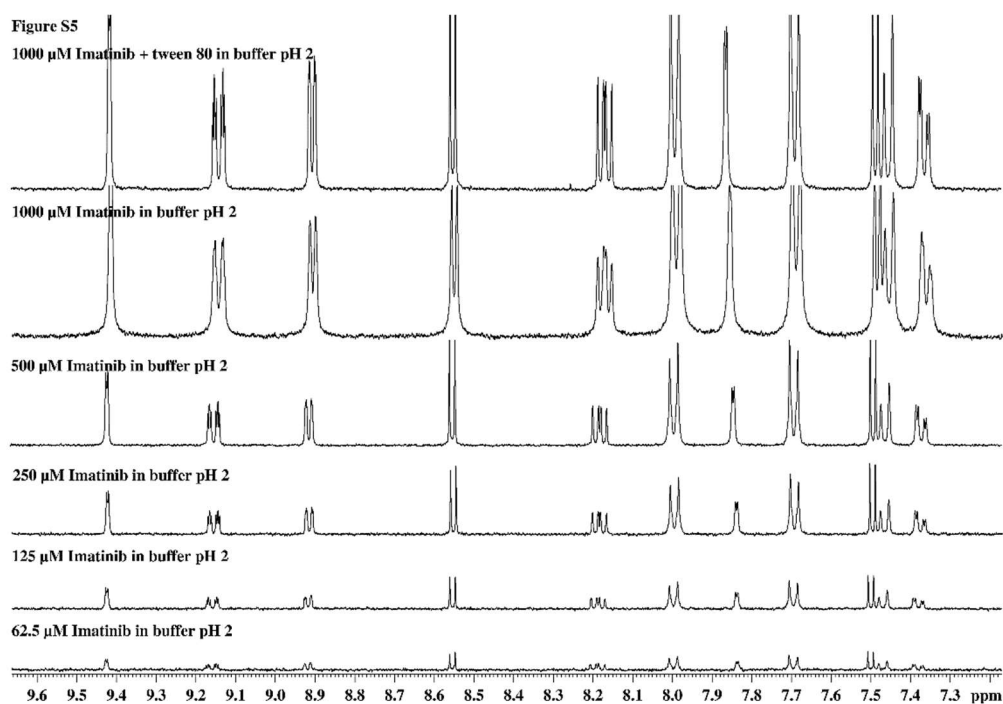
Figure S5: Concentration dependent ¹H NMR spectra of Imatinib in buffer pH 2.
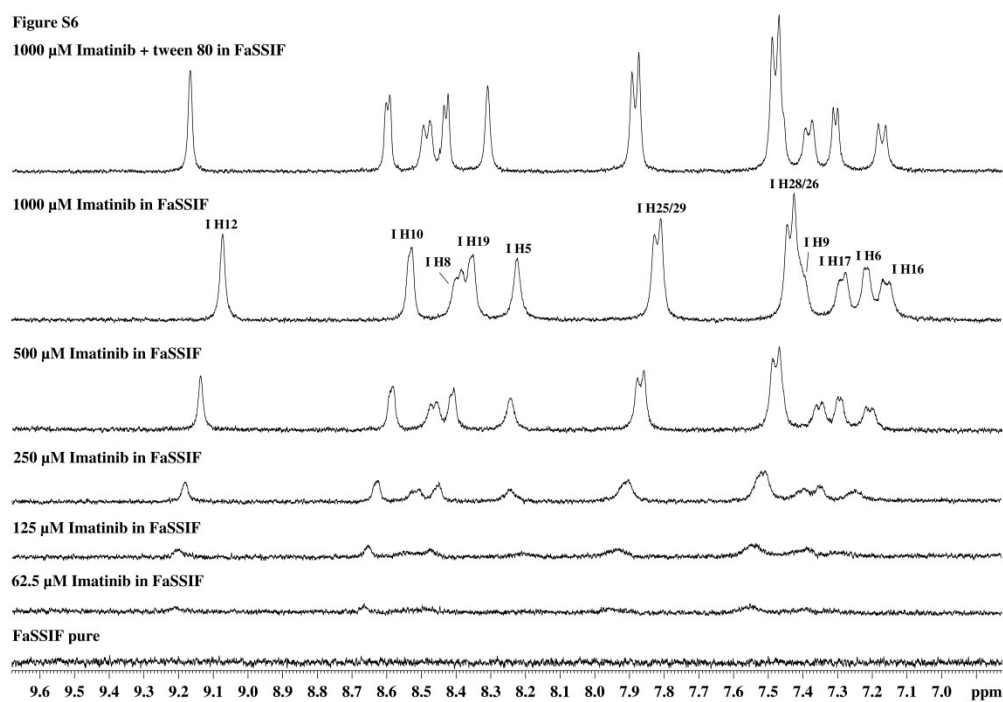
Figure S6: Concentration dependent ¹H NMR spectra of Imatinib (aromatic range) in FaSSIF.
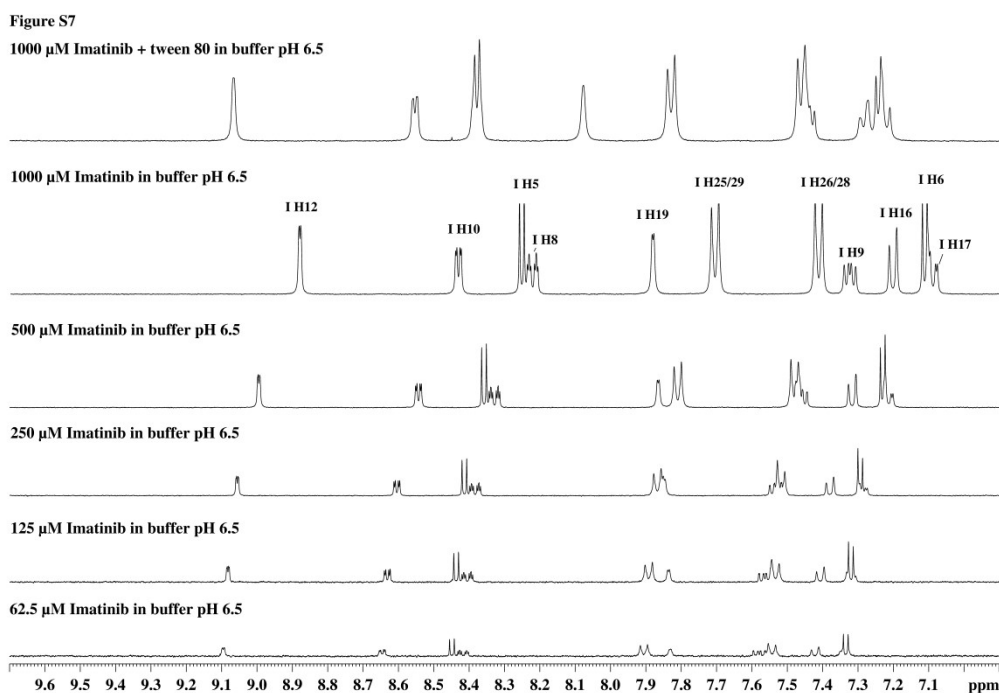
Figure S7: Concentration dependent ^{1}H NMR spectra of Imatinib (aromatic range) in buffer analogous to FaSSIF, but without TC/L.
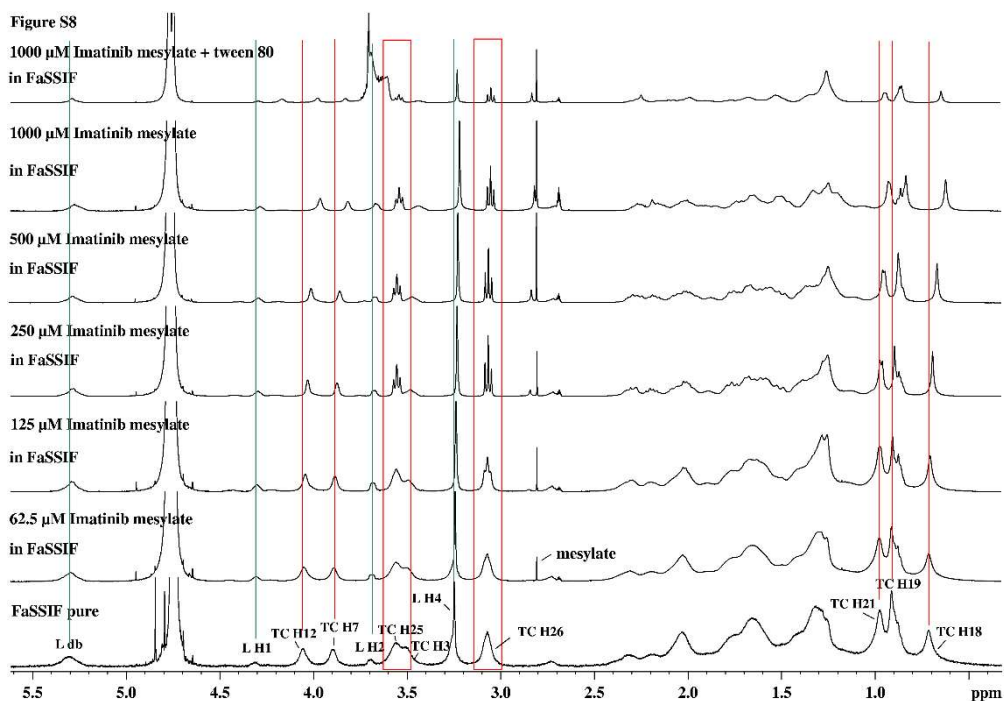
Figure S8: Concentration dependent ^{1}H NMR spectra of Imatinib mesylate in FaSSIF.

Figure S9
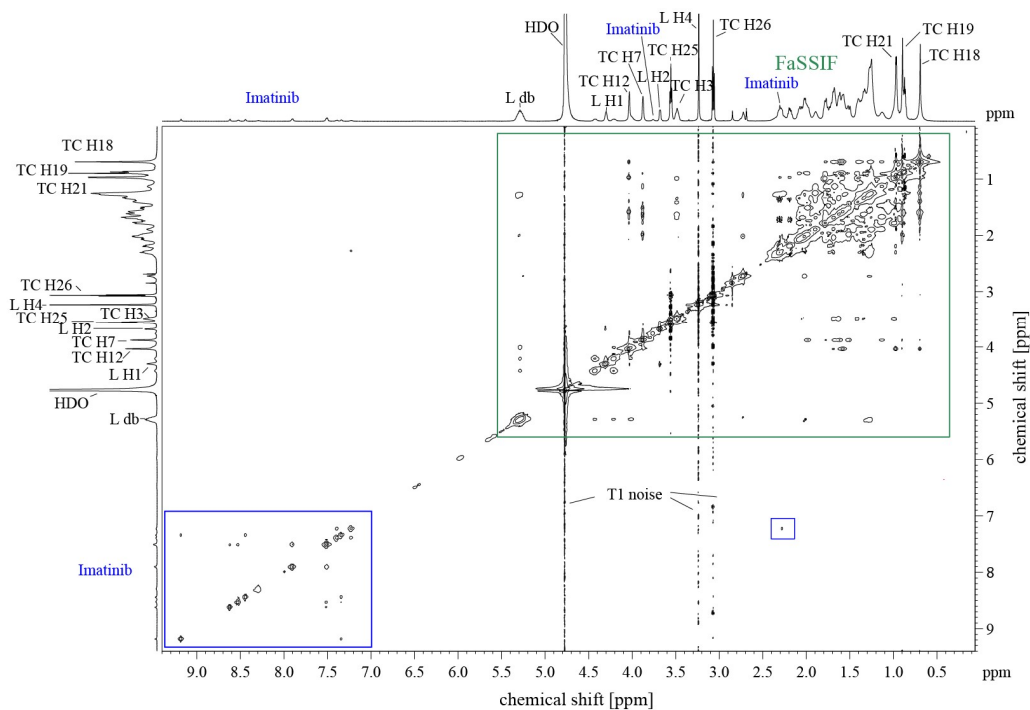
Figure S9: ^{1}H,^{1}H-NOESY spectrum of 250 µM Imatinib in FaSSIF recorded with a mixing time of 40 ms. No intermolecular NOEs between Imatinib and taurocholate / lecithin were observed.
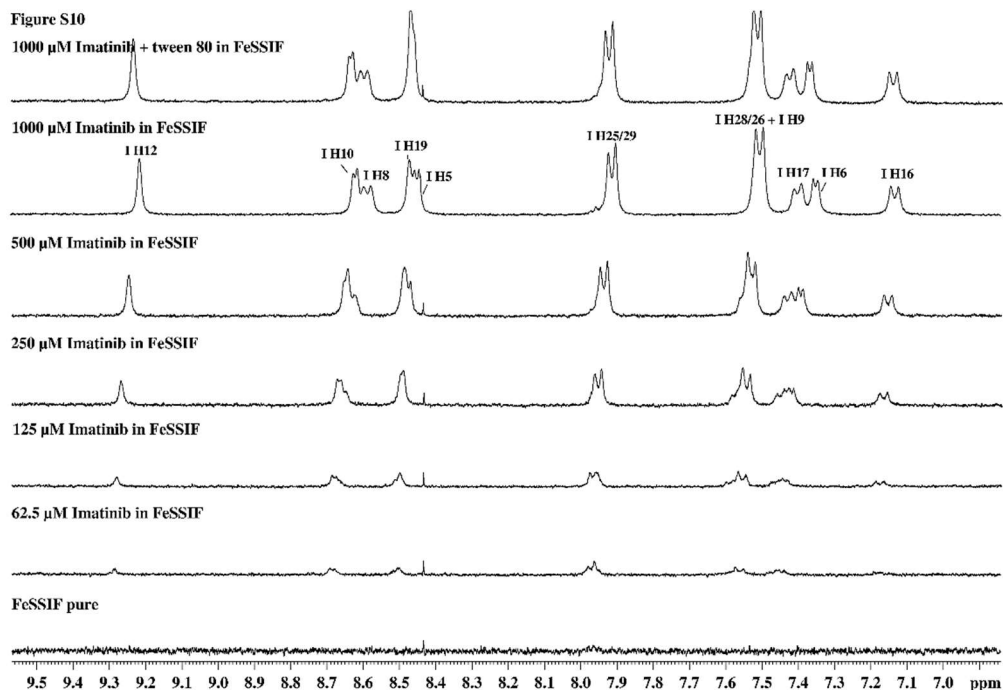
Figure S10: Concentration dependent ^{1}H NMR spectra of Imatinib (aromatic range) in FeSSIF.
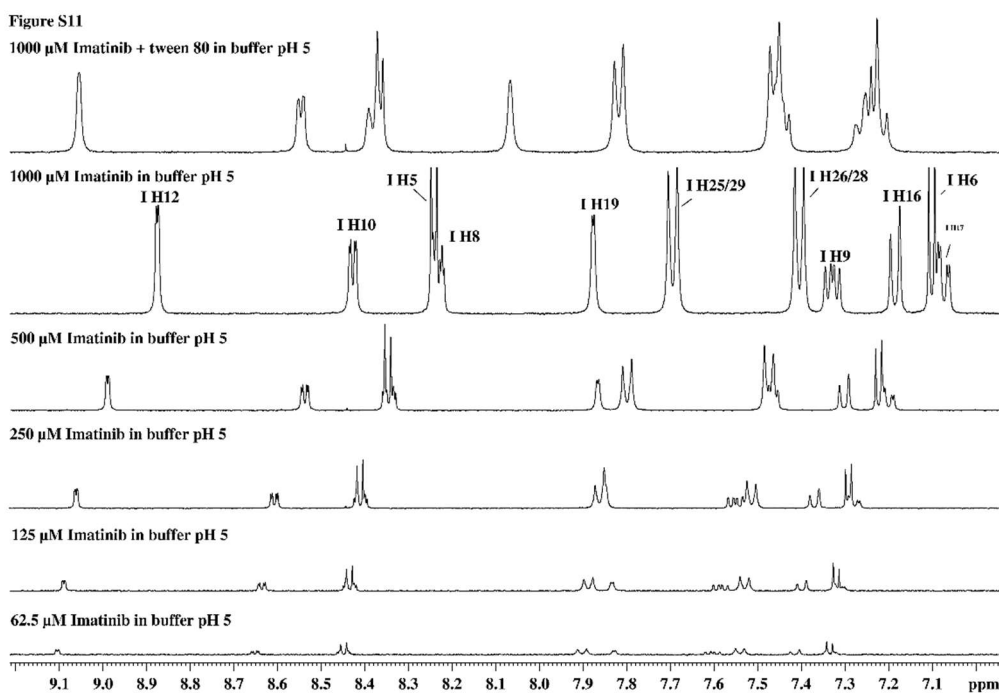
Figure S11: Concentration dependent ^{1}H NMR spectra of Imatinib (aromatic range) in buffer analogous FeSSIF, but without TC/L.
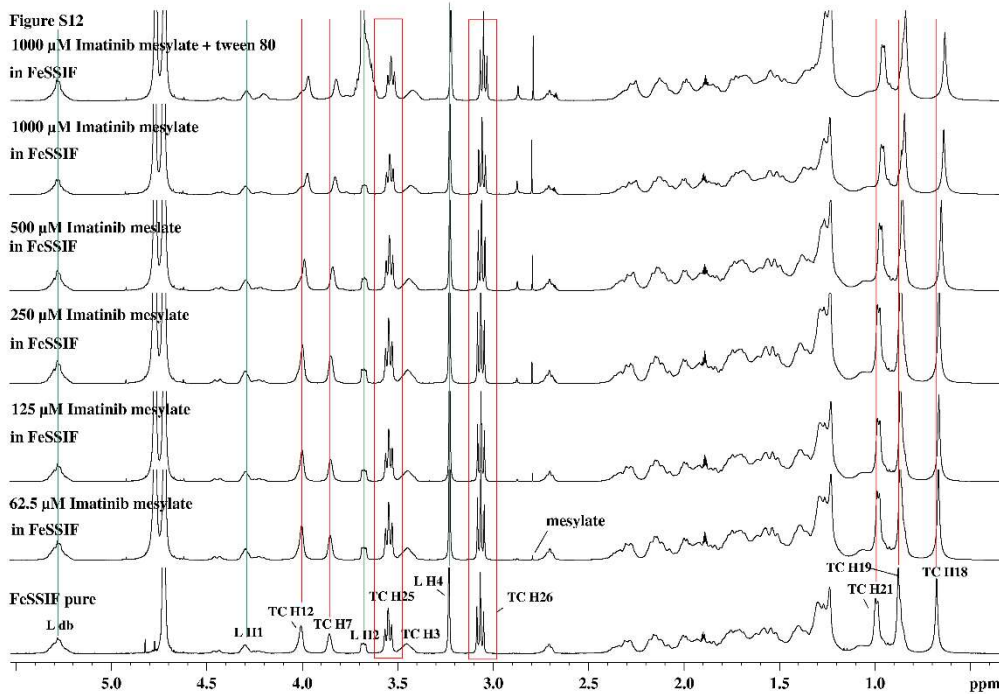
Figure S12: Concentration dependent ^{1}H NMR spectra of Imatinib mesylate in FeSSIF.
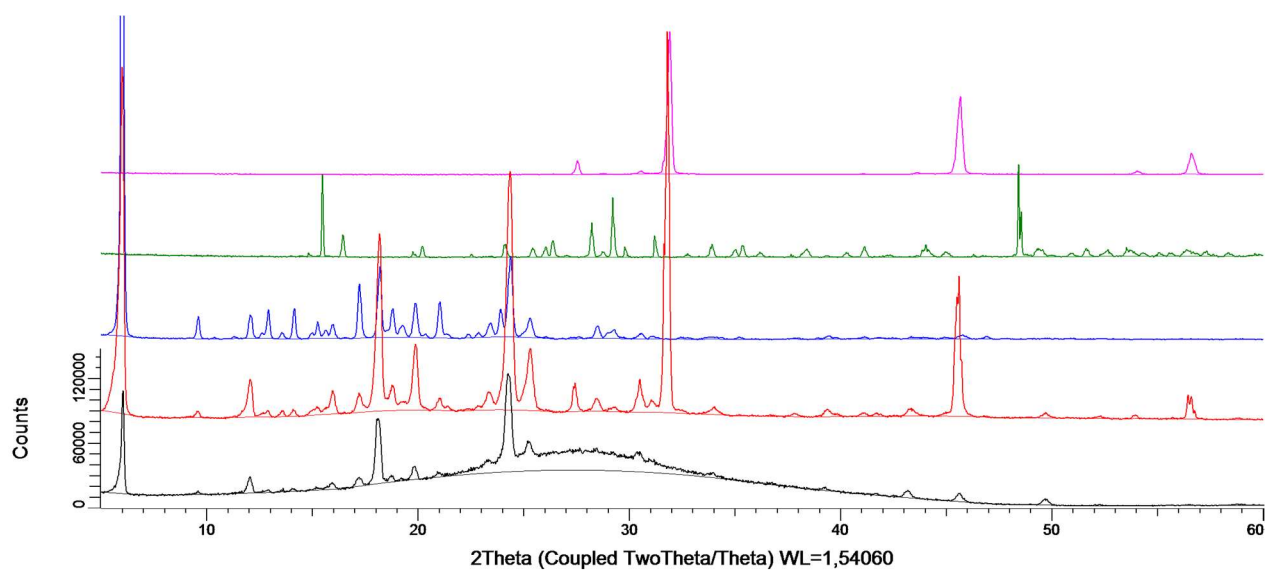
Figure S13: Overlay of the XRPD diffractograms of the residues in FaSSIF after 24 in wet state (black) and dried state (red) compared to the reference diffractograms of Imatinib free base (blue), sodium dihydrogen phosphate dihydrate (green) and sodium chloride (purple).
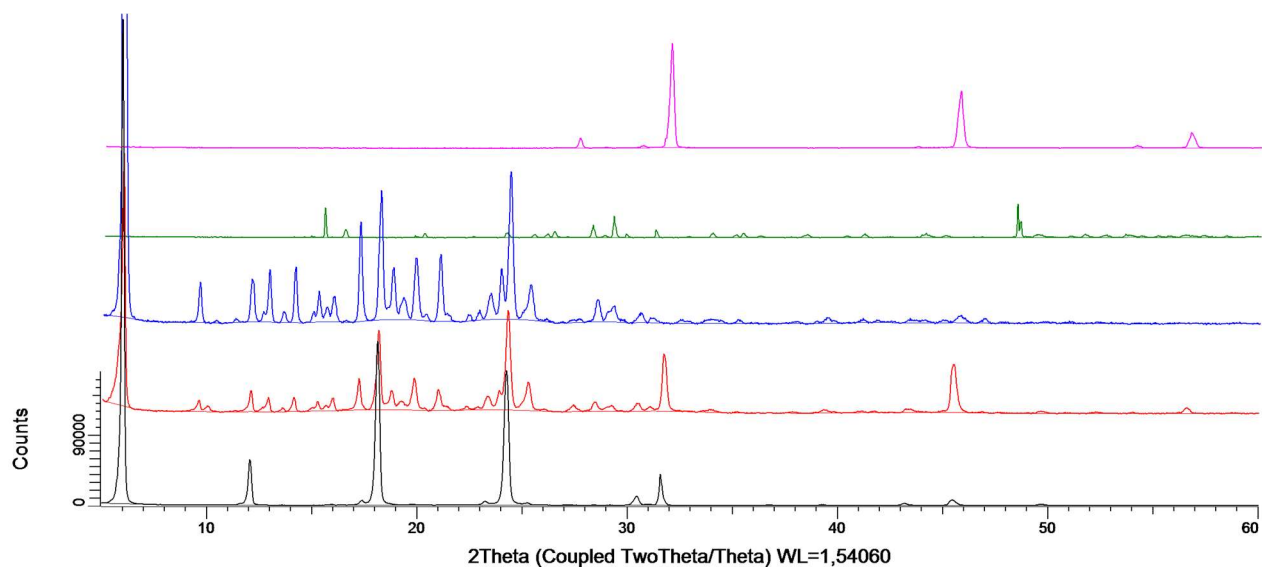
Figure S14: Overlay of the XRPD diffractograms of the residues in buffer pH 6.5 without TC/L after 24 in wet state (black) and dried state (red) compared to the reference diffractograms of Imatinib free base (blue), sodium dihydrogen phosphate dihydrate (green) and sodium chloride (purple).
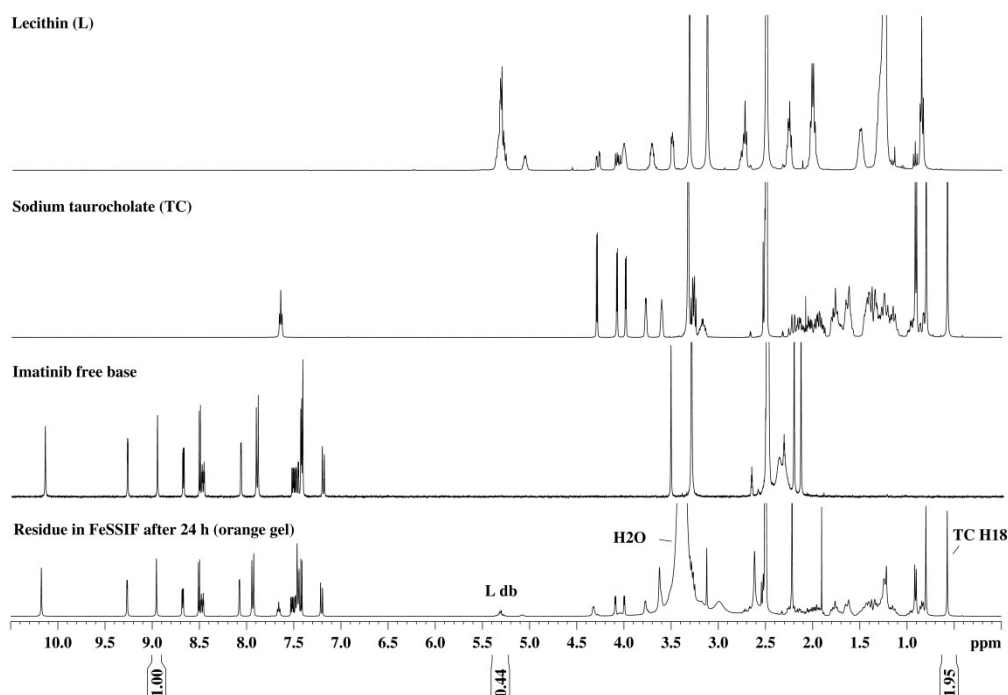
Figure S15: ^{1}H NMR spectrum of the residue in FeSSIF after 24 h (orange hydrogel) compared to Imatinib free base, sodium taurocholate (TC) and lecithin (L) dissolved in DMSO-d_6.
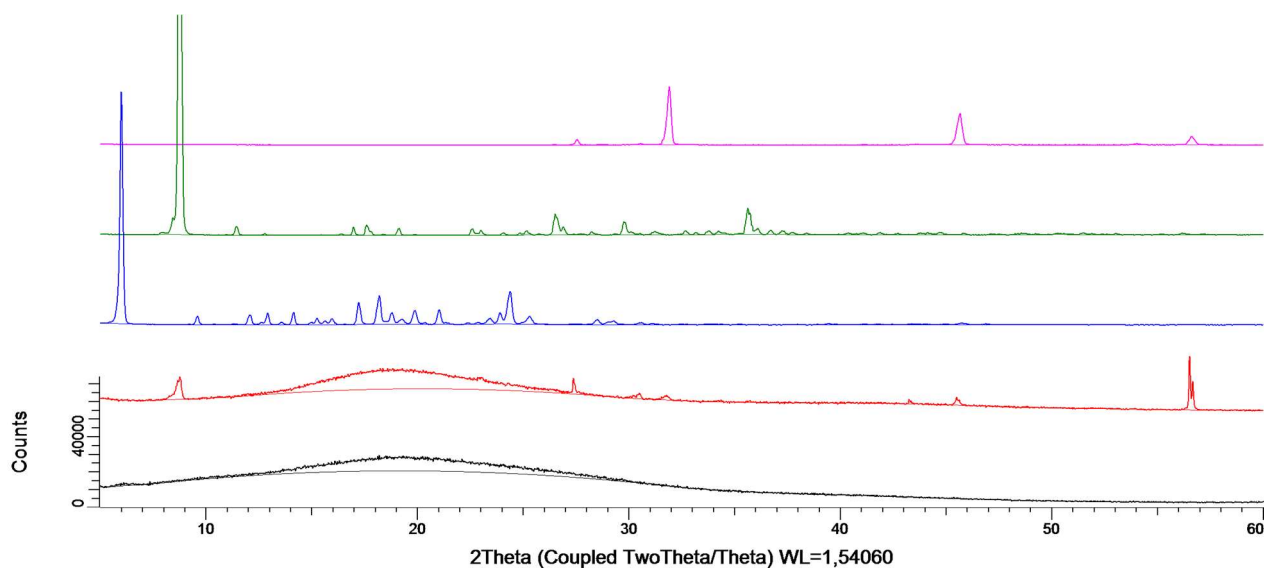
Figure S16: Overlay of the XRPD diffractograms of the residue in FeSSIF after 24 in wet state (black) and dried state (red) compared to the reference diffractograms of Imatinib free base (blue), sodium acetate (green) and sodium chloride (purple).
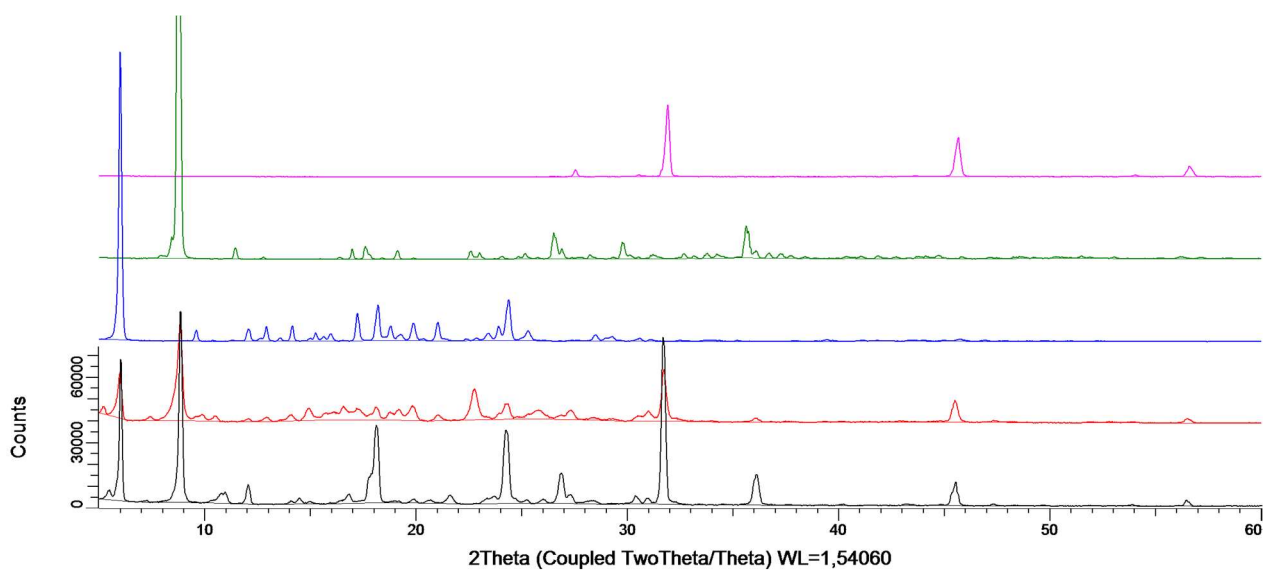
Figure S17: Overlay of the XRPD diffractograms of the residue in buffer pH 5 after 24 in wet state (black) and dried state (red) compared to the reference diffractograms of Imatinib free base (blue), sodium acetate (green) and sodium chloride (purple).
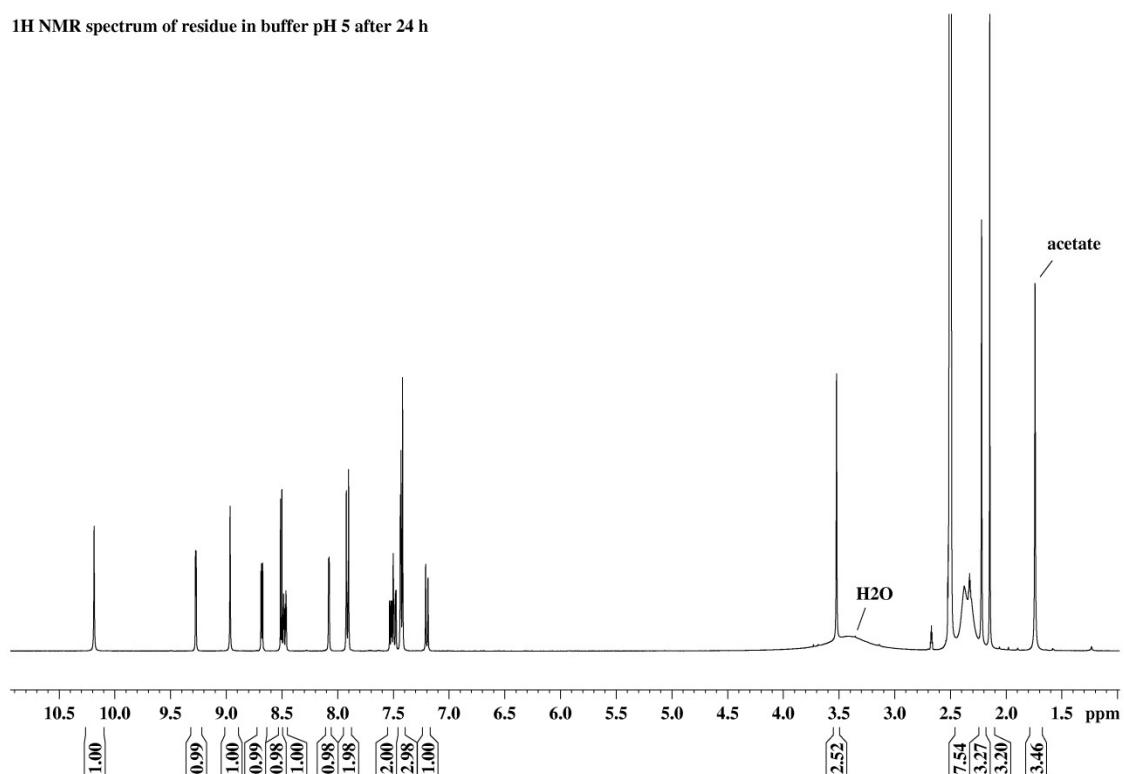
Figure S18: ^{1}H NMR spectrum of dried residue in DMSO-d$_6$ after shaking 24 h in buffer pH 5.

Chapter III: Antibacterial Anacardic Acid Derivatives

Marco Saedtler[1], Niclas Förtig[1], Knut Ohlsen[2], Franziska Faber[2], Nelson Masota[1], Kristin Kowalick[3], Ulrike Holzgrabe[1] and Lorenz Meinel[1]*

[1]Institute of Pharmacy and Food Chemistry, University of Würzburg,

Am Hubland, DE-97074 Würzburg, Germany,

[2]Institute for Molecular Infection Biology (IMIB), University of Würzburg,

Josef-Schneider-Straße 2, DE-97080 Würzburg, Germany,

[3]Labor LS SE & Co. KG, Mangelsfeld 4-6, DE-97708 Bad Bocklet, Germany
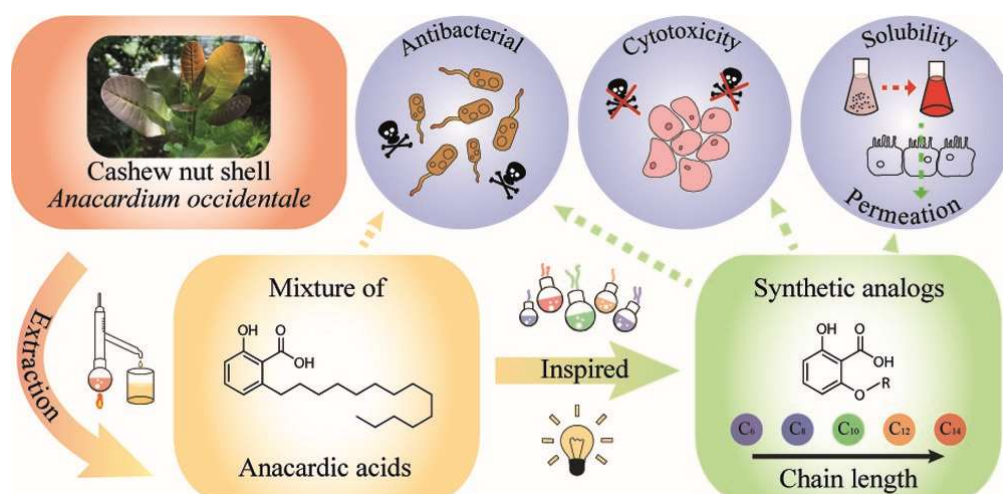
Abstract

We report on the antibacterial activity of five phenolic lipids derived from anacardic acid characterized by increasing alkyl chain lengths with 6, 8, 10, 12, or 14 carbon atoms. The compounds were profiled for their physicochemical properties, transport across epithelial monolayers, cytotoxicity, and antibacterial activity as compared to common antibiotics. No cytotoxicity was reported in cell lines of fibroblast, hepatic, colorectal, or renal origin. C_{10} and C_{12} significantly increased the survival in a Galleria mellonella model infected with multi-drugresistant *Staphylococcus aureus (*MRSA) or vancomycin-resistant *Enterococci* (VRE) as compared to the untreated control group. Future studies are required to corroborate these findings in relevant animal model systems of infection.

Introduction

Subtherapeutic doses of antibiotics selectively pressure bacteria toward resistance. Such subtherapeutic exposure is particularly probable for bacterial biofilms, within which antibiotics form a decreasing concentration gradient and hence lower (and then potentially subtherapeutic) antibiotic concentrations might be established in the vicinity of the bacteria.[1] It is for this ,among other effects, that multi-drug-resistant *Staphylococcus aureus* (MRSA) and vancomycin-resistant *Enterococci* (VRE) have formed.[2] A study from 2019 estimated that around 600 000 infections with antibiotic-resistant bacteria (63.5% considered nosocomial infections) lead to 30 000 deaths annually and cause 800 000 disability-adjusted life years in the European Union alone.[3] Within this context, biofilm-disrupting molecules with antiseptic activity are of increasing interest.[4] Although current disinfectants such as chlorhexidine, octenidine, and polyhexanide have antiseptic activity and a low tendency to induce bacterial resistance, their application is limited to a local administration leading to cytotoxic effects and tissue irritation. This limitation motivated us to screen for a novel starting off series of amphiphilic compounds derived from anacardic acid. Anacardic acid is naturally found in the cashew nut shell (Anacardium occidentale) or in the shell of a pistachio nut (Pistachia vera). Anacardic acid's antimicrobial activity against *Staphylococcus aureus*, *Bacillus subtilis*, and *Streptococcus mutans* has been reported and was attributed to its amphiphilic structure.[5–7] Additionally, anacardic acid has several other reported activities such as the inhibition of histone acetyl transferase (HAT),[8] the inhibition of matrix metalloproteinases (MMP),[9] and the chelation of metal ions as well as antioxidant

properties.[10] We built off these findings synthesizing derivatives of anacardic acid by elongating their lipophilic alkyl tail by analogy to a previous study on the derivatives of *ortho*-hydroxybenzoic acid.[11] The resulting compounds were physically and chemically characterized, and their antiseptic activity, cytotoxicity, and propensity for biofilm reduction were characterized in comparison to relevant antibiotics, including amoxicillin, ciprofloxacin, vancomycin, and linezolid, and to octenidine, a locally administered anti-infective.[12] Finally, the two most promising candidates were further assessed in vivo using a *Galleria mellonella* infection model. *G. mellonella* larvae demonstrate an innate immune response similar to that of vertebrates and have proved themselves as a reliable *in vivo* model for novel antibiotic drug candidates and toxicological studies.[13]
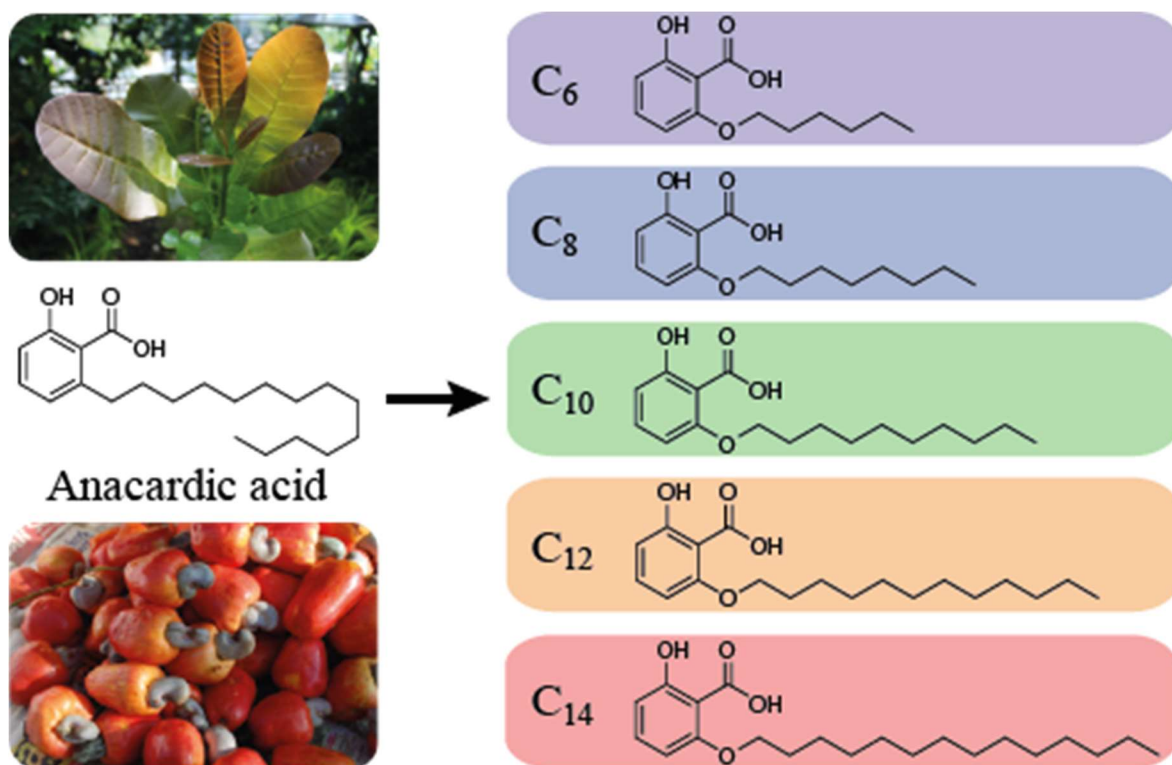
Figure 1 (Left) Cashew nut (Anacardium occidentale) fruit and plant and (right) the synthetic compounds derived from anacardic acid and used in this study.

Materials

Materials. Dulbecco's Modifed Eagle's Medium (DMEM; no. D6429, 500 mL), high glucose, Minimum Essential Eagle's Medium (MEM; no. M2279, 500 mL), Hanks' balanced salts powder (HBSS) without phenol red, MEM nonessential amino acid solution (100×), L-alanyl-L-glutamine solution (200 mM, sterile), sodium pyruvate solution (100 mM, sterile), penicillin− streptomycin solution (penicillin 10 000 units mL^{-1} and streptomycin 10 mg mL^{-1}, sterile), Endo Agar powder, fluorescein sodium salt, BioReagent suitable for fluorescence, Lucifer yellow CH dilithium salt, ginkgolic acid C13:0, and (15:0) anacardic acid were purchased from Sigma-Aldrich (Schnelldorf, Germany). Trypticasein soy broth (TSB) powder, Müller-Hinton-Bouillon (MH) powder, and brain heart infusion (BHI) powder were purchased from Carl Roth GmbH + Co. KG (Karlsruhe, Germany). Mowiol 4-88 for histology was purchased from AppliChem GmbH (Darmstadt, Germany), 4′,6-diamino-2-phenylindole (DAPI) was purchased from Invitrogen (Carlsbad, CA), mouse antibody against human ecadherin mAb was purchased from R&D systems (Minneapolis, MN), antimouse antibody Alexa Fluor 488 was purchased from Life Technologies (Darmstadt, Germany), and hexadeuteriodimethyl sulfoxide (DMSO-d$_6$, 99.8% D) was purchased from Euriso-top (Saarbrücken, Germany). Ciprofloxacin hydrochloride, vancomycin hydrochloride, and linezolid were purchased from Sigma-Aldrich. Amoxicillin was a gift from TAD Pharma GmbH (Cuxhaven, Germany). Deionized water was obtained from our in-house Merck Millipore water purification system (Darmstadt, Germany). Other chemicals and reagents used within this study were purchased from SigmaAldrich if not noted otherwise. The cell lines used for cell culture were obtained from ATCC with HEK293 (ATCC ID no. CRL1573), Hep G2 (ATCC ID no. HB-8065), and Caco-2 (ATCC ID nos. HTP-37 and NIH-3T3). The origin of the bacterial strains is shown below (**Table 1**).

Table 1 Tested Bacterial Strains, Including Information on Species, Source, and Culture Conditions.

species	code	source	anaerobic	medium	comment
Staphylococcus aureus	JE2	clin. isolate	no	MH	MRSA
Staphylococcus aureus	Lac*	clin. isolate	no	MH	MRSA
Staphylococcus aureus	ST228	clin. isolate	no	MH/TSB	biofilm-forming

Staphylococcus epidermidis	RP62a	clin. isolate	no	MH	-
Enterococcus faecalis	51229	ATCC	no	BHI	VRE
Enterococcus faecium	UL602570	clin. isolate	no	BHI	VRE
Streptococcus agalactiae	13813	ATCC	no	BHI	
Clostridium difficile	DSM27543	DSM	yes	BHI	

Scheme 1 Schematic Synthesis Route Used within this Study[a]
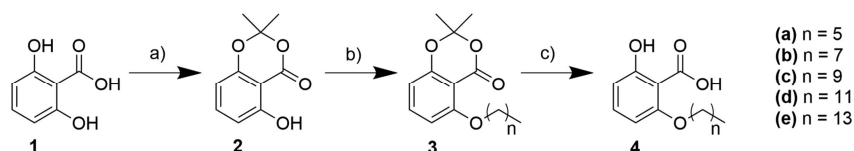
[a](a) Synthesis procedure 1; SOCl , DMAP, acetone, diethyl ether, 0 °C, 1 h, 25 °C, 1 day. (b) Synthesis procedure 2; 1-bromoalkane, K_2CO_3, acetonitrile, 50 °C, 4 days. (c) Synthesis procedure 3; KOH, tetrahydrofuran, 60 °C, 1 day.

Methods

Proton Nuclear Magnetic Resonance Spectroscopy

Proton nuclear magnetic resonance spectra (^{1}H NMR) of all compounds were recorded on a Bruker Avance 400 MHz spectrometer (Karlsruhe, Germany) operating at 400.13 MHz (Figures S22−S32) along with ^{13}C NMR spectra of all final products (Figures S33−S37). The spectra were referenced to the residual solvent signal of DMSO-d$_6$ at 2.54 ppm.[14]

Synthesis Procedures

Synthesis procedures 1−3 were obtained from previously described methods with small changes to obtain higher yields (Scheme 1).[11,15,16]

Synthesis Procedure 1

2,6-Dihydroxybenzoic acid (1) (6.16 g, 40 mmol) and N,N-dimethylpyridin-4-amine (244 mg, 2 mmol) were dissolved in 30 mL of diethyl ether under a nitrogen atmosphere. The resulting dispersion was cooled to 0 °C. Acetone (3.02 g, 3.85 mL, 52 mmol) and thionyl chloride (6.18 g, 3.77 mL, 52 mmol) were carefully added. The reaction was stirred for 1 h

at 0 °C and for 24 h at room temperature. The reaction mixture was diluted with 20 mL of aqueous saturated $NaHCO_3$ solution and extracted with diethyl ether (3 × 20 mL). The combined organic phases were washed with brine (3 × 10 mL), dried over $MgSO_4$, and concentrated under reduced pressure.

Synthesis Procedure 2

5-Hydroxy-2,2-dimethyl-4H-benzo[d][1,3]dioxin-4-one (2) (776 mg, 4 mmol) and potassium carbonate (1.10 g, 8 mmol) were suspended in 10 mL of acetonitrile under an argon atmosphere. The reaction was cooled to 0 °C, and 1-bromoalkane (5.2 mmol) was slowly added. The mixture was stirred for 30 min at 0 °C and for 96 h at 50 °C. The reaction mixture was diluted with 30 mL of deionized water and extracted with ethyl acetate (3 × 40 mL). The combined organic phases were washed with deionized water (2 × 30 mL), 1 M hydrochloric acid (1 × 30 mL), and brine (2 × 20 mL) and dried over Mg_2SO_4. The solvent was evaporated under reduced pressure.

Synthesis Procedure 3

5-(Alkyloxy)-2,2-dimethyl-4Hbenzo[d][1,3]dioxin-4-one (3a/3b/3c/3d/3e) (2.3−3.3 mmol) was dissolved in 10 mL of tetrahydrofuran, and 10 mL of 5 M potassium hydroxide aqueous solution was added. The reaction was stirred for 24 h at 70 °C. The mixture was acidified with 6 M hydrochloric acid and extracted with ethyl acetate (3 × 30 mL). The combined organic phases were washed with deionized water (1 × 30 mL) and brine (2 × 30 mL) and were dried over Mg_2SO_4. The organic solution was concentrated under reduced pressure.

High-Resolution Mass Spectrometry (HRMS)

HRMS of all final products was carried out by electrospray ionization mass spectrometry (ESI-MS) on a micrOTOF-Q III (Bruker Daltonics, Billerica, MA) equipped with an Apollo II ESI ion source. The instrument has a resolution of 20 000 and a mass accuracy of 5 ppm with external calibration. Briefly, samples were injected with a constant flow of 4 $\mu L\ min^{-1}$. The spectra were recorded continuously in the range from 50 to 2500 m/z with the capillary voltage set to −4.5 kV, an end plate voltage of −4 kV, a nitrogen nebulizer pressure of 0.3 bar, a dry gas flow of 4 $L\ min^{-1}$, and a dry temperature of 200 °C. Funnel 1 was 100 Vpp, funnel 2 RF was 200 Vpp, hexapole RF was 200 Vpp, the quadrupole ion energy was 5 eV, the quadrupole low mass was 50 m/z, the collision energy was 10 eV, the collision RF was

300 Vpp, the transfer time was 70 µs, and the prepulse storage was 10 µs. The instrument was calibrated with sodium formate, which was measured directly after the sample measurements. The spectra were recorded with the Compass software from Bruker Daltonics containing the OTOF control 3.4 software to control the instrument. For data evaluation, data analysis software DA 4.2 from Bruker Daltonics was used.

Critical Micelle Concentration (CMC)

CMC values were determined using a Krüss K12 tensiometer (Krüss GmbH, Hamburg, Germany) equipped with a heating device to maintain 25 °C. The surface tension was measured at different concentrations using the Wilhelmy plate method.[17] Briefly, 70 mL of deionized water and a magnetic stirring bar were added to a 120 mL glass vial, and a 1 mL aliquot of an aqueous stock solution was added and stirred for 30 s after each measuring point. Concentrations of the used stock solutions were 500, 150, 50, 100, and 100 µmol L^{-1} for C_6, C_8, C_{10}, C_{12}, and C_{14}, respectively. The surface tension (σ) was calculated by the software, measuring the force applied to a platinum plate which was slowly immersed in the aqueous solution. CMC values are presented as the concentration in µmol L^{-1} at the crossing point of two trend lines obtained by linear regression of the two linear sections before and after the CMC. Experiments were conducted in triplicate, and the results are displayed as the mean ± standard deviation.

Partition Coefficient (log D, pH 7.4)

Partition coefficients were determined following OECD guidelines on partition coefficients via the HPLC method.[18] Briefly, an Agilent 1200 series HPLC consisted of a G1322A degasser, a G1311A quaternary pump, a G1329A autosampler, a G1316A column oven, and a G1314 VWD detector equipped with a Synergi MaxRP 80 Å, 150 × 4.6 mm², 4 µm column from Phenomenex (Torrance, CA). The mobile phase consisted of 10 mmol L^{-1} pH 7.4 phosphate buffer, and methanol 30:70 and was used in an isocratic method for a total run time of 20 min with a flow of 1.5 mL/min. The temperature was set to 30 °C, the injection volume was 40 µL, and the detection wavelength was $\lambda = 254$ nm. Samples were prepared by dissolving 4 mg of the compound in 1 mL of methanol, diluting it 1:1000 with the same solvent, and filtering it through 0.2 µm and 4 mm PTFE filters from Whatman (Maidstone, U.K.). A calibration curve was prepared from thiourea measurements (dead time), acetanilide, benzene, biphenyl, anthracene, and triphenylamine using their calculated

capacity factor k (**eq 1**) ($R^2 = 0.99$). Partition coefficients log P were calculated from log $D_{pH\ 7.4}$ (**eq 2**).

$$k = \frac{t_R - t_0}{t_0} \qquad (1)$$

k   -   capacity factor
t_R -   retention time
t_0 -   dead-time

$$\log P = \log D_{pH} - \log\left(\frac{1}{1 + 10^{pH - pKa}}\right) \qquad (2)$$

logP   -   partition coefficient
logD   -   distribution coefficient
pK_a -   acid dissociation constant

Solubility Determination

Solubility was determined using a shake flask method.[19] The compound (5−10 mg) was placed in a 1.5 mL reaction vial (Eppendorf, Hamburg, Germany). One milliliter of pH 7.4 ± 0.05 phosphate-buffered saline (PBS) was added and placed in a ThermoMixer F1.5 (Eppendorf). The aliquots were shaken at 800 rpm for 48 h at 25 °C. After centrifugation at 17 880 rcf for 10 min at 25 °C in a Universal 302 R centrifuge (Hettich Zentrifugen, Tuttlingen, Germany), 0.25 mL was carefully withdrawn and immediately diluted with 0.75 mL of methanol. The UV Absorbance was measured at 254 nm with an Evolution 201 UV−visible spectrophotometer (Thermo Scientific, Waltham, MA), and if necessary, further dilution was done with methanol. Standard curves were measured in methanol from 100 to 5 μmol L^{-1} on the same instrument, all yielding coefficients of determination of $R^2 \geq 0.99$. Results were calculated as the means with a standard deviation (n = 3).

Dissociation Constant (pK$_a$)

Dissociation constants were determined using a UV-metric titration assay on a Sirius T3 titration platform from Pion Inc. (Woburn, MA) following the manufacturer's instructions.[20] Briefly, 0.001 mL of a 150 mmol L^{-1} stock solution in dimethyl sulfoxide (DMSO) was placed in a reaction vial, and 1.5 mL of ionic strength adjusted water (ISA water) was added automatically. The starting pH 12 value was automatically adjusted by the addition of 0.5 mol L^{-1} potassium hydroxide solution and stirred for 2 min. The solution was stepwise titrated to pH 2 by the addition of 0.5 mol L^{-1} hydrochloric acid solution aliquots. After each

addition, a UV spectrum and the respective pH value were recorded with a UV-dip probe and a AgCl electrode. The titration from pH 2−12 was repeated three times per experiment, and each experiment was performed in triplicate. The spectrum between 250 and 450 nm was used in the range of pH 2−6 to identify the protonated and deprotonated species and calculate the pK_a value. Analysis was done using the Sirius T3 Refine software (version 1.1.3.0) from Pion Inc.

High-Pressure Liquid Chromatography (HPLC)

HPLC analysis was performed on a Hitachi LaChrom Ultra equipped with an L-2400U UV detector, an L-2300 column oven, an L2200U autosampler, and two L-2160 pumps. A ZORBAX Eclipse XDB-C18 5 μm 4.1 × 150 mm column from Agilent Technologies (Waldbronn, Germany) was used at 23 °C, and a 0.01 mL injection volume with a detection wavelength of 254 nm was set. An isocratic method was used with acetonitrile and water (9:1) + 0.1% trifluoroacetic acid (TFA). The run time was up to 25 min.

Liquid Chromatography−Mass Spectrometry (LC−MS)

LC−MS analysis was performed on a Shimadzu LC-20AProminence HPLC instrument (Shimadzu, Kyoto, Japan) coupled with a UV detector set to λ = 254 nm and an electrospray ionization (ESI) and single quadrupole mass analyzer (QMS) operating in positive mode. Samples were prepared by dissolving 1 mg of compound in 1 mL of methanol (LC−MS grade) and further diluting it, resulting in a final concentration of 0.1 mg mL^{-1}. Separation after injection of 0.02 mL was achieved by using a Phenomenex-Synergy-Fusion-RP, 4.6 × 150 mm^2, 5 μm column (Phenomenex, Torrance, CA) and a methanol/water gradient. In detail, mobile phase A was deionized water with 0.1% (v/v) formic acid and mobile phase B was methanol with 0.1% (v/v) formic acid. For the separation %, the B content of the mobile phase was continuously increased from 5 to 90% over 18 min.

Differential Scanning Calorimetry (DSC)

Differential scanning calorimetry was measured with a DSC 8000 from PerkinElmer (Waltham, MA). Briefly, 3 to 4 mg of the substance was weighed into aluminum pans with a pinhole in the lid and analyzed at a scanning rate (heating and cooling rate) of 20 °C min^{-1} from −50 to 100 °C. The mass of the crucible was noted before and after the experiment to

calculate any loss of mass during the process. Three measurement cycles were performed for every sample, and the mean melting point was calculated.

X-ray Powder Diffraction (XRD)

X-ray powder diffraction was measured on a silicon single crystal holder and analyzed with a Bruker Discover D8 powder diffractometer (Karlsruhe, Germany) using Cu Kα radiation (unsplit Kα$_1$ + Kα$_2$ doublet, mean wavelength λ = 154.19 pm) at 40 mA and 40 kV, a focusing Goebel mirror, and a 1.0 mm microfocus alignment (1.0 mm pinhole with 1.0 mm snout). The scattered X-ray beam went through a receiving slit with a 7.5 mm opening and a 2.5° axial Soller slit, and detection was performed with a LynxEye-1D detector (Bruker AXS) using 192 channels. Measurements were made in reflection geometry in coupled 2θ/θ mode with a step size of 0.025° in 2θ and a 0.25 s measurement time per step in the range of 5−60° (2θ). Data collection and processing were carried out with the DIFFRAC suite (V2 2.2.69.0) and DIFFRAC.EVA 2.1 software packages from Bruker.

Caco-2 Permeation Assay

The Caco-2 permeation assay was performed as described before with small variations.[21] Transportation was studied in the apical-basolateral direction, and cells were used in passage 51−54. In brief, cells were incubated in culture medium (DMEM high glucose, 10% (v/v) FBS, and 1% (v/v) nonessential amino acid (NEAA) solution) at 37 °C in 5% CO$_2$. Passages were performed at 80% confluence in 1:2−1:4 ratios, and three passages were necessary to develop the phenotype. Afterward, cells were seeded in the trans wells at a 2.6×10^5 cells cm^{-2} density and maintained for 27 days. The culture medium for maintenance (DMEM high glucose, 10% (v/v) FBS, 1% (v/v) NEAA, 1% (v/v) penicillin G/ streptomycin solution) was changed every second to third day. Trans-epithelial electrical resistance (TEER) values were measured with an EVOM2 STX3 chopstick electrode connected to an EVOM2 epithelial voltammeter from World Precision Instruments (Sarasota, Florida) to follow the monolayer development. The transportation medium was HBSS at pH 7.4 altered by adding 25 mmol L^{-1} 2-(4-(2-hydroxyethyl)-1piperazinyl)-ethanesulfonic acid (HEPES) and 0.35 g L^{-1} NaHCO$_3$. Stock solutions (100 mmol L^{-1}) of all substances were prepared in DMSO and diluted with transportation medium, resulting in test solutions of 100 μmol L^{-1} with a maximum of 0.1% (v/v) DMSO in all cases. Fluorescein and Lucifer yellow solutions were used as controls. Trans wells were washed with HBSS to remove residual culture medium,

and 0.5 mL of test solution was applied in the apical chamber (donor). The basolateral chamber was filled with 1.2 mL of HBSS (acceptor). Immediately after apical application, 0.1 mL was withdrawn from the donor chamber to determine the initial concentration (c_0). The plates were incubated at 37 °C, 0% CO_2 while gently shaking at 150 RRM. Samples (0.1 mL each) were withdrawn from the receiving chamber after 30, 60, 90, and 120 min and immediately replaced with warm transportation buffer. Additionally, after 120 min a 0.1 mL sample was taken from the apical chamber as well to calculate the mass balance (c_{rest}). TEER values were measured directly before and after the experiment to monitor the integrity of the monolayer. Monolayers with a TEER value of ≥ 165 Ω cm^2 were considered integers. Apical and basolateral samples were stored at 4 °C and analyzed by HPLC on the next day. Fluorescein and Lucifer yellow (LY) were analyzed by fluorimetry. Experiments were performed in triplicate, and the results were calculated and reported as the apparent permeation coefficient (P_{app}). Representative cell monolayers were cut out and stained to evaluate their integrity.

Fluorimetric Analysis of Fluorescein and LY

Analysis was performed using LS50 B luminescence from PerkinElmer (Waltham, MA) equipped with a 96-well plate adapter as described before.[22] Briefly, samples were sufficiently diluted with HBSS buffer, and 0.09 mL was pipetted into white Nunc F96 microwell plates from ThermoFisher Scientific (Waltham, MA). Parameters for fluorescein measurements were set to an extinction wavelength of $\lambda = 450$ nm, an extinction slit of 2.5, an emission wavelength of $\lambda = 514$ nm, an emission slit of 15, and a read time of 0.4 s. A standard curve was conducted in a range of 1 to 0.05 μmol L^{-1} ($R^2 = 0.99$). LY analysis was performed on the same LS50 B luminescence setting the parameters to an extinction wavelength of $\lambda = 470$ nm, an extinction slit of 2.5, an emission wavelength of $\lambda = 535$ nm, an emission slit of 2.5, a read time of 5 s. A standard curve was conducted in the range of 10 to 0.1 μmol L^{-1} ($R^2 = 0.98$).

Staining and Visualization of Caco-2 Monolayers

Preparation of the Caco-2 monolayers attached to the transwell system was done by the single placement of representative trans wells in a six-well plate and staining with 4′,6-diamidino-2phenylindole (DAPI) and Alexa Fluor 488 as previously described.[23] In detail, monolayers were washed two times apically and basolaterally with PBS pH 7.4 and exposed

to cold methanol for 10 min (washing was always performed with PBS pH 7.4). They were washed again three times and blocked using 0.5 mL of Roti-Block (Carl Roth, Karlsruhe, Germany) in PBS for 1 h at room temperature. Inserts were washed three times, and mouse antibody against human e-cadherin, diluted 1:100 in PBS 4 °C, was added and incubated overnight at 4 °C. The next morning, the cells were washed five times, followed by the secondary antimouse antibody Alexa Fluor 488, diluted 1:200 in blocking solution and incubation for 90 min at room temperature in the dark. The cells were washed four times followed by DAPI, diluted 1:1000 in PBS. After incubation for 10 min at room temperature in the dark, cells were washed three times. Stained monolayers were cut out from the transwell inserts using a scalpel and embedded with Mowiol 4-88 on glass microscope slides. Samples were stored in the dark until further use. Representative pictures were taken using a Leica DMIRE2 confocal microscope (Leica Camera AG, Wetzlar, Germany) equipped with a HCX PL APO 63×/1.40 Oil lbd BL objective from Leica operated with Leica confocal software. Excitation was carried out with the blue channel and the green channel. The average of four pictures at a resolution of 1024 pixels × 1024 pixels with a 2.0× zoom was taken, and a series of 20 pictures per stack were collected for every sample.

Cell Proliferation Assay (WST-1)

Cytotoxicity was studied in human embryotic kidney cells (HEK 293), human liver cells (Hep G2), human epithelial colorectal cells (Caco-2), and murine fibroblasts (NIH 3T3) in their respective culture medium (**Table 2**).[23] After thawing, cells were passaged at least three times before the experiments were performed to develop their phenotype. Compound stock solutions were prepared in DMSO and diluted with culture medium. For the experiments, a 0.1 mL cell suspension in the appropriate seeding density (**Table 2**) was transferred to 96-well plates and incubated overnight at 5% CO_2 and 37 °C. A diluted substance solution (0.1 mL) was added and incubated for 24 h. Final DMSO concentrations did not exceed 0.5%. After incubation, cell proliferation reagent WST-1 (WST-1) was diluted (1:1 v/v) with culture medium, and 0.02 mL was added per well. The absorbance was measured after 2 h at 450 nm using 630 nm as the reference wavelength. The experiments on NIH 3T3 were performed in quadruplicate in three separate replicates (n = 12) covering a concentration range from 100 µmol L^{-1} to 195 nmol L^{-1}. Cytotoxicity on HEK 293, Hep G2, and Caco-2 was screened in triplicate in one repetition (n = 3) covering a concentration range from 100 to 6.25 µmol L^{-1}. The IC_{50} values were calculated, if possible, using controls without

compound and cells without WST-1 cell types used in the cell proliferation assay (WST-1). For an overview, please see **Table 2**.

Table 2 Tested cell-types including information on culture medium and seeding density.

Cell-type	Culture medium	Seeding density
HEK 293	DMEM high glucose, +10% (v/v) FCS, +1% (v/v) P/S	4×10^4 cells mL^{-1}
Hep G2	MEM, +10% (v/v) FCS, +1% (v/v) P/S, +1% (v/v) NEAA, +2 mmol L^{-1} glutamine, + 1 mmol L^{-1} sodium pyruvate, +1.5 g L^{-1} sodium bicarbonate	1.25×10^5 cells mL^{-1}
Caco-2	DMEM high glucose, +10% (v/v) FCS, +1% (v/v) NEAA, +1% (v/v) P/S	2×10^5 cells mL^{-1}
NIH 3T3	DMEM high glucose, +10% (v/v) FCS, +1% (v/v) P/S	5×10^4 cells mL^{-1}

Reverse Mutation Assay Using Bacteria (Ames Test)

The potential to cause mutations was assessed in *Salmonella typhimurium* and *Escherichia coli* following OECD Guidelines for the Testing of Chemicals and previous published protocols.[24-26] Four histidine-auxotrophic *S. typhimurium* strains (TA 98, TA 100, TA 1535, and TA 1537) and one tryptophan-auxotrophic *E. coli* strain (WP2) were tested with or without the addition of metabolic activity by S9 homogenate (Trinova Biochem GmbH, Giessen, Germany). Two different methods were tested: plate incorporation and preincubation. Prior to the experiments, bacteria were cultured in broth containing 25 g L^{-1} nutrient medium no. 2 for 10 h at 37 °C while gently shaking up to a bacterial density of approximately 10^9 cells mL^{-1} in the late exponential phase of growth. The final concentrations of the tested compounds were 500.7, 158.5, 50.1, 15.9, and 5.0 µg per agar plate. Briefly, for the plate incorporation method, 2000 µL of top agar, 100 µL of the test solution (dissolved test compound or control), 100 µL of a bacterial suspension, and 500 µL of teh S9Mix (with metabolic activity) or S9Mix substitution buffer were mixed at 45 °C and poured on minimal-agar plates supplemented with 0.05 mmol L^{-1} histidine (for S.

typhimurium strains) or 0.05 mmol L^{-1} L-tryptophan (for the *E. coli* strain). After solidification, agar plates were incubated at 37 °C for 40−72 h. For the preincubation method, 100 µL of a test solution, 100 µL of a bacterial suspension, and 500 µL of the S9Mix or S9Mix substitution buffer were mixed and incubated at 37 °C for 20 min. After this preincubation, 2000 µL of top agar was added and the solution was mixed and poured on minimal-agar plates, and after solidification, the mixture was incubated at 37 °C for 40−72 h. The negative control was DI water, and the solvent control was DMSO. Positive controls without metabolic activity were 5 µg of 2-nitrofluorene for TA 98, 10 µg of sodium azide for TA 100, 1.5 µg of sodium azide for TA 1535, 50 µg of 9-aminoacridine for TA 1537, and 0.05 µg of methylmethanesulfonate for WP2. A positive control with metabolic activity was 2-aminoanthracene: 1, 1, 3, 3, and 20 µg for TA 98, TA 100, TA 1535, TA 1537, and WP2, respectively. Revertant colonies were counted, and the mutation factor (MF) was calculated (**eq 3**). The test compound was considered to be mutagenic if there was a dose-dependent increase in the number of revertants and/or a biologically relevant positive response for one or more concentrations in at least one strain. A biologically relevant increase was defined as a revenant count at least twice as high for test strains TA 98, TA 100, and *E. coli* WP2 and at least three times as high for test strains TA 1535 and TA 1537 compared to the solvent control.[27] Experiments were performed in triplicate. For an overview of the used solutions, see **Table 3**.

$$\text{MF} = \frac{\text{Mean value of revertant counts (test item)}}{\text{Mean value of revertant counts (solvent control)}} \tag{3}$$

MF   -   mutation factor

Table 3 Solutions used for the Ames test.

Solution	Composition	Treatment
Top agar	6.0 g L^{-1} bacto agar, 5.0 g L^{-1} sodium chloride in DI water	Sterile; autoclaved for 20 min at 121 °C
S9 Mix	Prepared from S9 liver homogenate as specified by Trinova Biochem GmbH. 5% S9 Mix for *S. typhimurium* strains 10% S9 Mix for *E. coli* strain	-
S9 Mix substitution buffer	120 mL 0.2 mmol L^{-1} NaH$_2$PO$_4$ x H$_2$O, 880 mL 0.2 mmol L^{-1} Na$_2$HPO$_4$, pH adjusted to 7.4	Sterile, autoclaved for 20 min at 121 °C
Vogel-Bonner-salts	10 g L^{-1} MgSO$_4$ x 7 H$_2$O, 100 g L^{-1} citric acid, 175 g L^{-1} NaNH$_4$HPO$_4$ x 4 H$_2$O, 500 g L^{-1} K$_2$HPO$_4$ in DI water	Sterile; autoclaved for 20 min at 121 °C
Vogel Bonner Medium E agar plates	15 g L^{-1} agar agar, 20 mL L^{-1} Vogel-Bonner salts solution, 50 mL L^{-1} glucose solution (40%) in DI water	Sterile; autoclaved for 20 min at 121 °C

Biofilm-Inhibition Assay

Biofilm formation was quantified by crystal violet staining.[28] *Staphylococcus aureus* (ST228 clinical isolate) was plated on Mueller-Hinton agar plates and stored at 4 °C until use. Bacteria were cultured overnight in tryptic soy broth (TSB) at 37 °C and adjusted to an optical density (OD$_{600}$) of 0.05 the next day. Compound stock solutions were prepared in DMSO and diluted with TSB, resulting in a maximum DMSO concentration of 1% (v/v), which did not affect bacterial growth or biofilm formation (data not shown). A bacterial solution (0.2 mL) and a compound solution (0.05 mL) were added to each well of a 96-well plate and cultured overnight at 37 °C. Controls were 0.2 mL of bacterial solution plus 0.05 mL of TSB (negative control) and 0.25 mL of TSB without bacteria (positive control). On the next day, the optical density at 595 nm (OD$_{595}$) was measured using a Multiskan Ascent

(Thermo Electron Corporation, Waltham, MA) plate reader, after which all wells were carefully decanted and washed three times with phosphate-buffered saline (PBS) at pH 7.4. Plates were placed on a heating device at 60 °C for 1 h and afterward stained with 0.1 mL of crystal violet 0.1% (m/v) in water. After 15 min at room temperature (RT), the crystal violet solution was decanted, and the plates were washed with DI water and dried overnight at RT. Ethanol (0.1 mL) was added to each well and gently shaken in an orbital shaker for 20 min. The absorbance at 492 nm was measured in the same UV plate reader as above and used for the calculation of the relative biofilm formation. All experiments were performed three times with four replicates.

Minimal Inhibitory Concentration (MIC)

MIC values were determined according to CLSI guidelines.[29] Briefly, for aerobic bacteria these were frozen in the respective growth medium containing 20% (v/v) glycerol. These were streaked and incubated on agar plates before testing and used within 2 weeks to prevent autolysis or mutation. The day before the experiment, a colony was picked and cultured overnight at 37 °C in 3 mL of the respective growth medium on an orbital shaker. The next morning, 0.1 mL of this bacterial suspension was withdrawn and added to 30 mL of growth medium and cultured at 37 °C on an orbital shaker operating at 150 rpm. After 2−5 h depending on the bacterial growth, the optical density at a wavelength of 600 nm (OD_{600}) was measured using a Eppendorf Biophotometer Plus (Eppendorf, Hamburg, Germany), adjusted to $OD_{600} = 0.05$ with growth medium and used within 30 min. Stock solutions (100 or 50 mmol L^{-1}) in DMSO were prepared and diluted to 200 μmol L^{-1} with growth medium. A serial dilution was prepared in sterile, transparent U-bottomed 96-well plates (VWR, Darmstadt, Germany), with each well containing 0.1 mL of the respective concentration. The bacterial suspension (0.1 mL, $OD_{600} = 0.05$) was added, resulting in a tested concentration range of 100 μmol L^{-1} to 195 nmol L^{-1} where the maximum DMSO concentration did not exceed 0.2% (v/v). The negative control was a medium without compound and bacteria, and the growth control was bacteria without compound. The 96-well plates were cultured overnight at 37 °C and visually evaluated for bacterial growth the next morning. The MIC values were defined as the lowest concentration w/o visible growth and were reported as cautiously as possible by stating the highest observed value from a total of six repetitions in three independent experiments. All experiments were performed three

times in duplicate. Representative dilutions were plated on agar plates for every bacterial strain.

MIC values in anaerobic bacteria were determined inside an anaerobic chamber (Coy Laboratory Products Inc., Grass Lake, MI) with an anaerobic atmosphere composed of 85% N_2, 10% H_2, and 5% CO_2. Briefly, 96-well plates containing compound solutions, media, and agar plates were put into the chamber the day before the experiment to remove any residual oxygen. Bacteria were grown under static conditions at 37 °C within the chamber. Preparation and dilution of the solutions as well as evaluation of the MIC values was done as described above.

MIC Plating on Agar Plates

According to CLSI guidelines MIC values were confirmed after visual detection.[30] A 0.01 mL portion of the well with the detected MIC value and the next two concentrations above and below that value were withdrawn and diluted with 0.09 mL of the respective growth medium (1:10). Droplets (0.01 mL) of these five dilutions were separately placed side by side on an agar plate, and the plate was carefully inclined to allow the droplet to flow across it in a straight line. Plates were cultured overnight at 37 °C, and bacterial growth was evaluated on the next day by counting the colonies, if any were present.

Galleria mellonella Assay

Galleria mellonella were purchased (Feeders & more GmbH, Au in der Hallertau, Germany) with an overall weight of 0.45 ± 0.10 g for the E. faecium UL602570 group and 0.31 ± 0.07 g for the S. aureus Lac* group. All *G. mellonella* larvae were used within 4 days postdelivery to avoid maturing and pupating. Each group contained 20 G. mellonella larvae which were housed separately in Petri dishes with small amounts of wooden chips. Control groups were noninfected animals treated with phosphate-buffered saline pH 7.4 (PBS), and infected animals were treated with PBS. Bacteria were streaked on agar plates of the respective medium and used within 1 week. Cultures in 3 mL of growth medium were incubated at 37 °C on the evening before the experiment, and 0.2 mL of these cultures was transferred into 30 mL of growth medium the next morning and incubated at 37 °C (under gentle shaking). The optical density was adjusted in PBS, and the resulting bacterial suspension was mildly centrifuged at 3500 rcf for 5 min. The supernatant was carefully withdrawn, and the bacteria were resuspended in PBS. The suspension was again centrifuged at 3500 rcf for 5 min, and

the supernatant was removed and resuspended in PBS to remove any residual bacterial toxins. Resulting bacterial concentrations were 2.5×10^8 CFU mL^{-1} for ST228 and 1.25×10^7 CFU mL^{-1} for UL602570. Galleria were infected by injecting 0.02 mL of the bacterial suspension (or 0.02 mL of PBS for the noninfected group) into the lower part of their body using a BD Micro-Fine + Demi 0.3 mL, 0.30 mm (30 G) × 8 mm syringe. Compound stock solutions were prepared in DMSO, and further dilutions were done in PBS, resulting in a final concentration of 200 µmol L^{-1} for all compounds. All PBS media and compound dilutions in PBS used for treatment contained residual 5% DMSO (v/v). One hour after infection, 0.02 mL of a compound solution was injected into the same body part of the *G. mellonella*, and the animals were kept at 37 °C. The observation period was set to 94 h, and dead animals were counted (darkened color and no visible movement) and removed from the Petri dish every 6 h in the first 48 h and after that every 12 h until 96 h postinfection. Results for all groups are presented as a survival plot.

Statistics

Data and statistics evaluations were carried out using GraphPad Prism version 6.04 from GraphPad Software, Inc. (San Diego, CA). Robust regression and Outlier removal (ROUT) identification was performed for all data containing 10 or more data sets (n ≥ 10) using a ROUT coefficient Q of 1%. Data sets were compared using a One-way ANOVA test, and differences among groups were calculated using Dunnett's multiple comparison test and represented by asterisks (*$p \leq 0.05$, **$p \leq 0.01$, and ***$p \leq 0.001$).

Results

A series of 5 compounds, inspired by the naturally occurring anacardic acid, were synthesized, systematically extending the aliphatic alkane residue from 6 to 14 carbon atoms (**Figure 1**). Namely, 2-(hexyloxy)- (C$_6$), 2-(octyloxy)- (C$_8$), 2-(decyloxy)(C$_{10}$), 2-(dodecyloxy)- (C$_{12}$), and 2-(tetradecyloxy)-6-hydroxybenzoic acid (C$_{14}$) were obtained and fully characterized concerning their physicochemical properties (**Figure 2**). The purity of all products exceeded ≥95% as assessed by high-pressure liquid chromatography coupled UV metric (HPLC-UV) analysis (**Figures S2−S6**). All solid compounds were crystalline, except for C$_8$ which was liquid at room temperature. The endothermic melting points were at 32 °C (C$_6$), 20 °C (C$_8$), 33 °C (C$_{10}$), 45 °C (C$_{12}$), and 51 °C (C$_{14}$) (**Figures S12− S16**). Dissociation constants (pK$_a$) were similar for all substances: 3.32 ± 0.07 (C$_6$), 3.24 ± 0.04 (C$_8$), 3.21 ±

0.07 (C_{10}), 3.21 ± 0.06 (C_{12}), and 3.34 ± 0.05 (C_{14}), respectively. The apparent solubility was assessed in phosphate-buffered saline (PBS, pH 7.4) with 8.40 ± 0.18 mmol L^{-1} (C_6, 2 mg mL^{-1}), 3.19 ± 1.02 mmol L^{-1} (C_8, 0.85 mg mL^{-1}), 0.48 ± 0.07 mmol L^{-1} (C_{10}, 0.14 mg mL^{-1}), 0.45 ± 0.02 mmol L^{-1} (C_{12}, 0.15 mg mL^{-1}), and 0.18 ± 0.24 mmol L^{-1} (C_{14}, 0.06 mg mL^{-1}) (**Figure 2A**). The value of log P increased linearly with increasing alkyl-chain length ($R^2 =$ 0.99) with log P values of 4.42 ± 0.06 (C_6), 6.00 ± 0.02 (C_8), 7.29 ± 0.02 (C_{10}), 8.47 ± 0.03 (C_{12}), and 9.43 ± 0.02 (C_{14}) (**Figure 2B**). The critical micelle concentration (CMC) was the lowest for C_{10} (6.5 ± 0.4 μmol L^{-1}) and increased to 31.3 ± 1.2 and 176.3 ± 6.1 μmol L^{-1} for C_8 and C_6 as well as 16.9 ± 1.7 μmol L^{-1} for C_{12}, respectively (**Figure 2C**). As for its low aqueous solubility, we were unable to collect reliable data for the CMC of C_{14}.
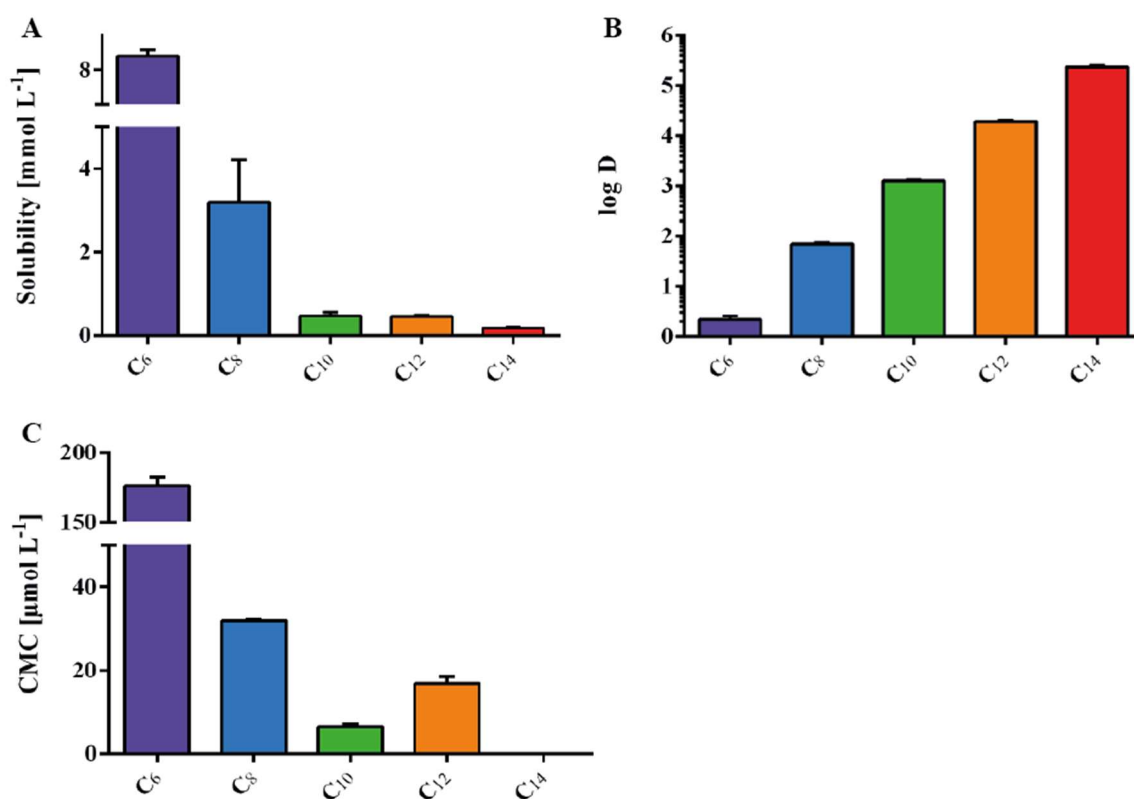
Figure 2 Physicochemical properties of the synthesized compounds. (A) Solubility in phosphate-buffered saline (PBS) at pH 7.4 at 25 °C. (B) Octanol/water partition coefficient log D at pH 7.4. (C) Critical micelle concentration of C_6, C_8, C_{10}, C_{12}, and C_{14}. The CMC determination of C_{14} was not possible due to low water solubility. All results are displayed as the mean ± standard deviation (n = 3).

Epithelial permeability was recorded across Caco-2 cell layers only after a trans epithelial electrical resistance (TEER) ≥ 200 Ω cm^2 was reached before and maintained throughout the experiment, respectively, and an intact state was confirmed histologically. Recovery rates

were $104.9 \pm 2.2\%$ (C_6), $78.8 \pm 2.4\%$ (C_8), and $5.4 \pm 2.2\%$ (C_{10}) (**Figure 3A**). The apparent permeation coefficients (P_{app}) were $9.84 \pm 0.20 \times 10^{-5}$ cm s^{-1} (C_6) and $7.95 \pm 0.34 \times 10^{-5}$ cm s^{-1} (C_8) (**Figure 3B**). We classified the data obtained for C_{10} as inconclusive (reflecting the low substance recovery rate) as we did for C_{12} and C_{14} (no compound was found in basolateral or initial apical samples). In order to characterize unspecific adsorption, the assay was repeated without cells (in a single experiment) with recoveries of 110% (C_6), 85% (C_8), 79% (C_{10}), 69% (C_{12}), and 58% (C_{14}, **Figure S39**).

A

B
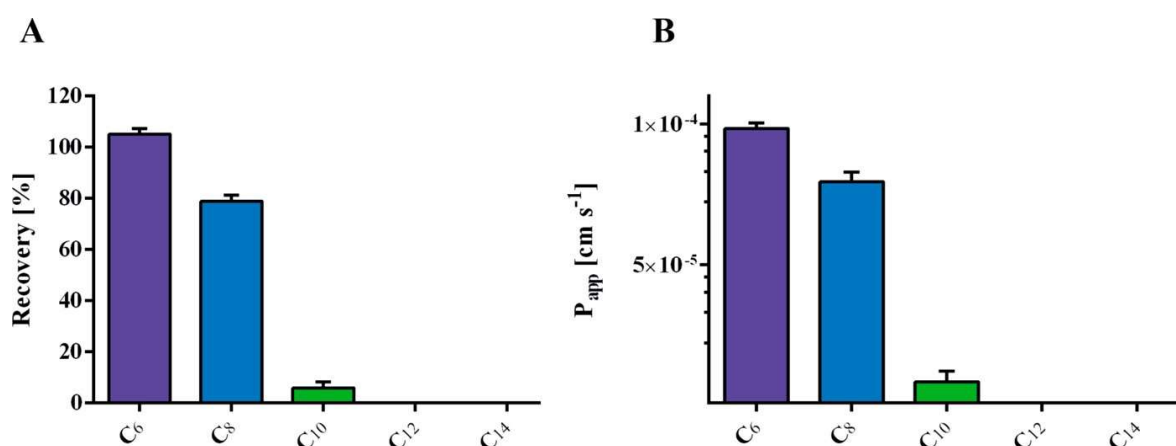
Figure 3 (A) Compound recovery and (B) apparent permeability coefficients (P_{app}) of C_6, C_8, and C_{10} (mean ± standard deviation, n = 3).

All compounds did have IC$_{50}$ values exceeding 100 μmol L^{-1} (the upper limit of compound solubility), hence demonstrating a desirable profile as assessed in cell lines of murine fibroblasts (NIH 3T3), human kidney cells (HEK 293), human liver cells (Hep G2), and human colorectal cells (Caco-2, **Figures S18−S21**) In general, the fibroblasts (**Figure 4A**) and liver cells (**Figure 4C**) responded more sensitively than the colorectal and kidney cells to the highest applied concentration for C_{10}, C_{12}, and C_{14}. Liquid/liquid phase separation was observed for C_{14} during solubility and CMC experiments, resulting in a high standard deviation and no observable surface activity. C_{14} was excluded from further investigations because poor water solubility limited its potential as an antibiotic drug candidate and antibiotic activity was not observed in preliminary experiments.
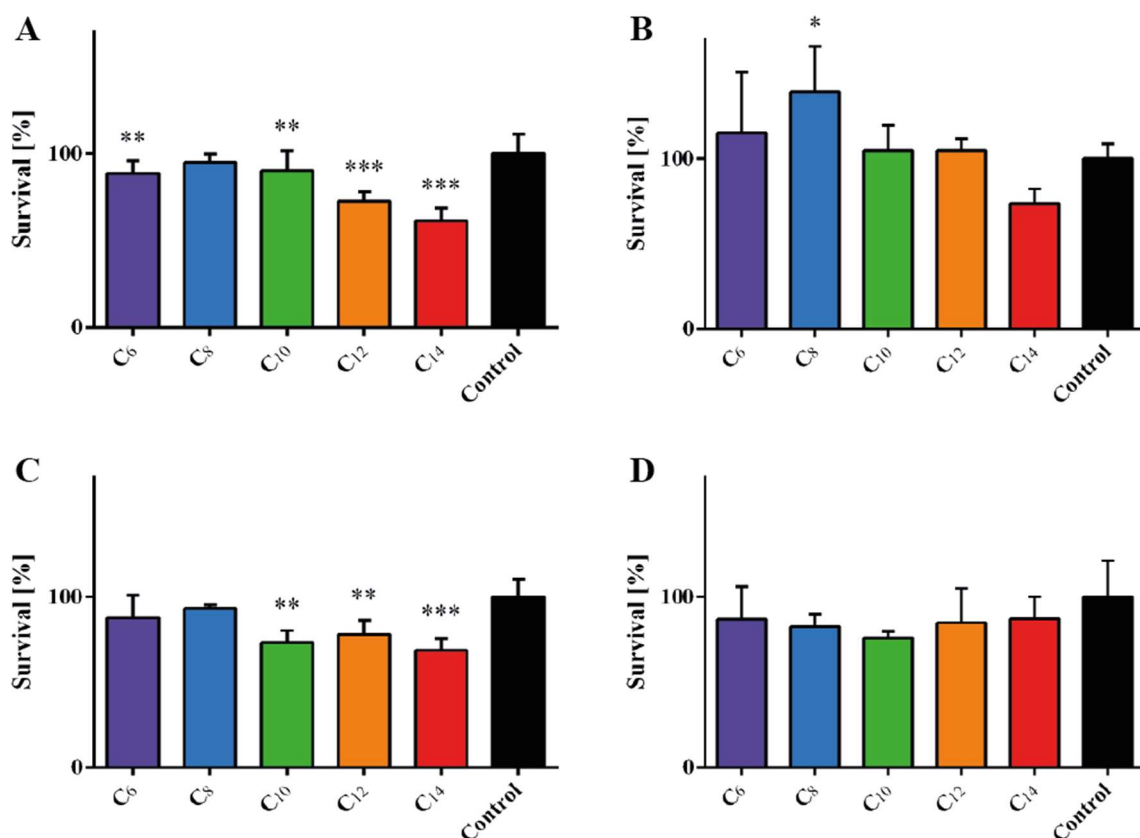
Figure 4 Cytotoxicity assay of C_6, C_8, C_{10}, C_{12}, and C_{14} in (A) NIH 3T3 fibroblasts (n = 12), (B) HEK 293 kidney cells (n = 3), (C) Hep G2 liver cells (n = 3), and (D) the Caco-2 epithelial colorectal cell line. Data was buffer-normalized (n = 3, mean ± standard deviation, significance represented by asterisks with *p ≤ 0.05, **p ≤ 0.01, and ***p ≤ 0.001).

The assessment of the minimal inhibitory concentration (MIC) values (**Table 4**, **Tables S1−S9**) was limited to C_8, C_{10}, and C_{12} in comparison to selected antibiotics but not for C_6 and C_{14} as these compounds did not show activity in pilot experiments. C_8 was not antibacterial up to the highest concentration tested (100 μmol L^{-1}) in any bacterial strain. C_{10} and C_{12} showed antibacterial activity in all strains with MIC values ranging from 100 to 50 μmol L^{-1} (C_{10}) and from 50 to 12.5 μmol L^{-1} (C_{12}, except for *C. difficile*). *S. aureus* strains ST228 and Lac* (MRSA), *S. epidermidis* RP62, and *E. faecalis* (VRE) and the Streptococcus agalactiae strain were most susceptible to C_{10} and C_{12} among all strains tested.

Table 4 Minimal inhibitory concentrations (MIC) for different bacterial strains in μmol L-1 (tested concentration range 100-0.2 μmol L-1). The highest observed MIC value of three independent experiments is reported. (For the full data set, refer to **Tables S1−S9**).

Compound	*Staphylococci*				*Enterococci*		GBS	*C. diff.*
	ST228	JE2	Lac*	RP62a	Faecium	Faecalis		
Octenidine	6.25	6.25	6.25	3.125	6.25	12.5	12.5	12.5
Vancomycin	1.563	1.563	1.563	3.125	> 100	25	6.25	3.125
Ciprofloxacin	> 100	> 100	> 100	25	> 100	3.125	3.125	100
Amoxicillin	> 100	> 100	100	> 100	> 100	3.125	12.5	25
Linezolid	n.d.	n.d.	n.d.	n.d.	> 100	> 100	50	> 100
C_8	> 100	> 100	> 100	> 100	> 100	> 100	> 100	> 100
C_{10}	100	100	50	50	100	50	50	100
C_{12}	25	50	25	25	50	12.5	12.5	100
GA (C_{13})	25	25	25	25	6.25	6.25	6.25	n.d.
AA (C_{15})	> 100	> 100	> 100	> 100	12.5	25	6.25	n.d.

GA = Ginkgolic acid
AA = Anacardic acid
n.d. = not determined
GBS = group B *streptococci*
C. diff = *Clostridium difficile*

We further assessed the impact of the compounds on a bacterial biofilm. While no effect on bacterial biofilm formation was observed with C_6, C_8, C_{12}, or C_{14}, compound C_{10} inhibited biofilm formation under subinhibitory concentrations in *S. aureus* ST228 (**Figure 5**). C_{10} reduced the growth of ST228 (**Figure 5A**) and reduced the biofilm mass significantly to 74 ± 13% when exposed to 0.39 μmol L^{-1} (**Figure 5B**). C_{10} and C_{12} were selected for a first assessment of *in vivo* activity in a *Galleria mellonella* larvae model infected with MRSA strain LAC* or vancomycin-resistant *E. faecium* strain UL602570 (VRE) against antibiotics amoxicillin, ciprofloxacin, vancomycin, and linezolid and disinfectant octenidine as

controls. The injection of 20 μL (200 μmol L^{-1}) of the compound solution into the VRE-infected group (body weight 0.45 ± 0.10 g) and the MRSA-infected group (body weight 0.31 ± 0.07 g) resulted in an applied dose of 9.10 ± 0.56 μmol kg^{-1} in the VRE group and 12.43 ± 0.77 μmol kg^{-1} in the MRSA group (**Tables S9−S12**).
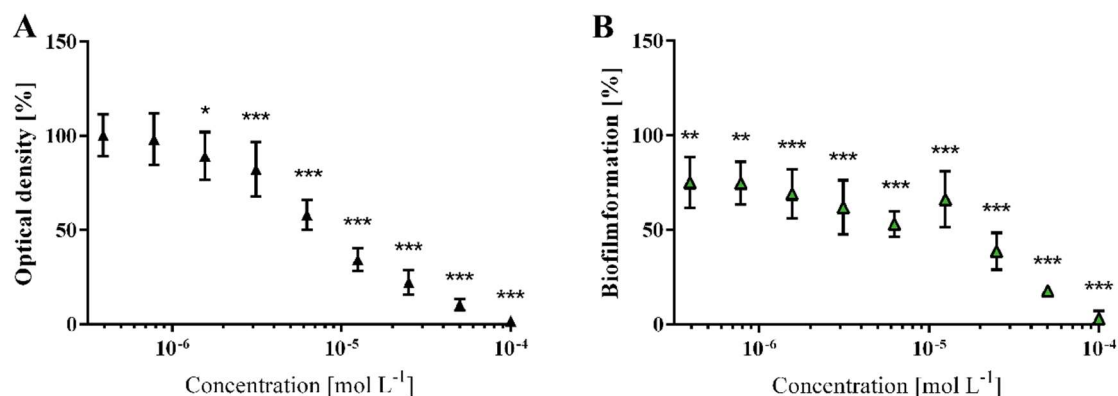
Figure 5 (A) Optical density or bacterial growth and (B) biofilm formation of *S. aureus* (ST228) after exposure to C$_{10}$ for 24 h. Data was buffer normalized (n = 12, mean ± standard deviation, one-way ANOVA with Tukey post hoc comparison among groups; significance represented by asterisks with *p ≤ 0.05, **p ≤ 0.01, and ***p ≤ 0.001).

Larvae infected with vancomycin-resistant *E. faecium* showed an overall survival rate of 35% in contrast to 90% observed in noninfected controls (**Figure 6**). Treatment with C$_{10}$ or C$_{12}$ resulted in a significantly better survival of 70% as compared to the infected control group (p ≤ 0.05). Vancomycin and linezolid treatment insignificantly increased the survival to 65%, and neither amoxicillin nor ciprofloxacin nor octenidine improved survival statistically. The compounds were further assessed in another model using multi-drug-resistant *S. aureus* (**Figure 7**). Whereas C$_{12}$ (5%) failed to improve survival, C$_{10}$ (25%) was significantly better as compared to the infected control (5% survival; p ≤ 0.05) or amoxicillin (0% survival; p ≤ 0.01) but inferior to vancomycin (45% survival; p ≤ 0.01).
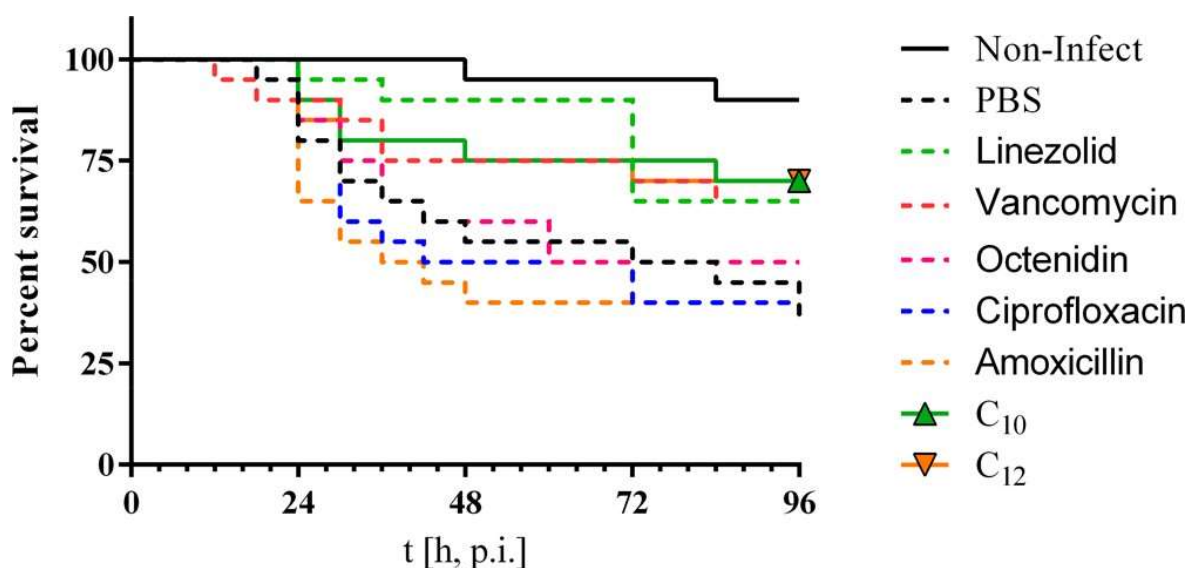
Figure 6 Survival of *Galleria mellonella* when infected with vancomycin-resistant *E. faecium* UL602570 and following treatment (Kaplan−Meier plot). Survival under C_{10} and C_{12} treatment was significantly better as compared to the PBS control group and not different as compared to vancomycin and linezolid. Amoxicillin, ciprofloxacin, and octenidine did not significantly differ from the PBS control group (n = 20).
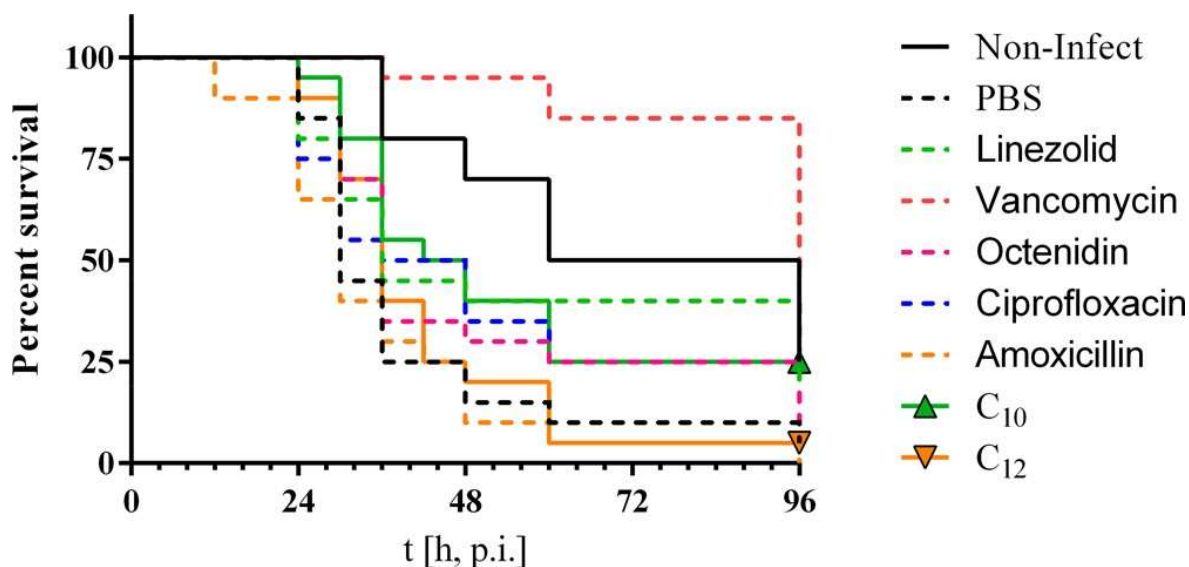
Figure 7 Survival of *Galleria mellonella* infected with multi-drug-resistant *S. aureus* strain LAC* (Kaplan−Meier plot, n = 20).

Discussion

Anacardic acid derivatives C_{10} and C_{12} showed good antibacterial activity as well as promising toxicological profiles, and both compounds challenged multiresistant bacterial strains in vitro and in vivo. Additionally, biofilm inhibition in *S. aureus* was found at subtherapeutic doses for C_{10}. Encouraging physicochemical results were obtained for

solubility and lipophilicity. The pK_a values suggested that the compounds will be charged/ionized in blood (pH 7.4) or the intestine (pH 6.8), thereby exhibiting amphiphilic properties resulting in interaction with biological barriers. Except for C_{14}, which was not surface-active in the tested concentration range, all compounds decreased the surface tension in water, with C_{10} resulting in the lowest observed CMC value as compared to all other tested compounds (**Figure 2C**). Permeation through human colorectal adenocarcinoma cell monolayers (Caco-2) reflected the importance of hydrophilic/lipophilic balance as the apparent permeability coefficient (P_{app}) correlated with the alkyl chain length (**Figure 3B**). While C_6 and C_8 had P_{app} values larger than $(2-5) \times 10^{-6}$ cm s^{-1}, suggesting complete absorption in the human intestine, the assessment of P_{app} values for the more lipophilic compounds (C_{10}, C_{12}, and C_{14}) suffered from a poor recovery rate, as previously reported for lipophilic compounds tested in Caco-2 permeation assays.[21,31] The poor recovery rate was not a result of unspecific absorption because repeating the experiment without cells revealed higher recovery rates for all compounds with a trend of decreasing recovery with increasing alkyl chain length (**Figure S39**). These experiments suggested that the overall poor recovery of C_{10}, C_{12}, and C_{14} in CaCo-2 monolayers was mainly driven by effective absorption onto/ within Caco-2 cells, an effect which was previously linked to the prokaryotic and eukaryotic cytotoxicity of surfactants on the one hand and the reason for antimicrobial activity on the other hand.[32,33] For example, octenidine displays similar surfactant-like properties with broad antiseptic activity, which is why it finds application in the topical treatment of skin and wound infections but prevents other administration routes because of cytotoxic effects, which in fact have also been reported for skin keratinocytes.[4,34] All tested compounds demonstrated encouraging cytotoxicity data, and no IC_{50} values were obtained in the tested concentration range. Additionally, the Ames test for C_{10} showed no increase in revenant colony numbers, neither in the presence or absence of metabolic activity, indicating non-mutagenicity of this compound concerning base pair changes and a frame shift in the genome (**Tables S13−S22**). However, a decrease in proliferation was observed at higher concentrations for C_{12} and C_{14} (**Figure 4**). This observation is in accordance with recent publications linking the cytotoxic behavior of lipophilic entities with their ability to interact with cellular membranes.[32,35] Compounds C_{10} and C_{12} show similar antibacterial activity when compared to their natural precursors anacardic acid (C_{15}) and ginkgolic acid (C_{13}, **Table 4**). While the activity in *Staphylococci* strains is unaffected by introducing an ether function, the activity in *Enterococci* and *Streptococcus* strains is slightly lower. However,

C_{10} and particularly C_{12} reflected broad antibacterial activity similar to that of octenidine and in contrast to that of the antibiotics for which the antibacterial activity depended on the selected strain and its resistance profile. Therefore, C_{10} and C_{12} were further tested in infection models in *Galleria mellonella* (**Figures 6** and **7**), a model in which pathogen virulence is compared to that of mice.[36−39] Findings in this study correlated with previously measured MIC values for amoxicillin, ciprofloxacin, vancomycin, and linezolid in *E. faecium* UL602570 (**Table 4**). One surprising finding for octenidine was that in spite of having higher antibacterial activity compared to that of C_{10} and C_{12} in vitro, this did not translate into better survival in vivo. We hypothesize that this might reflect the amphiphilic nature of C_{10}, C_{12}, and octenidine[4] alike, possibly reducing the available compound in vivo to that of strong cellular absorption and hence little availability at sites of infection. Additionally, low survival was observed for the uninfected control group in the MRSA *G. mellonella* experiment (**Figure 7**). A retrospective evaluation of our laboratory procedure revealed the survival for uninfected, PBS-treated groups to be $88 \pm 3\%$ (n = 7), in line with what was observed for the VRE-infected *G. mellonella* experiment presented in this study (**Figure 6**). The poor survival in the uninfected group within the MRSA-infected *G. mellonella* experiment was likely linked to longer transportation of the larvae and possibly starving of this particular *G. mellonella* larvae batch. Despite the resulting overall low survival, the data indicated noninferiority to vancomycin, linezolid, and PBS treatment in the MRSA-infected group. It is for these aspects and general differences in bacterial virulence in different hosts that the Galleria data reported here should be corroborated in mammalian hosts before final conclusions are drawn. The demonstrated *in vivo* superiority of C_{10} and C_{12}, while statistically significant in the MRSA strain, has to be interpreted cautiously and is encouraging further investigations in mammals to evaluate a potential benefit. In addition and from a cytotoxicity perspective, the compounds reported here are promising candidates for further testing and are much safer than commonly used antibiotics and antiseptics including erythromycin, dicloxacillin, and cefuroxime[40] as well as ciprofloxacin, povidone-iodine, and octenidine dihydrochloride.[34,41,42] As mentioned, experimental data in other animal model systems is required before drawing final conclusions about the promising risk−benefit profile of these anacardic acid derivatives.

Acknowledgments

References

1. Flemming, H. C., and Wingender, J. (2010) The biofilm matrix. Nat. Rev. Microbiol. 8 (9), 623−33.

2. Warnke, P. H., Lott, A. J., Sherry, E., Wiltfang, J., and Podschun, R. (2013) The ongoing battle against multi-resistant strains: in-vitro inhibition of hospital-acquired MRSA, VRE, Pseudomonas, ESBL E. coli and Klebsiella species in the presence of plant-derived antiseptic oils. J. Craniomaxillofac. Surg. 41 (4), 321−6.

3. Cassini, A.; Högberg, L. D.; Plachouras, D.; Quattrocchi, A.; Hoxha, A.; Simonsen, G. S.; Colomb-Cotinat, M.; Kretzschmar, M. E.; Devleesschauwer, B.; Cecchini, M.; Ouakrim, D. A.; Oliveira, T. C. et al. (2019) Attributable deaths and disability-adjusted life-years caused by infections with antibiotic-resistant bacteria in the EU and the European Economic Area in 2015: a population-level modelling analysis. Lancet Infect. Dis. 19 (1), 56−66.

4. Hubner, N. O., Siebert, J., and Kramer, A. (2010) Octenidine dihydrochloride, a modern antiseptic for skin, mucous membranes and wounds. Skin Pharmacol. Physiol. 23 (5), 244−58.

5. Kubo, I., Muroi, H., Himejima, M., Yamagiwa, Y., Mera, H., Tokushima, K., Ohta, S., and Kamikawa, T. (1993) Structure Antibacterial Activity Relationships of Anacardic Acids. J. Agric. Food Chem. 41 (6), 1016−1019.

6. Muroi, H., and Kubo, I. (1996) Antibacterial activity of anacardic acid and totarol, alone and in combination with methicillin, against methicillinresistantStaphylococcus aureus. J. Appl. Bacteriol. 80 (4), 387−394.

7. Yalpani, M., and Tyman, J. H. P. (1983) The phenolic acids of Pistachia vera. Phytochemistry 22 (10), 2263−2266.

8. Balasubramanyam, K., Swaminathan, V., Ranganathan, A., and Kundu, T. K. (2003) Small molecule modulators of histone acetyltransferase p300. J. Biol. Chem. 278 (21), 19134−40.

9. Omanakuttan, A., Nambiar, J., Harris, R. M., Bose, C., Pandurangan, N., Varghese, R. K., Kumar, G. B., Tainer, J. A., Banerji, A., Perry, J. J., and Nair, B. G. (2012) Anacardic acid inhibits the catalytic activity of matrix metalloproteinase-2 and matrix metalloproteinase-9. Mol. Pharmacol. 82 (4), 614−22.

10. Hamad, F. B., and Mubofu, E. B. (2015) Potential biological applications of bio-based anacardic acids and their derivatives. Int. J. Mol. Sci. 16 (4), 8569−90.

11. Wisastra, R., Kok, P. A., Eleftheriadis, N., Baumgartner, M. P., Camacho, C. J., Haisma, H. J., and Dekker, F. J. (2013) Discovery of a novel activator of 5-lipoxygenase from an anacardic acid derived compound collection. Bioorg. Med. Chem. 21 (24), 7763−78.

12. Kapoor, G., Saigal, S., and Elongavan, A. (2017) Action and resistance mechanisms of antibiotics: A guide for clinicians. J. Anaesthesiol., Clin. Pharmacol. 33 (3), 300−305.

13. Cutuli, M. A., Petronio Petronio, G., Vergalito, F., Magnifico, I., Pietrangelo, L., Venditti, N., and Di Marco, R. (2019) Galleria mellonella as a consolidated in vivo model hosts: New developments in antibacterial strategies and novel drug testing. Virulence 10 (1), 527−541.

14. Gottlieb, H. E., Kotlyar, V., and Nudelman, A. (1997) NMR chemical shifts of common laboratory solvents as trace impurities. J. Org. Chem. 62 (21), 7512−7515.

15. Ghizzoni, M., Boltjes, A., Graaf, C., Haisma, H. J., and Dekker, F. J. (2010) Improved inhibition of the histone acetyltransferase PCAF by an anacardic acid derivative. Bioorg. Med. Chem. 18 (16), 5826−34.

16. Uchiyama, M., Ozawa, H., Takuma, K., Matsumoto, Y., Yonehara, M., Hiroya, K., and Sakamoto, T. (2006) Regiocontrolled intramolecular cyclizations of carboxylic acids to carbon-carbon triple bonds promoted by acid or base catalyst. Org. Lett. 8 (24), 5517−20.

17. Yoon, J. K., and Burgess, D. J. (1992) Comparison of dynamic and static interfacial tension at aqueous/perfluorocarbon interfaces. J. Colloid Interface Sci. 151 (2), 402−409.

18. OECD Test No. 117: Partition Coefficient (n-octanol/water); HPLC Method, 2004.

19. Volgyi, G., Baka, E., Box, K. J., Comer, J. E., and Takacs-Novak, K. (2010) Study of pH-dependent solubility of organic bases. Revisit of Henderson-Hasselbalch relationship. Anal. Chim. Acta 673 (1), 40−6.

20. Schonherr, D., Wollatz, U., Haznar-Garbacz, D., Hanke, U., Box, K. J., Taylor, R., Ruiz, R., Beato, S., Becker, D., and Weitschies, W. (2015) Characterisation of selected active agents regarding pKa values, solubility concentrations and pH profiles by SiriusT3. Eur. J. Pharm. Biopharm. 92, 155−70.

21. Hubatsch, I., Ragnarsson, E. G., and Artursson, P. (2007) Determination of drug permeability and prediction of drug absorption in Caco-2 monolayers. Nat. Protoc. 2 (9), 2111−9.

22. Reggane, M., Wiest, J., Saedtler, M., Harlacher, C., Gutmann, M., Zottnick, S. H., Piechon, P., Dix, I., Muller-Buschbaum, K., Holzgrabe, U., Meinel, L., and Galli, B. (2018) Bioinspired co-crystals of Imatinib providing enhanced kinetic solubility. Eur. J. Pharm. Biopharm. 128, 290−299.

23. Balk, A., Widmer, T., Wiest, J., Bruhn, H., Rybak, J. C., Matthes, P., Muller-Buschbaum, K., Sakalis, A., Luhmann, T., Berghausen, J., Holzgrabe, U., Galli, B., and Meinel, L. (2015) Ionic liquid versus prodrug strategy to address formulation challenges. Pharm. Res. 32 (6), 2154−67.

24. OECD (1997) OECD Guidelines for the Testing of Chemicals, Section 4: Health Effects. No. 471; Bacterial Reverse Mutation Test, adopted July 21, 1997.

25. Mortelmans, K., and Zeiger, E. (2000) The Ames Salmonella/ microsome mutagenicity assay. Mutat. Res., Fundam. Mol. Mech. Mutagen. 455 (1−2), 29−60.

26. Green, M. H. L., and Muriel, W. J. (1976) Mutagen testing using TRP+ reversion in Escherichia coli. Mutat. Res., Environ. Mutagen. Relat. Subj. 38 (1), 3−32.

27. Kier, L. E., Brusick, D. J., Auletta, A. E., Von Halle, E. S., Brown, M. M., Simmon, V. F., Dunkel, V., McCann, J., Mortelmans, K., Prival, M., Rao, T. K., and Ray, V. (1986) The Salmonella typhimurium/ mammalian microsomal assay. Mutat. Res., Rev. Genet. Toxicol. 168 (2), 69−240.

28. Lerch, M. F., Schoenfelder, S. M. K., Marincola, G., Wencker, F. D. R., Eckart, M., Forstner, K. U., Sharma, C. M., Thormann, K. M., Kucklick, M., Engelmann, S., and Ziebuhr, W. (2019) A non-coding RNA from the intercellular adhesion (ica) locus of Staphylococcus epidermidis controls polysaccharide intercellular adhesion (PIA)mediated biofilm formation. Mol. Microbiol. 111 (6), 1571−1591.

29. Clinical and Laboratory Standards Institute (2015) Methods for Dilution Antimicrobial Susceptibility Tests for Bacteria That Grow Aerobically; Approved Standard, 10th ed.; CLSI document M07-A10.

30. Clinical and Laboratory Standards Institute (1999) Methods for Determining Bactericidal Activity of Antimicrobial Agents; Approved Guideline, CLSI document M26-A.

31. Cai, X., Walker, A., Cheng, C., Paiva, A., Li, Y., Kolb, J., Herbst, J., Shou, W., and Weller, H. (2012) Approach to improve compound recovery in a high-throughput Caco-2 permeability assay supported by liquid chromatography-tandem mass spectrometry. J. Pharm. Sci. 101 (8), 2755−62.

32. Yoo, B., Shah, J. K., Zhu, Y., and Maginn, E. J. (2014) Amphiphilic interactions of ionic liquids with lipid biomembranes: a molecular simulation study. Soft Matter 10 (43), 8641−51.

33. Pernak, J., and Chwała, P. (2003) Synthesis and anti-microbial activities of choline-like quaternary ammonium chlorides. Eur. J. Med. Chem. 38 (11−12), 1035−1042.

34. Hirsch, T., Jacobsen, F., Rittig, A., Goertz, O., Niederbichler, A., Steinau, H. U., Seipp, H. M., and Steinstraesser, L. (2009) [A comparative in vitro study of cell toxicity of clinically used antiseptics]. Hautarzt 60 (12), 984−91.

35. Stolte, S., Matzke, M., Arning, J., Böschen, A., Pitner, W.-R., Welz-Biermann, U., Jastorff, B., and Ranke, J. (2007) Effects of different head groups and functionalised side chains on the aquatic toxicity of ionic liquids. Green Chem. 9 (11), 1170.

36. Brennan, M., Thomas, D. Y., Whiteway, M., and Kavanagh, K. (2002) Correlation between virulence of Candida albicans mutants in mice and Galleria mellonella larvae. FEMS Immunol. Med. Microbiol. 34 (2), 153−7.

37. Hoffmann, J. A. (1999) Phylogenetic Perspectives in Innate Immunity. Science 284 (5418), 1313−1318.

38. Mylonakis, E., Moreno, R., El Khoury, J. B., Idnurm, A., Heitman, J., Calderwood, S. B., Ausubel, F. M., and Diener, A. (2005) Galleria mellonella as a model system to study Cryptococcus neoformans pathogenesis. Infect. Immun. 73 (7), 3842−50.

39. Jander, G., Rahme, L. G., and Ausubel, F. M. (2000) Positive correlation between virulence of Pseudomonas aeruginosa mutants in mice and insects. J. Bacteriol. 182 (13), 3843−5.

40. Lanbeck, P., and Paulsen, O. (1995) Cytotoxic Effects of Four Antibiotics on Endothelial Cells. Pharmacol. Toxicol. 77 (6), 365−370.

41. Sharma, P. C., Jain, A., Jain, S., Pahwa, R., and Yar, M. S. (2010) Ciprofloxacin: review on developments in synthetic, analytical, and medicinal aspects. J. Enzyme Inhib. Med. Chem. 25 (4), 577−89.

42. Gurbay, A., Garrel, C., Osman, M., Richard, M. J., Favier, A., and Hincal, F. (2002) Cytotoxicity in ciprofloxacin-treated human fibroblast cells and protection by vitamin E. Hum. Exp. Toxicol. 21 (12), 635−41.

Supporting Information

Synthesized Compounds

5-hydroxy-2,2-dimethyl-4H-benzo[d][1,3]dioxin-4-one (2)

5-hydroxy-2,2-dimethyl-4H-benzo[d][1,3]dioxin-4-one **2** was obtained from 2,6-dihydroxybenzoic acid **1** following synthetic procedure 1. The resulting purple crystals were purified by silica gel column chromatography (hexane/ethyl acetate 3:1) and recrystallization from hexane yielding white crystals (4.73 g, 61%). The substance is pure, judged by TLC. mp 63 °C. R_f = 0.42 (hexane/EtOAc 10:1). ^{1}H NMR (400 MHz, DMSO-d6, δ [ppm], J [Hz]): 10.30 (s, 1H), 7.52 (t, J = 8.3, 1H), 6.66 (dd, J = 8.3, J = 0.8, 1H), 6.55 (dd, J = 8.3, J = 0.8, 1H), 1.70 (s, 6H).

5-(hexyloxy)-2,2-dimethyl-4H-benzo[d][1,3]dioxin-4-one (3a)

5-(hexyloxy)-2,2-dimethyl-4H-benzo[d][1,3]dioxin-4-one **3a** was obtained from 5-hydroxy-2,2-dimethyl-4H-benzo[d][1,3]dioxin-4-one **2** (776 mg, 4 mmol) and 1-bromohexane (858 mg, 0.73 mL, 5.2 mmol) following synthetic procedure 2. The resulting colorless oil is stored at 4 °C overnight resulting in white crystals (743 mg, 67%). The substance is pure, judged by TLC. mp 53 °C. R_f = 0.29 (hexane/EtOAc 10:1). ^{1}H NMR (400 MHz, DMSO-d6, δ [ppm], J [Hz]): 7.54 (t, J = 8.3, 1H), 6.80 (dd, J = 8.3, J = 0.8, 1H), 6.61 (dd, J = 8.3, J = 0.8, 1H), 4.05 (t, J = 6.4, 2H), 1.72 (m, 2H), 1.63 (s, 6H), 1.46 (m, 2H), 1.30 (m, 4H), 0.87 (m, 3H).

2,2-dimethyl-5-(octyloxy)-4H-benzo[d][1,3]dioxin-4-one (3b)

2,2-dimethyl-5-(octyloxy)-4H-benzo[d][1,3]dioxin-4-one **3b** was obtained from 5-hydroxy-2,2-dimethyl-4H-benzo[d][1,3]dioxin-4-one **2** (776 mg, 4 mmol) and 1-bromooctane (1.00 g, 0.90 mL, 5.2 mmol) following synthetic procedure 2. The resulting colorless oil is stored at 4 °C overnight resulting in white crystals (714 mg, 59%). The substance is pure, judged by TLC. mp 60 °C. R_f = 0.32 (hexane/EtOAc 10:1). ^{1}H NMR (400 MHz, DMSO-d6, δ [ppm], J [Hz]): 7.55 (t, J = 8.3, 1H), 6.81 (dd, J = 8.3, J = 0.7, 1H), 6.61 (dd, J = 8.3, J = 0.7, 1H), 4.06 (t, J = 6.4, 2H), 1.74 (m, 2H), 1.64 (s, 6H), 1.46 (m, 2H), 1.38 - 1.19 (m, 8H), 0.87 (m, 3H).

5-(decyloxy)-2,2-dimethyl-4H-benzo[d][1,3]dioxin-4-one (3c)

5-(decyloxy)-2,2-dimethyl-4H-benzo[d][1,3]dioxin-4-one **3c** was obtained from 5-hydroxy-2,2-dimethyl-4H-benzo[d][1,3]dioxin-4-one **2** (776 mg, 4 mmol) and 1-bromodecane (1.15 g, 1.07 mL, 5.2 mmol) following synthetic procedure 2. The resulting colorless oil is stored at 4 °C overnight resulting in white crystals (980 mg, 73%). The substance is pure, judged by TLC. mp 56 °C. R_f = 0.34 (hexane/EtOAc 10:1). ^{1}H NMR (400 MHz, DMSO-d6, δ [ppm], J [Hz]): 7.54 (t, J = 8.3, 1H), 6.80 (dd, J = 8.3, J = 0.8, 1H), 6.61 (dd, J = 8.3, J = 0.8, 1H), 4.05 (t, J = 6.4, 2H), 1.73 (m, 2H), 1.64 (s, 6H), 1.46 (m, 2H), 1.34 - 1.19 (m, 12H), 0.85 (m, 3H).

5-(dodecyloxy)-2,2-dimethyl-4H-benzo[d][1,3]dioxin-4-one (3d)

5-(dodecyloxy)-2,2-dimethyl-4H-benzo[d][1,3]dioxin-4-one **3d** was obtained from 5-hydroxy-2,2-dimethyl-4H-benzo[d][1,3]dioxin-4-one **2** (776 mg, 4 mmol) and 1-bromododecane (1.29 g, 1.24 mL, 5.2 mmol) following synthetic procedure 2. The resulting colorless oil is stored at 4 °C overnight resulting in white crystals (1.32 g, 91%). The substance is pure, judged by TLC. mp 53 °C. R_f = 0.37 (hexane/EtOAc 10:1). ^{1}H NMR (400 MHz, DMSO-d6, δ [ppm], J [Hz]): 7.54 (t, J = 8.3, 1H), 6.80 (dd, J = 8.3, J = 0.7, 1H), 6.60 (dd, J = 8.3, J = 0.7, 1H), 4.05 (t, J = 6.4, 2H), 1.72 (m, 2H), 1.63 (s, 6H), 1.45 (m, 2H), 1.36 - 1.17 (m, 16H), 0.85 (m, 3H).

2,2-dimethyl-5-(tetradecyloxy)-4H-benzo[d][1,3]dioxin-4-one (3e)

2,2-dimethyl-5-(tetradecyloxy)-4H-benzo[d][1,3]dioxin-4-one **3e** was obtained from 5-hydroxy-2,2-dimethyl-4H-benzo[d][1,3]dioxin-4-one **2** (776 mg, 4 mmol) and 1-bromotetradecane (1.43 g, 1.53 mL, 5.2 mmol) following synthetic procedure 2. The resulting colorless oil is stored at 4 °C overnight resulting in white crystals (1.29 g, 83%). The substance is pure, judged by TLC. mp 61 °C. R_f = 0.37 (hexane/EtOAc 10:1). ^{1}H NMR (400 MHz, DMSO-d6, δ [ppm], J [Hz]): 7.54 (t, J = 8.3, 1H), 6.80 (dd, J = 8.3, J = 0.7, 1H), 6.60 (dd, J = 8.3, J = 0.7, 1H), 4.04 (t, J = 6.4, 2H), 1.72 (m, 2H), 1.63 (s, 6H), 1.45 (m, 2H), 1.35 - 1.17 (m, 20H), 0.84 (m, 3H).

2-(hexyloxy)-6-hydroxybenzoic acid (4a; C$_6$)

2-(hexyloxy)-6-hydroxybenzoic acid **4a** was obtained from 5-(hexyloxy)-2,2-dimethyl-4H-benzo[d][1,3]dioxin-4-one **3a** (743 mg, 2.67 mmol) by following synthetic procedure 3. The concentrated residue was purified by silica gel column chromatography. Hexane was used as eluent until all educts were removed, followed by ethyl acetate as eluent to obtain the product. The solvent was evaporated under reduced pressure yielding a slightly yellow oil (504 mg, 79%). Purity 98% judged by HPLC. mp 32 °C. R$_f$ = 0.36 (hexane/EtOAc/HAc 10:1:0.1). ^{1}H NMR (400 MHz, DMSO-d6, δ [ppm], J [Hz]): 7.16 (t, J = 8.2, 1H), 6.47 (m, 2H), 3.94 (t, J = 6.3, 2H), 1.65 (m, 2H), 1.39 (m, 2H), 1.34 - 1.21 (m, 4H), 0.87 (m, 3H). ^{13}C NMR (100 MHz, DMSO-d$_6$, δ [ppm]): 168.7, 157.2, 156.9, 131.4, 108.6, 103.1, 68.2, 30.9, 28.6, 25.1, 22.1, 14.0. ESI-MS: *m/z* calc. for C$_{13}$H$_{18}$O$_4^+$ [M+H]$^+$: 239.1278, found: 239.1274.

2-hydroxy-6-(octyloxy)benzoic acid (4b; C$_8$)

2-hydroxy-6-(octyloxy)benzoic acid **4b** was obtained from 2,2-dimethyl-5-(octyloxy)-4H-benzo[d][1,3]dioxin-4-one **3b** (714 mg, 2.33 mmol) by following synthetic procedure 3. The concentrated residue was purified by silica gel column chromatography. Hexane was used as eluent until all educts were removed, followed by ethyl acetate as eluent to obtain the product. The solvent was evaporated under reduced pressure yielding a slightly yellow oil (509 mg, 82%). Purity >98% judged by HPLC. mp 20 °C. R$_f$ = 0.37 (hexane/EtOAc/HAc 10:1:0.1). ^{1}H NMR (400 MHz, DMSO-d6, δ [ppm], J [Hz]): 7.16 (t, J = 8.2, 1H), 6.47 (m, 2H), 3.94 (t, J = 6.3, 2H), 1.65 (m, 2H), 1.39 (m, 2H), 1.34 - 1.18 (m, 8H), 0.86 (m, 3H). ^{13}C NMR (100 MHz, DMSO-d$_6$, δ [ppm]): 168.6, 157.1, 156.9, 131.3, 110.7, 108.5, 103.0, 68.1, 31.2, 28.7, 25.4, 22.1, 13.9. ESI-MS: *m/z* calc. for C$_{15}$H$_{22}$O$_4^+$ [M+Na]$^+$: 289.1410, found: 289.1405.

2-(decyloxy)-6-hydroxybenzoic acid (4c; C$_{10}$)

2-(decyloxy)-6-hydroxybenzoic acid **4c** was obtained from 5-(decyloxy)-2,2-dimethyl-4H-benzo[d][1,3]dioxin-4-one **3c** (980 mg, 2.93 mmol) by following synthetic procedure 3. The concentrated residue was purified by silica gel column chromatography. Hexane was used as eluent until all educts were removed, followed by ethyl acetate as eluent to obtain the product. The solvent was evaporated under reduced pressure yielding a slightly yellow solid (652 mg, 76%). Purity >98% judged by HPLC. mp 33 °C. R$_f$ = 0.38 (hexane/EtOAc/HAc

10:1:0.1). ^{1}H NMR (400 MHz, DMSO-d6, δ [ppm], J [Hz]): 7.16 (t, J = 8.3, 1H), 6.47 (m, 2H), 3.94 (t, J = 6.4, 2H), 1.65 (m, 2H), 1.38 (m, 2H), 1.33 - 1.18 (m, 12H), 0.85 (m, 3H). ^{13}C NMR (100 MHz, DMSO-d$_6$, δ [ppm]): 169.0, 157.6, 157.3, 131.8, 111.1, 109.0, 103.5, 68.6, 31.8, 29.5, 29.4, 29.2, 29.1, 25.8, 22.6, 14.4. ESI-MS: *m/z* calc. for C$_{17}$H$_{26}$O$_4^+$ [M+Na]$^+$: 317.1723, found: 317.1731.

2-(dodecyloxy)-6-hydroxybenzoic acid (4d; C$_{12}$)

2-(dodecyloxy)-6-hydroxybenzoic acid **4d** was obtained from 5-(dodecyloxy)-2,2-dimethyl-4H-benzo[d][1,3]dioxin-4-one **3d** (1.32 g, 3.64 mmol) by following synthetic procedure 3. The concentrated residue was purified by silica gel column chromatography. Hexane was used as eluent until all educts were removed, followed by ethyl acetate as eluent to obtain the product. The solvent was evaporated under reduced pressure yielding a slightly yellow solid (689 mg, 58%). Purity >98% judged by HPLC. mp 45 °C. R$_f$ = 0.44 (hexane/EtOAc/HAc 10:1:0.1). ^{1}H NMR (400 MHz, DMSO-d6, δ [ppm], J [Hz]): 7.16 (t, J = 8.3, 1H), 6.46 (m, 2H), 3.94 (t, J = 6.3, 2H), 1.65 (m, 2H), 1.38 (m, 2H), 1.33 - 1.15 (m, 16H), 0.85 (t, J = 7.0, 3H). ^{13}C NMR (100 MHz, DMSO-d$_6$, δ [ppm]): 168.7, 157.2, 157.0, 131.4, 110.7, 108.6, 103.1, 68.2, 31.3, 29.0, 28.7, 28.7, 25.4, 22.1, 14.0. ESI-MS: *m/z* calc. for C$_{19}$H$_{30}$O$_4^+$ [M+Na]$^+$: 345.2036, found: 345.2035.

2-(tetradecyloxy)-6-hydroxybenzoic acid (4e; C14)

2-hydroxy-6-(tetradecyloxy)benzoic acid **4e** was obtained from 2,2-dimethyl-5-(tetradecyloxy)-4H-benzo[d][1,3]dioxin-4-one **3e** (1.29 g, 3.30 mmol) by following synthetic procedure 3. The concentrated residue was purified by silica gel column chromatography. Hexane was used as eluent until all educts were removed, followed by ethyl acetate as eluent to obtain the product. The solvent was evaporated under reduced pressure yielding a slightly yellow solid (697 mg, 60%). Purity 96% judged by HPLC. mp 51 °C. R$_f$ = 0.48 (hexane/EtOAc/HAc 10:1:0.1). ^{1}H NMR (400 MHz, DMSO-d6, δ [ppm], J [Hz]): 7.16 (t, J = 8.3, 1H), 6.47 (m, 2H), 3.94 (t, J = 6.3, 2H), 1.65 (m, 2H), 1.38 (m, 2H), 1.33 - 1.14 (m, 20H), 0.85 (t, J = 7.0, 3H). ^{13}C NMR (100 MHz, DMSO-d$_6$, δ [ppm]): 168.7, 157.2, 157.0, 131.4, 110.7, 108.6, 103.1, 68.2, 31.3, 29.1, 28.7, 28.7, 25.4, 22.1, 14.0. ESI-MS: *m/z* calc. for C$_{21}$H$_{35}$O$_4^+$ [M+Na]$^+$: 373.2349, found: 373,2357.

CMC Data
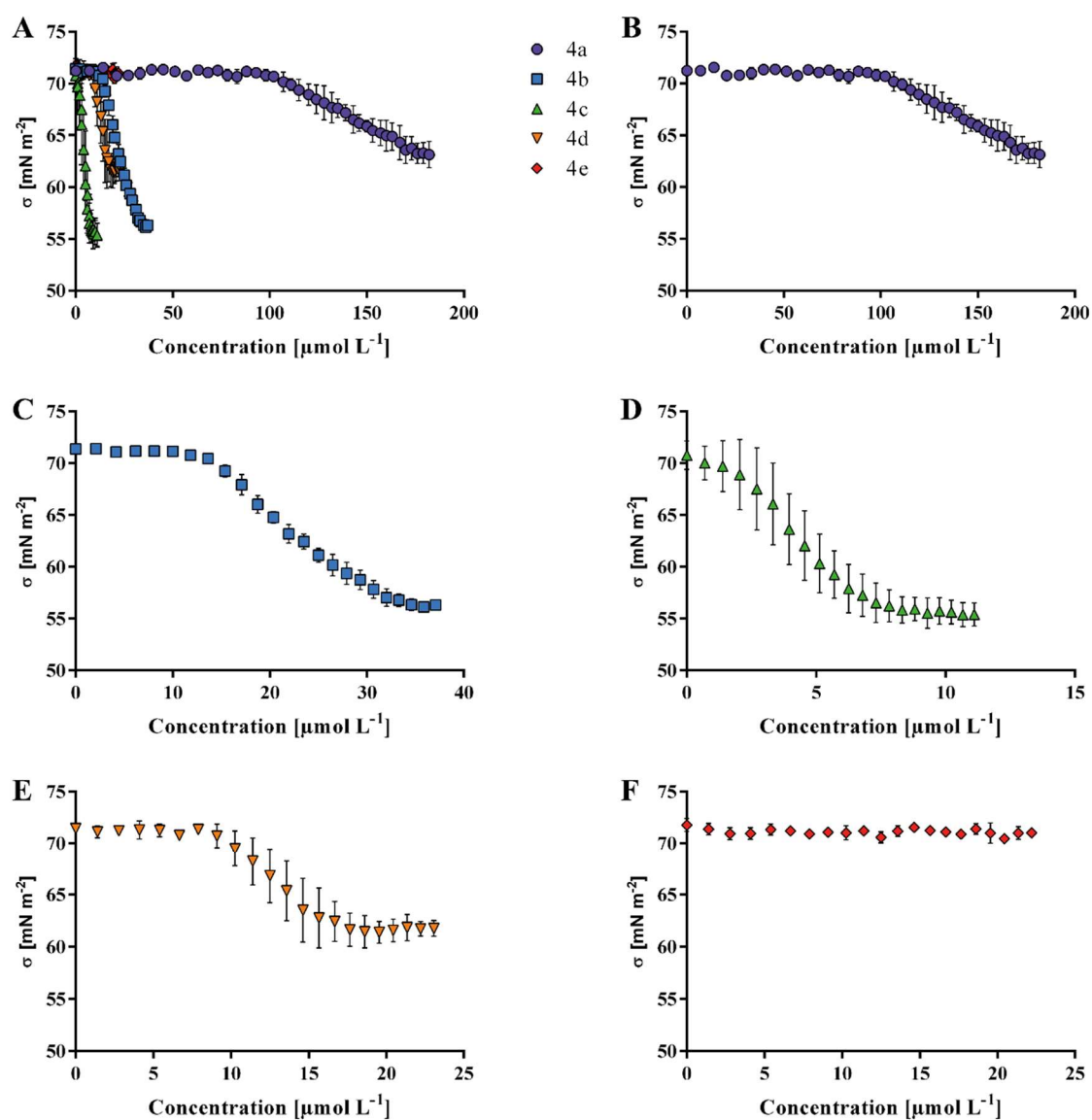
Figure S 1 Surface tension (σ) in mN m^{-2} of different concentrations of (A) all studied compounds, (B) C_6, (C) C_8, (D) C_{10}, (E) C_{12} and (F) C_{14} in deionized water. σ was measured using the Wilhelmy plate method and data is represented as mean ± standard deviation from three individual replications.

HPLC Data
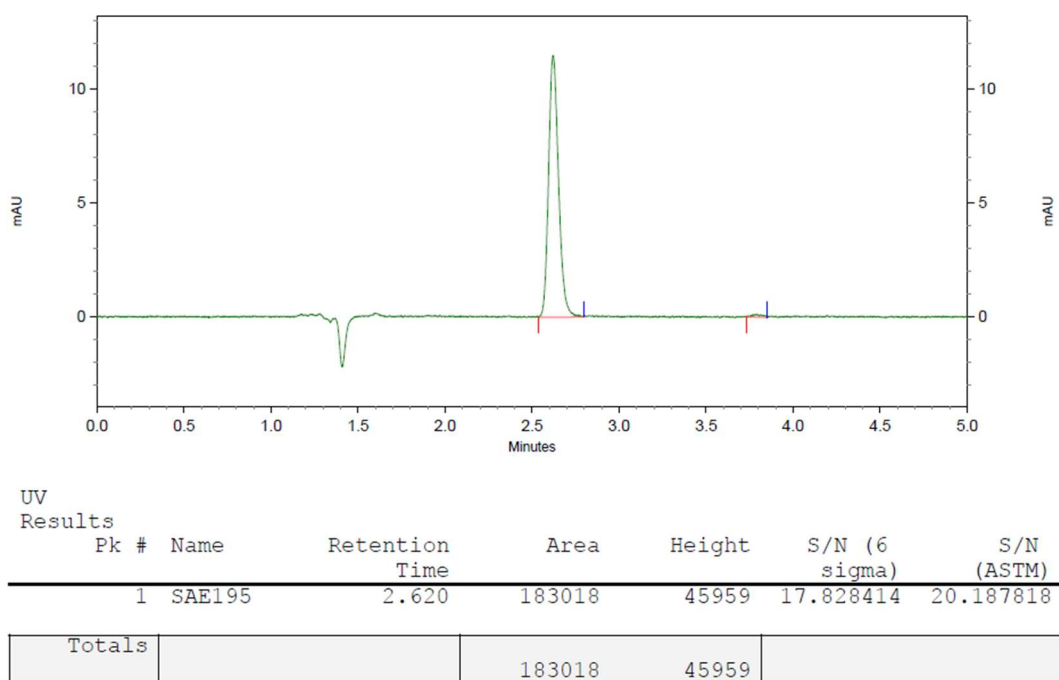
Figure S 2 Chromatogram of after injection of 0.01 mL of 10 µmol L^{-1} **C_6** in acetonitrile. UV-detection at $\lambda = 254$ nm.
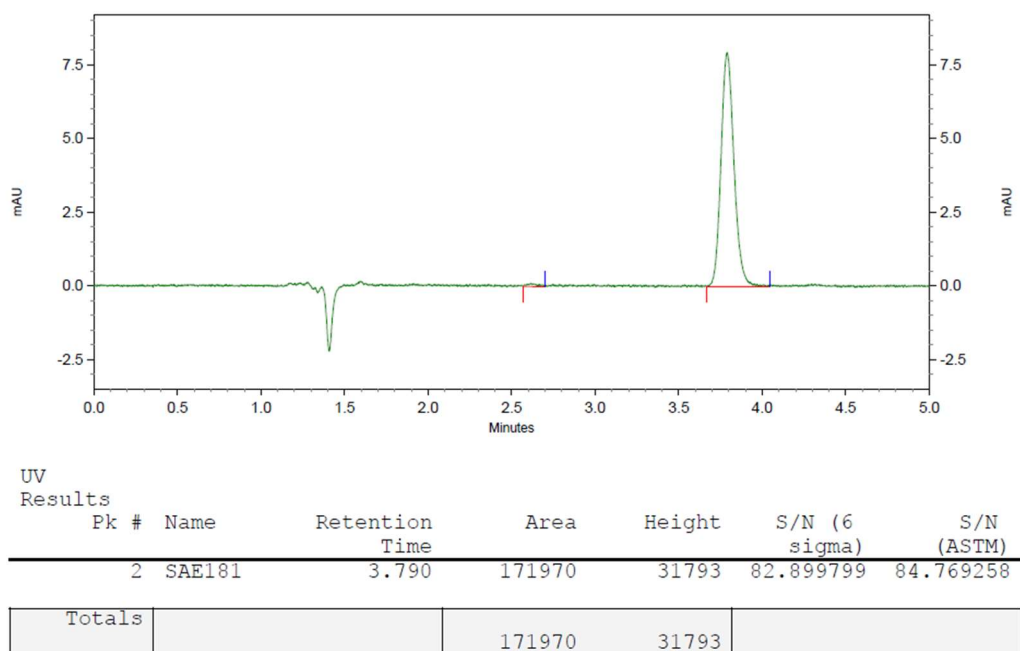
Figure S 3 Chromatogram after injection of 0.01 mL of 10 µmol L^{-1} **C_8** in acetonitrile. UV-detection at $\lambda = 254$ nm.

UV
Results

Pk #	Name	Retention Time	Area	Area Percent	S/N (6 sigma)	S/N (ASTM)
2	SAE180	6.109	165586	99.265	52.644868	53.909538
Totals			165586	99.265		
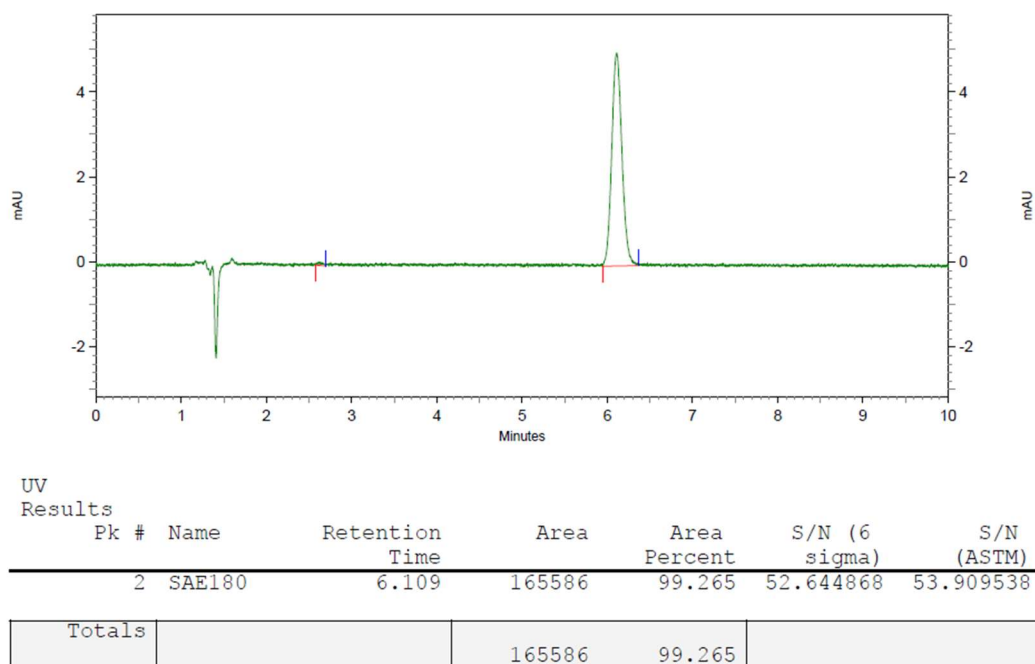
Figure S 4 Chromatogram after injection of 0.01 mL of 10 μmol L^{-1} **C$_{10}$** in acetonitrile. UV-detection at λ = 254 nm.

UV
Results

Pk #	Name	Retention Time	Area	Height	S/N (6 sigma)	S/N (ASTM)
1	SAE196	10.728	163578	11772	13.408026	14.258758
Totals			163578	11772		
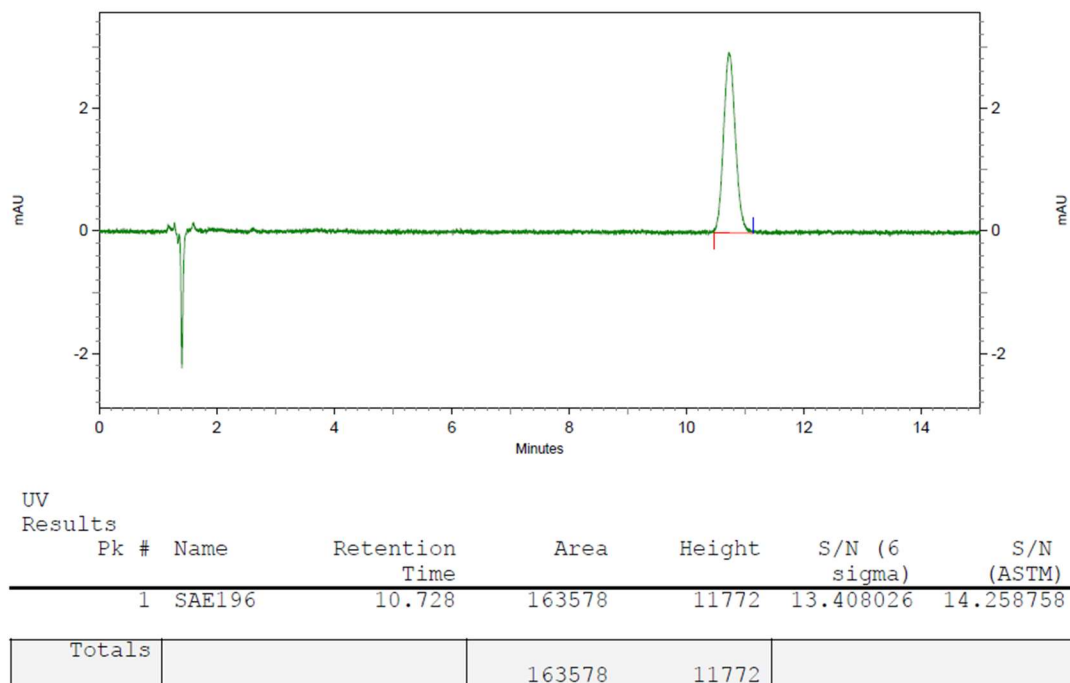
Figure S 5 Chromatogram after injection of 0.01 mL of 10 μmol L^{-1} **C$_{12}$** in acetonitrile. UV-detection at λ = 254 nm.

UV
Results

Pk #	Name	Retention Time	Area	Height	S/N (6 sigma)	S/N (ASTM)
2	SAE197	19.978	182268	7159	20.175480	20.079572
Totals			182268	7159		
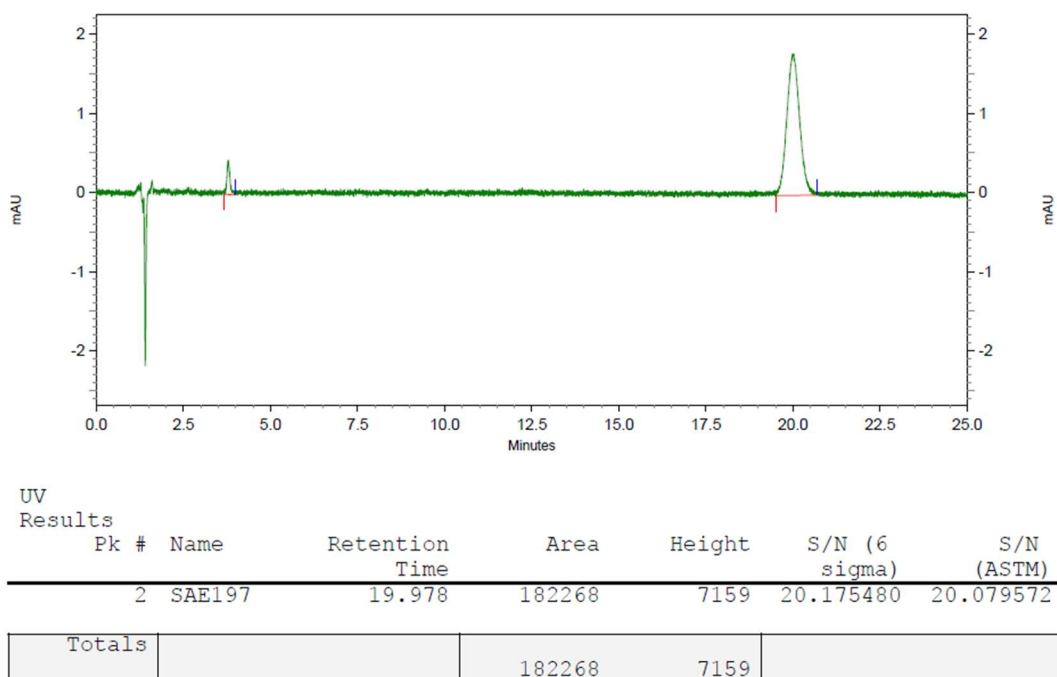
Figure S 6 Chromatogram after injection of 0.01 mL of 10 µmol L^{-1} **C_{14}** in acetonitrile. UV-detection at λ = 254 nm.

ESI-MS Data (HRMS)
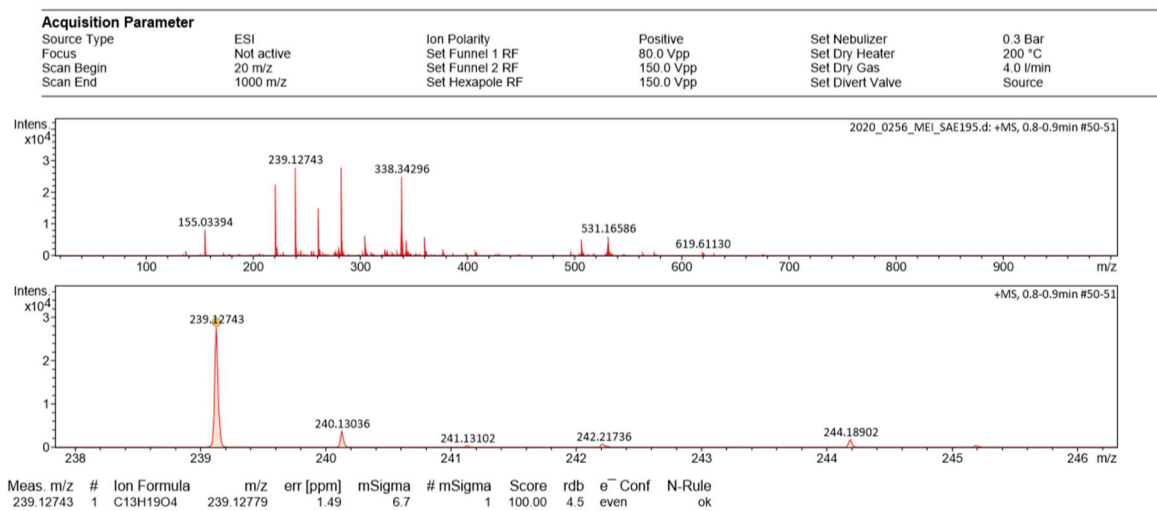
Figure S 7 ESI-MS spectrum of **C_6** in methanol.
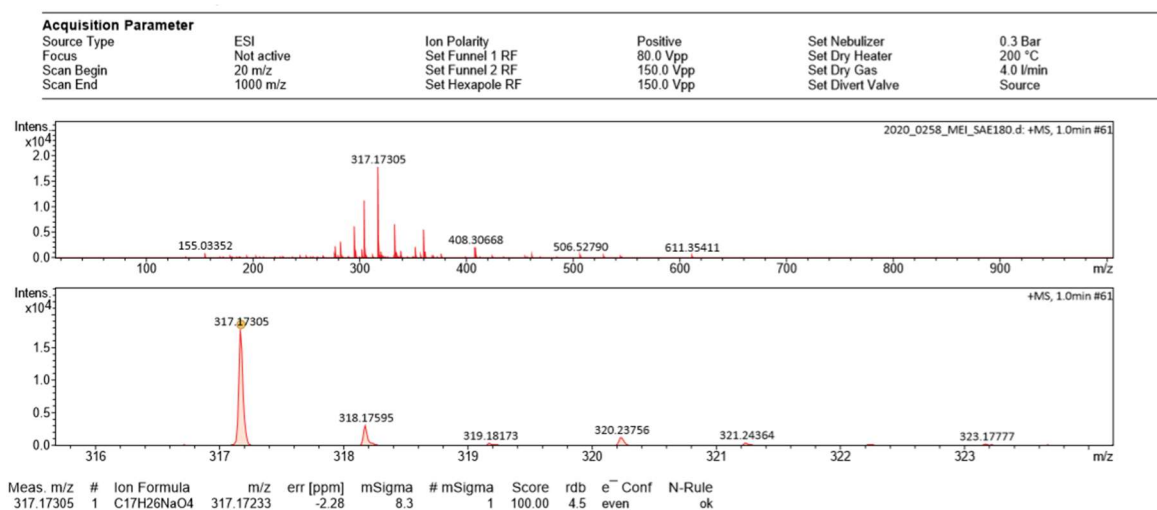
Figure S 8 ESI-MS spectrum of **C$_8$** in methanol.
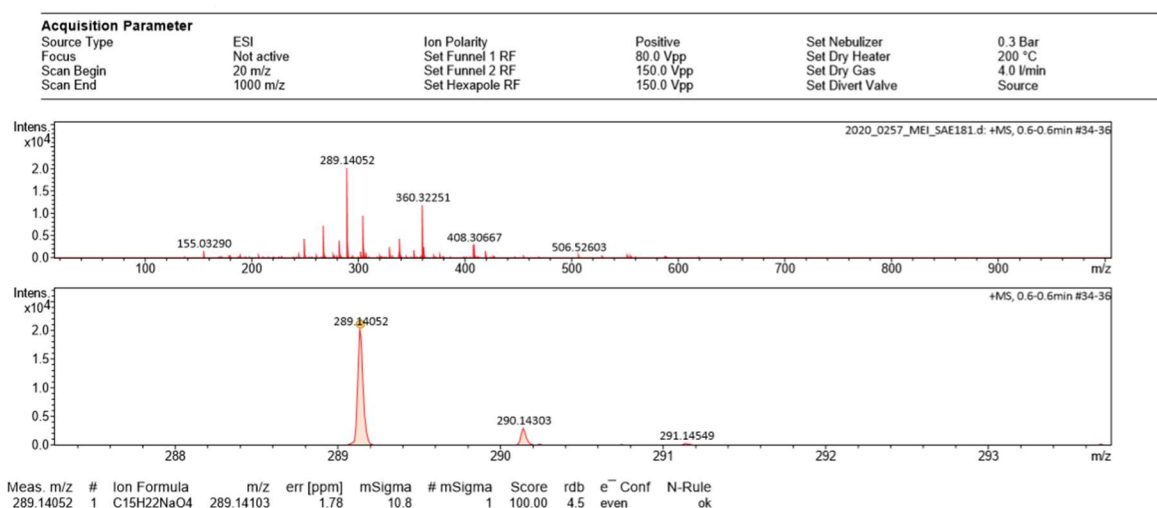
Figure S 9 ESI-MS spectrum of **C$_{10}$** in methanol.

Acquisition Parameter

Source Type	ESI	Ion Polarity	Positive	Set Nebulizer	0.3 Bar
Focus	Not active	Set Funnel 1 RF	100.0 Vpp	Set Dry Heater	200 °C
Scan Begin	50 m/z	Set Funnel 2 RF	200.0 Vpp	Set Dry Gas	4.0 l/min
Scan End	2500 m/z	Set Hexapole RF	200.0 Vpp	Set Divert Valve	Source

2020_0259_MEI_SAE196_2.d: +MS, 0.5-0.6min #30-33

345.20347
667.41423
528.50449
850.71242

+MS, 0.5-0.6min #30-33

345.20347
346.20430
347.20530

Meas. m/z	#	Ion Formula	m/z	err [ppm]	mSigma	# mSigma	Score	rdb	e⁻ Conf	N-Rule
345.20347	1	C19H30NaO4	345.20363	0.47	31.4	1	100.00	4.5	even	ok

Figure S 10 ESI-MS spectrum of C_{12} in methanol.

Acquisition Parameter

Source Type	ESI	Ion Polarity	Positive	Set Nebulizer	0.3 Bar
Focus	Not active	Set Funnel 1 RF	100.0 Vpp	Set Dry Heater	200 °C
Scan Begin	50 m/z	Set Funnel 2 RF	200.0 Vpp	Set Dry Gas	4.0 l/min
Scan End	2500 m/z	Set Hexapole RF	200.0 Vpp	Set Divert Valve	Source

2020_0260_MEI_SAE197.d: +MS, 5.4min #322

373.23567
528.51003
723.47944

+MS, 5.4min #322

373.23567
374.23630
375.23702
376.29646

Meas. m/z	#	Ion Formula	m/z	err [ppm]	mSigma	# mSigma	Score	rdb	e⁻ Conf	N-Rule
373.23567	1	C21H34NaO4	373.23493	-1.97	25.6	1	100.00	4.5	even	ok

Figure S 11 ESI-MS spectrum of C_{14} in methanol.

DSC Data
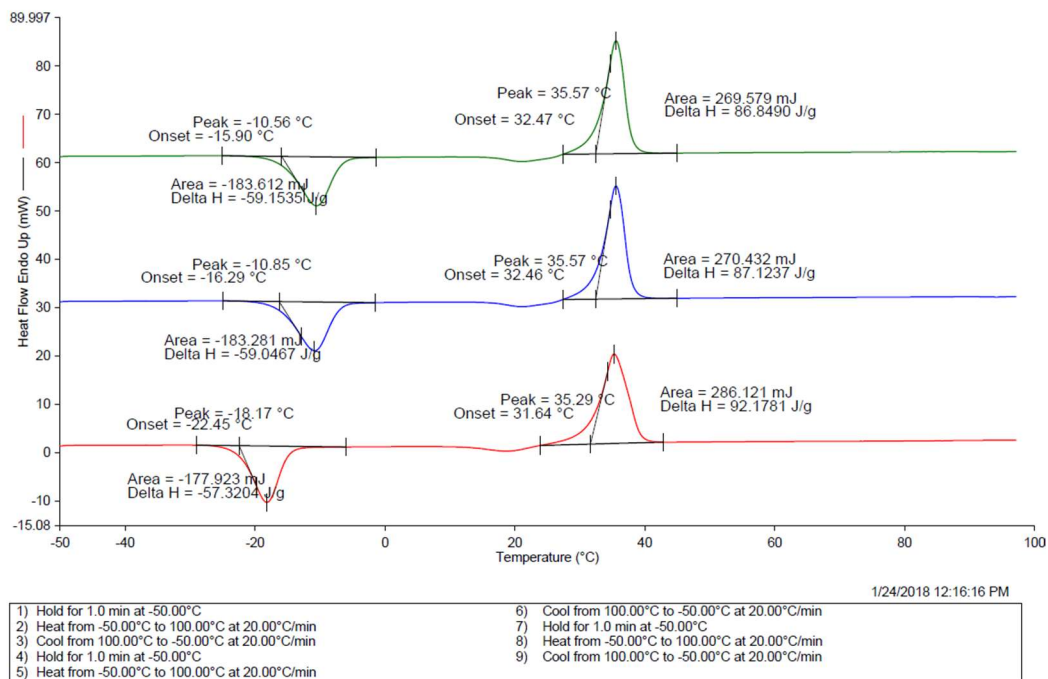
Figure S 12 DSC diagram of **C₆**. First heating cycle (red), second heating cycle (blue) and third heating cycle (green). Sample weight was 3.104 mg and mass loss after measurement 0.3%.
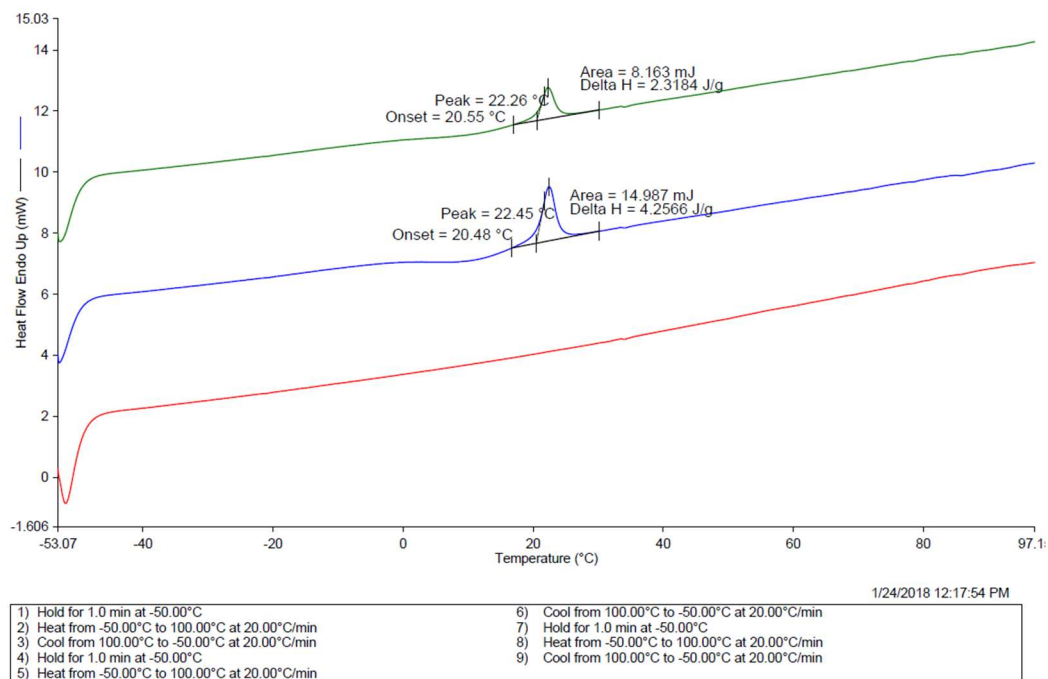
Figure S 13 DSC diagram of **C₈**. First heating cycle (red), second heating cycle (blue) and third heating cycle (green). Sample weight was 3.521 mg and mass loss after measurement 0.3%.
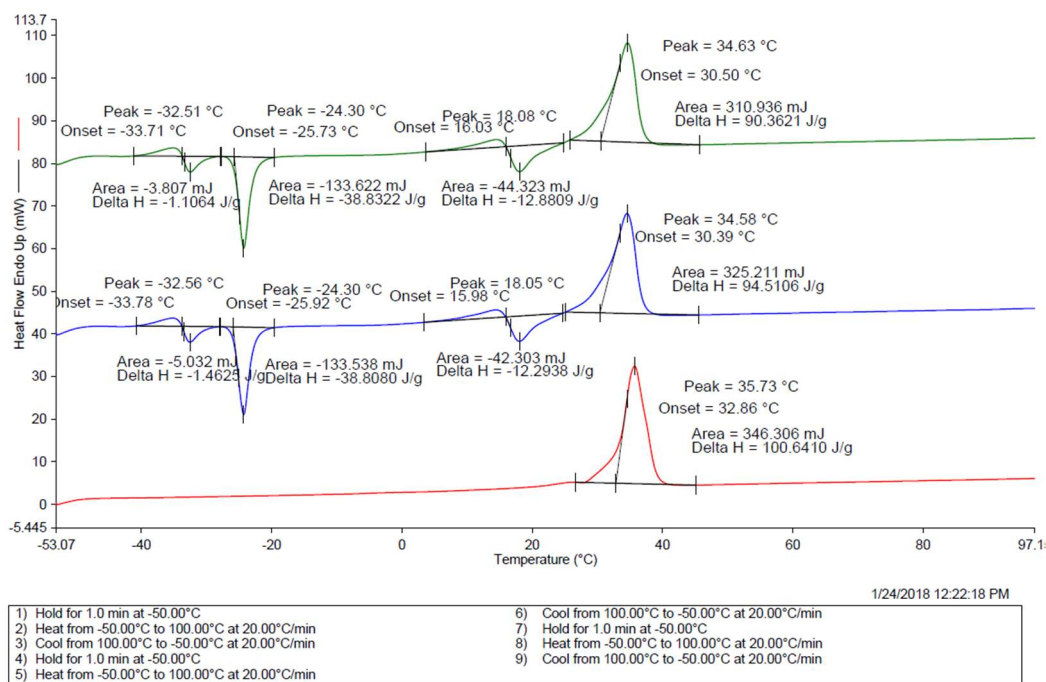
Figure S 14 DSC diagram of **C₁₀**. First heating cycle (red), second heating cycle (blue) and third heating cycle (green). Sample weight was 3.441 mg and mass loss after measurement 0.0%.
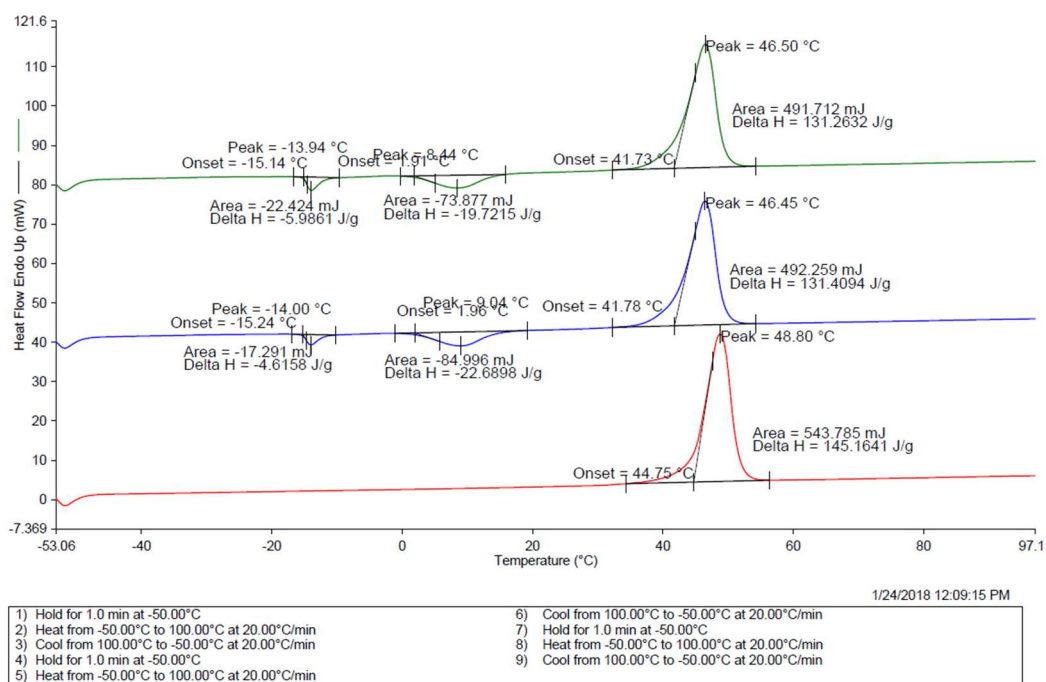
Figure S 15 DSC diagram of **C₁₂**. First heating cycle (red), second heating cycle (blue) and third heating cycle (green). Sample weight was 3.746 mg and mass loss after measurement 0.4%.
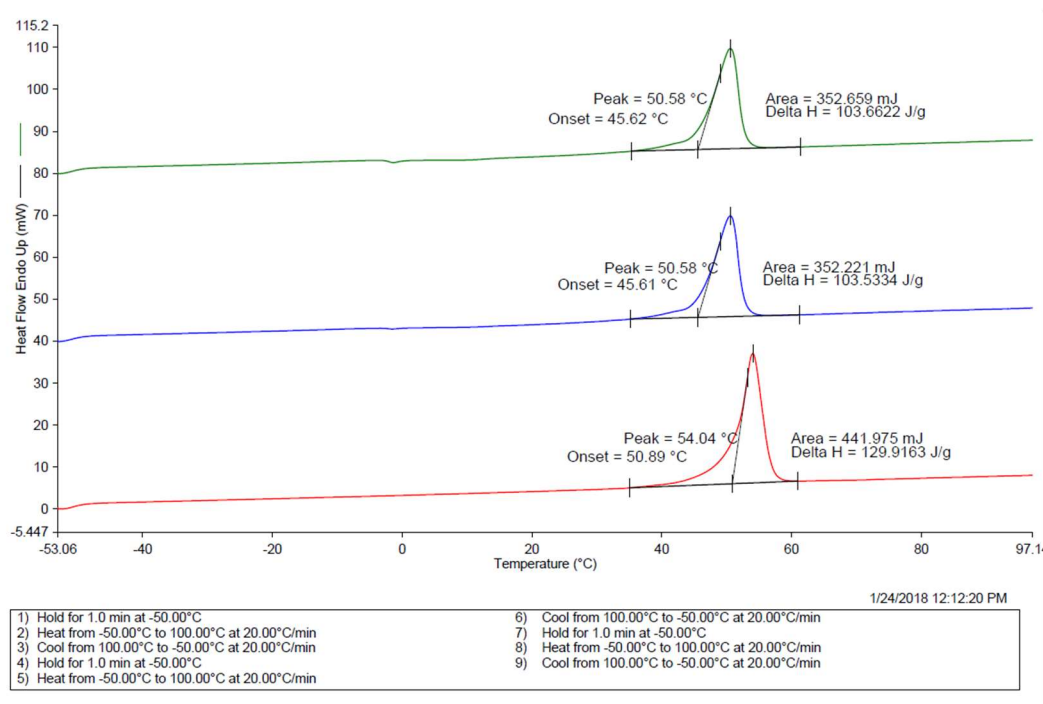
Figure S 16 DSC diagram of **C₁₄**. First heating cycle (red), second heating cycle (blue) and third heating cycle (green). Sample weight was 3.402 mg and mass loss after measurement 0.3%.

XRPD Data
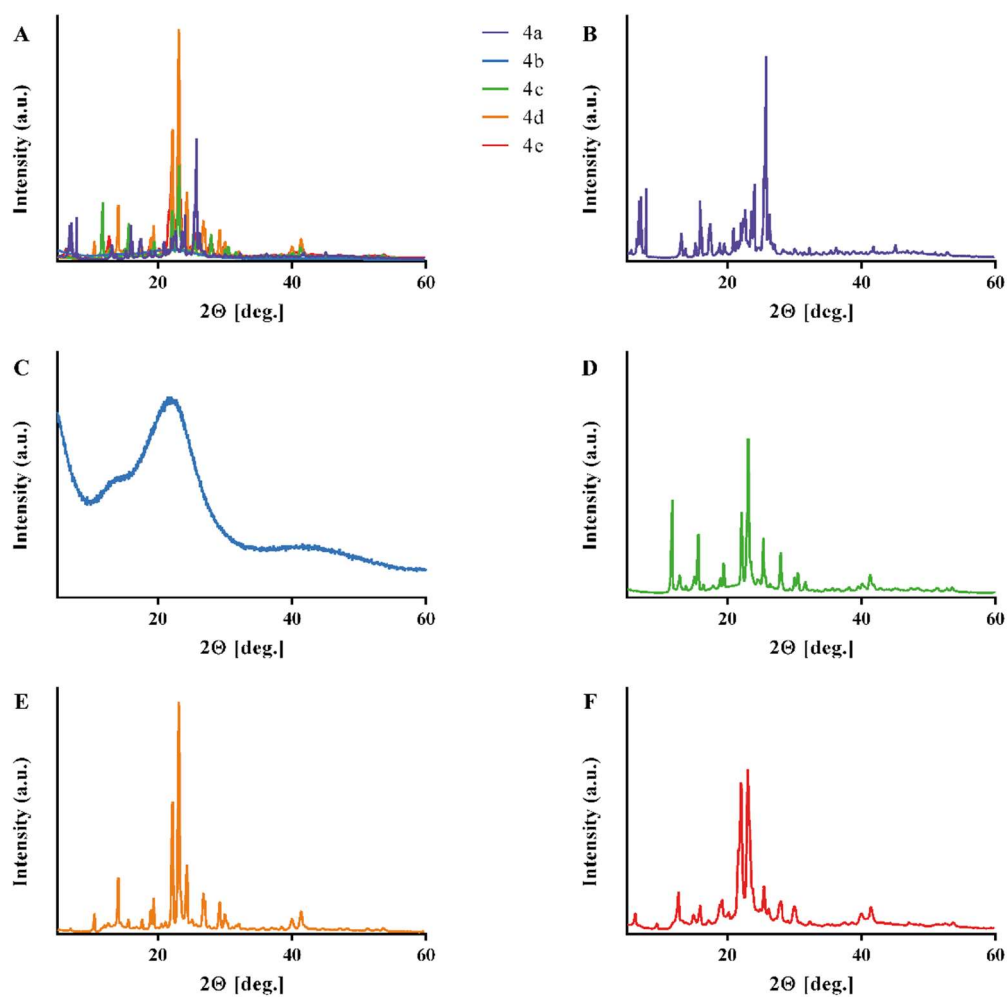
Figure S 17 X-Ray Powder Diffraction patterns of (A) all compounds combined, (B) C_6, (C) C_8, (D) C_{10}, (E) C_{12} and (F) C_{14}. Data was recorded on a Bruker Discover D8 powder diffractometer at 5° – 60° (2Θ).

Cell Proliferation Data
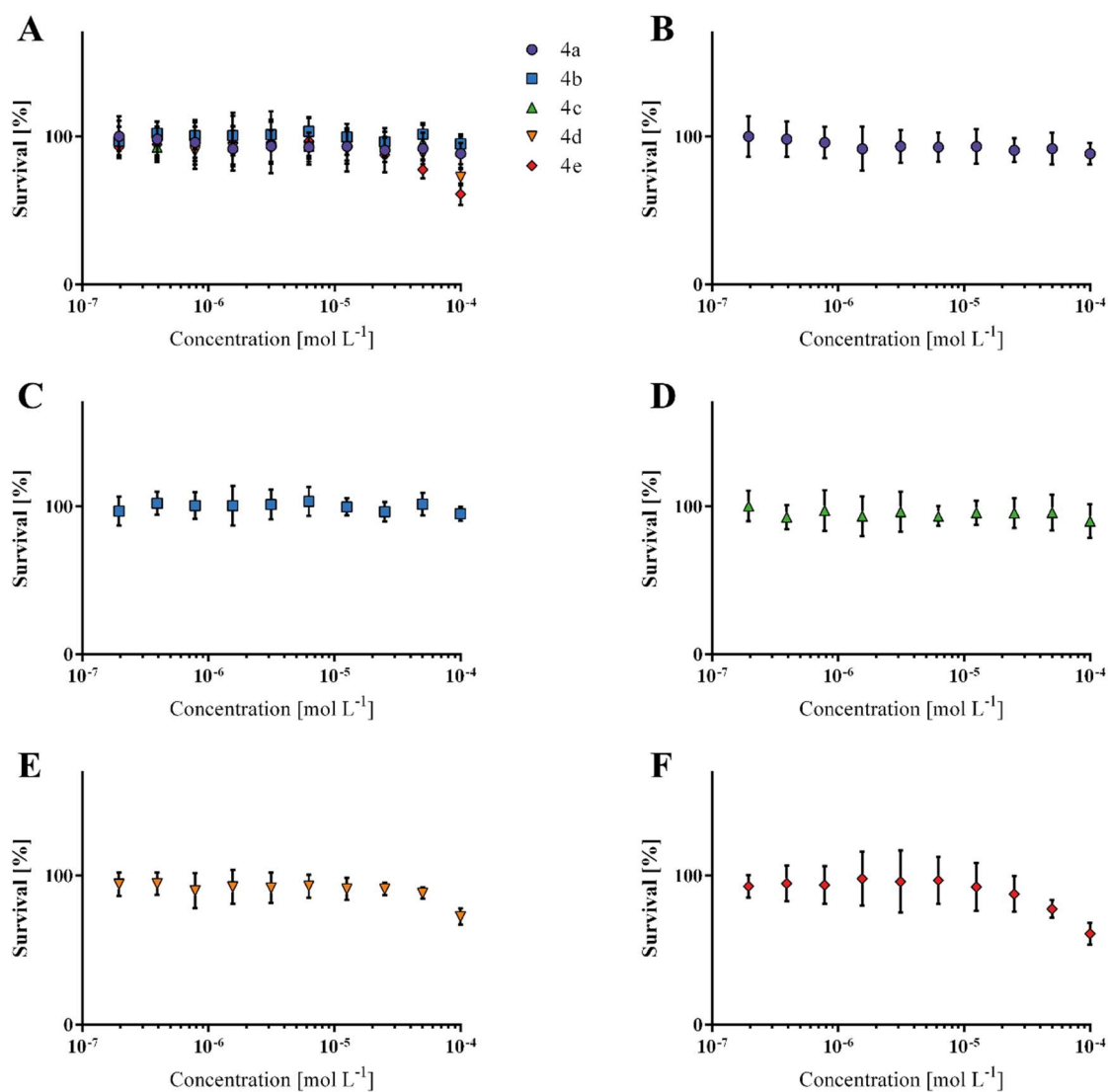
Figure S 18 Cytotoxic evaluation in NIH 3T3 fibroblasts using a WST-1 Proliferation Assay. Cellular survival plotted for (A) all data sets combined, (B) C_6, (C) C_8, (D) C_{10}, (E) C_{12} and (F) C_{14}. Data was normalized to control and is displayed as mean ± standard deviation (n = 12). Data was tested for outliners with a ROUT outliners test in the GraphPad Prism Software (no outliners identified). Calculation of an IC_{50} value was not possible.
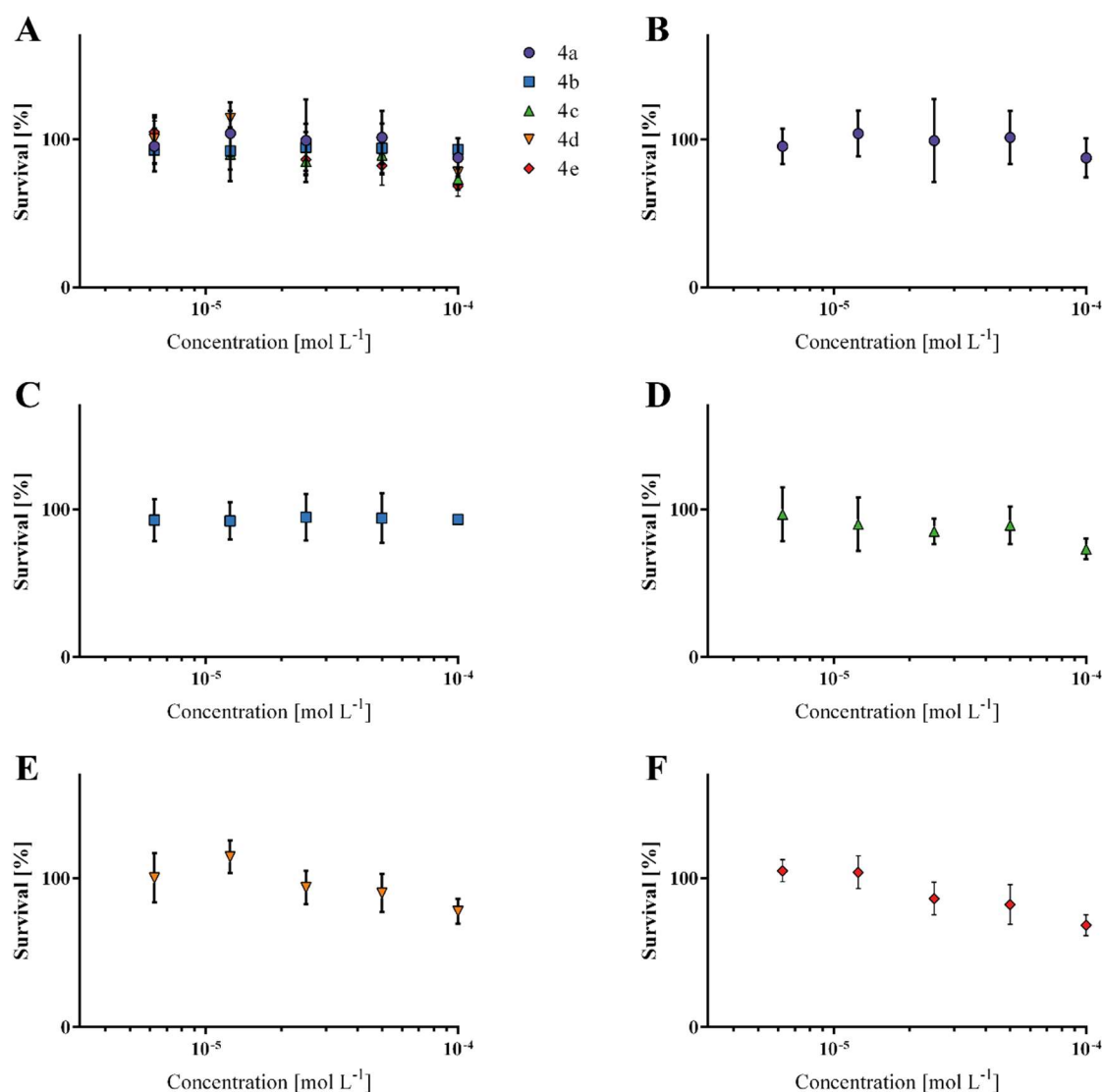
Figure S 19 Cytotoxic screening in Hep G2 liver cell line using a WST-1 Proliferation Assay. Cellular survival plotted for (A) all data sets combined, (B) C_6, (C) C_8, (D) C_{10}, (E) C_{12} and (F) C_{14}. Data was normalized to control and is displayed as mean ± standard deviation (n = 3). Calculation of an IC_{50} value was not possible.
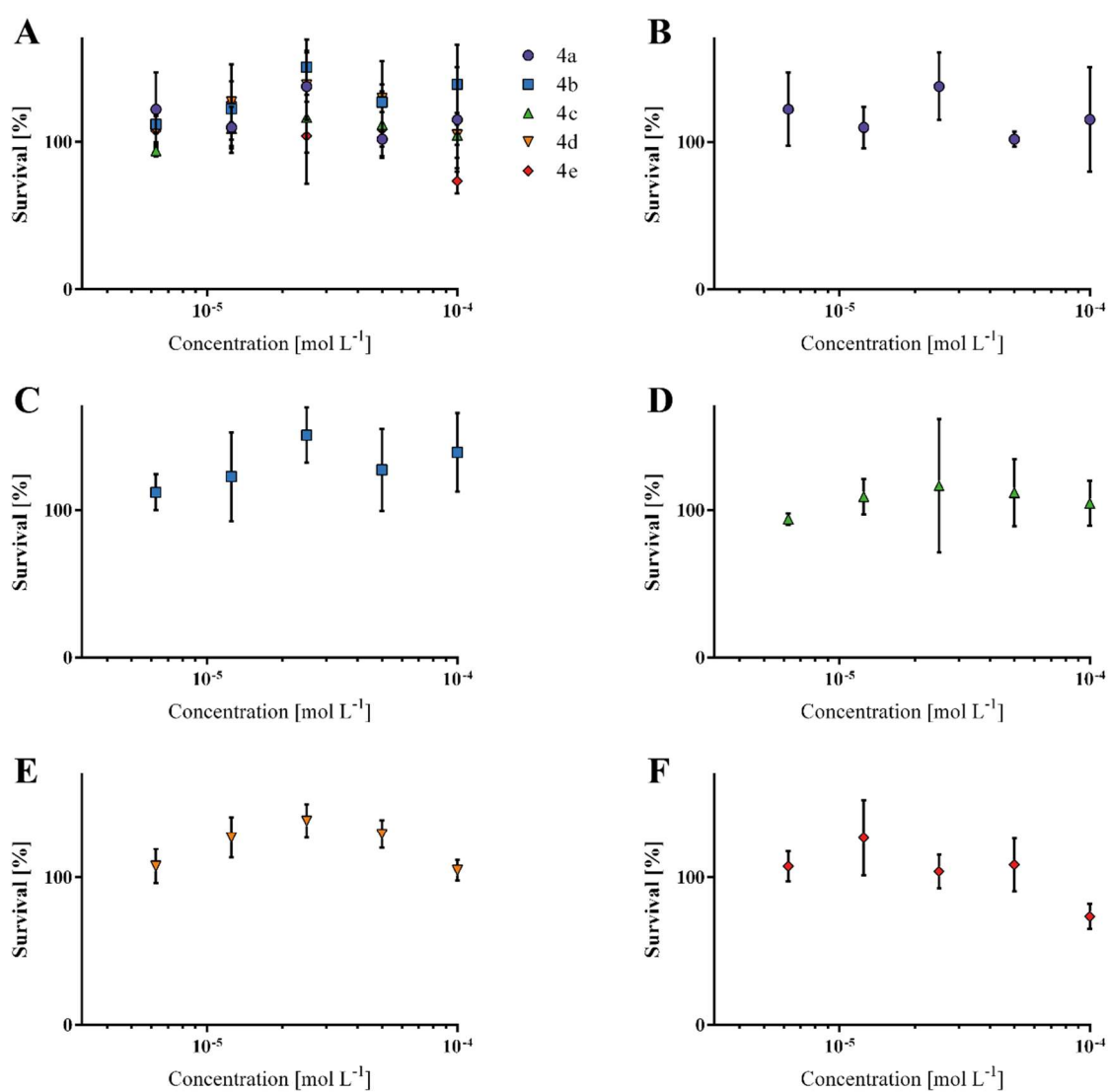
Figure S 20 Cytotoxic screening in HEK 293 kidney cell line using a WST-1 Proliferation Assay. Cellular survival plotted for (A) all data sets combined, (B) C_6, (C) C_8, (D) C_{10}, (E) C_{12} and (F) C_{14}. Data was normalized to control and is displayed as mean ± standard deviation (n = 3). Calculation of an IC_{50} value was not possible.
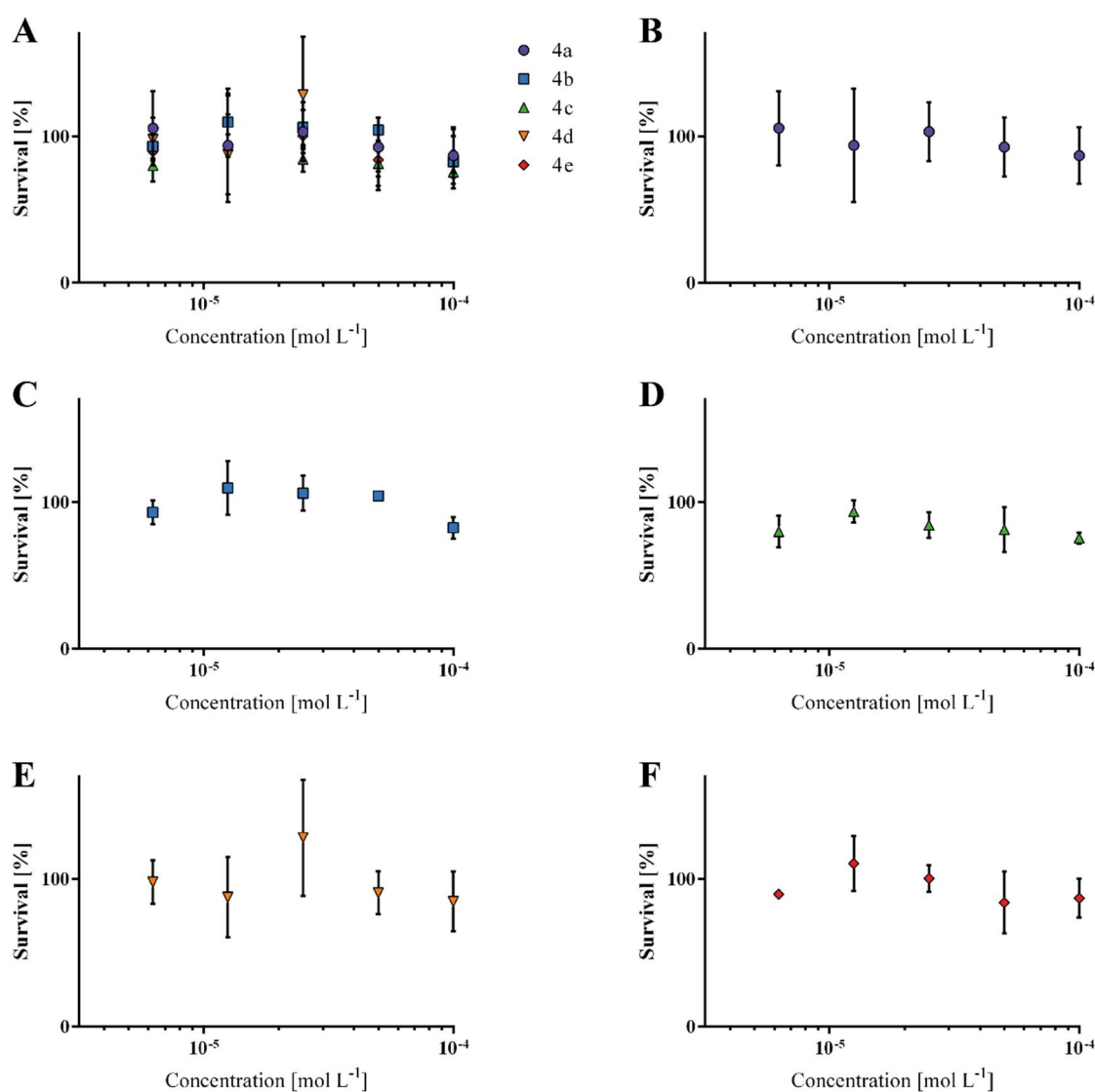
Figure S 21 Cytotoxic screening in Caco-2 epithelial colorectal cell line using a WST-1 Proliferation Assay. Cellular survival plotted for (A) all data sets combined, (B) C_6, (C) C_8, (D) C_{10}, (E) C_{12} and (F) C_{14}. Data was normalized to control and is displayed as mean ± standard deviation (n = 3). Calculation of an IC_{50} value was not possible.

^{1}H-NMR Data
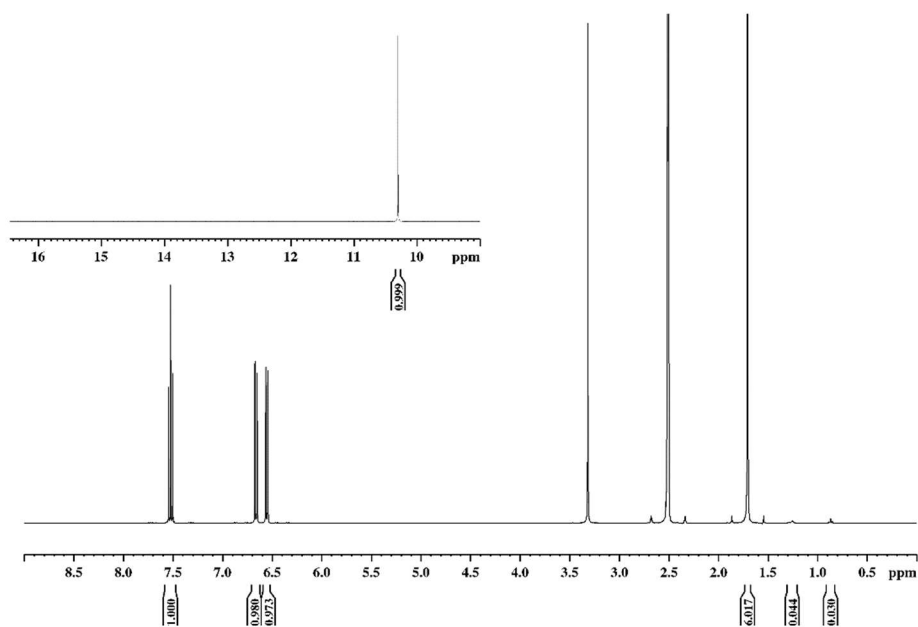
Figure S 22 ^{1}H-NMR of **2** in DMSO-d_6, referenced to the residual solvent signal at 2.50 ppm. Magnification of 9 – 16.4 ppm is shown in the upper left corner. Additional signals are due to smaller impurities and residual water (3.31 ppm).
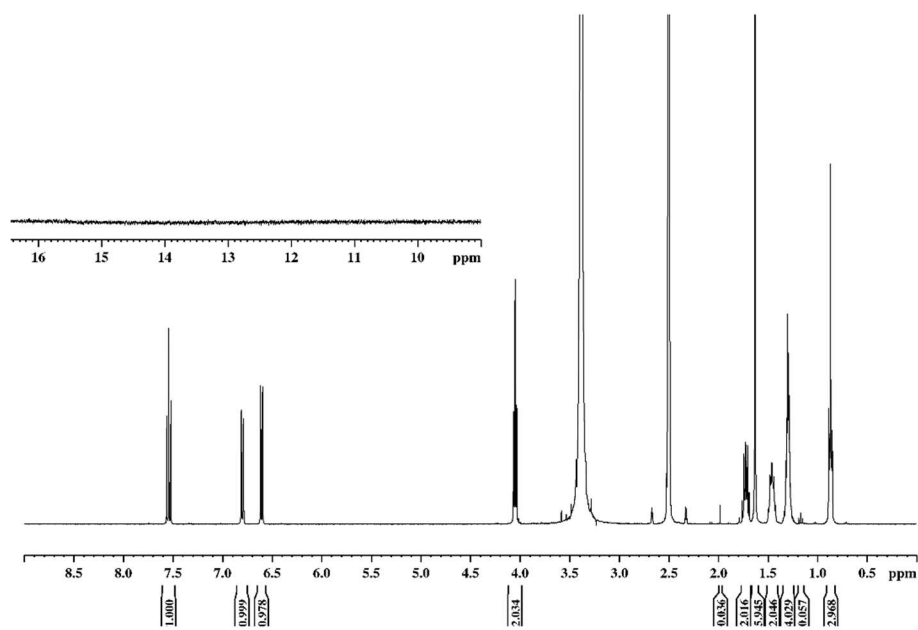
Figure S 23 ^{1}H-NMR of **3a** in DMSO-d_6, referenced to the residual solvent signal at 2.50 ppm. Magnification of 9 – 16.4 ppm is shown in the upper left corner. Additional signals are due to smaller impurities and residual water (3.31 ppm).
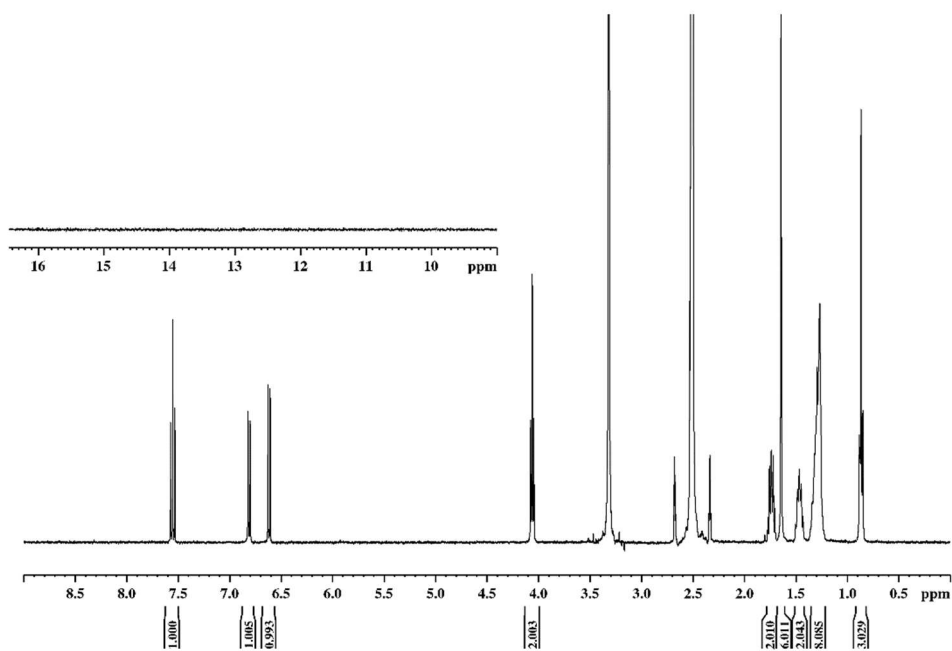
Figure S 24 ^{1}H-NMR of **3b** in DMSO-d$_6$, referenced to the residual solvent signal at 2.50 ppm. Magnification of 9 – 16.4 ppm is shown in the upper left corner. Additional signal is due to residual water (3.31 ppm).
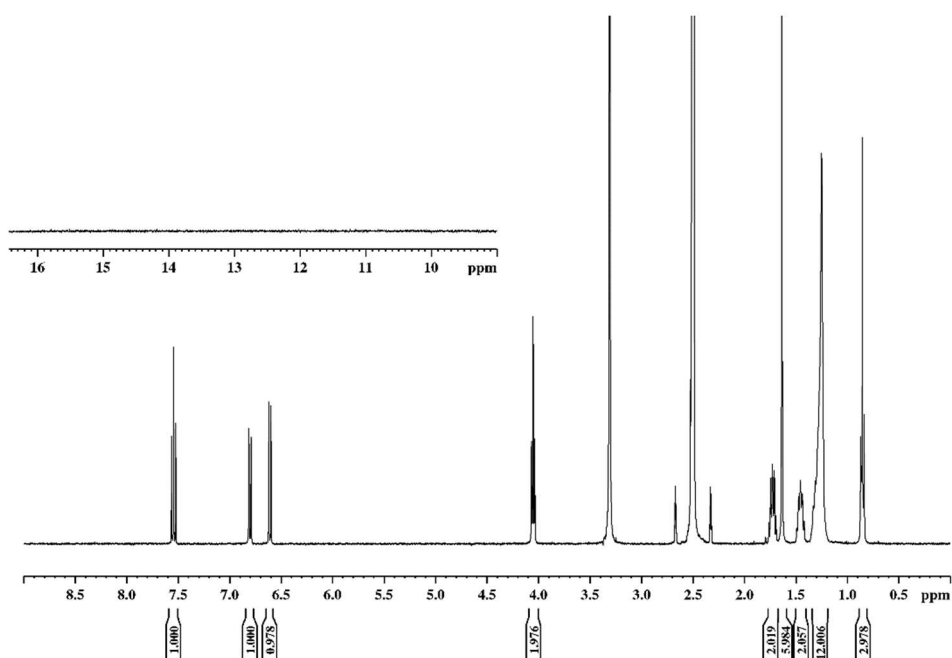
Figure S 25 ^{1}H-NMR of **3c** in DMSO-d$_6$, referenced to the residual solvent signal at 2.50 ppm. Magnification of 9 – 16.4 ppm is shown in the upper left corner. Additional signal is due to residual water (3.31 ppm).
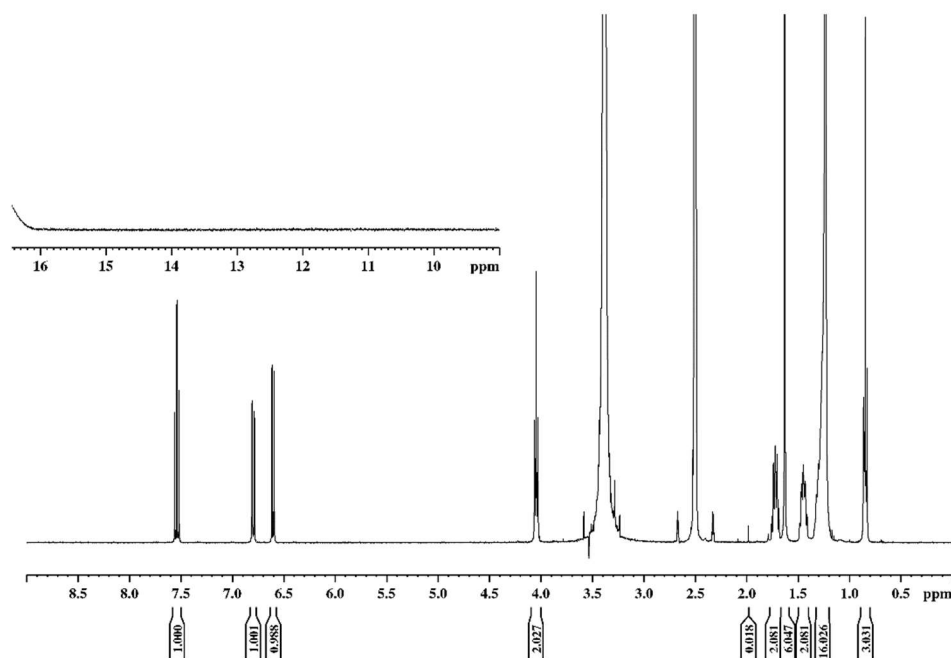
Figure S 26 ^{1}H-NMR of **3d** in DMSO-d$_6$, referenced to the residual solvent signal at 2.50 ppm. Magnification of 9 – 16.4 ppm is shown in the upper left corner. Additional signals are due to smaller impurities and residual water (3.31 ppm).
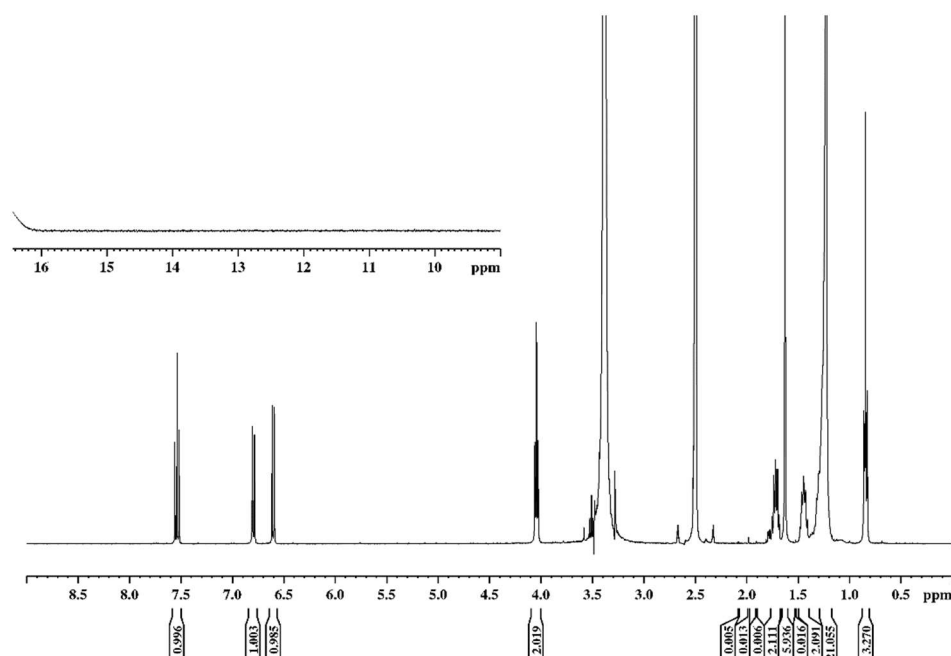
Figure S 27 ^{1}H-NMR of **3e** in DMSO-d$_6$, referenced to the residual solvent signal at 2.50 ppm. Magnification of 9 – 16.4 ppm is shown in the upper left corner. Additional signals are due to smaller impurities and residual water (3.31 ppm). Larger integrals for 1.29 ppm (expected 20 H) and 0.88 ppm (expected 3 H) is due to impurity of residual reactant 1-bromododecane.
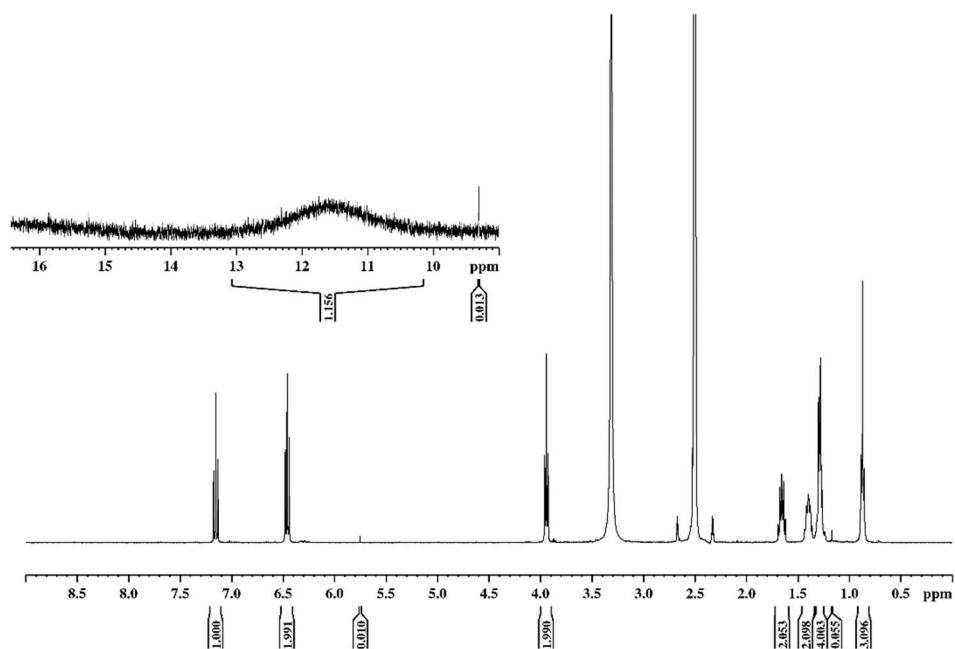
Figure S 28 ^{1}H-NMR of **4a** (**C$_6$**) in DMSO-d$_6$, referenced to the residual solvent signal at 2.50 ppm. Magnification of 9 – 16.4 ppm is shown in the upper left corner. Additional signals are due to smaller impurities and residual water (3.31 ppm).
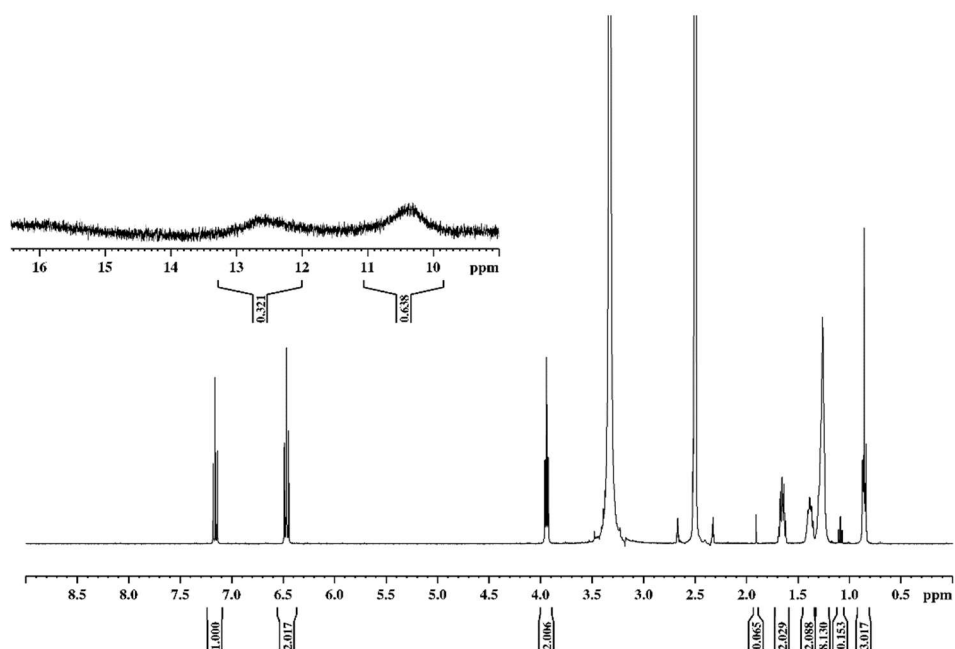
Figure S 29 ^{1}H-NMR of **4b** (**C$_8$**) in DMSO-d$_6$, referenced to the residual solvent signal at 2.50 ppm. Magnification of 9 – 16.4 ppm is shown in the upper left corner. Additional signals are due to smaller impurities and residual water (3.31 ppm).
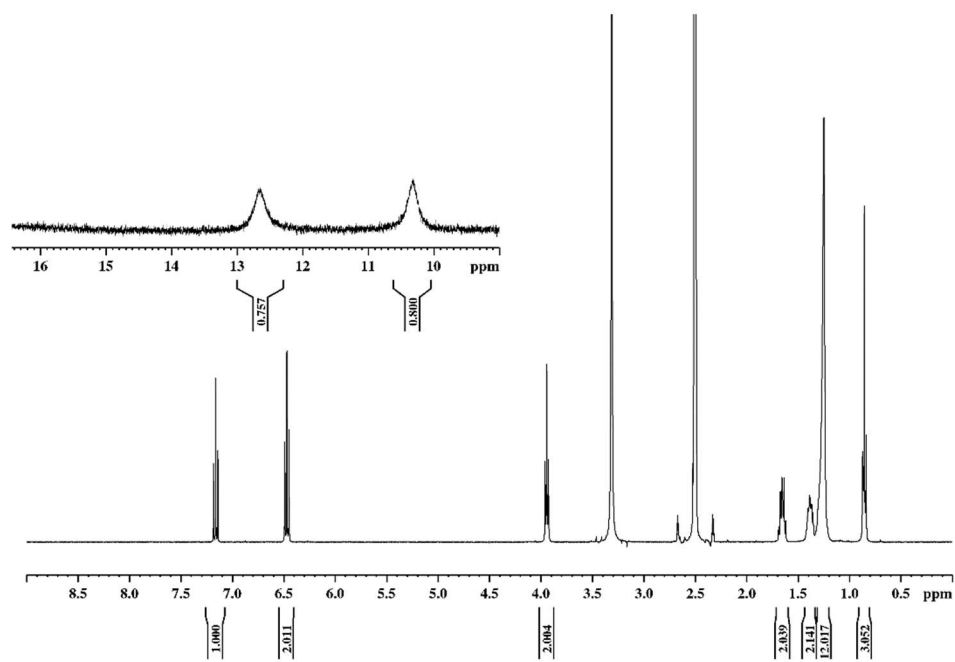
Figure S 30 ^{1}H-NMR of **4c** (**C$_{10}$**) in DMSO-d$_6$, referenced to the residual solvent signal at 2.50 ppm. Magnification of 9 – 16.4 ppm is shown in the upper left corner. Additional signal at 3.31 ppm is due to residual water.
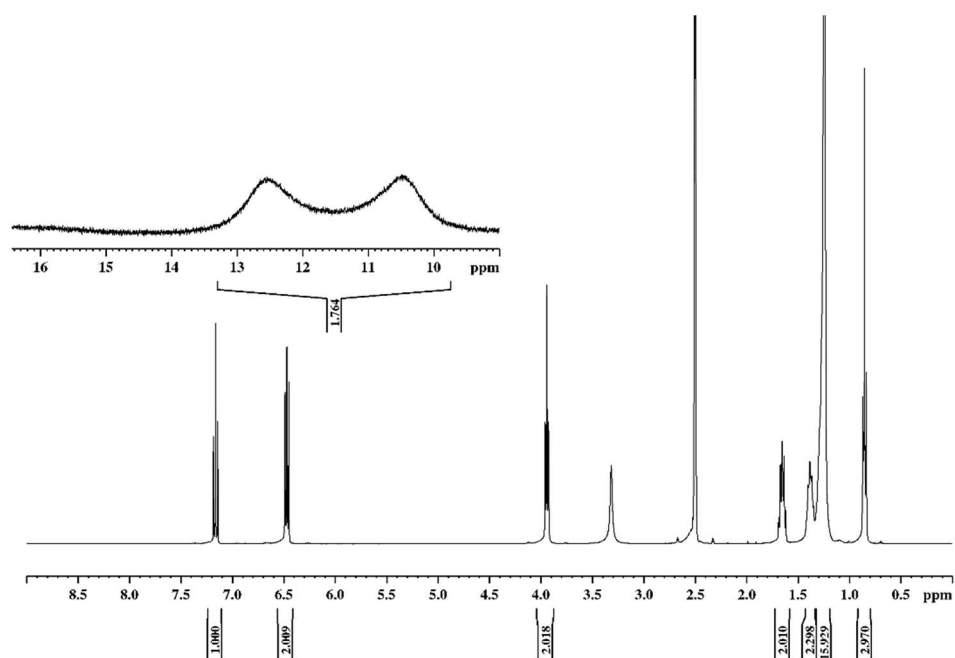
Figure S 31 ^{1}H-NMR of **4d** (**C$_{12}$**) in DMSO-d$_6$, referenced to the residual solvent signal at 2.50 ppm. Magnification of 9 – 16.4 ppm is shown in the upper left corner. Additional signal at 3.31 ppm is due to residual water.
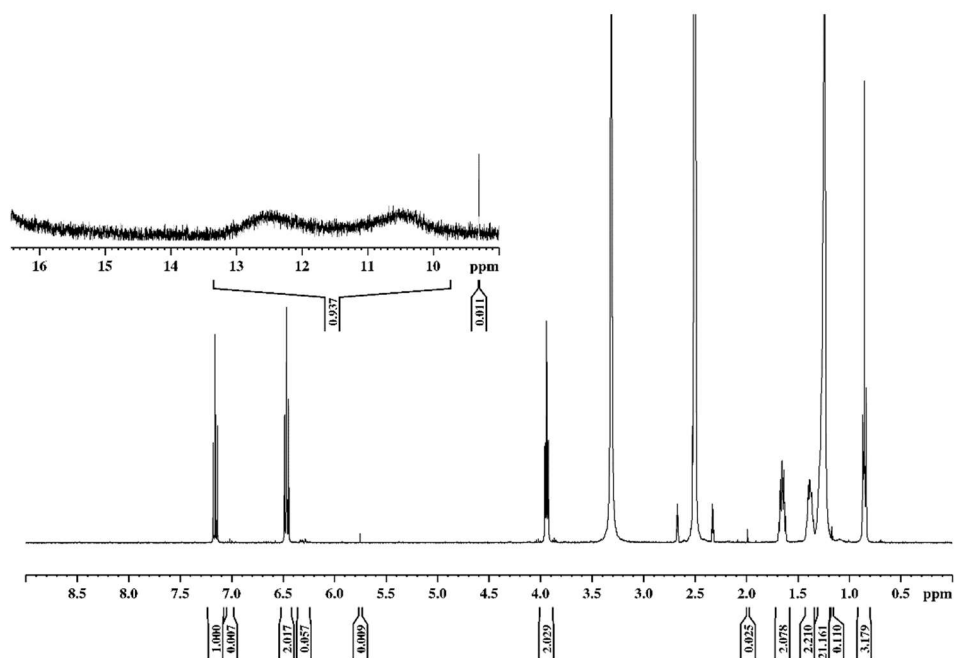
Figure S 32 ^{1}H-NMR of **4e** (**C$_{14}$**) in DMSO-d$_6$, referenced to the residual solvent signal at 2.50 ppm. Magnification of 9 – 16.4 ppm is shown in the upper left corner. Additional signals are due to smaller impurities and residual water (3.31 ppm).

^{13}C-NMR Data
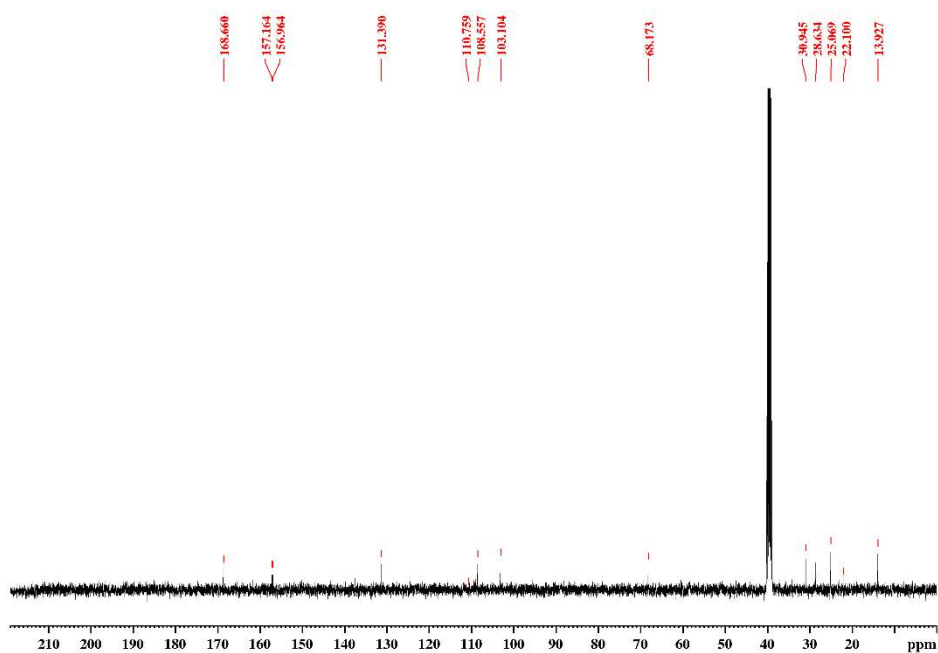
Figure S 33 ^{13}C-NMR of **4a** (**C$_6$**) in DMSO-d$_6$, referenced to the residual solvent signal at 40.45 ppm.
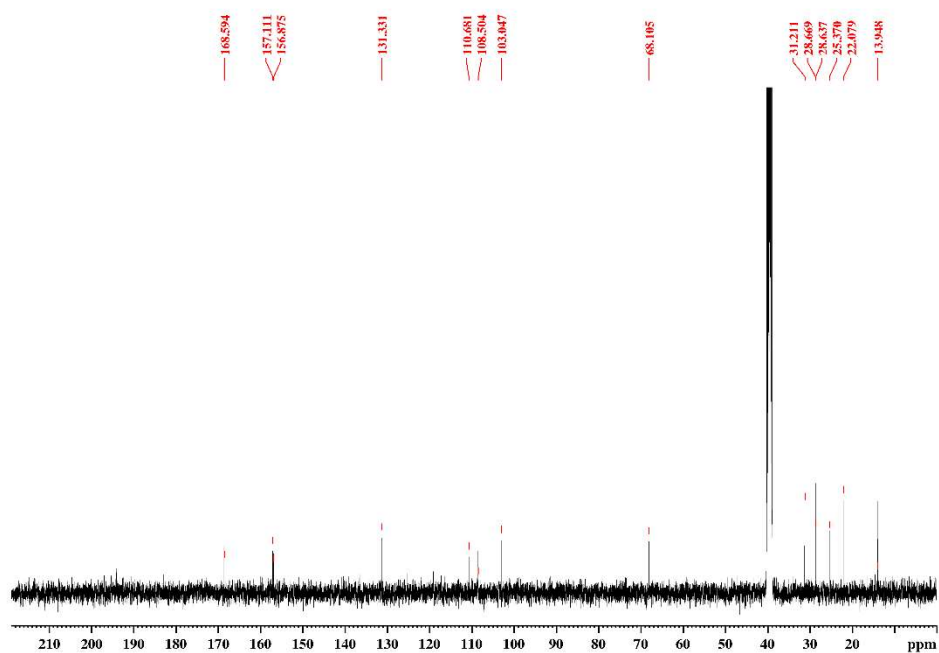
Figure S 34 ^{13}C-NMR of **4b** (**C$_8$**) in DMSO-d$_6$, referenced to the residual solvent signal at 40.45 ppm.
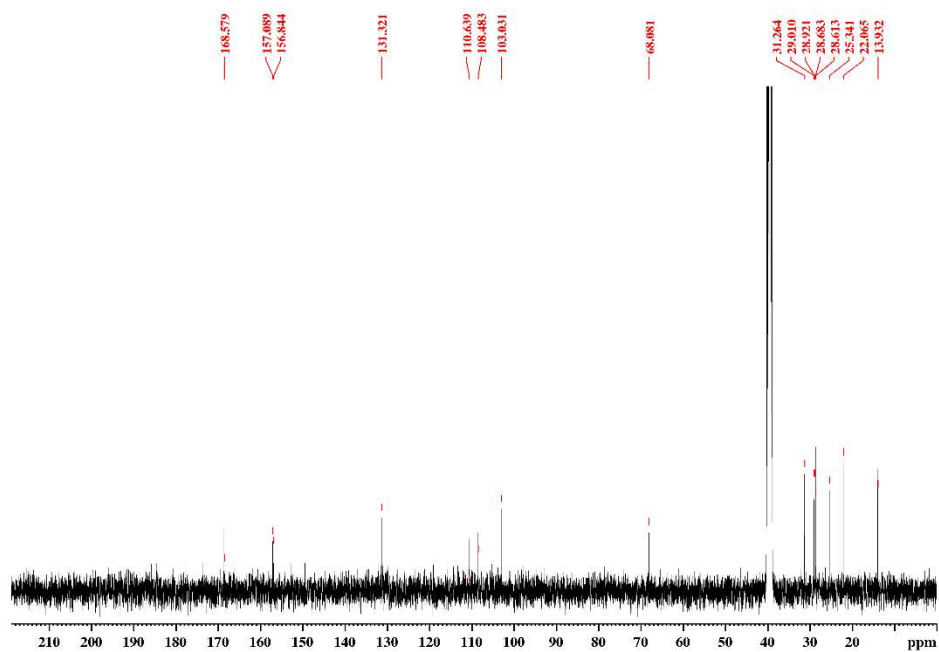
Figure S 35 ^{13}C-NMR of **4c** (**C$_{10}$**) in DMSO-d$_6$, referenced to the residual solvent signal at 40.45 ppm.
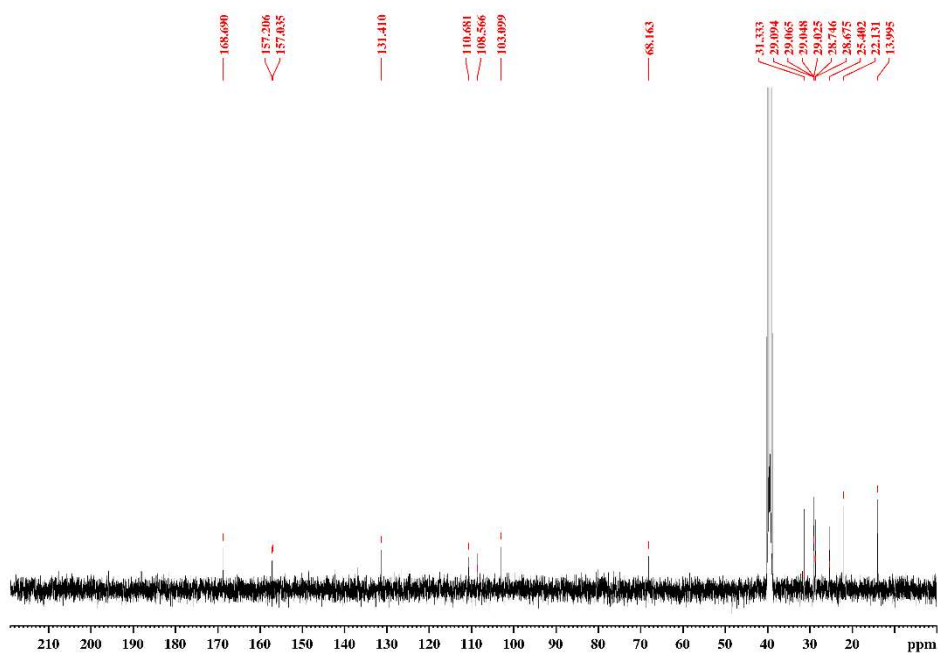
Figure S 36 ^{13}C-NMR of **4d** (**C$_{12}$**) in DMSO-d$_6$, referenced to the residual solvent signal at 40.45 ppm.
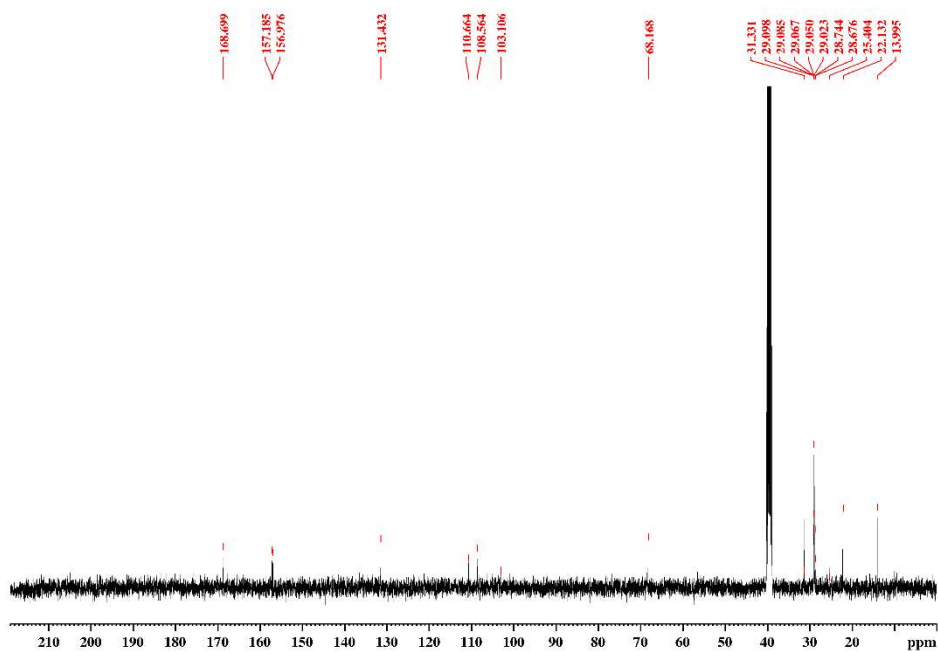
Figure S 37 ^{13}C-NMR of **4e** (**C$_{14}$**) in DMSO-d$_6$, referenced to the residual solvent signal at 40.45 ppm.

Biological Data

Caco-2 Permeation Data
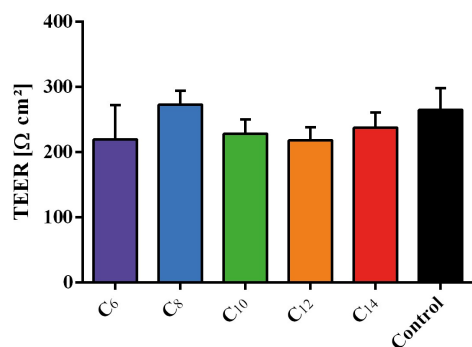
Figure S 38 Trans epithelial electric resistance (TEER) values was measured after the experiment and compared to the untreated control group. Data is given as mean ± standard deviation (n=3).
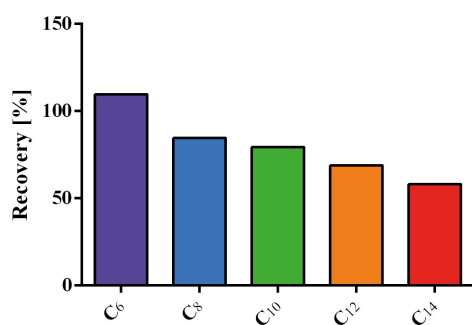
Figure S 39 Recovery obtained after two hours incubation following a Caco-2 permeation assay without cells present (single experiment).
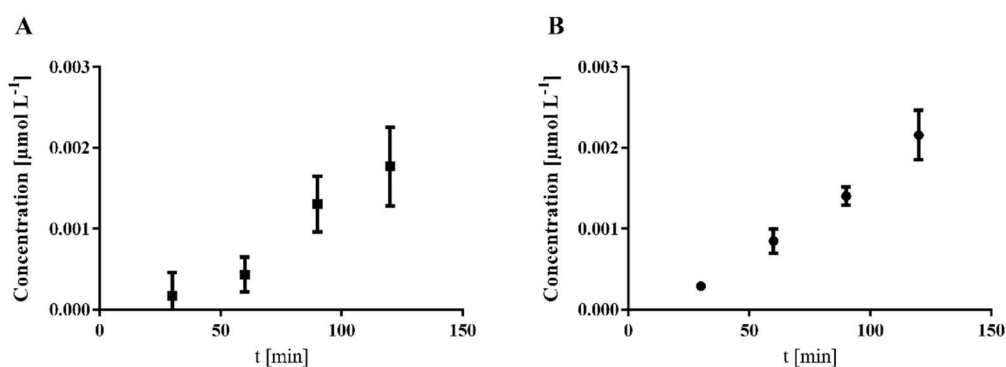
Figure S 40 Basolateral concentrations of (A) Lucifer Yellow and (B) sodium Fluorescein after 30, 60, 90 and 120 minutes, quantified via fluorimetric analysis. Data is given as mean ± standard deviation (n=3).

MIC Data

Table S 1 MIC values for biofilm-forming *S. aureus* (ST228) from three independent experiments. Each experiment included two serial dilutions resulting in six MIC values. Careful selection of the MIC resulted in highest concentration observed within this series of results. MIC values are given in μmol L^{-1} und μg mL^{-1}.

Compound	MIC 1.1	MIC 1.2	MIC 2.1	MIC 2.2	MIC 3.1	MIC 3.2	MIC μmol L^{-1}	MIC μg mL^{-1}
Octenidin	3.125	3.125	1.5625	1.5625	6.25	6.25	6.25	4
Vancomycin	1.5625	1.5625	0.78125	0.78125	1.5625	1.5625	1.563	2
Ciprofloxacin	> 100	> 100	> 100	> 100	> 100	> 100	>100	> 39
Amoxicillin	> 100	> 100	> 100	> 100	> 100	> 100	>100	> 42
C$_8$	> 100	> 100	> 100	> 100	> 100	> 100	>100	> 27
C$_{10}$	100	100	100	100	100	100	100	29
C$_{12}$	25	25	25	25	25	25	25	8
GA (C$_{13}$)	25	25	25	25	25	25	25	8
AA (C$_{15}$)	> 100	> 100	> 100	> 100	> 100	> 100	> 100	> 35

Table S 2 MIC values for multidrug resistant *S. aureus* (JE2) from three independent experiments. Each experiment included two serial dilutions resulting in six MIC values. Careful selection of the MIC resulted in highest concentration observed within this series of results. MIC values are given in μmol L^{-1} und μg mL^{-1}.

Compound	MIC 1.1	MIC 1.2	MIC 2.1	MIC 2.2	MIC 3.1	MIC 3.2	MIC μmol L^{-1}	MIC μg mL^{-1}
Octenidin	6.25	6.25	3.125	6.25	6.25	6.25	6.25	4
Vancomycin	1.5625	1.5625	1.5625	1.5625	1.5625	1.5625	1.563	2
Ciprofloxacin	> 100	> 100	> 100	> 100	> 100	> 100	> 100	> 39
Amoxicillin	50	50	50	50	> 100	> 100	> 100	> 42
C$_8$	> 100	> 100	> 100	> 100	> 100	> 100	>100	> 27
C$_{10}$	50	50	50	50	100	100	100	29
C$_{12}$	25	25	25	25	50	50	50	16
GA (C$_{13}$)	25	25	25	25	25	25	25	8
AA (C$_{15}$)	> 100	> 100	> 100	> 100	> 100	> 100	> 100	> 35

Table S 3 MIC values for multidrug resistant *S. aureus* (Lac*) from three independent experiments. Each experiment included two serial dilutions resulting in six MIC values. Careful selection of the MIC resulted in highest concentration observed within this series of results. MIC values are given in µmol L^{-1} und µg mL^{-1}.

Compound	MIC 1.1	MIC 1.2	MIC 2.1	MIC 2.2	MIC 3.1	MIC 3.2	MIC µmol L^{-1}	MIC µg mL^{-1}
Octenidin	6.25	6.25	6.25	6.25	6.25	6.25	6.25	4
Vancomycin	1.5625	1.5625	1.5625	1.5625	1.5625	1.5625	1.563	2
Ciprofloxacin	> 100	> 100	> 100	> 100	> 100	> 100	> 100	> 39
Amoxicillin	100	100	100	100	50	50	100	42
C$_8$	> 100	> 100	> 100	> 100	> 100	> 100	> 100	> 27
C$_{10}$	50	50	50	50	50	50	50	15
C$_{12}$	25	25	25	25	12.5	12.5	25	8
GA (C$_{13}$)	25	25	25	25	25	25	25	8
AA (C$_{15}$)	> 100	> 100	> 100	> 100	> 100	> 100	> 100	> 35

Table S 4 MIC values for *S. epidermidis* (RP62a) from three independent experiments. Each experiment included two serial dilutions resulting in six MIC values. Careful selection of the MIC resulted in highest concentration observed within this series of results. MIC values are given in µmol L^{-1} und µg mL^{-1}.

Compound	MIC 1.1	MIC 1.2	MIC 2.1	MIC 2.2	MIC 3.1	MIC 3.2	MIC µmol L^{-1}	MIC µg mL^{-1}
Octenidin	3.125	3.125	3.125	3.125	3.125	3.125	3.125	2
Vancomycin	3.125	3.125	1.5625	1.5625	1.5625	1.5625	3.125	5
Ciprofloxacin	0.1953	0.1953	0.1953	0.1953	25	25	25	10
Amoxicillin	50	> 100	100	> 100	> 100	> 100	> 100	> 42
C$_8$	25	25	50	25	> 100	> 100	> 100	> 27
C$_{10}$	3.125	3.125	3.125	3.125	50	50	50	15
C$_{12}$	12.5	12.5	12.5	12.5	25	25	25	8
GA (C$_{13}$)	12.5	12.5	12.5	12.5	12.5	12.5	12.5	4
AA (C$_{15}$)	> 100	> 100	> 100	> 100	> 100	> 100	> 100	> 35

Table S 5 MIC values for *E. faecium* (UL602570) from three independent experiments. Each experiment included two serial dilutions resulting in six MIC values. Careful selection of the MIC resulted in highest concentration observed within this series of results. MIC values are given in µmol L^{-1} und µg mL^{-1}.

Compound	MIC 1.1	MIC 1.2	MIC 2.1	MIC 2.2	MIC 3.1	MIC 3.2	MIC µmol L^{-1}	MIC µg mL^{-1}
Octenidin	3.125	3.125	6.25	6.25	6.25	6.25	6.25	4
Vancomycin	> 100	> 100	> 100	> 100	> 100	> 100	> 100	> 145
Ciprofloxacin	> 100	> 100	> 100	> 100	> 100	> 100	> 100	> 39
Amoxicillin	> 100	> 100	> 100	> 100	> 100	> 100	> 100	> 42
Dequalinium	12.5	12.5	12.5	12.5	12.5	12.5	12.5	4
Linezolid	> 100	> 100	> 100	> 100	> 100	> 100	> 100	> 53
C$_8$	> 100	> 100	> 100	> 100	> 100	> 100	> 100	> 27
C$_{10}$	100	100	50	50	50	50	100	29
C$_{12}$	50	50	12.5	12.5	12.5	12.5	50	16
GA (C$_{13}$)	6.25	6.25	6.25	6.25	6.25	6.25	6.25	2
AA (C$_{15}$)	12.5	12.5	12.5	12.5	6.25	6.25	12.5	4

Table S 6 MIC values for *E. faecalis* (ATCC 51229) from three independent experiments. Each experiment included two serial dilutions resulting in six MIC values. Careful selection of the MIC resulted in highest concentration observed within this series of results. MIC values are given in µmol L^{-1} und µg mL^{-1}.

Compound	MIC 1.1	MIC 1.2	MIC 2.1	MIC 2.2	MIC 3.1	MIC 3.2	MIC µmol L^{-1}	MIC µg mL^{-1}
Octenidin	12.5	6.25	12.5	12.5	12.5	12.5	12.5	8
Vancomycin	25	25	25	25	25	25	25	36
Ciprofloxacin	0.7813	0.7813	1.5625	1.5625	3.125	3.125	3.125	1
Amoxicillin	0.7813	0.7813	1.5625	1.5625	3.125	3.125	3.125	1
Dequalinium	50	50	50	50	25	25	50	17
Linezolid	> 100	> 100	> 100	> 100	> 100	> 100	> 100	> 53
C$_8$	> 100	> 100	> 100	> 100	> 100	> 100	> 100	> 27
C$_{10}$	50	50	50	50	50	50	50	15

Compound	MIC 1.1	MIC 1.2	MIC 2.1	MIC 2.2	MIC 3.1	MIC 3.2	MIC µmol L^{-1}	MIC µg mL^{-1}
C$_{12}$	12.5	12.5	12.5	12.5	12.5	12.5	12.5	4
GA (C$_{13}$)	6.25	6.25	6.25	6.25	6.25	6.25	6.25	2
AA (C$_{15}$)	12.5	12.5	25	25	12.5	12.5	25	9

Table S 7 MIC values for *Streptococcus agalactiae* (ATCC13813) from three independent experiments. Each experiment included two serial dilutions resulting in six MIC values. Careful selection of the MIC resulted in highest concentration observed within this series of results. MIC values are given in µmol L^{-1} und µg mL^{-1}.

Compound	MIC 1.1	MIC 1.2	MIC 2.1	MIC 2.2	MIC 3.1	MIC 3.2	MIC µmol L^{-1}	MIC µg mL^{-1}
Octenidin	12.5	12.5	6.25	6.25	1.5625	1.5625	12.5	8
Vancomycin	0.78125	0.78125	3.125	6.25	0.78125	0.78125	6.25	9
Ciprofloxacin	1.5625	1.5625	3.125	3.125	1.5625	1.5625	3.125	1
Amoxicillin	< 100	< 100	12.5	12.5	< 100	< 100	12.5	5
Dequalinium	6.25	6.25	12.5	12.5	6.25	6.25	12.5	4
Linezolid	50	50	50	50	50	25	50	26
C$_8$	> 100	> 100	> 100	> 100	> 100	> 100	> 100	> 27
C$_{10}$	25	25	50	50	50	50	50	15
C$_{12}$	6.25	6.25	12.5	12.5	12.5	12.5	12.5	4
GA (C$_{13}$)	6.25	6.25	3.125	3.125	3.125	3.125	3.125	1
AA (C$_{15}$)	3.125	3.125	6.25	6.25	6.25	6.25	6.25	2

Table S 8 MIC values for *C. difficile* (DSM 27543) from three independent experiments. Each experiment included two serial dilutions resulting in six MIC values. Careful selection of the MIC resulted in highest concentration observed within this series of results. MIC values are given in µmol L^{-1} und µg mL^{-1}.

Compound	MIC 1.1	MIC 1.2	MIC 2.1	MIC 2.2	MIC 3.1	MIC 3.2	MIC µmol L^{-1}	MIC µg mL^{-1}
Octenidin	12.5	12.5	6.25	6.25	6.25	6.25	12.5	8
Vancomycin	3.125	3.125	1.5625	1.5625	1.5625	1.5625	3.125	5
Ciprofloxacin	100	100	100	100	50	50	100	39
Amoxicillin	25	25	12.5	12.5	12.5	12.5	25	10
Dequalinium	50	50	6.25	6.25	6.25	6.25	6.25	2
Linezolid	> 100	> 100	> 100	> 100	> 100	> 100	> 100	> 53
C$_8$	> 100	> 100	> 100	> 100	> 100	> 100	> 100	> 27
C$_{10}$	100	100	100	100	50	50	100	29
C$_{12}$	100	100	50	50	25	25	100	32

Galleria Efficacy Data

Table S 9 Overview drug efficacy study in *Galleria mellonella* larvae infected with Vancomycin-resistant *E. faecium* UL602570.

Group	Number of animals	Maggot weight g	Appl. volume µL	Drug conc. µmol L^{-1}	Dose µmol kg^{-1} BW	Dose mg kg^{-1} BW
Non-Infected	20	0.47 ± 0.11	20	200	-	-
PBS	20	0.43 ± 0.06	20	200	-	-
Octenidine	20	0.43 ± 0.10	20	200	9.31 ± 2.15	5.81 ± 1.34
Vancomycin	20	0.41 ± 0.08	20	200	9.71 ± 1.88	14.08 ± 2.73
Ciprofloxacin	20	0.46 ± 0.10	20	200	8.78 ± 1.99	3.39 ± 0.77
Amoxicillin	20	0.47 ± 0.09	20	200	8.54 ± 1.65	3.59 ± 0.69
Linezolid	20	0.46 ± 0.07	20	200	8.65 ± 1.31	2.92 ± 0.44
C$_{10}$	20	0.45 ± 0.10	20	200	8.82 ± 1.90	2.59 ± 0.56
C$_{12}$	20	0.40 ± 0.09	20	200	9.99 ± 2.15	3.22 ± 0.69

Table S 10 Animal survival of *Galleria mellonella* larvae post infection with Vancomycin-resistant *E. faecium* UL602570.

Group	6 h	12 h	18 h	24 h	30 h	36 h	42 h	48 h	60 h	72 h	84 h	96 h
Non-Infected	20	20	20	20	20	20	20	19	19	19	18	18
PBS	20	20	19	16	14	13	12	11	11	10	9	7
Octenidine	20	20	18	17	15	13	12	12	10	10	10	10
Vancomycin	20	19	18	18	17	15	15	15	15	14	13	13
Ciprofloxacin	20	20	19	17	12	11	10	10	10	8	8	8
Amoxicillin	20	20	19	13	11	10	9	8	6	6	6	5
Linezolid	20	20	20	19	19	18	18	18	18	13	13	13
C$_{10}$	20	20	20	18	16	16	16	15*	15	15	14	14
C$_{12}$	20	20	20	17	16	16	16	15	15	14	14	14

* Larvae removed because of pupation

Table S 11 Overview drug efficacy study in *Galleria mellonella* larvae infected with multi-drug resistant *S. aureus* Lac*.

Group	Number of animals	Maggot weight g	Appl. volume μL	Drug conc. μmol L^{-1}	Dose μmol kg^{-1} BW	Dose mg kg^{-1} BW
Non-Infected	20	0.29 ± 0.07	20	200	-	-
PBS	20	0.30 ± 0.09	20	200	-	-
Octenidine	20	0.33 ± 0.06	20	200	12.31 ± 0.72	7.68 ± 0.45
Vancomycin	20	0.35 ± 0.06	20	200	11.56 ± 0.70	16.76 ± 1.01
Ciprofloxacin	20	0.30 ± 0.05	20	200	13.29 ± 0.65	5.13 ± 0.25
Amoxicillin	20	0.30 ± 0.08	20	200	13.22 ± 1.09	5.55 ± 0.46
Linezolid	20	0.35 ± 0.07	20	200	11.43 ± 0.85	3.86 ± 0.28
C$_{10}$	20	0.31 ± 0.06	20	200	13.03 ± 1.03	3.83 ± 0.23
C$_{12}$	20	0.33 ± 0.07	20	200	12.29 ± 0.80	3.96 ± 0.26

Table S 12 Animal survival of *Galleria mellonella* maggots post infection with multi-drug resistant *S. aureus* Lac*.

Group	6 h	12 h	18 h	24 h	30 h	36 h	42 h	48 h	60 h	72 h	84 h	96 h
Non-Infected	20	20	20	20	20	16	16	14	10	n.d.	n.d.	5
PBS	20	20	20	17	9	5	5	3	2	n.d.	n.d.	1
Octenidine	20	20	20	17	14	7	7	6	5	n.d.	n.d.	2
Vancomycin	20	20	20	20	20	19	19	19	17	n.d.	n.d.	9
Ciprofloxacin	20	20	20	15	11	10	10	7	5	n.d.	n.d.	4
Amoxicillin	20	18	18	13	8	6	5	2	2	n.d.	n.d.	0
Linezolid	20	20	20	16	13	9	9	8	8	n.d.	n.d.	4
C$_{10}$	20	20	20	19	16	11	10	8	5	n.d.	n.d.	5
C$_{12}$	20	20	20	18	14	8	5	4	1	n.d.	n.d.	1

n.d. (not determined)

Reverse Mutation assay Data

Table S 13 Revertant colonies count from Ames test of **C$_{10}$** on *S. typhimurium* TA 98 strain w/ or w/o metabolic activity following the plate incorporation method. Controls were DI water (negative), DMSO (solvent), 1 µg 2-aminoanthracene (positive w/ S9 Mix) and 5 µg 2-nitrofluorene (positive w/o S9 Mix). Concentrations are displayed as µg per agar plate. Geometrical mean und standard deviation (sdv) are calculated from three independent experiments (n=3). Mutation factor (MF) is calculated from mean values.

Compound	Revertant colonies w/ S9 Mix*			Revertant colonies w/o S9 Mix*		
	mean	sdv	MF	mean	sdv	MF
Negative control	65.3	9.5	0.90	99.3	4.5	1.27
Solvent control	72.7	8.3	1.00	78.0	3.5	1.00
Positive control	232.3	14.0	3.20	160.0	14.4	2.05
500.7 µg	0.3	0.6	0.00	0.0	0.0	0.00
158.5 µg	14.7	2.9	0.20	13.0	2.7	0.17
50.1 µg	53.0	7.0	0.73	79.7	8.6	1.02
15.9 µg	103.3	13.0	1.42	88.0	6.9	1.13
5.0 µg	110.0	17.3	1.51	88.7	20.0	1.14

* S9 Mix = 5% S9 liver homogenate mixture

Table S 14 Revertant colonies count from Ames test of **C$_{10}$** on *S. typhimurium* TA 100 strain w/ or w/o metabolic activity following the plate incorporation method. Controls were DI water (negative), DMSO (solvent), 1 µg 2-aminoanthracene (positive w/ S9 Mix) and 10 µg sodium azide (positive w/o S9 Mix). Concentrations are displayed as µg per agar plate. Geometrical mean und standard deviation (sdv) are calculated from three independent experiments (n=3). Mutation factor (MF) is calculated from mean values.

Compound	Revertant colonies w/ S9 Mix*			Revertant colonies w/o S9 Mix*		
	mean	sdv	MF	mean	sdv	MF
Negative control	128.3	26.7	1.01	162.7	20.2	1.22
Solvent control	126.7	16.0	1.00	133.7	26.7	1.00
Positive control	971.3	70.0	7.67	1749.3	390.7	13.09
500.7 µg	0.0	0.0	0.00	44.0	6.2	0.33
158.5 µg	81.3	14.1	0.64	92.7	8.7	0.69
50.1 µg	123.3	20.8	0.97	132.7	6.7	0.99
15.9 µg	122.7	12.2	0.97	150.3	12.9	1.12
5.0 µg	141.7	12.0	1.12	157.7	12.6	1.18

* S9 Mix = 5% S9 liver homogenate mixture

Table S 15 Revertant colonies count from Ames test of **C₁₀** on *S. typhimurium* TA 1535 strain w/ or w/o metabolic activity following the plate incorporation method. Controls were DI water (negative), DMSO (solvent), 3 µg 2-aminoanthracene (positive w/ S9 Mix) and 1.5 µg sodium azide (positive w/o S9 Mix). Concentrations are displayed as µg per agar plate. Geometrical mean und standard deviation (sdv) are calculated from three independent experiments (n=3). Mutation factor (MF) is calculated from mean values.

Compound	Revertant colonies w/ S9 Mix*			Revertant colonies w/o S9 Mix*		
	mean	sdv	MF	mean	sdv	MF
Negative control	8.3	1.2	0.96	11.7	2.9	1.17
Solvent control	8.7	1.5	1.00	10.0	2.7	1.00
Positive control	156.0	26.2	18.00	778.7	120.1	77.87
500.7 µg	0.0	0.0	0.00	0.0	0.0	0.00
158.5 µg	1.3	2.3	0.15	0.7	1.2	0.07
50.1 µg	4.3	1.2	0.50	6.0	1.0	0.60
15.9 µg	8.3	3.8	0.96	7.0	1.7	0.70
5.0 µg	8.0	1.0	0.92	9.7	2.1	0.97

* S9 Mix = 5% S9 liver homogenate mixture

Table S 16 Revertant colonies count from Ames test of **C₁₀** on *S. typhimurium* TA 1537 strain w/ or w/o metabolic activity following the plate incorporation method. Controls were DI water (negative), DMSO (solvent), 3 µg 2-aminoanthracene (positive w/ S9 Mix) and 50 µg 9-aminoacridine (positive w/o S9 Mix). Concentrations are displayed as µg per agar plate. Geometrical mean und standard deviation (sdv) are calculated from three independent experiments (n=3). Mutation factor (MF) is calculated from mean values.

Compound	Revertant colonies w/ S9 Mix*			Revertant colonies w/o S9 Mix*		
	mean	sdv	MF	mean	sdv	MF
Negative control	5.0	1.7	1.36	4.7	0.6	0.88
Solvent control	3.7	2.1	1.00	5.3	1.5	1.00
Positive control	84.0	8.7	22.91	142.0	50.5	26.63
500.7 µg	0.0	0.0	0.00	0.0	0.0	0.00
158.5 µg	1.3	0.6	0.36	0.0	0.0	0.00
50.1 µg	3.7	1.5	1.00	2.0	1.0	0.38
15.9 µg	3.0	2.7	0.82	2.7	1.2	0.50
5.0 µg	4.7	1.5	1.27	4.7	4.7	0.88

* S9 Mix = 5% S9 liver homogenate mixture

Table S 17 Revertant colonies count from Ames test of **C₁₀** on *E. coli* WP2 strain w/ or w/o metabolic activity following the plate incorporation method. Controls were DI water (negative), DMSO (solvent), 20 μg 2-aminoanthracene (positive w/ S9 Mix) and 0.05 μg methyl methanesulfonate (positive w/o S9 Mix). Concentrations are displayed as μg per agar plate. Geometrical mean und standard deviation (sdv) are calculated from three independent experiments (n=3). Mutation factor (MF) is calculated from mean values.

Compound	Revertant colonies w/ S9 Mix*			Revertant colonies w/o S9 Mix*		
	mean	sdv	MF	mean	sdv	MF
Negative control	128.0	5.0	1.12	113.7	3.5	1.30
Solvent control	114.7	21.4	1.00	87.7	5.7	1.00
Positive control	247.3	21.1	2.16	930.7	146.7	10.62
500.7 μg	79.7	15.2	0.69	59.7	16.3	0.68
158.5 μg	92.7	2.1	0.81	77.3	4.6	0.88
50.1 μg	110.7	1.5	0.97	84.0	8.0	0.96
15.9 μg	112.0	7.2	0.98	74.3	10.7	0.85
5.0 μg	107.3	6.7	0.94	65.0	8.9	0.74

* S9 Mix = 10% S9 liver homogenate mixture

Table S 18 Revertant colonies count from Ames test of **C₁₀** on *S. typhimurium* TA 98 strain w/ or w/o metabolic activity following the pre-incubation method. Controls were DI water (negative), DMSO (solvent), 1 μg 2-aminoanthracene (positive w/ S9 Mix) and 5 μg 2-nitrofluorene (positive w/o S9 Mix). Concentrations are displayed as μg per agar plate. Geometrical mean und standard deviation (sdv) are calculated from three independent experiments (n=3). Mutation factor (MF) is calculated from mean values.

Compound	Revertant colonies w/ S9 Mix*			Revertant colonies w/o S9 Mix*		
	mean	sdv	MF	mean	sdv	MF
Negative control	16.3	1.5	1.14	15.3	4.0	1.18
Solvent control	14.3	3.2	1.00	13.0	3.6	1.00
Positive control	271.3	68.4	18.93	472.0	24.3	36.31
500.7 μg	0.0	0.0	0.00	0.0	0.0	0.00
158.5 μg	6.0	3.61	0.42	1.3	1.2	0.10
50.1 μg	17.3	1.2	1.21	0.3	0.6	0.03
15.9 μg	18.3	6.8	1.28	6.0	3.6	0.46
5.0 μg	18.7	5.7	1.30	10.7	4.6	0.82

* S9 Mix = 5% S9 liver homogenate mixture

Table S 19 Revertant colonies count from Ames test of **C₁₀** on *S. typhimurium* TA 100 strain w/ or w/o metabolic activity following the pre-incubation method. Controls were DI water (negative), DMSO (solvent), 1 µg 2-aminoanthracene (positive w/ S9 Mix) and 10 µg sodium azide (positive w/o S9 Mix). Concentrations are displayed as µg per agar plate. Geometrical mean und standard deviation (sdv) are calculated from three independent experiments (n=3). Mutation factor (MF) is calculated from mean values.

Compound	Revertant colonies w/ S9 Mix*			Revertant colonies w/o S9 Mix*		
	mean	sdv	MF	mean	sdv	MF
Negative control	116.0	8.7	0.90	133.3	21.9	1.07
Solvent control	128.7	9.5	1.00	124.7	18.9	1.00
Positive control	542.7	23.4	4.22	1306.7	200.1	10.48
500.7 µg	6.0	8.7	0.05	0.7	1.2	0.01
158.5 µg	68.7	26.0	0.53	21.0	27.2	0.17
50.1 µg	131.3	11.0	1.02	49.0	35.1	0.39
15.9 µg	136.0	10.6	1.06	125.3	28.4	1.01
5.0 µg	102.0	3.5	0.79	152.0	37.5	1.22

* S9 Mix = 5% S9 liver homogenate mixture

Table S 20 Revertant colonies count from Ames test of **C₁₀** on *S. typhimurium* TA 1535 strain w/ or w/o metabolic activity following the pre-incubation method. Controls were DI water (negative), DMSO (solvent), 3 µg 2-aminoanthracene (positive w/ S9 Mix) and 1.5 µg sodium azide (positive w/o S9 Mix). Concentrations are displayed as µg per agar plate. Geometrical mean und standard deviation (sdv) are calculated from three independent experiments (n=3). Mutation factor (MF) is calculated from mean values.

Compound	Revertant colonies w/ S9 Mix*			Revertant colonies w/o S9 Mix*		
	mean	sdv	MF	mean	sdv	MF
Negative control	11.0	4.6	0.92	10.3	1.2	0.70
Solvent control	12.0	4.4	1.00	14.7	5.9	1.00
Positive control	174.0	29.6	14.50	342.7	6.1	23.36
500.7 µg	0.0	0.0	0.00	4.3	5.1	0.30
158.5 µg	3.3	0.6	0.28	1.7	2.9	0.11
50.1 µg	6.0	2.7	0.50	5.0	1.7	0.34
15.9 µg	9.7	2.1	0.81	6.3	3.2	0.43
5.0 µg	9.0	6.6	0.75	6.0	2.7	0.41

* S9 Mix = 5% S9 liver homogenate mixture

Table S 21 Revertant colonies count from Ames test of **C$_{10}$** on *S. typhimurium* TA 1537 strain w/ or w/o metabolic activity following the pre-incubation method. Controls were DI water (negative), DMSO (solvent), 3 µg 2-aminoanthracene (positive w/ S9 Mix) and 50 µg 9-aminoacridine (positive w/o S9 Mix). Concentrations are displayed as µg per agar plate. Geometrical mean und standard deviation (sdv) are calculated from three independent experiments (n=3). Mutation factor (MF) is calculated from mean values.

Compound	Revertant colonies w/ S9 Mix*			Revertant colonies w/o S9 Mix*		
	mean	sdv	MF	mean	sdv	MF
Negative control	3.7	2.5	1.38	2.3	2.3	0.70
Solvent control	2.7	1..2	1.00	3.3	2.1	1.00
Positive control	504.0	34.9	189.00	134.0	28.4	40.20
500.7 µg	0.0	0.0	0.00	0.0	0.0	0.00
158.5 µg	0.7	0.6	0.25	0.0	0.0	0.00
50.1 µg	3.7	0.6	1.38	0.3	0.6	0.10
15.9 µg	2.7	2.1	1.00	1.0	0.0	0.30
5.0 µg	4.3	1.2	1.63	2.7	2.1	0.80

* S9 Mix = 5% S9 liver homogenate mixture

Table S 22 Revertant colonies count from Ames test of **C$_{10}$** on *E. coli* WP2 strain w/ or w/o metabolic activity following the pre-incubation method. Controls were DI water (negative), DMSO (solvent), 20 µg 2-aminoanthracene (positive w/ S9 Mix) and 0.05 µg methyl methanesulfonate (positive w/o S9 Mix). Concentrations are displayed as µg per agar plate. Geometrical mean und standard deviation (sdv) are calculated from three independent experiments (n=3). Mutation factor (MF) is calculated from mean values.

Compound	Revertant colonies w/ S9 Mix*			Revertant colonies w/o S9 Mix*		
	mean	sdv	MF	mean	sdv	MF
Negative control	39.0	9.0	0.93	72.0	6.1	1.00
Solvent control	42.0	6.6	1.00	71.7	15.0	1.00
Positive control	84.0	7.0	2.00	2106.7	752.2	29.40
500.7 µg	26.7	4.6	0.63	45.0	8.9	0.63
158.5 µg	43.3	10.0	1.03	61.0	11.8	0.85
50.1 µg	42.7	8.4	1.02	56.7	3.1	0.79
15.9 µg	34.0	12.5	0.81	68.7	9.9	0.96
5.0 µg	31.7	4.0	0.75	61.3	16.7	0.86

* S9 Mix = 10% S9 liver homogenate mixture

Chapter IV: Pharmaceutical formulation using salt metathesis and 2D/3D printing techniques

Marco Saedtler[1], Niclas Förtig[1], Knut Ohlsen[2], Florian Sahr[3], Khaled Hussein[3], Markus Dachtler[3], Ulrike Holzgrabe[1] and Lorenz Meinel[1]*

[1]Institute of Pharmacy and Food Chemistry, University of Würzburg,
Am Hubland, DE-97074 Würzburg, Germany,

[2]Institute for Molecular Infection Biology (IMIB), University of Würzburg,
Josef-Schneider-Straße 2, DE-97080 Würzburg, Germany,

[3]Gen-Plus GmbH & Co. KG, Staffelseestraße 6, DE-81477 München, Germany

Unpublished manuscript

Introduction

Anacardic acids, a mixture of lipophilic phenolic acids, derived as main component from the shell of the cashew nut (*Anacardium occidentale*) or the shell of the pistachio nut (*Pistachia vera*) have shown to exhibit antimicrobial activity towards *Staphylococcus aureus* and other bacteria.[1-2] Synthetic variations of these compounds have been previously described mostly keeping their ortho-hydroxybenzoic acid partial structure while the lipophilic residue was altered.[3] A recent study synthesized a series of anacardic acid analogues, systematically increasing their alkyl-chain length and linking it to their antimicrobial activity, cytotoxicity as well as physicochemical properties identify two potential candidates for antibiotic drug development.[4] While both of these compounds demonstrated antibacterial activity, only one exhibited antibiofilm activity in subtherapeutic concentration. The aim of this study is to identify possible options for drug formulation for these antibiotic drug candidates. Namely, salt formation with poorly water-soluble fluoroquinolones on one side and utilization of 2D/3D printing techniques for antibacterial surface modifications on the other. Solid-state characterization techniques as well as antimicrobial assessment are applied to study the feasibility of both approaches.

Pharmaceutical formulation of new chemical entities (NCE) is a crucial step in pre-clinical as well as clinical research and development (R&D). Generally, the route of administration can be distinguished in local or systemic application, driven by the desired mode of action. If a disease can be located in a specific area of the body (e.g. localized bacterial infections or increased eye pressure), local treatment is often advantageous in terms of limited systemic circulation and reduced side effects. In contrast, systemic routes of administration have to be selected if the disease is not localized in a specific area or local application does not provide sufficient bioavailability. These administration strategies can be further distinguished into enteral and parenteral dosage forms.[5] Herein, enteral applications represent dosage forms that are administered orally and adsorbed via the human gastrointestinal tract and include solid granules, tablets and capsules as well as liquid solutions and suspensions. Favorable drug properties for enteral dosing are sufficient chemical stability, solubility in human intestinal fluids, permeability through the intestinal epithelia and absences of high hepatic clearance after absorption (first-pass effect).[6-8] While physicochemical properties can be tailored by e.g. salt formation or selection of an oral

dosage form which can increase oral bioavailability, metabolization during hepatic first-pass cannot be controlled via drug formulation. Therefore, if the oral bioavailability is not sufficient to achieve biorelevant drug concentrations in specific tissues, parenteral dosage forms are the administration route of choice. In these lines, the Ph. Eur. recognizes several dosage forms for parental application including solids, semisolids and liquids.[5] While liquid formulations e.g. solutions and suspensions for intramuscular (i.m.), intravenous (i.v.) or subcutaneous (s.c.) application represent the vast majority of parental administered drugs, semisolids (e.g. transdermal patches and suppositories) and solids (e.g. inhalative) contribute to a smaller extent to this class. However, some of these distinct dosage forms can inherit properties of both routes of administration including local and systemic effects. For example, suppositories are indeed adsorbed in the intestine but circumvent the first-pass effect as well as inhalative drugs can demonstrate local (β-sympathomimetics) or systemic (insulin) effects based on the applied drug.[9-10] In general, pharmaceutical dosage forms became more and more manifold in the recent decades as a result of increased high throughput screening (HTS) and computational screening for NCEs. In addition, more challenging classes of compounds ascended such as peptides, proteins or antibodies, so called new biological entities (NBE). In this context, HTS tended to favor more lipophilic candidates which often showed promising activity on the target but lacked sufficient aqueous solubility. It is estimated that up to 70% of these drug candidates are considered poorly water-soluble what entails problems related to the processability and bioavailability of a compound.[11] Several strategies try to improve the dissolution and kinetic solubility of these compounds including formulations utilizing polymer excipients, cyclodextrins or cosolvents. Looking on the healthcare market, salt formulations of the parent compound are by far the most popular strategy in the pharmaceutical development with an estimated volume of 50% for marketed solid drug formulations.[12] The advantage of a salt compared to its neutral parent drug is linked to a faster dissolution rate and often higher solubility in aqueous solutions.[13] In this context, the counterion, which often originated from a strong base or acid, influenced the pH in the aqueous boundary layer and thereby increased the dissolution rate of the drug. For some drugs this resulted in an enhanced kinetic solubility which can be stabilized by the counterion itself leading to a higher intestinal concentration and therefore oral bioavailability. However, salt formation is not applicable for all drug candidates as the molecule needs an ionizable (acidic or basic) position and as a general rule the difference in

pK_a between drug and counterion has to be at least 3 log units.[14] R&D facilities are constantly developing new technologies to cope the challenges related to pharmaceutical formulation.

Production of pharmaceutical drugs (e.g. tablets and capsules) is to this date a large-scale fabrication with batchwise approval and tracking of the final products. However, newly emerging technologies as 2D and 3D printing techniques are emphasizing a delocalized production. Several studies reported the utilization of these techniques to print biomaterials and tissues, biodegradable implants and active pharmaceutical ingredients (API).[15-19] The major advantage of this point of care production is the facilitated manufacturing process of personalized medicine. Drug doses, combinations of different drugs and exchange of excipients (i.e. ink) can contribute to tailored dosage forms for each individual patient and the decline of physical and chemical degradation during storage. Since genomic techniques and the knowledge of the human genome became more significant in the clinical medicine, interindividual genetic variability such as metabolic activity and its impact on pharmacokinetics is known to healthcare providers.[20] Despite normal metabolizers four different phenotypes are classified: poor, intermediate, rapid and ultra-rapid, increasing in their enzymatic activity from low to very fast, respectively.[21] If not considered correctly, rapid or poor metabolizers can exhibit strongly increased or reduced bioavailability jeopardizing the pharmacological treatment. Sub therapeutic drug concentrations at the side of action as well as increased side effects are possible results and dosage adjustment is advised. However, large-scale drug production does not provide flexible dosing and for most of the drugs 2D/3D printing in combination with a routinely performed pharmacogenetic testing can contribute to an appropriate medication. Several 3D printing techniques are state-of-the-art and commercially available. Briefly, the desired object is designed in a 3D model file using computer-aided design (CAD) software and printed layer by layer applying 3D printing. While seven main categories of 3D printing technologies have been described, only five of those have been utilized for pharmaceuticals so far; binder jet printing, stereolithography (SLA), semi-solid extrusion (SSE), selective laser sintering (SLS), and fused deposition modeling (FDM).[22] Briefly, for binder jet printing thin layers of binder solution are sprayed on a powder bed and dried to receive a solid specimen;[23] in SLA photosensitive material is polymerized from solution using UV light;[24] and material layers in a powder bed are sintered during SLS using high energy lasers.[25] FDM is a widely used technique, present in many commercially available 3D printers for industrial and private use.

Herein a polymeric filament is melted while passing a nozzle and placed on a printing bed via a movable robotic arm. Several drug-loaded polymers such as polylactic acid (PLA), polyvinyl alcohol (PVA), polyvinylpyrrolidone (PVP), methacrylate, hydroxypropyl cellulose and hydroxypropylmethyl cellulose acetate succinate (HPMCAS) have been printed using FDM.[19, 26-30] Several of these studies utilized the combination of hot melt extrusion (HME) to provide drug-loaded polymer filaments and printed these into 3D specimen via FDM. While the FDM technique is widely available and flexible in selection of printable polymers, the mandatory temperature during fabrication remains the main obstacle. Thermolabile APIs and excipients may undergo degradation during HME or FDM printing. However, to this date Spritam® a levetiracetam containing dosage form from Aprecia Pharmaceuticals is the only 3D printed tablet approved by the Food and Drug Administration (FDA).[31] Spritam® is a high dose, fast disintegrating tablet produced with the ZipDose® binder jet printing technology and approved for epilepsy treatment. Hereby individual doses as well as rapid dissolution due to its porous structure incorporate the main advantages of 3D printed dosage forms. In contrast to 3D printing, two-dimensional printing techniques do not incorporate the API into the dosage form while building up the structure but print it on a previously produced polymeric substrate with often a much higher throughput. Briefly, two different methods for 2D printing are available: roll-to-roll with direct contact between ink-transferring rolls and substrate as well as inkjet where ink is dispensed contact-free from a nozzle on the substrate.[32] While roll-to-roll transfers a pattern or relief on the substrate using several rolls to pick up, spread and print the ink, inkjet is differentiated into continuous and drop-on-demand (DOD) methods. Continuous inkjet printing is a high volume and speed application particularly used in textile printing, while DOD allows the dispensing of lower volumes with higher accuracy and has been investigated for its pharmaceutical application in several studies. DOD applications such as piezoelectric inkjet (PIJ), thermal inkjet (TIJ) and solenoid-valve based printing, have been utilized for API printing so far.[33] PIJ includes a piezoelectric transducer within the dispensing chamber which deforms when an electric current is applied forcing ink droplets out of the nozzle and refills the chamber when collapsing. In TIJ the piezoelectric transducer is replaced with a resistive element which heats up on electric current application, vaporizes solvent, drives out ink and refills when the solvent bubble deflates.[34] These processes take $3 - 10$ μs and dispense droplets with 2 - 180 pL. Higher volumes of 8-200 nL per droplet can be achieved when applying solenoid-valve based printing where an electromechanical solenoid controls

the volume of ink passing the nozzle.[33] It has to be noted, that even though temperatures up to 300 °C can be reached during TIJ printing, no degradation of human growth hormone or insulin was observed.[35] DOD printable inks have been identified as aqueous solutions or nano-suspensions (often mixtures with ethanol, propylene glycol or polymers) with a maximum viscosity of 20 mPa s and a favorable surface tension between 28 – 350 mN m⁻¹.[15, 33] Several studies report the application of PIJ and TIJ to print indomethacin, theophylline, prednisolone, caffeine, loperamide or rasagiline on different flat surfaces, ranging from regular paper sheets, porous polymeric substrates, topical patches to edible icing sheets.[34, 36-40] However, 2D printing is not limited to flat surfaces as a drug embedded in a polymeric controlled carrier could be printed on a 3D metal stent exhibiting higher drug loading efficacy compared to conventional dipping or spraying.[41] Even combinations of 3D and 2D printing have been studied when micro-stereolithography and PIJ were applied to yield miconazole coated microneedles or flexographic printing and PIJ were combined for riboflavin and propranolol dosage forms.[42-43] Low cost, high speed and accurate dosing of DOD printing techniques are major advantages compared to 3D techniques. Patient-to-patient individual dosing by the pharmacist for highly potent drugs with narrow therapeutic indices, combination of different APIs or drugs for paediatric use could be realized using polymeric substrates imprinted with drug-containing inks.[44] Oral thin films (OTF) provide this platform for point-of-care production of individual medication. Several names have been applied for these dosage forms by academia and , such as oral soluble film by the FDA, orodispersible film by the European Medicines Agency (EMA), thin film or thin strip.[45] OTF are designed to disintegrate in the mouth of the patient, targeting for oral application through the gastrointestinal tract or buccal administration often in combination with mucoadhesive properties of the film. In 2001 Pfizer launched Listerine® PocketPacks as breath freshener, which was followed by a benzocaine containing OTF in 2003 as well as ondansetron and risperidone in 2010.[45] However, no decentralized fabrication by pharmacies or other healthcare providers has been approved for OTF to this day and proper quality control is considered the bottleneck of such an approach. In this context, development of frugal analytical methods to secure content uniformity, purity and stability is key in this process and techniques such as near infrared (NIR) spectroscopy have already been applied and discussed for qualitative and quantitative quality control of 2D printed dosage forms.[38]

Increased prescription numbers and reckless use of antibiotics in industrial livestock farming led to an emerging variation of drug resistant bacterial strains often jeopardizing the treatment with antimicrobial agents in clinical use.[46] Recent findings report around 600,000 infections related to antibiotic-resistant bacteria, causing annually 30,000 deaths and 800,000 disability-adjusted life-years in the European Union.[47] Resistance mechanisms are manifold and spread from mutation in the antibiotic target to efflux pumps reducing the effective drug concentration at the side of action.[48] Besides these provoked mutations often caused by selective pressure on a bacterial population, biofilms as natural habitat for many strains is another obstacle which needs to be hurdled when treating bacterial infections.[49] Briefly, the biofilm matrix is a polymeric matrix build by extracellular polymeric substances (EPS) surrounding bacterial communities which mediates a whole series of advantages for the survival of its inhabitants. Besides the facilitated transfer of genetic material and therefore distribution of drug resistances, bacterial metabolism can be lower within the biofilm – decreasing the effectivity of antibiotics depending on bacterial proliferation – and the matrix structure itself protects the bacteria against desiccation as well as antibiotics. In these lines, reduced metabolic activity and persistence of bacteria was found to be the primary reason for insufficient treatment of *Pseudomonas aeruginosa* biofilms and to this point diagnosis and effective treatment of biofilm mediated infections is lacking.[50-51] Consequently, the healthcare professional has to select from a declining number of effective antibiotic drugs as the research and discovery of novel drug candidates stagnated during the last decades.[52] It is for these reasons that bacterial biofilms cause severe infections in cystic fibrosis patients, chronic wounds or invasive medical devices.[53-55] Briefly, it has been investigated that chronic wounds or ulcers do not heal due to insufficient eradication of infecting pathogens and 80% of persistent infections involve biofilm-forming bacteria.[56] The involvement of different bacterial strains in these diseases mostly depends on the infected tissue. While *P. aeruginosa* is mostly associated with pulmonary infections especially in cystic fibrosis patients it was only found in 50% of chronic wounds.[57] However, *Staphylococcus aureus* and *Enterococcus faecalis* were present in 90% and 70% of the cases, respectively. Essentially, *Staphylococci* have been identified as the most common biofilm-forming bacteria with *S. aureus* found in 76% of skin and soft-tissue-infections in U.S. emergency departments in 2004, 59% of which were considered multi-drug resistant staphylococcus aureus (MRSA) strains.[58-59] Treatment of these biofilm-associated infections can be difficult as the minimal biofilm inhibitory concentration (MBIC) can be up to 1000-

fold higher than the corresponding minimal inhibitory concentration (MIC) of planktonic growing strains.[60] Besides antibiotic prophylaxis (e.g. after surgery), early and aggressive antibiotic treatment in combination with following chronic suppressive therapy is often the last option in these infections.[61] Combinations of different antibiotic classes and selection of well-penetrating agents such as macrolides, lincosamides, tetracyclines, quinolones or sulfonamides is preferable.[62] However, new strategies for biofilm treatment are in development and in these lines quorum sensing (QS) has been already identified as potential target for antibacterial treatment. QS is an inter-bacterial communication system responding to local population density. This results in the expression of different genes and therefore change of phenotypes in the surrounding bacteria. Briefly, QS is present in gram-positive and gram-negative species and relies on the continuous secretion of signaling molecules by each individual bacterial cell. Signal molecules differ between the bacterial species and range from small molecules (e.g. homoserine lactones) to peptides enabling a distinctive recognition of a local bacterial population density. Autoinducer cascades detect the change in concentration and subsequently regulate gene expression. QS influence on virulence factors, motility, adhesion, production of EPS and therefore biofilm formation has already been studied and consequently, QS inhibition is currently under investigation.[63] Several natural products secreted by plants such as rosmarinic acid, unsaturated fatty acids or flavonoids and even bacteria themselves were found to interfere with the QS system of different bacterial species and prevent colonization or expression of virulence factors.[64-68] Another strategy for biofilm-associated infections which is already in clinical application addresses the biofilm-matrix itself by disrupting its structure with surfactant-like molecules. In wound management the cleaning is a routinely applied practice and aims to remove debris and bacteria with liquid cleansers to enable healing processes and avoid infections. Cleaning with saline is often considered insufficient especially when biofilms are expected and cleansers with antiseptics such as polyhexamethylene biguanide or chlorhexidine are applied.[69] Direct comparison in the care of chronic wounds between cleaning with normal saline and propylbetaine-polihexanide revealed reduced inflammatory signs and accelerated healing for patients treated with surfactant containing solution.[70] In these lines, several studies report the disruption of bacterial biofilms treated with surfactants from natural or synthetical origin and the prevention of biofilm formation when surfactant based wound dressings were applied.[4, 71-74] Therefore, combination of biofilm disruption by surfactant-

like molecules and antibiotic treatment can be a promising strategy in tackling biofilm infections.

Invasive medical devices indwelling the human body and the associated stay in health care facilities are a major contributor to nosocomial infections in the industrial world. Recent estimations state that 722,000 health care facility acquired infections lead to 75,000 deaths in the US alone and at least 25% of those are directly associated to implanted medical devices.[75] Central venous catheters (CVC) as part of these cases lead to approximate 80,000 catheter-related bloodstream infections with a mortality rate of 12-25% and estimated costs up to 2,3 billion annually.[76] In total more than 30 million urinary tract catheters and 5 million CVCs are inserted each year with infection rates between 10-30% and 3-8%, respectively.[55] These numbers while already indicating the sheer number of implanted medical devices are projected to grow even more in the next decades and therefore the number of device-related infections will increase too. Compared to 2005, the number of total hip and total knee arthroplasties in the US is estimated to grow until 2030 by 174% to 570,000 and 673% to 3,48 million surgeries, respectively.[77] Especially, bacterial biofilm formation and the presence of MRSA strains is hampering the antibiotic treatment and removal of the medical device is often necessary.[78-79] Two factors particularly drive *S. aureus* biofilm infections: foreign bodies and therefore implanted medical devices were found to downregulate bactericidal effects of leukocytes as well as *S. aureus* itself polarizing macrophages towards an anti-inflammatory phenotype, evading immune response and significantly increasing biofilm-associated infections.[80-81] It is for these reasons and an ideal surface for bacterial colonization that device-related infections became a major healthcare problem with the increasing usage of vascular and urinary catheters, stents, endotracheal tubes, prosthetic joints and orthopedic implants in general. Several strategies have already been developed and applied to minimize the risk for an indwelling medical device. While diabetes, liver diseases and an unhealthy lifestyle were identified as patient-related risk factors most of these infections are related to the surgery itself.[82] Increased hygiene standards in combination with an antibiotic prophylaxis provide an effective measure especially as most device-related infections are acquired while the patient is still cared for in a professional healthcare facility. However, biofilm infections are difficult to diagnose and eradicate often leading to insufficient antibiotic treatment and removal of the foreign body (not limited to medical devices e.g. biliary and urinary stones). If this is not applicable, the biofilm burden

has to be lowered with an antibiotic treatment followed by a continuous suppressing therapy.[62] The usage of high dosed rifampicin, vancomycin or linezolid in combination with a pathogen specific antibiotic for 2-6 weeks followed by rifampicin together with a companion drug such as fluoroquinolones, co-trimoxazole or doxycycline for 3-6 months can be an adequate therapy.[82] Avoiding long-term antibiotic therapies, the indwelling medical device itself can be modified to prevent microbial adhesion (antifouling) or eliminate adhering bacteria (antimicrobial). While the latter relies on the presence of contact-killing moieties on the surface or release of antibacterial agents, antifouling prevents the bacterial colonization by steric repulsion e.g. polyethylene glycol (PEG), by low energy surfaces e.g. polytetrafluoroethylene (PTFE) or polydimethylsiloxane (PDMS) or passivation of the surface with albumin or heparin.[55] Antimicrobial agents include silver compounds or ions, biocompatible disinfectants like chlorhexidine or antibiotics such as rifampicin or minocycline which can be coated to the surface or incorporated into the polymeric medical device. Several processing techniques are reported to obtain antifouling and antimicrobial properties. (i) Physical adsorption often achieved by spay-coating or dip-coating with a biocide-containing solution, (ii) impregnation with thermostable agents by melt extrusion or thermolabile agents by swelling in a suitable solvent, (iii) covalent attachment to the surface e.g. heparin or (iv) bulk incorporation by covalently attaching functionalized sidechains to a polymeric backbone.[55] In these lines, polymer functionalization not only yielded passively repelling hydrophilic surfaces but contact-active materials where quaternary ammonium functions disrupt the bacterial cell wall/membrane.[83] While hydrophilic/heparin coated surfaces only showed modest clinical success, antibiotics coated prostheses as well as antibiotic loaded acrylic based cements showed promising results in animal studies and clinical application, respectively.[51, 84] Thus, functionalized surfaces may overcome antibiotic resistances acquired during long-term antibiotic prophylaxis and identification of appropriate strategies for polymeric materials is key in this context. Materials for indwelling medical devices are manifold and reach from mineral based bone substituents to metals in orthopedic implants and polymers in stents and catheters. Focusing on biocompatible polymeric materials reveals a variety of polymers including but not limited to synthetical derived polyethylene (PE), polyethylene terephthalate (PET), polyvinyl chloride (PVC), polylactic acid (PLA), polyvinyl alcohol (PVA), polyacrylate and polystyrene as well as natural polymers such as collagen or chitosan.[85-86] These synthetic polymers differ in their mechanical and chemical properties as well as their ability to undergo

degradation in the human body leading to biostable polymeric joints on the one side and decomposing surgical suture material on the other. In these lines, biocompatibility of the material and its leachables is often the main challenge in developing and approving new synthetical polymers and inadequate biocompatibility can cause inflammation and encapsulation of the foreign body.[86] In the last decades PLA and its copolymers with polyglycolic acid (PGA) became an inexpensive and renewable material. Its relatively dimensional stability, biocompatibility, biodegradability and non-toxicity of degradation products paved its way for FDA approval for clinical use and application in orthopedic devices, tissue engineering, drug carriers and stents so far.[87-88] Furthermore, PLA demonstrates a relatively low meting point of 150-190 °C with high thermal stability making it one of the most used polymer filaments in 3D printing technologies. Exploring options for biocompatible surface modifications of PLA is therefore a promising strategy which can elaborate its usage in indwelling medical devices.

Materials

Endo Agar powder was purchased from Sigma Aldrich (Schnelldorf, Germany). Müller-Hinton-Bouillon (MH) powder was purchased from Carl Roth GmbH + Co. KG (Karlsruhe, Germany). Hexadeuterio-dimethyl sulfoxide (DMSO-d_6, 99.8% D) was purchased from Euriso-top (Saarbrücken, Germany). Ethanol absolute, methanol, isopropyl alcohol, acetone, dimethyl sulfoxide, ethyl acetate, ciprofloxacin and ciprofloxacin hydrochloride monohydrate were purchased from Sigma Aldrich. Acetonitrile, chloroform and n-hexane were purchased from VWR (Darmstadt, Germany). Levofloxacin and norfloxacin were purchased from Tokyo Chemical Industry Co. (Tokyo, Japan). Levofloxacin hydrochloride monohydrate was purchased from Biomol GmbH (Hamburg, Germany). Deionized water was obtained from in-house Merck Millipore water purification system (Darmstadt, Germany). Other chemicals and reagents used within this study were purchased from Sigma Aldrich if not noted otherwise. Bacterial strains used within this study are summarized in **Table 1**.

Table 1 Bacterial strains used for Zone of Inhibition Test.

Species	Code	Source	Medium	Comment
Staphylococcus aureus	JE2	Clinical isolate	MH	MRSA
Staphylococcus aureus	Lac*	Clinical isolate	MH	MRSA
Staphylococcus aureus	ST228	Clinical isolate	MH	Biofilm-forming

MH = Müller-Hinton Bouillon

Methods

Salt metathesis I

Salt formation experiments were conducted using different metathesis in solution approaches. Briefly, 0.30 ± 0.02 mmol of the respective counterion was weighted into a 50 mL round bottom flask. An equimolar amount of levofloxacin was added, and the two substances were suspended in 20 mL methanol 30% (v/v). The suspension was heated while stirring for 1 h at 70 °C under reflux cooling; all solid particles dissolved, and a yellow solution was formed. The heater was turned off, and the reaction was allowed to slowly cool to room temperature; the yellowish solution changed to colorless and a fine white solid precipitated. The resulting suspension was stored at 4 °C over night, filtered through a P3 borosilicate Nutsche filter from Neubert-Glas (Geschwenda, Germany) on the next morning and dried at 40 °C *in vacuo* for 24 h. Products were stored in a desiccator until further usage.

Salt metathesis II

Recrystallisation was performed in ethanol 70% (v/v) with the products obtained by the salt metathesis I procedure. Briefly, 10 mg of the respective product was weighted into a 50 mL round bottom flask and 5-10 mL ethanol 70% (v/v) was added. The suspension was heated while stirring for 30 min at 80 °C under reflux cooling; all solid particles dissolved, and a yellow solution was formed. The solution was hot-filtered through a P3 borosilicate Nutsche filter, allowed to cool to room temperature and stored at 4 °C over night. On the next day the white precipitated was filtered and dried at 40 °C *in vacuo* for 5 days. Products were stored in a desiccator until further usage.

Salt metathesis III

Salt metathesis was performed using levofloxacin hydrochloride, norfloxacin hydrochloride or ciprofloxacin hydrochloride in combination with SAE180 potassium salt or SAE196 potassium salt in pH adjusted deionized water. Briefly, 100.84 ± 1.09 mg of levofloxacin hydrochloride monohydrate, norfloxacin hydrochloride or ciprofloxacin hydrochloride monohydrate were weighted into a 50 mL round bottom flask and 5 mL deionized water were added. All fluoroquinolone drugs completely dissolved and formed a yellow solution. An equimolar amount of SAE180 potassium salt or SAE196 potassium salt was dissolved in 2 mL deionized water and added dropwise to the reaction while constantly stirring at room temperature. 13 mL deionized water were added, and the pH was adjusted using 0.5 mol L^{-1} HCl to pH 5.00 ± 0.05 for levofloxacin and ciprofloxacin metathesis and pH 6.00 ± 0.05 for norfloxacin metathesis, respectively. A white solid precipitated and the solution was stirred for 1 h at room temperature before the suspension was filtered through a P3 borosilicate Nutsche filter. The residue was dried at 40 °C *in vacuo* for 5 days. Products were stored in a desiccator until further usage.

Solubility screening

Solubility was assessed in deionized water, methanol, ethanol, ethanol 70% (v/v), ethanol 50% (v/v), ethanol 30% (v/v), isopropyl alcohol, acetone, dimethyl sulfoxide, ethyl acetate, acetonitrile, diethyl ether and n-hexane. Briefly, 2.03 ± 0.06 mg were placed in a 2 mL reaction vial from Eppendorf (Hamburg, Germany) and a previously calculated volume of solvent was added. The sample was vortexed for 1 min in and the vial was checked for the presence of solid compound. If the solution was free of visible particles the solubility was noted otherwise solid was present, another aliquot of solvent was added, and the procedure was repeated until a clear solution was observed. Tested concentrations were 50, 40, 30, 20, 10, 5, 2.5 and 1 mg mL^{-1}.

3D-Print of Polylactic acid (PLA) and Polyvinyl alcohol (PVA) scaffolds

PLA and PVA scaffolds were 3D printed and provided for printing experiments by Gen-Plus GmbH & Co. KG (Munich, Germany) using the fused filament fabrication (FFF) technique (**Figure 1A**). Briefly, cylindrical tablets were designed as a CAD model in Fusion 360 software from AutoDesk (San Rafael, CA) with 5 mm in diameter, 0.8 mm in height and a

diagonal infill with 90 ° rotation between individual layers (**Figure 1B**). The obtained model was sliced horizontal cross-sectional using Simplify3D from Simplify3D Software (Cincinnati, OH). PLA or PVA scaffolds were printed using the sliced model and Raise3D Premium PLA Filament or Premium PVA Filament, both 1.75 mm in thickness from Raise3D (Irvine, CA) on a Raise3D N2 printer, respectively. The printer was equipped with a 0.4 mm nozzle and operated at an extruder temperature of 200 °C on a 60 °C printing bed. Extrusion multiplier was set to 0.90 and infill was set to 60, resulting in a printing thickness of 0.4 mm. After printing products were stored in a sealed plastic bag at ambient conditions until further usage.
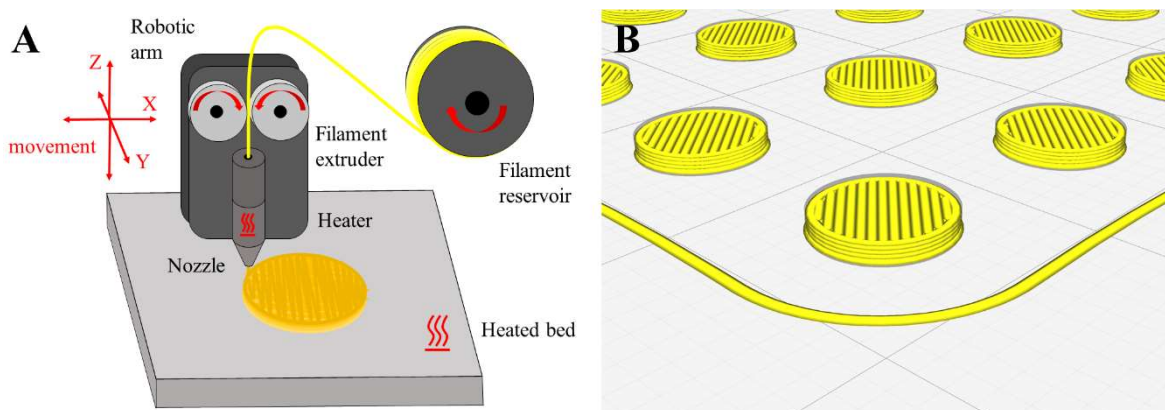

Figure 1 Schematic model of a fused deposition modeling (FDM) 3D printer. The Polymer filament is actively transported by the extruder, melted within the temperature-controlled heater and printed through the nozzle on a heated printing bed. The melted polymer is placed by positioning of the robotic arm.

Oral thin film (OTF) preparation

Oral thin films (OTF) were produced and provided for printing experiments by Gen-Plus GmbH & Co. KG (Munich, Germany). Briefly, OTF were prepared using a MBCD 1.3 film coating machine (Optimags Dr. Zimmermann GmbH, Karlsruhe, Germany) operated with the MBCD 1.3 Build 2001 software from the manufacturer. 30 g Sorbitol were dissolved in 420 mL 70% (v/v) ethanol and 150 g Opadry® II white was slowly added under stirring. The resulting dispersion was stored overnight on a roll mixer (Ingenieurbüro CAT, Staufen, Germany) at 20 RPM and used on the next day. The dispersion was pumped at 0.098 g/s using the included gear pump and dispensed on a PET-Primeliner™ 78 HL, 75 μm foil (Loparex Holding B.V., Apeldoorn, The Netherlands) which was transported at 0.05 m/min passing the dispenser. The homogenous coated foil was dried at 60 °C in the following drying zone and stored in a sealed plastic bag at RT until further usage.

Drug print using nano dispenser system

Drug prints on OTF and PLA scaffolds were performed using a customized sciDROP NANO dispensing system from SCIENION AG (Dortmund, Germany) operated with the sciDROP NANO software from the same supplier (**Figure 2**). The system consisted of four channels, each equipped with a 50 mL bulk solution container connected to a borosilicate glass nozzle and a solenoid valve, adjusted to dispense ink volumes between $50 - 200$ nL drop^{-1}. The software calculated the droplet volumes and standard deviation before printing by measuring the diameter and size of 20 droplets at a separate measuring station equipped with a live camera. Droplet volume mean was 69 ± 3 nL, respectively. The nozzles were mounted on a robotic arm which operated in two dimensions with a positioning accuracy of 10 μm. The X Offset was -150 and the Y Offset was -100, respectively. Nozzles were washed and flushed with deionized water using a washing station connected to a disposal flask. During printing only channel one was used and loaded with at least 25 mL of drug containing ethanol 70% (v/v) ink in a 50 mL reservoir container. A pressure of 2.8. a.u. was applied on the ink using an air compressor and the solenoid valve pulse was 200 μs with a frequency of 40 s^{-1}. Two inks were prepared and used within a day, 5 mg mL^{-1} SAE180 in ethanol 70% (v/v) and 5 mg mL^{-1} ciprofloxacin HCl in ethanol 70% (v/v); no incompatibilities between the ink and polylactic acid or oral thin films were observed in preliminary experiments.
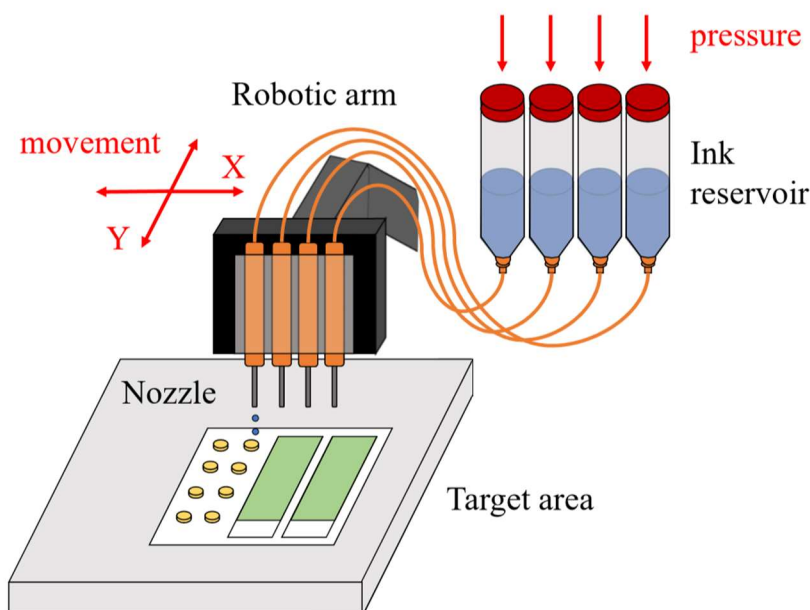

Figure 2 Schematic model of the customized sciDROP NANO dispensing system used for printing of drug loaded ethanol 70% (v/v) ink on oral thin films and 3D-printed polylactic acid scaffolds.

Drug print on PLA scaffolds (nano dispenser)

The nano dispenser sciDROP NANO was used to print drug loaded ink on PLA scaffolds with a surface of 39 mm² per scaffold. Briefly, a template was designed for PLA scaffolds (d = 5 mm) with a batch size of 24 (**Figure 3**; left). Target field was defined within the operating software; field offset was 21151 µm for X and 24860 µm for Y and with a distance of 0.5 mm between each droplet the field was divided into 141 x 91 spots. 60 spots per scaffold were selected for dispensing of one droplet per spot (**Figure 3**; right). After application of drug loaded ink, the scaffolds were allowed to dry at room temperature for 6 min. The procedure was repeated if a second or third layer had to be applied and the final products were stored in a sealed plastic bag at room temperature.
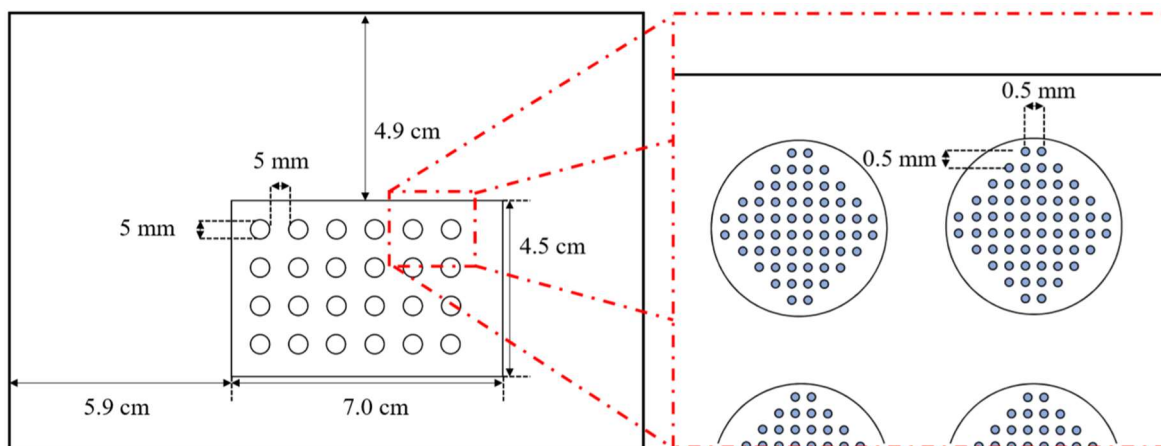

Figure 3 (left) Template used for 2D printing on PLA scaffolds with the nano dispenser. Circles represent scaffold positions on the target field during printing. (right) Magnification with target field setting for dispensing of 60 droplets (blue) per scaffold.

Drug print on OTF (nano dispenser)

The nano dispenser sciDROP NANO was used to print drug loaded ink on OTF with a surface of 800 mm² per thin film. Briefly, a template was designed for OTF (h = 40 mm, l = 20 mm) with a batch size of 3 (**Figure 4**; left). Target field was defined within the operating software; field offset was 21151 µm for X and 24860 µm for Y and with a distance of 1 mm between each droplet the field was divided into 71 x 46 spots. 800 spots per OTF were selected for dispensing of one droplet per spot (**Figure 4**; right). After application of drug loaded ink, the thin films were allowed to dry at room temperature for 10 min. The procedure was repeated if a second or third layer had to be applied and the final products were stored in a sealed plastic bag at room temperature.
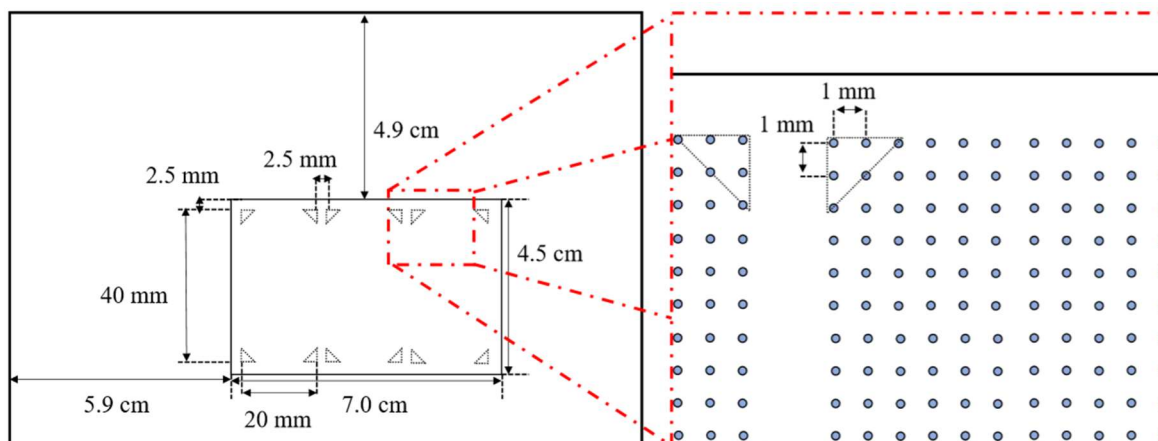
Figure 4 (left) Template used for 2D printing on OTF with the nano dispenser. Triangles represent OTF positions on the target field during printing. (right) Magnification with target field setting for dispensing of 800 droplets (blue) per OTF.

Drug print on OTF (inkjet printer)

OTF were printed using an Epson XP-760 inkjet printer (Epson, Suwa, Japan) operated by Windows 7 and Microsoft Office 2016 (version 16.0) both from Microsoft (Redmond, WA). A set of empty CYMK (cyan, magenta, yellow and black) ink cartridges obtained from Colortank (Hamburg, Germany), suitable for the Epson XP-760, was provided by Gen-Plus GmbH & Co. KG (Munich. Germany) and filled with drug loaded solutions. Cyan was 5 mg mL^{-1} ciprofloxacin hydrochloride in 70% (v/v) ethanol, yellow was 5 mg mL^{-1} SAE180 in 70% (v/v) ethanol and black was 70% (v/v) ethanol without drug. The magenta cartridge was filled with a drug candidate in ethanol which is not part of this report. Four colors were defined representing combinations of these solutions (**Table 2**) and their corresponding CYMK color codes in percentual composition were translated to RGB (red, green, blue) additive color model using Adobe Illustrator 9.0 (Adobe Inc., San José, CA).

Table 2 Combinations of ink with their corresponding color, CYMK and RGB codes used during inkjet printing on OTF.

	Color		C %	Y %	M %	K %	RGB
Ciprofloxacin	Cyan		100	0	0	0	(0,255,255)
SAE180	Yellow		0	100	0	0	(255,255,0)
SAE180 + CIP	Green		50	50	0	0	(127,255,127)

	Color		C %	Y %	M %	K %	RGB
Control	Black	■	0	0	0	100	(0,0,0)

CIP = ciprofloxacin hydrochloride

Polyethylene (PE) foil carrying the OTF matrix was cut into 29.7 cm long bands to match the length of a DIN A4 page. The PE foil (14 cm wide) with a central lane of 8 cm width OTF matrix (**Figure 5A**) was single placed into the top loading of the inkjet printer and color-printed using PowerPoint schematics (**Figure 5B**). Five drug combinations were prepared (**Table 3**). If several layers were applied, OTF pages were dried for 1 min in between. The resulting OTF pages were sealed in plastic bags and store at room temperature until further usage.

Table 3 Drug combinations printed on OTF matrix pages using an Epson XP-760 inkjet printer.

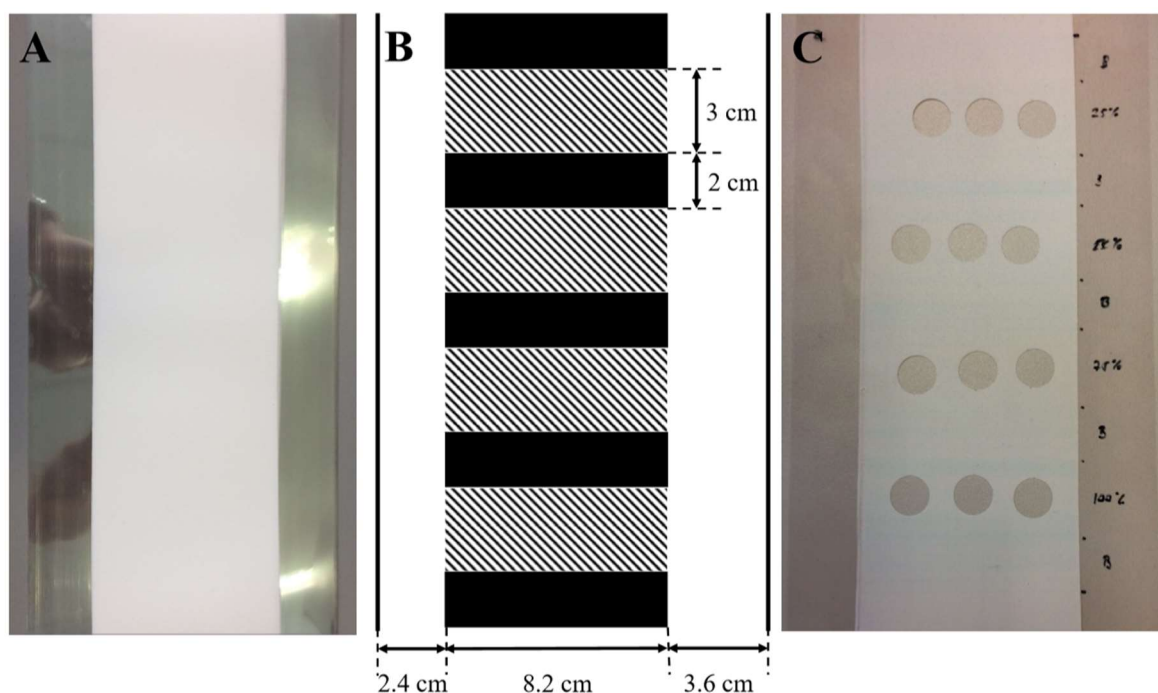|	Layer 1	Layer 2	Layer 3
SAE180	Yellow (255,255,0)	-	-
SAE180 x2	Yellow (255,255,0)	Yellow (255,255,0)	-
SAE180 + CIP	Green (127,255,127)	Green (127,255,127)	-
SAE180 x2 + CIP	Green (127,255,127)	Green (127,255,127)	Yellow (255, 255, 0)
CIP	Cyan (0, 255, 255)	-	-

CIP = ciprofloxacin hydrochloride

Figure 5 (A) Original picture of the DIN A4 length cut OTF-PE foil. (B) Schematic printer setting for the inkjet print. The hatched area represents drug loaded OTF either carrying SAE180 and ciprofloxacin hydrochloride alone or in combination; The black area represents control OTF with ethanol 70% (v/v). (C) Representative picture of cutouts from printed OTF for quantitative HPLC analysis.

Microscopic characterization

Representative microscopic pictures of PLA and OTF specimens were recorded using a VHX-5000 (System version 1.04) from Keyence (Osaka, Japan) equipped with a 20-200x magnification VH-Z20R/W/T objective and operated with the VHX-5000 communication software (version 1.6.1.0). Pictures were taken w/ or w/o polarization filters equipped on the instrument. Height analysis was performed as described by the manufacturer and displayed as heatmap by the software.

High-Pressure Liquid Chromatography (HPLC)

Quantification of SAE180 and ciprofloxacin printed on OTF and PLA scaffolds was performed via UV-coupled HPLC. Samples were prepared prior measurement by extracting the drug from the specimen. Briefly, PLA scaffolds were placed in a 1.5 mL reaction vial (Eppendorf, Hamburg, Germany) and 0.5 mL chloroform/methanol 90:10 (v/v) were added. After disintegration, the resulting suspension was centrifuged in a Fresco 17 Centrifuge (Thermo Scientific, Waltham, MA) at 13,300 rpm for 15 min. The supernatant was carefully withdrawn and analyzed. For analysis of the OTF, circular specimens were cut out from the

thin films using a 6/15 mm in diameter stamp punch. OTF samples printed with PML were 6 mm in diameter and samples printed with the inkjet printer were 15 mm in diameter, because of their lower loading. Circular specimens were placed in a 1.5 mL reaction vial, 1 mL ethanol/DI water 70:30 (v/v) was added and sonicated for 30 min. The resulting suspension was centrifuged at 13,300 rpm for 15 min und the supernatant was carefully withdrawn and analyzed.

HPLC analysis was performed on an Agilent Technologies 1200 series system (Agilent Technologies, Waldbronn, Germany) consisting of an autosampler G1329A, degasser G1322A, quaternary pump G1311A, column oven G1316A and variable wavelength UV detector G13148. The HPLC system was operated and chromatograms recorded and integrated by the ChemStation® software from Agilent. Knauer Eurosphere II 100-5 C18H 250x4.6 mm column from Knauer (Berlin, Germany) was used at 30 °C with of flow of 1 mL/min and 0.005 mL injection volume. Mobile phase A was DI water + 0.1% (v/v) trifluoroacetic acid (TFA) and mobile phase B was acetonitrile + 0.1% (v/v) TFA. For SAE180, gradient method started at 80% B for 6 min, increased to 90% B in 1 min, hold time by 13 min at 90% B and back to 80% B in 1 min followed by equilibration for 14 min at 80% B; detection wavelength was set to 254 nm. For ciprofloxacin OTF samples, gradient method started at 20% B for 15 min, increased to 90%B in 5 min, hold time by 10 min at 90% B and back to 20% B in 5 min followed by equilibration at 20% B for 10 min. For ciprofloxacin PLA samples, gradient method started at 25% B for 15 min, increased to 90%B in 5 min, hold time by 10 min at 90% B and back to 25% B in 5 min followed by equilibration at 25% B for 10 min. Detection wavelength for both ciprofloxacin methods was set to 278 nm.

Nuclear Magnetic Resonance (NMR)

Nuclear Magnetic Resonance method was adapted from a previous study.[89] Briefly, ^{1}H NMR measurements were performed on a Bruker Avance 400 MHz spectrometer (Karlsruhe, Germany) operating at 400.13 MHz with a BBO BB-H 5 mm probe head. Processing was done with the TopSpin 3.0 software from Bruker. The temperature was adjusted by a BCU-05 (Bruker) temperature control unit. Compounds were dissolved in DMSO-d_6 with and 0.7 mL with an approximate concentration of 5 mg mL^{-1} were filled into standard 5 mm NMR tubes. Spectra were recorded using the following parameters: 16 scans at a temperature of

300 K, 30° flip angle, spectral width of 20.552 ppm and a transmitter offset of 6.175 ppm. The acquisition time was set to 3.985 sec, the relaxation delay to 1.0 sec with a collection of 64,000 data points at a sample spinning frequency of 20 Hz. Processing parameters were set to an exponential line broadening window function of 0.3 Hz, a manual phase correction and an automatic baseline correction. The spectra were referenced to the residual solvent signal of DMSO-d_6 at 2.54 ppm.[90]

Calculation of ionicity

Degree of ionicity was calculated following equation 1 and $\Delta\delta$ H-proton from levofloxacin.[91] Briefly, the ^{1}H NMR chemical shifts in ppm of the levofloxacin N-methylene signal (piperazine residue; **Figure 27**) between neutral levofloxacin (δ_{Levo}; 2.23 ppm, s, 3H), levofloxacin hydrochloride (δ_{HCl}; 2.84 ppm, s, 3H) and the salt (δ_S) were used to calculate the ionization of the product (**Equation 1**).

$$\text{Ionicity [\%]} = \left[\frac{\delta_{HCl} - \delta_S}{\delta_{HCl} - \delta_{Levo}}\right] * 100 \tag{1}$$

δ_{Levo}	-	chemical shift (δ H-proton) levofloxacin
δ_{Ref}	-	chemical shift (δ H-proton) levofloxacin hydrochloride
δ_S	-	chemical shift (δ H-proton) salt

Differential Scanning Calorimetry (DSC)

Differential Scanning Calorimetry method was adapted from a previous study.[4] Briefly, DSC measurements were performed on a DSC 8000 from Perkin Elmer (Waltham, MA). 3 – 5 mg substance were weighed into aluminum pans from Perkin Elmer with a pinhole in the lid and analyzed at a scanning rate (heating and cooling rate) of 20 °C min^{-1} from -50 °C to 200 °C. The mass of the crucible was noted before and after the experiment to calculate any loss of mass during the process. Measurement of one cycle was performed.

X-Ray Powder Diffraction (XRPD)

X-Ray powder diffraction method was adapted from a previous study.[4] Briefly, XRD was measured on a silicon single crystal holder and analyzed with a Bruker Discover D8 powder diffractometer (Karlsruhe, Germany) using Cu-Kα radiation (unsplit Kα_1+Kα_2 doublet, mean wavelength λ = 154.19 pm) at 40 mA and 40 kV, a focusing Goebel mirror and a 1.0 mm microfocus alignment (1.0 mm pinhole with 1.0 mm snout). The scattered X-ray beam

went through a receiving slit with 7.5 mm opening, a 2.5° axial Soller slit and detection was performed with a LynxEye-1D-Detector (Bruker AXS) using 192 channels. Measurements were done in reflection geometry in coupled two theta/theta mode with a step size of 0.025° in 2θ and 0.25 s measurement time per step in the range of 5 – 60° (2θ). Data collection and processing was carried out with the software packages DIFFRAC.Suite (V2 2.2.69.0) and DIFFRAC.EVA 2.1 from Bruker.

Agar Diffusion Test

For the Agar Diffusion Test Agar plates were prepared by suspending 21 g Müller-Hinton (MH) Bouillon and 15 g Endo Agar in 1 L deionized water. The resulting suspension was autoclaved at 121 °C for 15 min and the solution was stored in a 50 °C water bath till further usage. Approximately 25 mL of the hot solution were poured into 96 x 16 mm petri dishes (nerbe plus, Winsen, Germany) and were allowed to cool down to room temperature in a laminar flow bench. After hardening of the agar, plates were stored at 4 °C and used within 3 weeks.

Bacteria were stored at -80 °C in MH Bouillon containing 20% (v/v) glycerol, streaked out on MH agar plates before testing and used within two weeks to prevent mutation. A colony was picked on the day before the experiment, transferred into approximate 30 mL MH Bouillon and cultured overnight at 37 °C. On the next morning optical density of the overnight culture was measured at 600 nm (OD_{600}) on an Eppendorf Biohotometerplus (Eppendorf, Hamburg, Germany), adjusted to OD_{600} = 0.05 with sterile MH Bouillon and used within 30 min. Working in a laminar flow bench, stored MH agar plates were allowed to prewarm at room temperature and dry till condensed water evaporated completely. 200 µL of the bacterial suspension were placed on the agar plates and spread by rotation of the plate using a Drigalski spatula (**Figure 6A**). Excessive Bouillon was allowed to evaporate for 5 min and a maximum number of 4 test specimen were placed on the agar plates (**Figure 6B**). Positive control was Oxoid Vancomycin Antimicrobial Susceptibility Disk (ThermoFisher Scientific, Waltham, MA) and negative controls were untreated and ethanol 70% (v/v) treated OTF or PLA specimen. The agar plates were cultured overnight at 37 °C and the zone of inhibition was measured on the next day. Following guidelines, inhibition was defined as absence of visible bacterial growth while, while additionally a zone of reduced bacterial growth was noted if visible.
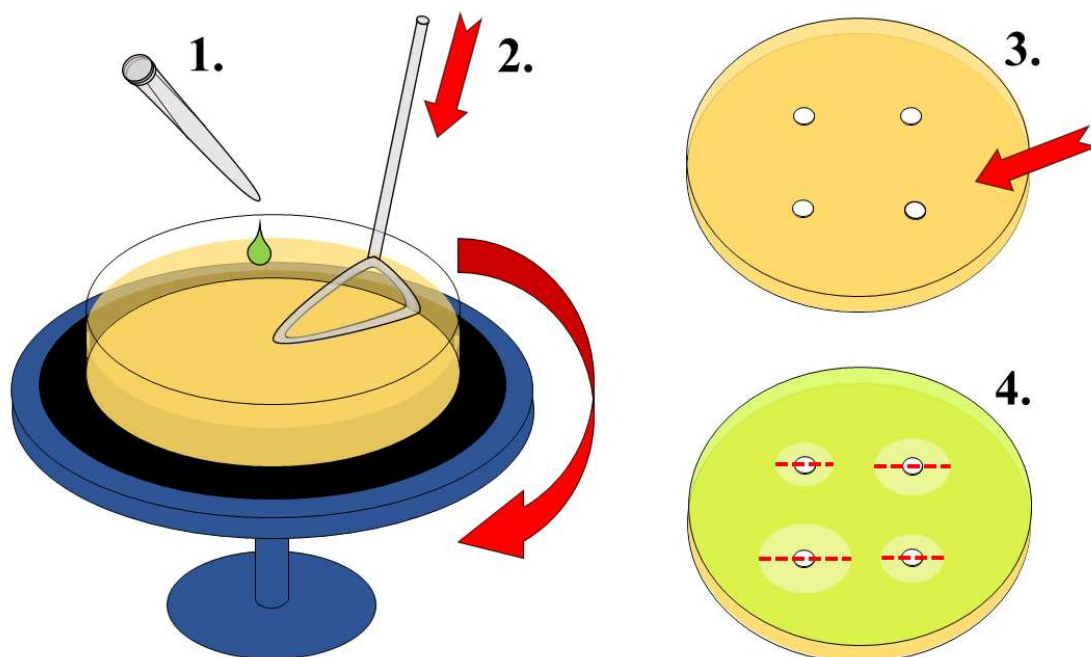
Figure 6 Procedure for the Zone of Inhibition Test. (1.) 200 µL bacterial suspension placed on agar plate. (2.) Bacterial suspension spread on an agar plate using a Drigalski spatula. (3.) Test specimen were placed on the agar plate (4.) Measuring the diameter of the zone of inhibition.

Statistics

Data evaluation and statistics was done using GNU PSPP version 0.10.2-g654fff from Free Software Foundation, Inc. (Boston, MA). Data sets were compared using a One-way ANOVA test, differences among groups were calculated using post hoc Tukey analysis and is represented by asterisks (* p-value ≤ 0.05; ** p-value ≤ 0.01).
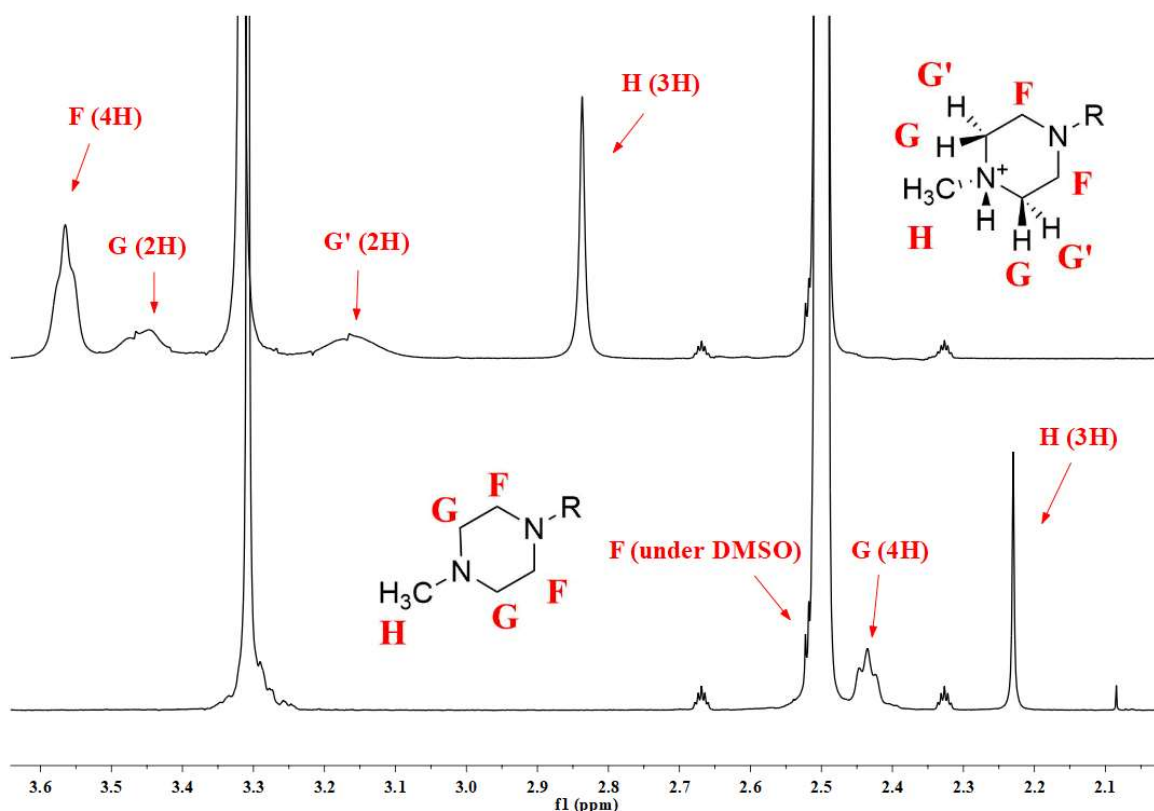
Results

Salt metathesis

Figure 7 Magnification of ^{1}H NMR of levofloxacin hydrochloride (top) and levofloxacin (bottom) in DMSO-d_6. Shifted ^{1}H signals from the piperazine residue in protonated and unprotonated form are highlighted.

^{1}H NMR spectra of levofloxacin and levofloxacin hydrochloride in DMSO-d_6 showed a downfield shift for several hydrochloride-signals compared to their neutral species (**Figure 7**). Proton signals of the piperazine residue were affected, resulting in differences in chemical shifts for F, G and H. Furthermore, the proton signal from G in neutral levofloxacin was split into two signals in the levofloxacin hydrochloride spectrum G and G'. Chemical shifts from neutral to levofloxacin hydrochloride were 2.50 ppm (under DMSO-d_5) to 3.60 – 3.53 ppm (m, 4H) for F, 2.44 ppm (t, 4.6 Hz, 4H) to 3.21 – 3.10 ppm (m, 2H) as well as 3.51 – 3.41 ppm (m, 2H) for G and 2.23 ppm (s, 3H) to 2.84 ppm (s, 3H) for H, respectively.
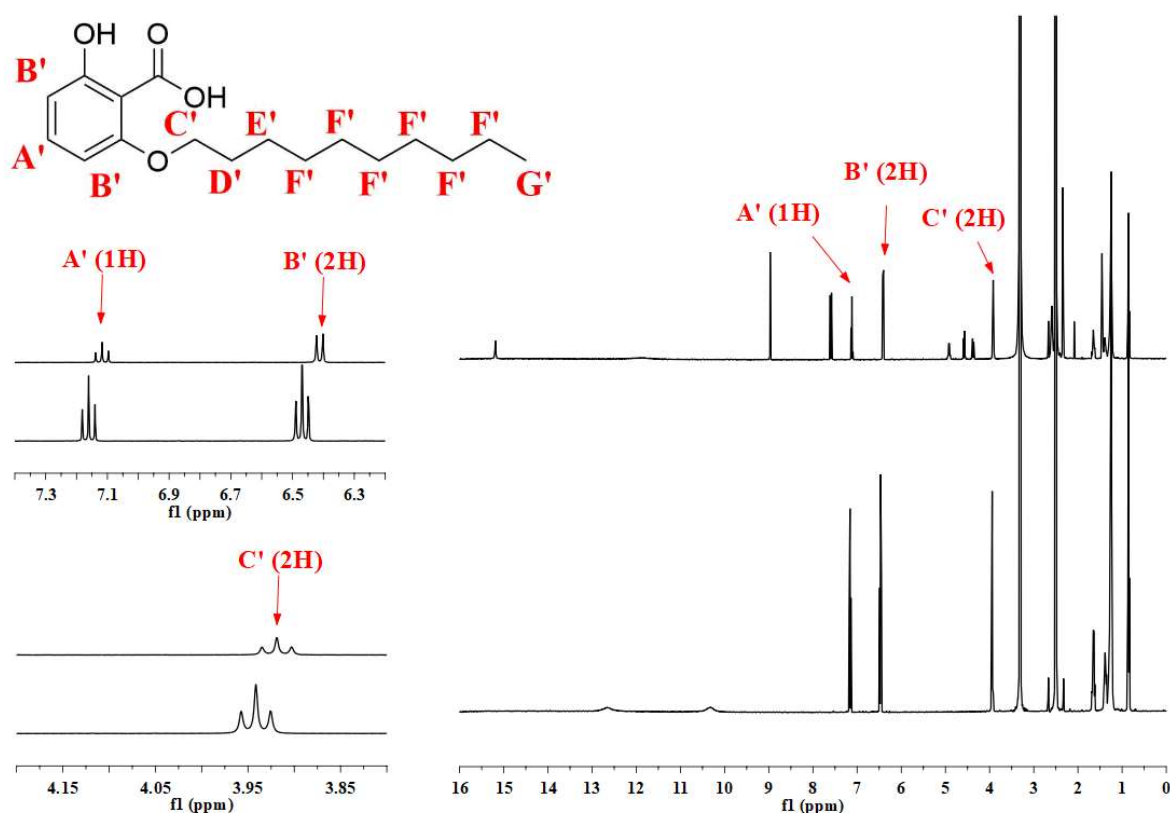
Figure 8 Full spectrum and magnifications of ^{1}H NMR of levofloxacin : SAE180 (SAE204a) from salt metathesis II (top) and SAE180 alone (bottom) in DMSO-d_6. Shifted ^{1}H signals in protonated and partly unprotonated form are highlighted.

^{1}H NMR spectra of SAE180, SAE196 and levofloxacin salts of these in DMSO-d_6 showed an upfield shift for several salt-signals compared to their neutral species, as exemplary shown for SAE180 (**Figure 8**). Aromatic proton signals A' and B' as well as aliphatic C' were affected, resulting in differences in chemical shifts for these signals. Chemical shifts from neutral SAE180 to its levofloxacin salt were 7.16 ppm (t, 8.3 Hz, 1H) to 7.12 ppm (t, 8.0 Hz, 1H) for A', 6.47 ppm (t, 8.2 Hz, 2H) to 6.42 ppm (dd, 8.0 Hz, 1.6 Hz, 2H) for B' and 3.94 ppm (t, 6.4 Hz, 2H) to 3.92 ppm (t, 6.4 Hz, 2H) for C', respectively.

Salt metathesis I

Figure 9 ^{1}H NMR spectra (0-5 ppm) of (A) levofloxacin : SAE195 (SAE202), (B) levofloxacin :SAE181 (SAE203), (C) levofloxacin : SAE180 (SAE204), (D) levofloxacin : SAE196 (SAE205) and (E) levofloxacin : SAE197 (SAE206) in DMSO-d$_6$; dried products obtained by salt metathesis I. Displayed spectra are the counterion (top), salt product (middle) and levofloxacin (bottom). Δ δ(H) from levofloxacin and product was used to calculate ionicity and is highlighted in the spectra.

^{1}H NMR spectra of dried salts obtained by salt metathesis I procedure in DMSO-d_6 exhibited downfield chemical shift for levofloxacin proton signals F, G and H as well as upfield chemical shifts for counterion proton signals A', B' and C' compared to their neutral species (**Figure 9**). Prepared salts were SAE202 (levofloxacin : SAE195), SAE203 (levofloxacin : SAE181), SAE204 (levofloxacin : SAE180), SAE205 (levofloxacin : SAE196) and SAE206 (levofloxacin : SAE197), respectively. Differences in chemical shifts between neutral and salt species (Δ δ) were calculated and are summarized (**Table 4**). Degree of ionicity, calculated from chemical shift of levofloxacin signal H was 20%, 20%, 20%, 18% and 16% for SAE202, SAE203, SAE204, SAE205 and SAE206 with a mean of 19% $\pm$ 1.5%, respectively.

Table 4 ^{1}H NMR chemical shifts of salt metathesis I compared to counterions alone (A', B' and C') and levofloxacin (F, G, G' and H). Δ δ values are displayed in ppm, downfield shift is indicated by positive values and upfield shift by negative values.

	Δ δ(A')	Δ δ(B')	Δ δ(C')	Δ δ(F)	Δ δ(G)	Δ δ(G')	Δ δ(H)
SAE202	-0.03	-0.04	-0.02	n.d.	0.15	n.d.	0.12
SAE203	-0.05	-0.06	-0.02	n.d.	0.15	n.d.	0.12
SAE204	-0.04	-0.06	-0.02	n.d.	0.15	n.d.	0.12
SAE205	-0.04	-0.06	-0.02	n.d.	0.15	n.d.	0.11
SAE206	-0.05	-0.07	-0.03	n.d.	0.13	n.d.	0.10

n.d. = not determined

Salt metathesis II
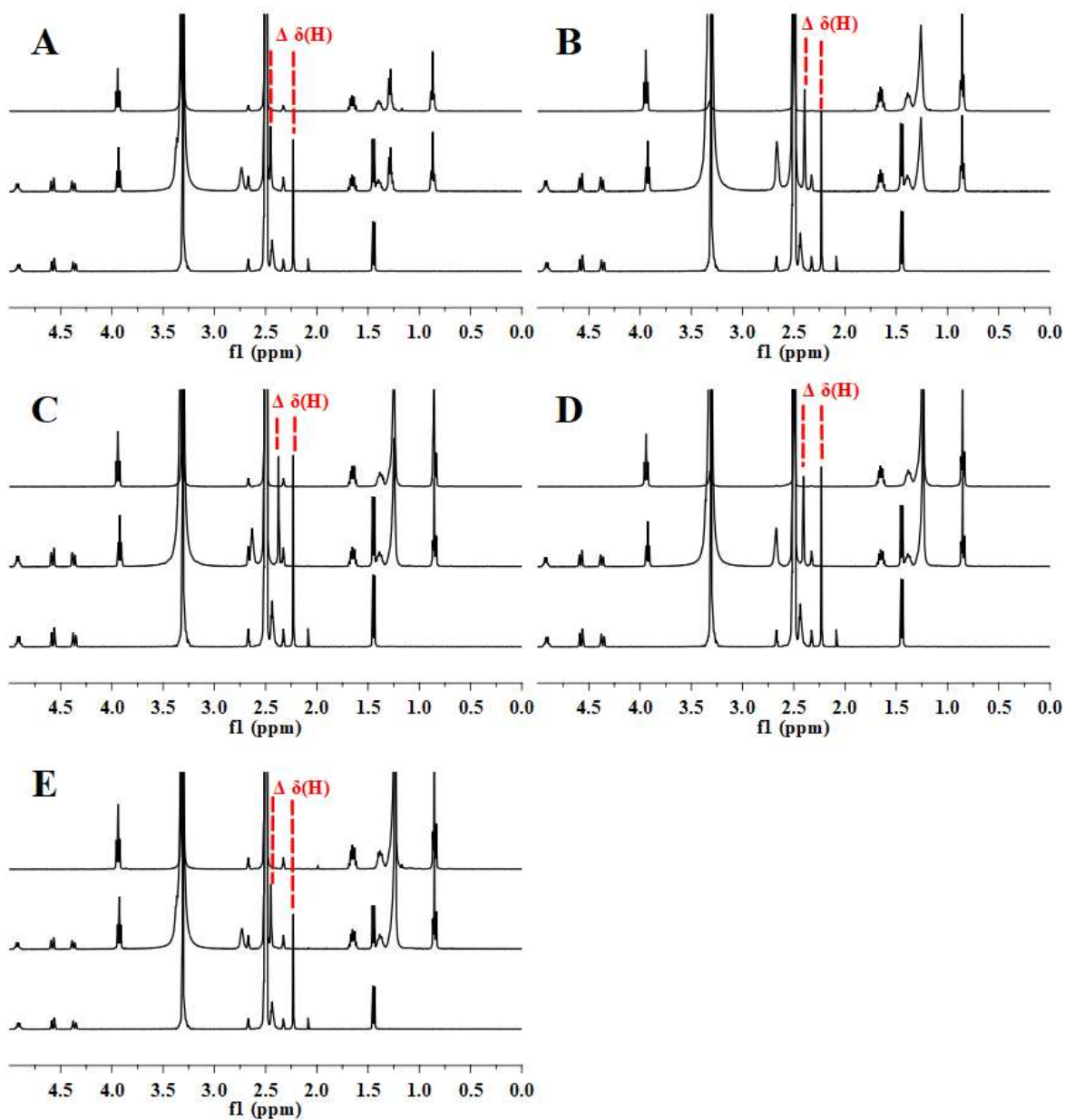
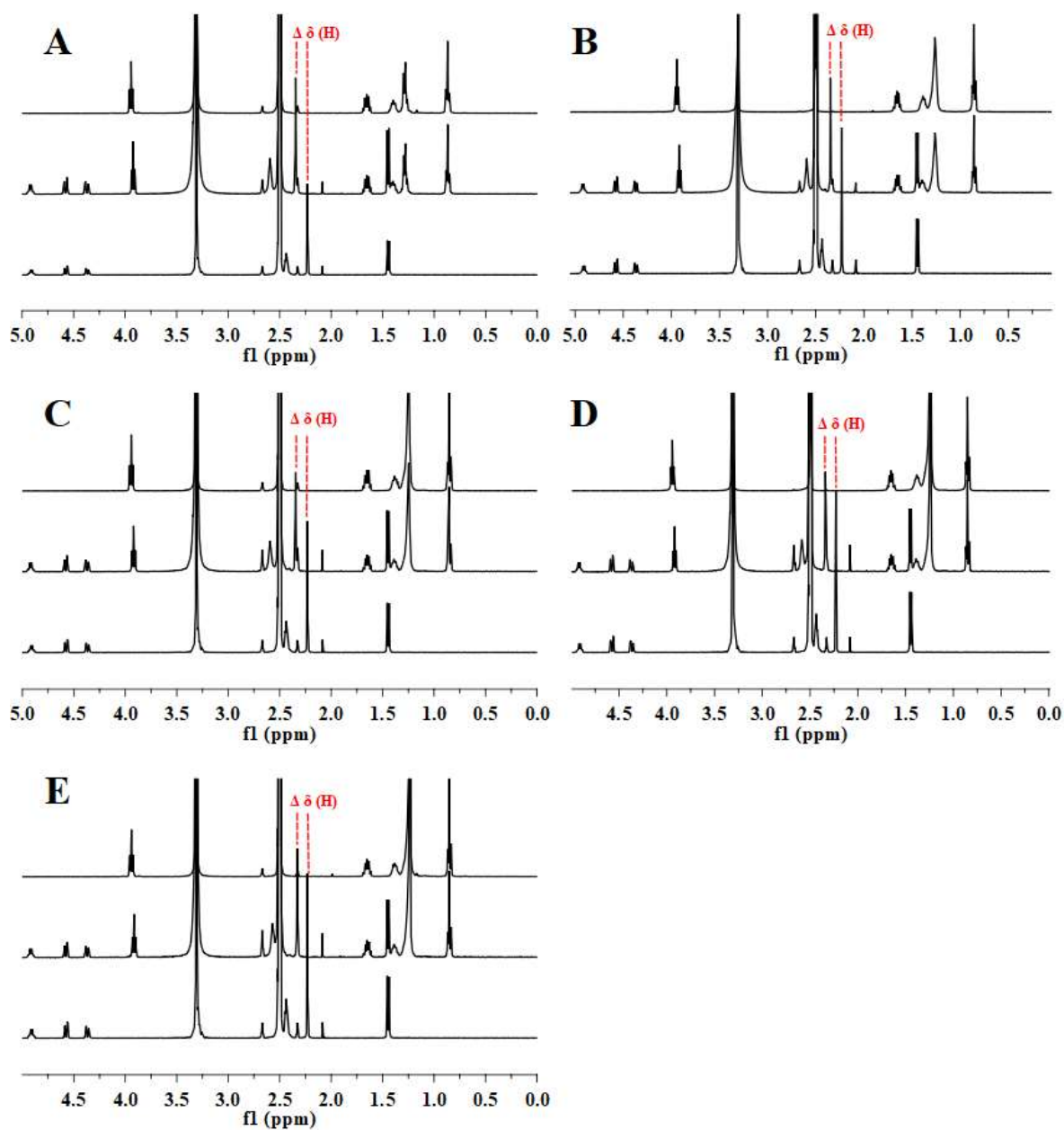**Figure 10** ^{1}H NMR spectra (0-5 ppm) of (A) levofloxacin : SAE195 (SAE202a), (B) levofloxacin :SAE181 (SAE203a), (C) levofloxacin : SAE180 (SAE204a), (D) levofloxacin : SAE196 (SAE205a) and (E) levofloxacin : SAE197 (SAE206a) in DMSO-d_6.; dried products obtained by salt metathesis II. Displayed spectra are the counterion (top), salt product (middle) and levofloxacin (bottom). $\Delta \delta(H)$ from levofloxacin and product was used to calculate ionicity and is highlighted in the spectra.

^{1}H NMR spectra of dried salts obtained by salt metathesis II procedure in DMSO-d$_6$ exhibited downfield chemical shift for levofloxacin proton signals F, G and H as well as upfield chemical shifts for counterion proton signals A', B' and C' compared to their neutral species (**Figure 10**). Prepared salts were SAE202a (levofloxacin : SAE195), SAE203a (levofloxacin :SAE181), SAE204a (levofloxacin : SAE180), SAE205a (levofloxacin : SAE196) and SAE206a (levofloxacin : SAE197), respectively. Differences in chemical shifts between neutral and salt species ($\Delta \delta$) were calculated and are summarized (**Table 5**). Degree of ionicity, calculated from chemical shift of levofloxacin signal H was 36%, 28%, 23%, 30% and 36% for SAE202a, SAE203a, SAE204a, SAE205a and SAE206a with a mean of 30% $\pm$ 5.6%, respectively.

Table 5 ^{1}H NMR chemical shifts of salt metathesis II compared to counterions alone (A', B' and C') and levofloxacin (F, G, G' and H). $\Delta \delta$ values are displayed in ppm, downfield shift is indicated by positive values and upfield shift by negative values.

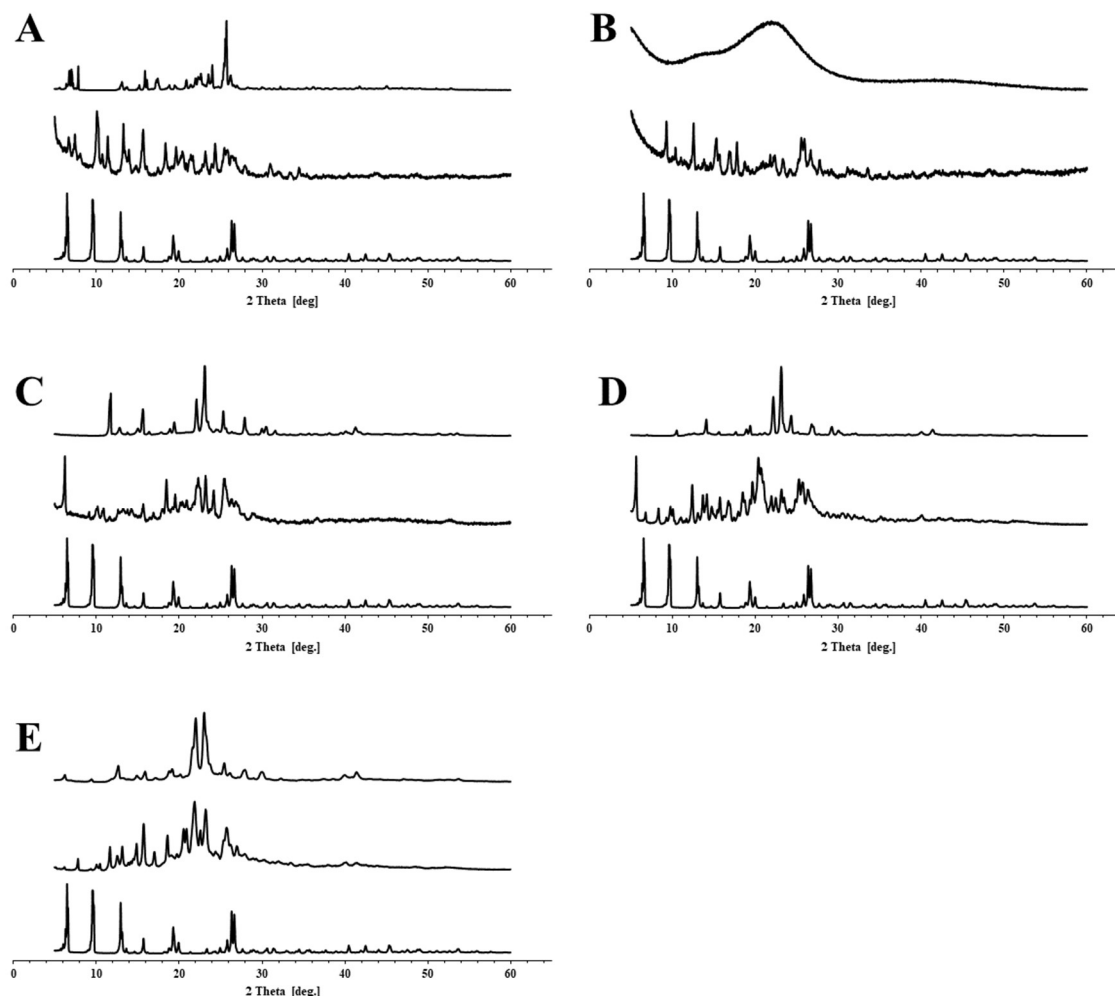|	$\Delta \delta$(A')	$\Delta \delta$(B')	$\Delta \delta$(C')	$\Delta \delta$(F)	$\Delta \delta$(G)	$\Delta \delta$(G')	$\Delta \delta$(H)
SAE202a	-0.01	-0.02	-0.01	0.06	0.30	n.d.	0.22
SAE203a	-0.03	-0.04	-0.01	n.d.	0.23	n.d.	0.17
SAE204a	-0.04	-0.05	-0.02	n.d.	0.19	n.d.	0.14
SAE205a	-0.03	-0.04	-0.01	n.d.	0.23	n.d.	0.18
SAE206a	-0.02	-0.04	-0.01	0.06	0.29	n.d.	0.22

n.d. = not determined

Figure 11 XRPD diffraction patterns of (A) levofloxacin : SAE195 (SAE202a), (B) levofloxacin :SAE181 (SAE203a), (C) levofloxacin : SAE180 (SAE204a), (D) levofloxacin : SAE196 (SAE205a) and (E) levofloxacin : SAE197 (SAE206a); dried products obtained by salt metathesis II. Diffraction patterns are displayed by (top) counterion, (middle) salt and (bottom) levofloxacin.

XRPD diffraction patterns of dried salts obtained by salt metathesis II were measured between 5° – 60° 2Theta (**Figure 11**). Several strong reflexes were selected for each diffraction pattern. Selected reflexes for levofloxacin were 6.52°, 9.63°, 12.97°, 26.38° and 26.68° 2Theta. Selected reflexes for the counterions were 25.72° 2Theta for SAE195, 11.75°, 22.08° and 23.11° 2Theta for SAE180, 22.08° and 23.06° 2Theta for SAE196 as well as 21.95° and 22.99° 2Theta for SAE197, respectively. SAE181, liquid at room temperature, did not show any reflexes but an amorphous halo.
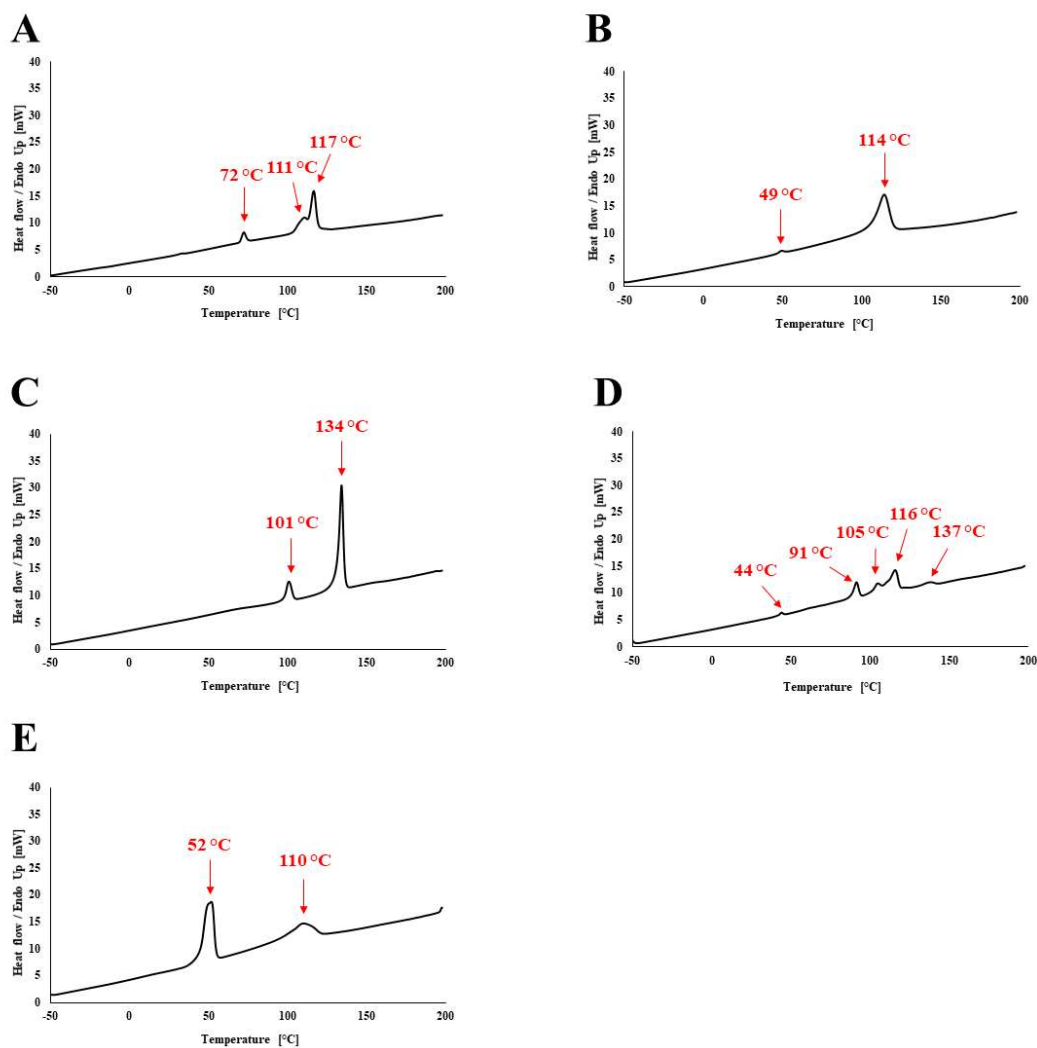
Figure 12 DSC heating curves of (A) levofloxacin : SAE195 (SAE202a), (B) levofloxacin :SAE181 (SAE203a), (C) levofloxacin : SAE180 (SAE204a), (D) levofloxacin : SAE196 (SAE205a) and (E) levofloxacin : SAE197 (SAE206a); dried products obtained by salt metathesis II. Temperature of calorimetric events are highlighted in the curves.

DSC heating curves of dried salts obtained by salt metathesis II were measured between -50 °C and 200 °C (**Figure 12**). Measured calorimetric events were 72 °C ($\Delta H = 5.72$ J g^{-1}), 111 °C ($\Delta H = 18.56$ J g^{-1}) and 117 °C ($\Delta H = 34.02$ J g^{-1}) for SAE202a; 46 °C ($\Delta H = 4.83$ J g^{-1}) and 105 °C ($\Delta H = 50.22$ J g^{-1}) for SAE203a; 101 °C ($\Delta H = 10.26$ J g^{-1}) and 134 °C ($\Delta H = 54.24$ J g^{-1}) for SAE204a; 44 °C ($\Delta H = 1.12$ J g^{-1}), 91 °C ($\Delta H = 10.02$ J g^{-1}), 105 °C ($\Delta H = 8.87$ J g^{-1}) and 116 °C ($\Delta H = 23.50$ J g^{-1}) for SAE205a; 52 °C ($\Delta H = 49.04$ J g^{-1}) and 110 °C ($\Delta H = 24.18$ J g^{-1}) for SAE206a, respectively.
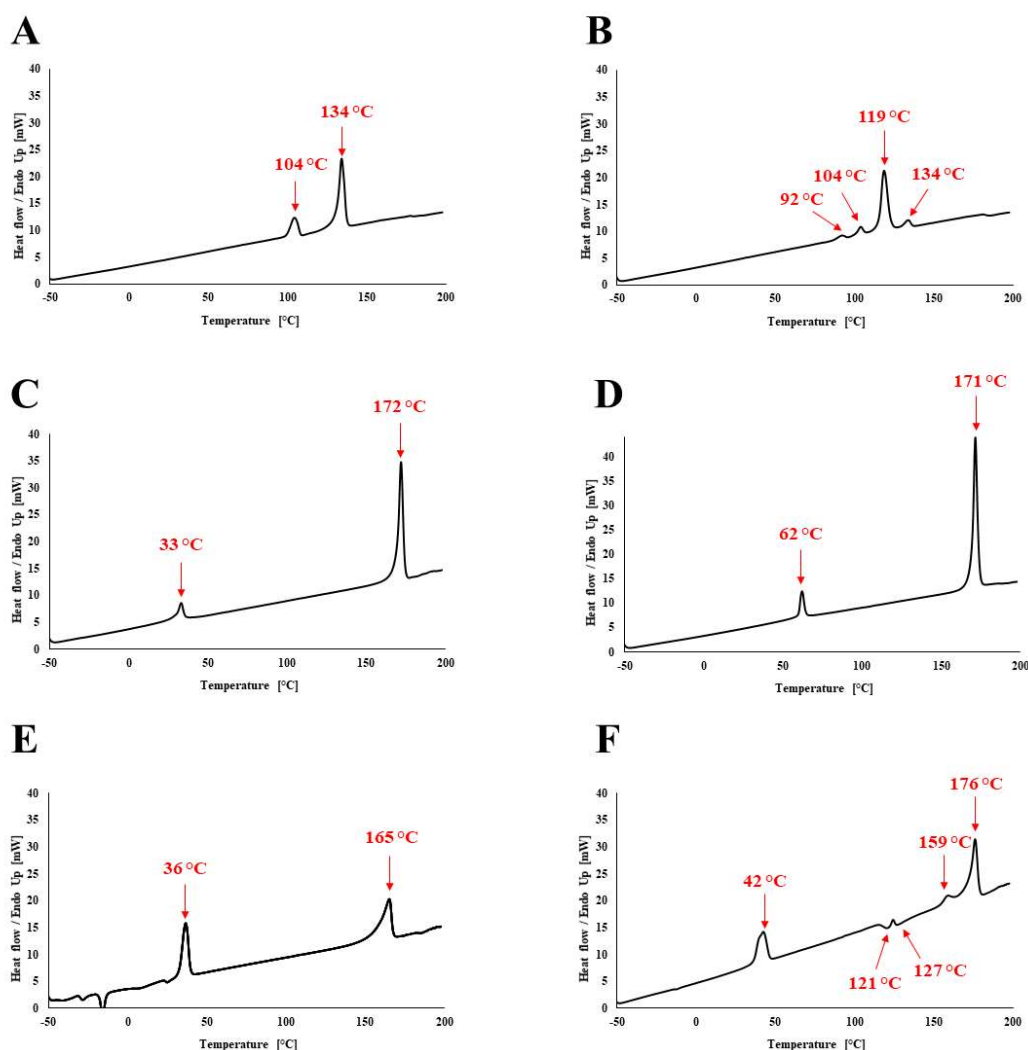
Salt metathesis III

Figure 13 DSC heating curves of (A) levofloxacin : SAE180 (SAE204e), (B) levofloxacin :SAE196 (SAE205c), (C) norfloxacin : SAE180 (SAE208), (D) norfloxacin : SAE196 (SAE209), (E) ciprofloxacin : SAE180 (SAE210) and (F) ciprofloxacin : SAE196 (SAE210); dried products obtained by salt metathesis III. Temperature of calorimetric events are highlighted in the curves.

DSC heating curves of dried salts obtained by salt metathesis III were measured between -50 °C and 200 °C (**Figure 13**). Measured calorimetric events were 104 °C ($\Delta H = 15.06$ J g^{-1}) and 134 °C ($\Delta H = 51.43$ J g^{-1}) for SAE204e; 92 °C ($\Delta H = 2.74$ J g^{-1}), 104 °C ($\Delta H = 4.19$ J g^{-1}) , 119 °C ($\Delta H = 48.50$ J g^{-1}) and 134 °C ($\Delta H = 4.25$ J g^{-1}) for SAE205c; 33 °C ($\Delta H = 10.75$ J g^{-1}) and 172 °C ($\Delta H = 80.55$ J g^{-1}) for SAE208; 62 °C ($\Delta H = 12.45$ J g^{-1}) and 171 °C ($\Delta H = 86.91$ J g^{-1}) for SAE209; 36 °C ($\Delta H = 34.98$ J g^{-1}) and 165 °C ($\Delta H = 44.92$ J g^{-1}) for SAE210; 42 °C ($\Delta H = 28.15$ J g^{-1}), 121 °C ($\Delta H = -4.81$ J g^{-1}), 127 °C ($\Delta H = -6.59$ J g^{-1}), 159 °C ($\Delta H = 7.46$ J g^{-1}) an 176 °C ($\Delta H = 45.80$ J g^{-1}) for SAE211, respectively.

Printing experiments

Figure 14 Representative pictures of OTF during compatibility testing. (left) polarized light microscope (right) height-heatmap. (A) untreated and 24 h after treatment with 2.5 µL (B) ethanol 70% (v/v), (C) 5 mg mL^{-1} ciprofloxacin in ethanol 70% (v/v) and (D) 5 mg mL^{-1} SAE180 in ethanol 70% (v/v). Red circle indicates area where ink-droplet was applied. White bar represents 500 µm, heatmap mean 0 – 363 µm

Application of ethanol 70% (v/v) ink w/ or w/o 5 mg mL^{-1} ciprofloxacin or SAE180 on sorbitol based OTF samples was studied. Incompatibility was defined as presence of recrystallization of applied compound, disruption of the sorbitol integrity or serious change in height, as studied in the height-heatmap (**Figure 14**). No incompatibilities were observed immediately or after 24 h of drying when studied under a polarized light microscope. Compared to the untreated control, no morphological changes were observed for any nano dispenser printed OTF product (**Figure 15**).
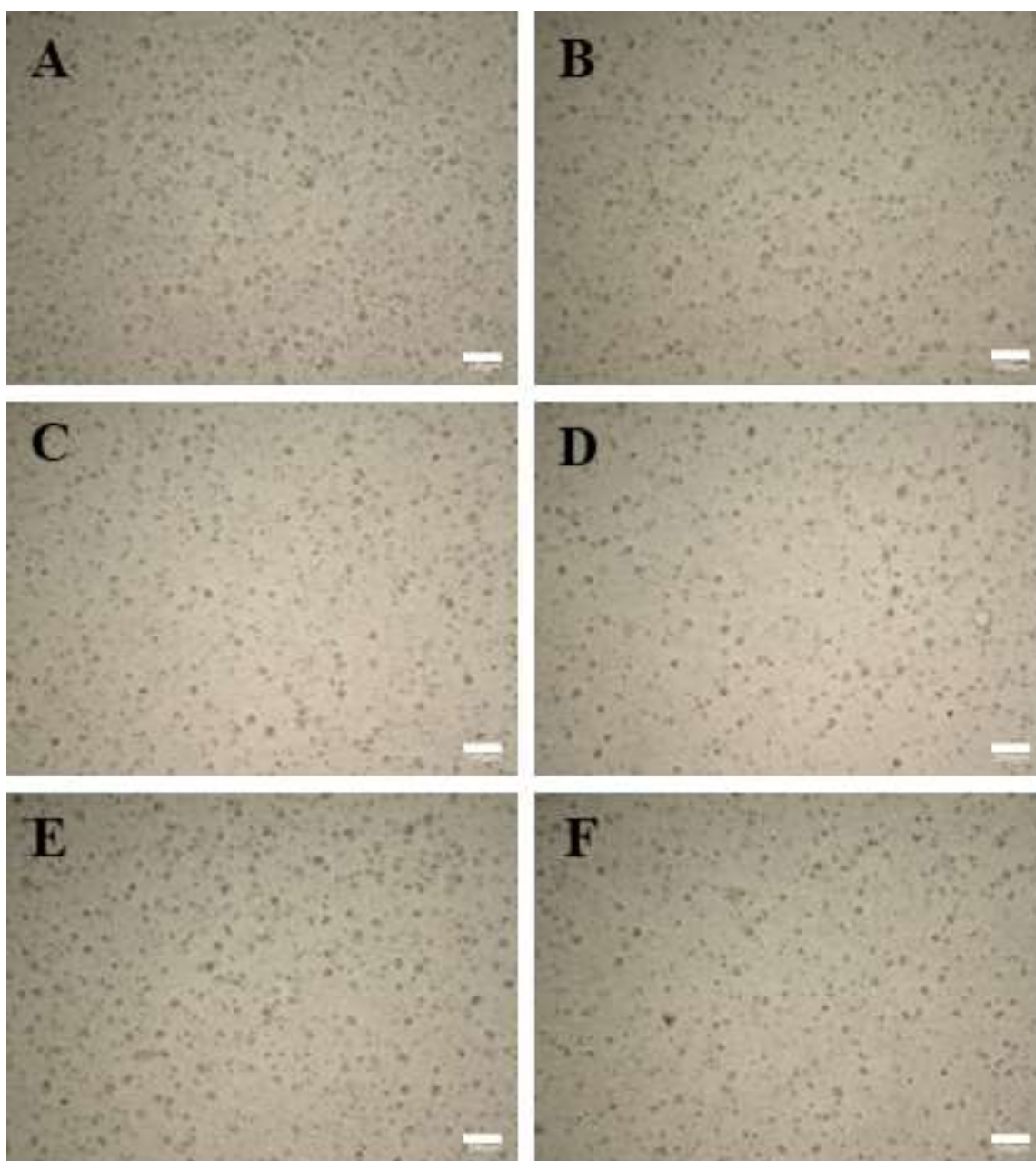
Figure 15 Representative pictures of nano dispenser printed OTF products (A) untreated, (B) CIP, (C) SAE180 x1, (D) SAE180 x2 (E) SAE180 x1 + CIP and (F) SAE180 x2 + CIP. White bar represents 500 μm.
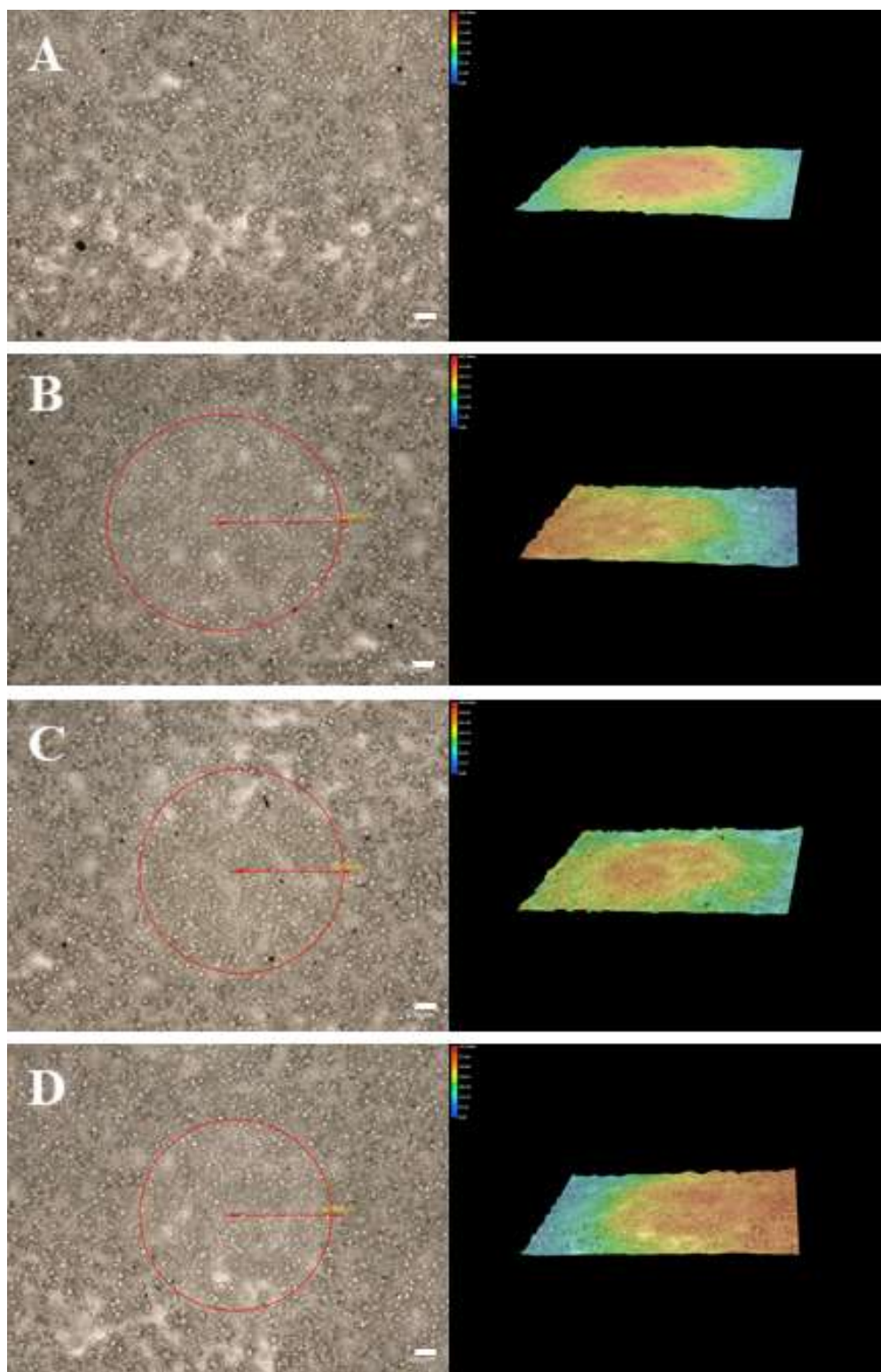
Figure 16 Representative pictures of PVA scaffolds during compatibility testing. (left) polarized light microscope (right) height-heatmap. (A) untreated and 24 h after treatment with 10 µL (B) ethanol 70% (v/v), (C) 5 mg mL^{-1} ciprofloxacin in ethanol 70% (v/v) and (D) 5 mg mL^{-1} SAE180 in ethanol 70% (v/v). White bar represents 500 µm, heatmap mean 0 – 1150 µm

Application of ethanol 70% (v/v) ink w/ or w/o 5 mg mL^{-1} ciprofloxacin or SAE180 and compatibility with 3D printed PVA scaffolds was studied (**Figure 16**). Morphological changes were visible for all tested scaffolds, regardless of the compound present within the ink. Compared to untreated control, formation of a film was observed under the polarized light microscope where ink was applied as well as change in geometry and height of these areas. However, no recrystallization of compound was observed.

Figure 17 Representative pictures of nano dispenser printed PLA controls. (left) polarized light microscope (right) height-heatmap. (A) untreated and (B) 10 μL ethanol 70% (v/v) treated. White bar represents 500 μm, heatmap mean 0 – 1305 μm.
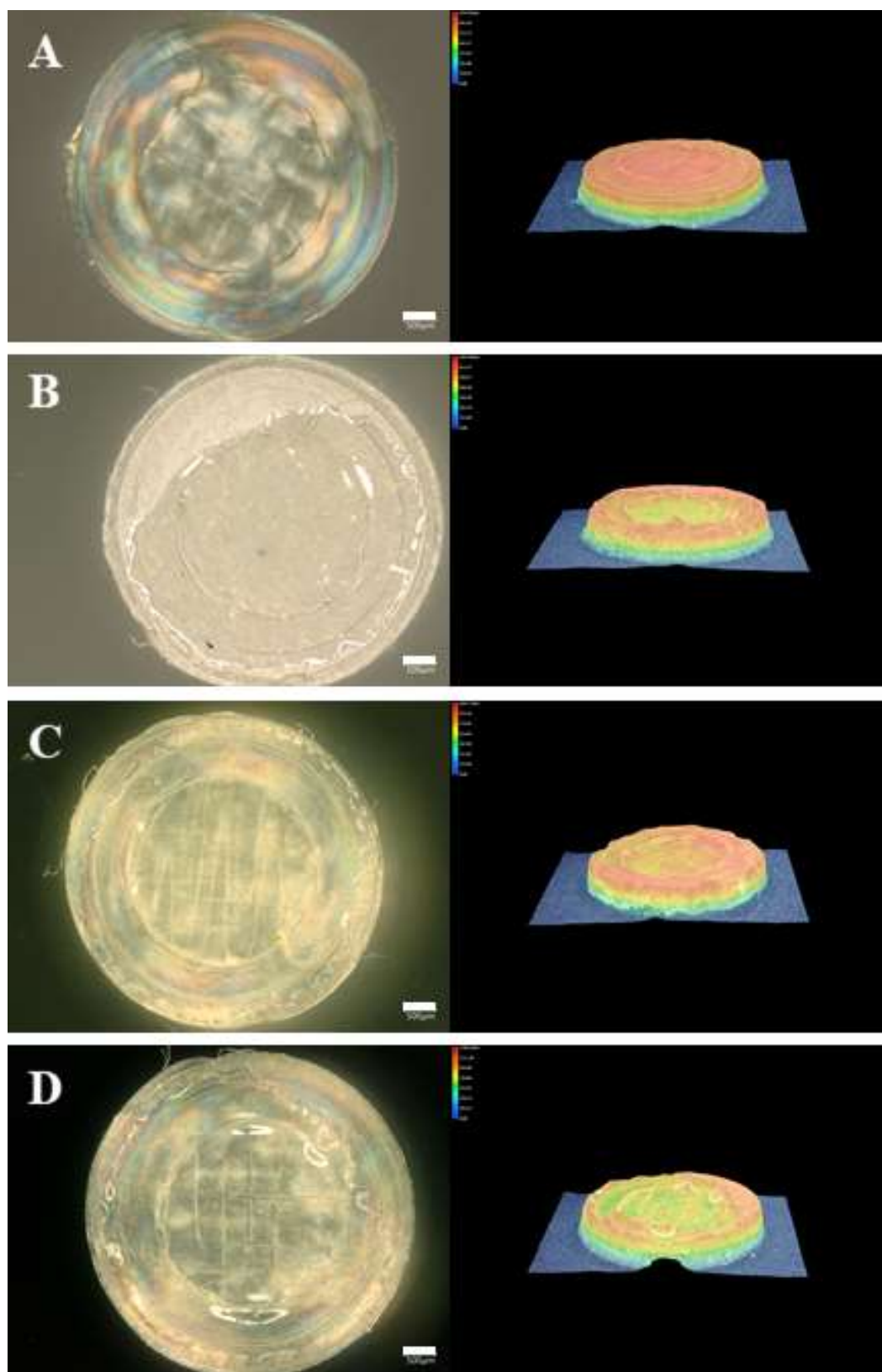
Application of ethanol 70% (v/v) ink and compatibility with 3D printed PLA scaffolds was studied (**Figure 17**).Compared to untreated controls no morphological changes or changes in height or geometry of the scaffolds were observed when ethanol containing ink was applied. Furthermore, all nano dispenser printed PLA products did not show any morphological changes under a polarized light microscope when compared to untreated control (**Figure 18**). Comparing drug containing products to ethanol 70% (v/v) treated did not show drug recrystallization on the scaffold. Differences in height or geometry were not observed.
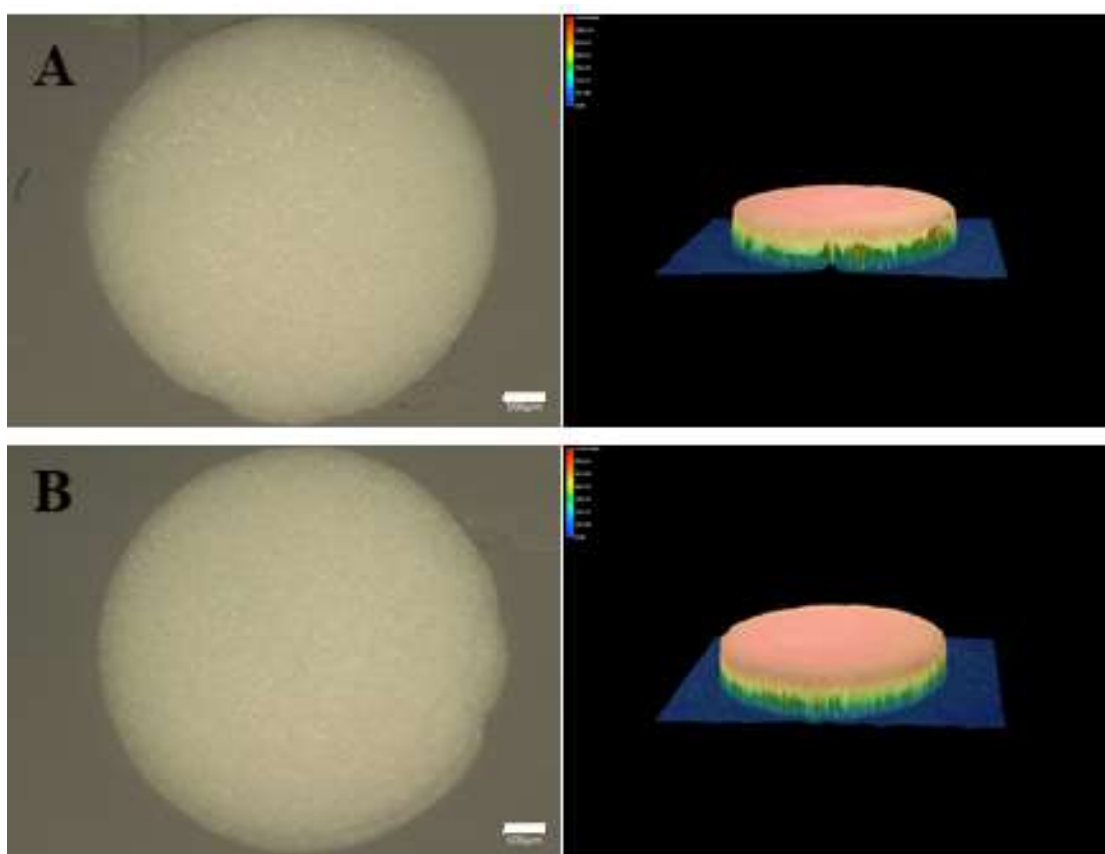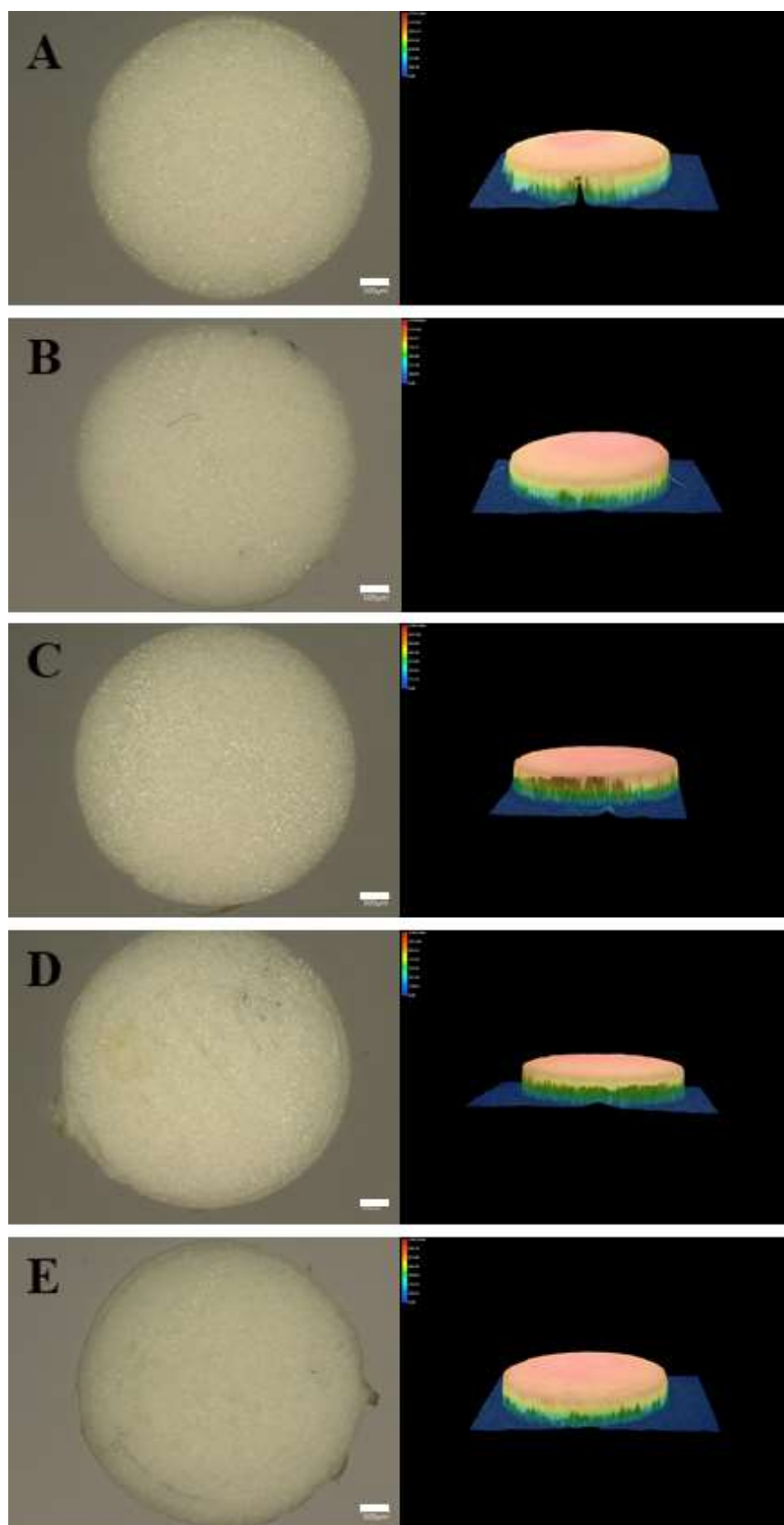
Figure 18 Representative pictures of nano dispenser printed PLA products. (left) polarized light microscope (right) height-heatmap. (A) CIP, (B) SAE180 x1, (C) SAE180 x2, (D) SAE180 x1 + CIP and (E) SAE180 x2 + CIP. White bar represents 500 μm, heatmap mean 0 – 1305 μm.
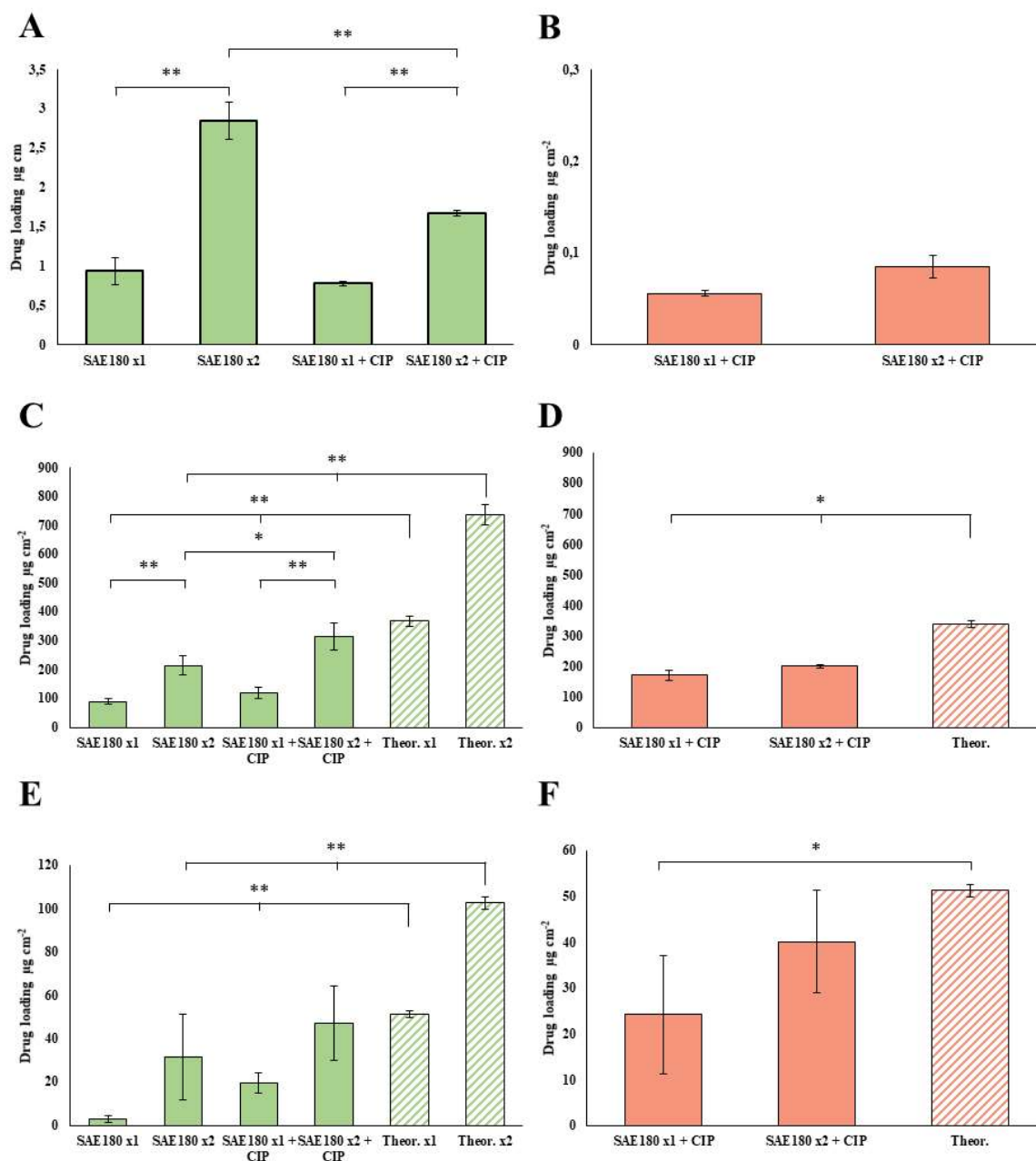
Figure 19 Drug load of (A) SAE180 in inkjet printed OTF, (B) ciprofloxacin in inkjet printed OTF, (C) SAE180 in nano dispenser printed OTF, (D) ciprofloxacin in nano dispenser printer OTF, (E) SAE180 in nano dispenser printed PLA scaffolds and (F) ciprofloxacin in nano dispenser printed PLA scaffolds. Solid bars represent HPLC determined drug content in $\mu g\ cm^{-2}$ and hatched bars represent theoretical drug load in $\mu g\ cm^{-2}$, calculated from mean drop size and ink concentration. No theoretical drug load available for inkjet printed batches. Values are presented as mean ± standard deviation (n=3). Significant differences are represented by asterisks (* p-value ≤ 0.05; ** p-value ≤ 0.01)

Drug loading of nano dispenser printed OTF and PLA scaffolds as well as inkjet printed OTF was assessed (**Figure 19**). For OTF analysis circular specimen, 15 mm in diameter for inkjet printed OTF and 6 mm in diameter for nano dispenser printed OTF, were cut out, extracted and analyzed by HPLC. SAE180 drug loads for inkjet printed OTF were 0.9 ± 0.2 µg cm^{-2} for SAE180 x1, 2.8 ± 0.2 µg cm^{-2} for SAE180 x2, 0.8 ± 0.02 µg cm^{-2} for SAE180 x1 + CIP and 1.7 ± 0.04 µg cm^{-2} for SAE180 x2 + CIP. Ciprofloxacin drug loads for inkjet printed OTF were 0.06 ± 0.003 µg cm^{-2} for SAE180 x1 + CIP and 0.08 ± 0.01 µg cm^{-2} for SAE180 x2 + CIP. SAE180 drug loads for nano dispenser printed OTF were 89.1 ± 9.8 µg cm^{-2} for SAE180 x1, 214.4 ± 32.2 µg cm^{-2} for SAE180 x2, 118.4 ± 20.6 µg cm^{-2} for SAE180 x1 + CIP and 315.9 ± 47.1 µg cm^{-2} for SAE180 x2 + CIP. Theoretical values for SAE180 drug load were calculated to 369.0 ± 17.6 µg cm^{-2} for x1 batches and 738.0 ± 35.4 µg cm^{-2} for x2 batches. Ciprofloxacin drug loads for nano dispenser printed OTF were 172.2 ± 16.9 µg cm^{-2} for SAE180 x1 + CIP and 201.8 ± 6.4 µg cm^{-2} for SAE180 x2 + CIP. Theoretical value for ciprofloxacin drug load were calculated to 338.0 ± 10.8 µg cm^{-2}. SAE180 drug loads for nano dispenser printed PLA scaffolds were 2.9 ± 1.7 µg cm^{-2} for SAE180 x1, 31.6 ± 19.9 µg cm^{-2} for SAE180 x2, 19.8 ± 4.7 µg cm^{-2} for SAE180 x1 + CIP and 47.4 ± 17.1 µg cm^{-2} for SAE180 x2 + CIP. Theoretical values for SAE180 drug load were calculated to 51.3 ± 1.4 µg cm^{-2} for x1 batches and 102.8 ± 2.8 µg cm^{-2} for x2 batches. Ciprofloxacin drug loads for nano dispenser printed PLA scaffolds were 24.3 ± 12.9 µg cm^{-2} for SAE180 x1 + CIP and 40.2 ± 11.2 µg cm^{-2} for SAE180 x2 + CIP. Theoretical value for ciprofloxacin drug load were calculated to 51.3 ± 1.4 µg cm^{-2}.
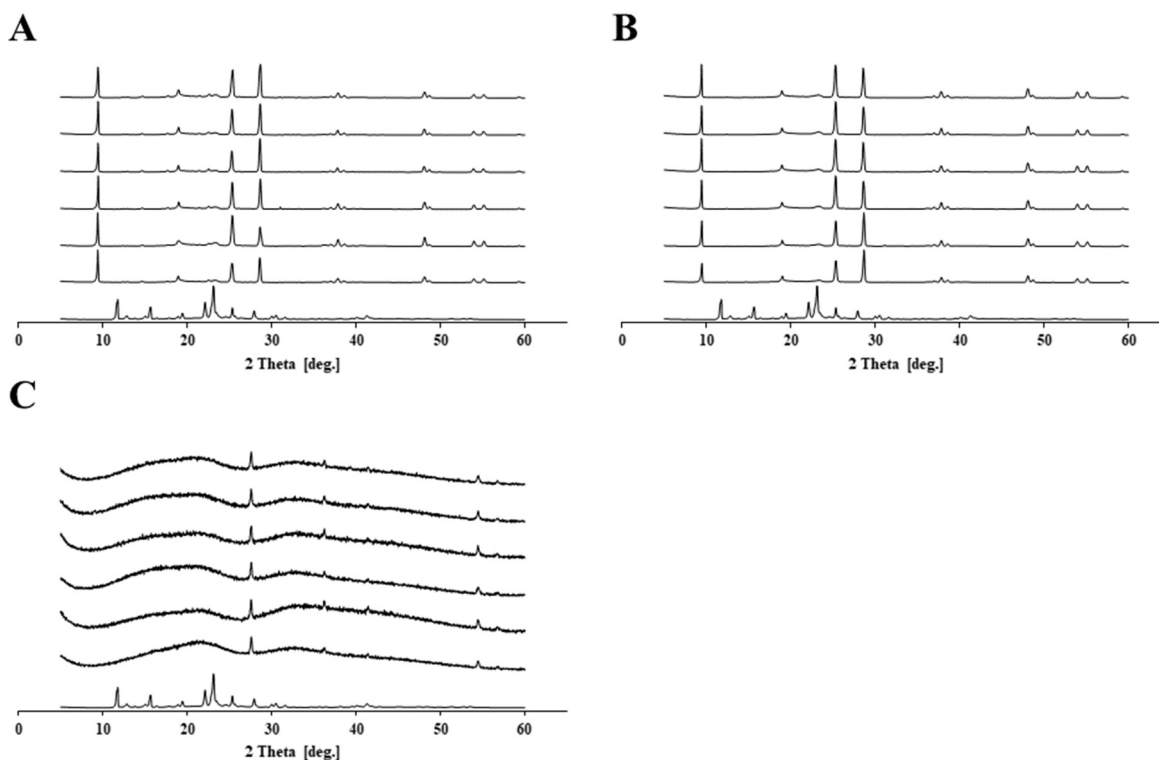
Figure 20 XRPD diffraction patterns of (A) inkjet printed OTF, (B) nano dispenser printed OTF, (C) nano dispenser printed PLA scaffolds. Diffraction patterns are ordered down to top in the following order: Blank, SAE180 counterion, CIP, SAE180 x1, SAE180 x2, SAE180 x1 + CIP, SAE180 x2 + CIP.

XRPD diffraction patterns of inkjet and nano dispenser printed OTF as well as nano dispenser printed PLA scaffolds were measured between 5° – 60° 2Theta (**Figure 20**). The polyethylene carrier foil was removed from OTF prior the measurements. Several strong reflexes were selected for each diffraction pattern. Strong reflexes were 11.75°, 22.08° and 23.11° 2Theta for SAE180, 9.40°, 25.44° and 28.65° 2Theta for OTF and 27.62°, 36.67° and 54.33° 2Theta for PLA scaffolds. Additionally, PLA scaffolds showed an amorphous halo.

Antibacterial evaluation
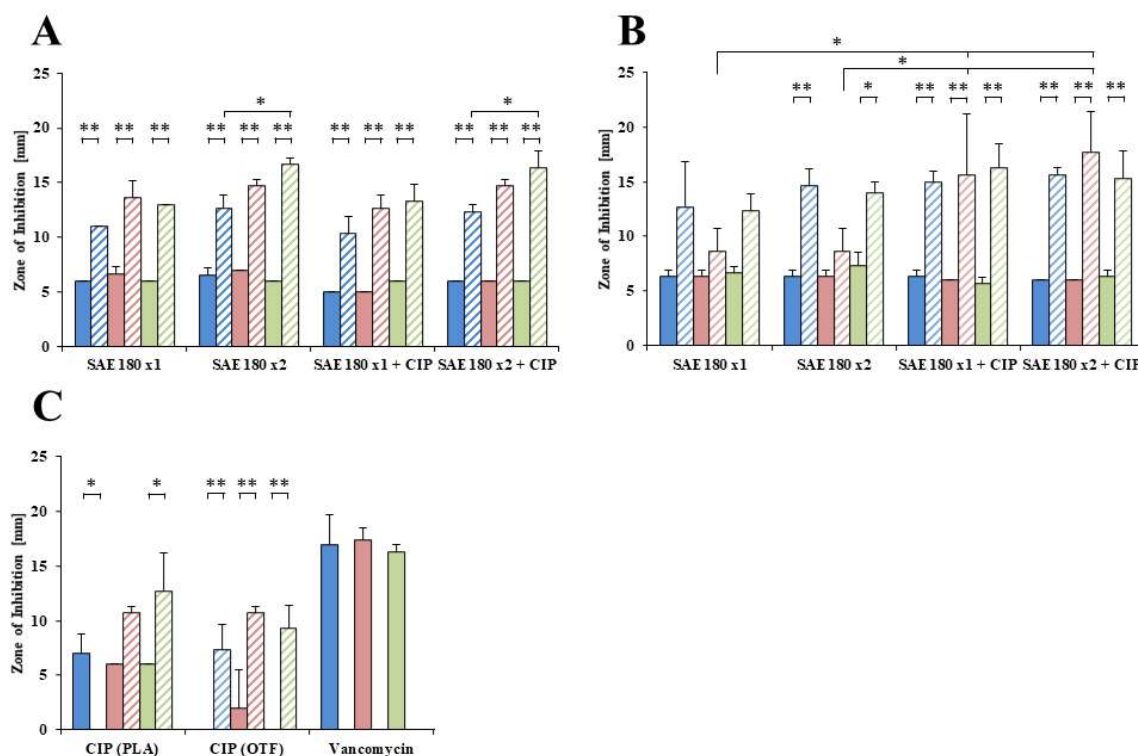
Figure 21 Zone of inhibition obtained by agar diffusion test using three bacterial strains (blue) ST228, (red) JE2 and (green) Lac* for (A) nano dispenser printed OTF, (B) nano dispenser printed PLA scaffolds and (C) ciprofloxacin and vancomycin. Solid bars represent zone with no visible bacterial growth, hatched bars represent zone with reduced visible growth. Values are displayed as mean $\pm$ standard deviation (n=3). Significant differences are represented by asterisks (* p-value $\leq$ 0.05; ** p-value $\leq$ 0.01).

Antibacterial activity of printed OTF and PLA scaffolds was tested on three *S. aureus* strains ST228, JE2 (MRSA) and Lac* (MRSA) using an agar diffusion test and measuring the inhibition zone diameter (IZD) (**Figure 21**). Two categories of inhibition were defined, the true zone of inhibition where no bacterial growth was visible, and a second/larger zone of inhibition were reduced bacterial growth was visible (diameter of second zone of inhibition if any was visible is displayed in brackets). Inkjet printed OTF did not show bacterial inhibition or reduced growth (data not shown). No inhibition in bacterial growth was visible for untreated and ethanol 70% (v/v) printed specimen (data not shown). IZD for positive control vancomycin were 17.0 $\pm$ 2.6 mm for ST228, 17.3 $\pm$ 1.2 mm for JE2 and 16.3 $\pm$ 0.6 mm for Lac*. IZD for nano dispenser printed OTF (**Figure 21A**) against ST228 were 6.0 $\pm$ 0.0 mm (11.0 $\pm$ 0.0 mm) for SAE180 x1, 6.5 $\pm$ 0.7 mm (12.7 $\pm$ 1.2 mm) for SAE180 x2, 5.0 $\pm$ 0.0 mm (10.3 $\pm$ 1.5 mm) for SAE180 x1 + CIP, 6.0 $\pm$ 0.0 mm (12.3 $\pm$ 0.6 mm) for SAE180 x2 + CIP and (7.3 $\pm$ 2.3 mm) for CIP. IZD for nano dispenser printed OTF against JE2 were

6.7 ± 0.6 mm (13.7 ± 1.5 mm) for SAE180 x1, 7.0 ± 0.0 mm (14.7 ± 0.6 mm) for SAE180 x2, 5.0 ± 0.0 mm (12.7 ± 1.2 mm) for SAE180 x1 + CIP, 6.0 ± 0.0 mm (14.7 ± 0.6 mm) for SAE180 x2 + CIP and 2.0 ± 3.5 mm (10.7 ± 0.6 mm) for CIP. IZD for nano dispenser printed OTF against Lac* were 6.0 ± 0.0 mm (13.0 ± 0.0 mm) for SAE180 x1, 6.0 ± 0.0 mm (16.7 ± 0.6 mm) for SAE180 x2, 6.0 ± 0.0 mm (13.3 ± 1.5 mm) for SAE180 x1 + CIP, 6.0 ± 0.0 mm (16.3 ± 1.5 mm) for SAE180 x2 + CIP and (9.3 ± 2.1 mm) for CIP. IZD for nano dispenser printed PLA scaffolds (**Figure 21B**) against ST228 were 6.3 ± 0.6 mm (12.7 ± 4.2 mm) for SAE180 x1, 6.3 ± 0.6 mm (14.7 ± 1.5 mm) for SAE180 x2, 6.3 ± 0.6 mm (15.0 ± 1.0 mm) for SAE180 x1 + CIP, 6.0 ± 0.0 mm (15.7 ± 0.6 mm) for SAE180 x2 + CIP and 7.0 ± 1.7 mm for CIP. IZD for nano dispenser printed PLA scaffolds against JE2 were 6.3 ± 0.6 mm (8.7 ± 2.1 mm) for SAE180 x1, 6.3 ± 0.6 mm (8.7 ± 2.1 mm) for SAE180 x2, 6.0 ± 0.0 mm (15.7 ± 1.0 mm) for SAE180 x1 + CIP, 6.0 ± 0.0 mm (17.7 ± 3.8 mm) for SAE180 x2 + CIP and 6.0 ± 0.0 mm (10.7 ± 0.6 mm) for CIP. IZD for nano dispenser printed PLA scaffolds against Lac* were 6.7 ± 0.6 mm (12.3 ± 1.5 mm) for SAE180 x1, 7.3 ± 1.2 mm (14.0 ± 1.0 mm) for SAE180 x2, 5.7 ± 0.6 mm (16.3 ± 2.1 mm) for SAE180 x1 + CIP, 6.3 ± 0.6 mm (15.3 ± 2.5 mm) for SAE180 x2 + CIP and 6.0 ± 0.0 mm (12.7 ± 3.5 mm) for CIP.

Discussion

Salt formation of synthesized anacardic acid derivates with levofloxacin and norfloxacin was performed using different salt metathesis reactions in solution. Protonation of the resulting products via ^{1}H-NMR in an aprotic solvent (DMSO-d_6) and solid state via XRPD and DSC were assessed. Salts of fluoroquinolones have been reported in the literature with various counterions such as citrate, fumarate, maleate, oxalate, benzoate, succinate or adipic acid salts.[92-95] While most of these studies used mechanochemical reactions e.g. solvent assisted grinding for salt preparation, salt metathesis in solution was selected within this study as it was considered to be more robust and has been already applied for ciprofloxacin maleate, fumarate and adipicate in water-methanol mixtures.[95] However, ciprofloxacin was excluded from salt metathesis experiments as its temperature-dependent solubility was found to be very poor in preliminary experiments in water and water/organic solvent mixtures (data not shown). In these lines, intrinsic solubilities (zwitterionic species) of 0.08 mg mL^{-1}, 0.27 mg mL^{-1} and 0.32 mg mL^{-1} in buffered aqueous systems were reported for ciprofloxacin, levofloxacin and norfloxacin, respectively.[96-97] Levofloxacin (the levo-isomere of ofloxacin)

with fairly good solubility in water and water-methanol mixtures was selected as model fluoroquinolone for salt preparation. Levofloxacin salts were prepared with SAE195, SAE181, SAE180, SAE196 and SAE197 from methanol 30% (v/v) and the stoichiometry of drug and counterion as well as degree of ionization in DMSO-d_6 was calculated using ^{1}H-NMR (**Figure 7**-**Figure 9**). Briefly, levofloxacin and the counterion precipitated in an 1:1 molar ratio regardless of the respective counterions structure and the obtained solids were in average a mixture of 19.5% salt and 80.5% non-ionic complex, where counterions with shorter alkyl chain length (SAE195, SAE181 and SAE180) exhibited slightly higher proportion of salt than those with longer chains (SAE196 and SAE197). Recrystallization of these mixtures with ethanol 70% yielded a slightly higher degree of ionization of 30% in average while the molar ratio of 1:1 was maintained (**Figure 10**). Such poor salt formation could be attributed to insufficient pK$_a$ difference between levofloxacin and the counterion (ΔpK$_a$), the zwitterionic nature of levofloxacin or a crystal environment in the resulting complex which hindered proton transfer. The latter was already demonstrated in a previous study where different crystal environments of the same acid-base pair governed the protonation state of the obtained solid while the ΔpK$_a$ was proposed to not be the most important aspect in successful salt formation.[98] However, it is generally acknowledged that the influence of ΔpK$_a$ between acid and base is significant and often allows a theoretical assessment if salt formation is likely to happen. Moreover, the value of ΔpK$_a$ = pK$_a^{base}$-pK$_a^{acid}$ is expected to be ΔpK$_a \geq 3$ for a successful proton transfer, which is already known as the 'rule of three'.[12, 95] Successful fluoroquinolone salt formation was often reported for dicarboxylic acids, which are rather small and demonstrate a high acidity e.g. maleic acid with a molecular weight of 116.07 g mol^{-1} and two acidic pK$_a$ values of 1.9 and 6.1.[95] In this example proton transfer is likely to happen as the ΔpK$_a$ is greater than 6 and the small counterion size enables tight crystal packing of the resulting salt. Attributed to their 2-Hydroxybenzoic acid moiety, the herein anacardic acid derivatives demonstrate acidic pK$_a$ values in the range of 3.2 to 3.3 resulting in ΔpK$_a \geq 4.8$ calculated from levofloxacin, basic pK$_a$ = 8.0.[4, 99] Methanol content (30% v/v) in the metathesis reaction was kept as low as possible to prevent further pK$_a$ shift and thereby decrease of ΔpK$_a$ while maintaining a sufficient concentration of both compounds in solution. However, despite their relatively high acidity, compared to aromatic or aliphatic carboxylic acids, complete proton transfer did not occur. This could be potentially attributed to the molecular size, the number of rotatable bonds and the surfactant like structure of the anacardic acid derivatives which

hindered a successful salt formation with levofloxacin. The existence of several crystalline species e.g. levofloxacin, the respective anacardic acid derivative as well as ionized and non-ionized complexes of both, was further elaborated by the reflexes in their XRPD patterns (**Figure 11**). Representative reflexes of levofloxacin were found in the obtained solids from SAE195 (**Figure 11A**) and SAE181 (**Figure 11B**) indicating precipitation of the free form. Reflexes from the initial crystalline forms of anacardic acid derivatives could not be found in the respective XRPD patterns with the amorphous halo of SAE181 disappearing in the metathesis product (**Figure 11B**). New reflexes appeared in all XRPD patterns and could not be attributed to any of the involved compounds. Therefore, precipitation of new crystalline phases of either the compounds alone or in unionized/ionized complexes occurred, maintaining the molar ratio of 1:1 judged by ^{1}H-NMR. Identification of different crystalline phases was carried out with the dried products using DSC experiments in non-sealed crucibles yielding several endothermic events up to 200 °C (**Figure 12**). Melting points of SAE195, SAE181, SAE180, SAE196 and SAE197 were found at 32 °C, 20 °C, 33 °C, 45 °C and 51 °C in a recent study and the melting point of levofloxacin was reported at 222-230 °C by the supplier, respectively.[4] Multiple endothermic events attributed to melting events have been measured in all products indicating more than one crystalline species in each sample. Melting events from anacardic acid derivates where only found in the metathesis products of levofloxacin with SAE196 (**Figure 12D**) and SAE197 (**Figure 12E**). The formation of new crystalline species was observed in all cases. While the enthalpy of transition (ΔH) for residual counterion was lower for levofloxacin : SAE196, several endothermic events with low ΔH could be identified indicating a variety of crystalline species in the sample. Moreover, the melting event of residual counterion was more pronounced in levofloxacin : SAE197 and the counterion was considered unsuitable for salt formation with levofloxacin attributed to its size, lipophilicity and flexible structure. Contrary, heating curves of levofloxacin : SAE195, SAE181 or SAE180 metathesis products demonstrated two endothermic events where the second one was calculated with higher ΔH (**Figure 12A-C**). Despite signal shape of levofloxacin : SAE181 and SAE195 was rather broad and levofloxacin : SAE195 having a shoulder in front of its second event, these three counterions were considered to form a unionized or ionized complex with levofloxacin in the tested metathesis conditions. Overall levofloxacin : SAE180 demonstrated the most promising heating curve with a sharp endothermic event. However, the metathesis process was considered not successful as it was not possible to obtain a single crystalline species

(ionized or not) from the reaction. In a second metathesis approach the reaction was altered to obtain pure products with a single crystalline species. The absence of cosolvent was selected to avoid possible pK_a shift of counterion and drug decreasing ΔpK_a, as well as induced precipitation by pH shift to circumvent deprotonation of the fluroquinolone's carboxylic acid and thereby its zwitterionic nature. SAE180 was selected being the most promising counterion for salt formation as well as SAE196 with highest antibacterial activity in a previous study.[4] Furthermore, norfloxacin and ciprofloxacin were selected to be tested next to levofloxacin to assess the overall possibility for salt formation between anacardic acid derivatives and fluoroquinolones. Following the procedure of salt metathesis III solid precipitates could be obtained for each combination of SAE180 or SAE196 with levofloxacin, norfloxacin or ciprofloxacin. Melting points have been previously reported at 270-275 °C for ciprofloxacin and 217-219 °C for norfloxacin.[96] Multiple endothermic events were detected in the respective heating curves for all metathesis reactions with norfloxacin and levofloxacin overall showing more promising results than ciprofloxacin (**Figure 13**). Melting events in the heating curve of levofloxacin : SAE180 form metathesis III were congruent with the ones observed in the product from previous metathesis II. Compared to its previous metathesis II reaction, similar trends could be observed for levofloxacin : SAE196 where the melting event attributed to the SAE196 counterion disappeared while ΔH increased for the melting event at 119 °C potentially indicating a higher proportion of this crystalline species in the sample (**Figure 13B**). Metathesis reaction III with norfloxacin yielded sharp endothermic melting event around 170 °C and a small endothermic event at lower temperatures. While the endothermic event for norfloxacin : SAE180 at 33 °C can be attributed to the precipitated counterion itself (**Figure 13C**), the responsible species for the endothermic event at 62 °C in the heating curve of norfloxacin : SAE196 could not be identified (**Figure 13D**). Next to a main endothermic event, heating curves of the dried metathesis III products of ciprofloxacin with either SAE180 or SAE196 revealed melting events attributed the respective counterion in both cases as well as smaller unidentified events for ciprofloxacin : SAE196 and an exothermic event for ciprofloxacin : SAE180 at -13 °C. Interestingly, despite all tested fluoroquinolones have comparable acidic pK_a values of 5.5, 6.3 and 6.1 (carboxylic acid) and basic pK_a values of 8.0, 8.4 and 8.7 (piperazine) for levofloxacin, norfloxacin and ciprofloxacin, precipitation did not occur for norfloxacin at pH 6.0.[96, 99] However, when the pH was lowered precipitation in norfloxacin salt metathesis III occurred at pH 5.0 and solid product could be obtained and dried. Conclusively, it was

not possible to obtain solid salts or co-crystals from anacardic acid derivatives with levofloxacin, norfloxacin or ciprofloxacin with a pure single crystalline phase. However, it was possible to obtain partly ionized solid crystalline mixtures of fluoroquinolone counterion complexes. Overall, from the data presented anacardic acid derivatives with shorter alkyl chain length in combination with norfloxacin or levofloxacin were identified to be more suitable for salt/co-crystal formation within the tested metathesis strategies.

2D/3D printing was selected as a potential formulation strategy for anacardic acid derivatives alone or in combination with ciprofloxacin. The anacardic acid derivative SAE180 demonstrated good antibacterial activity as well as biofilm inhibition properties in subinhibitory concentrations and was favored as drug candidate.[4] Prior printing process development a suitable ink was selected with two major aspects driving the ink selection: (i) sufficient solubility of the compounds of interest within the ink and (ii) physical compatibility between ink and the matrix. The solubility of SAE180 in water, different alcohols and ethanol-water mixtures (**Table S 1**) was assessed next to various organic solvents (**Table S 2**). Solubility of SAE180 in all tested organic solvents including alcohols exceeded the highest tested concentration ($\geq$ 50 mg mL^{-1}) and solubility in ethanol-water mixtures was considered sufficient. Solubility of ciprofloxacin was tested in the same manner and considered poor in alcohols, water and most organic solvents (data not shown). Preliminary experiments of physical stability revealed non-compatibility between most organic solvents and the OTF matrix as well as PLA and limited selectable solvent systems. However, ethanol-water 70% (v/v) was considered a non-toxic, pharmaceutical acceptable solvent and demonstrated sufficient solubility of both compounds. Two inks were prepared with either 5 mg mL^{-1} for ciprofloxacin or 5 mg mL^{-1} SAE180 in ethanol 70% (v/v). Compatibility testing of OTF specimen with these drug containing inks revealed slight changes in the morphology of the (hydroxypropyl)methyl cellulose (HPMC) based matrix when examined with a polarized light microscope (PLM) but no signs of recrystallization of drug or change in height were observed (**Figure 14** and **Figure 15**). However, recrystallization was reported by a previous study for the preparation of rasagiline mesylate printed OTF and was observed for a second compound which was tested alongside with SAE180 (data not shown).[40] This crystalline compound on the OTFs surface was found to be major cause for dose inaccuracy due to friction and thereby drug loss during storage or transportation. Therefore, matrix adsorbed drug as observed for SAE180 was considered

preferable for OTF products. 3D printed PLA or PVA based cylindric scaffolds 5 mm in diameter and 0.8 mm in height were produced using FDM technology. Physical compatibility of PVA scaffolds with drug containing ink was investigated and no recrystallization was observed in the polarized light microscope (**Figure 16**). However, changes in height and morphology were present after treatment what was attributed to its aqueous solubility and swelling in ethanol-water mixtures as it was reported for PVA membranes in a previous study.[100] Despite its favorable biocompatibility and usage in orthopedic devices, PVA was excluded from further investigations in this study.[101] Contrary, PLA scaffolds were assessed in the same manner and yielded no recrystallization of drug or change in morphology what was in line with PLA's limited aqueous solubility and previously reported insolubility in pure ethanol and other alcohols (**Figure 17** and **Figure 18**).[102] Applying the ethanol 70% (v/v) ink, SAE180 in two different concentrations (single and double layer printed), ciprofloxacin and combinations of both were printed on PLA scaffolds using a 2D nano dispenser system and on HPMC based OTF using the nano dispenser as well as an commercially available inkjet printer. Quantification of the drug load was carried out and compared to its theoretical values for nano dispenser printed samples (**Figure 19**). Overall, inkjet printed OTF demonstrated a lower variability in their drug loading compared to nano dispenser printed samples. While SAE180 concentration in single layer printed OTF w/ and w/o ciprofloxacin remained constant, SAE180 concentration in double layer printed samples w/ ciprofloxacin was significantly higher (**Figure 19A**). These findings are in contrast to the expected linearity of dispensed ink volume by the inkjet printer as judged by the doubling in SAE180 concentration for single and double layer printed OTF w/ ciprofloxacin linearity was initially assumed. Moreover, despite ciprofloxacin was applied in the same concentration (5 mg mL^{-1}) its quantified drug load was 10-fold lower compared to SAE180 (**Figure 19B**). In these lines, while a Hewlett-Packard printer was reported to demonstrated lower salbutamol doses for each additional layer of an aqueous ink, a recent study for the commercial Epson XP-760 inkjet printer (the very same used in this study) exhibited concentration and thereby dispensed volume linearity when dispensing doxorubicin in an aqueous ink.[44, 103] Conclusively, it remains to be investigated whether SAE180 concentration in batch SAE180 x2 was an outliner by falsely carrying out the printing process or simultaneously printing from multiple ink cartridges is not feasible in the Epson XP-760 inkjet printer. Comparing nano dispenser printed OTF to inkjet printed OTF revealed an increase in concentration by 2 orders of magnitude (**Figure 19C-D**). Briefly,

quantified drug loadings were significantly lower than what was calculated as theoretical values, while SAE180 concentration in single- and double layer printed SAE180 doubled as expected (**Figure 19C**). Ciprofloxacin drug loadings however were 2-fold higher than those SAE180 drug loadings quantified for a single layer despite being applied in the same concentration (**Figure 19D**). Similar trends were observed when comparing nano dispenser printed OTF and PLA scaffolds. Lower drug loadings than theoretical calculated as well as differences in drug loadings in single layer printed samples could be observed (**Figure 19E-F**). Furthermore, drug loading standard deviation of nano dispenser printed PLA scaffolds was overall higher compared to OTF samples, which was attributed to spillage observed during printing on the PLA samples. Herein, following the impact of the nanosized drops on PLA scaffolds, smaller droplets splashed from the surface on the surrounding printing bed. Aside from spillage, the printing process itself – especially deviations in dispensed volume – might have caused a decrease in drug loading compared to the theoretical values. Furthermore, adsorption of compound to the instrument e.g. plastic reservoir or tubes, and thereby decrease of the ink's concentration cannot be excluded as adsorption of SAE180 on labware was already reported.[4] Solid characterization of the printed specimen was carried out using XRPD and revealed no reflexes from SAE180 or ciprofloxacin on the PLA surface or OTF matrix (**Figure 20**). Conclusively, SAE180 and ciprofloxacin alone or in combination could be printed on PLA and HPMC based OTF surfaces and yielded homogenous products without indications for physical incompatibility or recrystallization what indicated an adsorption of the drug to the matrix. Drug loadings could be increased by printing several layers of drug containing ink on the scaffolds but did not match the theoretical calculated values. Moreover, robustness of the printing process was not achieved as drug loadings between several batches were not congruent.

Antibacterial activity of the SAE180 and ciprofloxacin printed PLA and OTF scaffolds was assessed on biofilm forming *S. aureus* strain ST228 and MRSA strains JE2 and Lac* using a zone of inhibition assay. In a previous study SAE180 already demonstrated growth inhibition activity towards these strains in µmolar concentration as well as biofilm inhibition towards ST228 in subinhibitory concentrations.[4] While blank OTF and PLA samples (negative controls) did not exhibit growth inhibition, all tested specimen showed antibacterial effects which where inferior to the vancomycin reference disk (**Figure 21**). It should be noted that the zone of inhibition is defined as the radial area around the tested

specimen where no bacterial growth is visible. In addition to this primary zone of inhibition a second zone with reduced bacterial growth was observed. This was the case for almost all samples except for commercial vancomycin disks and a second compound which was tested alongside with SAE180, the latter one not being included in this study. However, for samples containing SAE180 or ciprofloxacin alone or in combination, secondary zones were observed and included in the antibacterial evaluation. These zones of reduced growth were attributed to a gradual decrease in drug concentration from the center to the periphery in combination with potential effects on bacterial growth phenotype e.g. biofilm formation and was more pronounced in SAE180 containing samples. Furthermore, inkjet printed OTF samples did not show antibacterial activity in any tested bacterial strain (data not shown). For nano dispenser printed PLA and OTF samples, zones of inhibition without visible bacterial growth were constant throughout all strains, drug combinations and matrices despite OTF samples having a higher drug loading for SAE180 and ciprofloxacin. However, differences between the tested samples were observed when comparing the zones of reduced bacterial growth which were significantly lager for all OTF samples and some PLA samples (**Figure 21**, hatched bars). Herein, inconsistent antibacterial activity for PLA samples was potentially related to lower drug load and higher variability. A slight trend in susceptibility was recognized in between the different bacterial strains, Lac* being the most susceptible followed by JE2 and ST228, what was in line with a recent report on the antibacterial activity of SAE180.[4] Synergistic effects between SAE180 and ciprofloxacin could not be observed. Conclusively, all samples exhibited antibacterial activity when tested against three *S. aureus* strains, two of which were considered MRSA strains. Evaluation of the zone of inhibition yielded no significant differences in between the applied concentrations and combinations. However, zones of reduced growth were visible for all combinations what emphasized activity in subinhibitory concentrations for ciprofloxacin as well as SAE180.

Conclusion

Different pharmaceutical formulation strategies have been evaluated for anacardic acid derivatives and antibacterial activity of the resulting specimen was tested against one biofilm forming *S. aureus* strain and two MRSA strains. Salt formation experiments between anacardic acid derivatives and ciprofloxacin resulted in partly ionization but did not yield a salt with a single crystalline phase and were therefore not considered for further

development. 3D printing technology, a 2D nano dispenser system as well as a commercially available inkjet printer were utilized to print SAE180 alone or in combination with ciprofloxacin on HPMC based OTF stripes or PLA scaffolds. Except for the specimen printed with the commercial inkjet printer, all samples exhibited antibacterial activity towards the tested strains in a zone of inhibition assay. However, lower than theoretically calculated drug loadings indicated that more development will be necessary to ensure a robust printing process with the printing techniques used in this study.

Acknowledgments

References

1. Kubo, I.; Muroi, H.; Himejima, M.; Yamagiwa, Y.; Mera, H.; Tokushima, K.; Ohta, S.; Kamikawa, T. (1993) Structure Antibacterial Activity Relationships of Anacardic Acids. J. Agr. Food. Chem. 41 (6), 1016-1019.

2. Muroi, H.; Kubo, I. (1996) Antibacterial activity of anacardic acid and totarol, alone and in combination with methicillin, against methicillinresistantStaphylococcus aureus. J. of Appl. Bacteriol. 80 (4), 387-394.

3. Wisastra, R.; Kok, P. A.; Eleftheriadis, N.; Baumgartner, M. P.; Camacho, C. J.; Haisma, H. J.; Dekker, F. J. (2013) Discovery of a novel activator of 5-lipoxygenase from an anacardic acid derived compound collection. Bioorg. Med. Chem. 21 (24), 7763-78.

4. Saedtler, M.; Förtig, N.; Ohlsen, K.; Faber, F.; Masota, N.; Kowalick, K.; Holzgrabe, U.; Meinel, L. (2020) Antibacterial Anacardic Acid Derivatives. ACS Infect. Dis. 6 (7), 1674-1685.

5. Europe, C. o., European Pharmacopoeia (Ph. Eur.) 10th Edition. In *07 Dosage Forms*, Council of Europe: Strasbourg, 2020.

6. Kostewicz, E. S.; Abrahamsson, B.; Brewster, M.; Brouwers, J.; Butler, J.; Carlert, S.; Dickinson, P. A.; Dressman, J.; Holm, R.; Klein, S.; Mann, J.; McAllister, M. et al. (2014) In vitro models for the prediction of in vivo performance of oral dosage forms. Eur. J. Pharm. Sci. 57, 342-66.

7. Peterson, B.; Weyers, M.; Steenekamp, J. H.; Steyn, J. D.; Gouws, C.; Hamman, J. H. (2019) Drug Bioavailability Enhancing Agents of Natural Origin (Bioenhancers) that Modulate Drug Membrane Permeation and Pre-Systemic Metabolism. Pharmaceutics 11 (1), 33.

8. Gibaldi, M.; Boyes, R. N.; Feldman, S. (1971) Influence of first-pass effect on availability of drugs on oral administration. J. Pharm. Sci. 60 (9), 1338-40.

9. Anderson, S. D. (2018) Repurposing drugs as inhaled therapies in asthma. Adv. Drug Deliv. Rev. 133, 19-33.

10. Al-Tabakha, M. M. (2015) Future prospect of insulin inhalation for diabetic patients: The case of Afrezza versus Exubera. J. Control. Release 215, 25-38.

11. Kawabata, Y.; Wada, K.; Nakatani, M.; Yamada, S.; Onoue, S. (2011) Formulation design for poorly water-soluble drugs based on biopharmaceutics classification system: basic approaches and practical applications. Int. J. Pharm. 420 (1), 1-10.

12. Stahl, P. H.; Wermuth, C. G., *Handbook of Pharmaceutical Salts: Properties, Selection, and Use*. 2nd Ed. ed.; Wiley-VCH, VHCA: Weinheim, Zurich, 2011.

13. Serajuddin, A. T. (2007) Salt formation to improve drug solubility. Adv. Drug Deliv. Rev. 59 (7), 603-16.

14. Bastin, R. J.; Bowker, M. J.; Slater, B. J. (2000) Salt Selection and Optimisation Procedures for Pharmaceutical New Chemical Entities. Org. Process Res. Dev. 4 (5), 427-435.

15. de Gans, B. J.; Duineveld, P. C.; Schubert, U. S. (2004) Inkjet Printing of Polymers: State of the Art and Future Developments. Adv. Mater. 16 (3), 203-213.

16. Campbell, P. G.; Weiss, L. E. (2007) Tissue engineering with the aid of inkjet printers. Expert Opin. Biol. Ther. 7 (8), 1123-7.

17. Mironov, V.; Kasyanov, V.; Drake, C.; Markwald, R. R. (2008) Organ printing: promises and challenges. Regen. Med. 3 (1), 93-103.

18. Lin, S.; Chao, P. Y.; Chien, Y. W.; Sayani, S.; Kuma, S.; Mason, M.; Wes, T.; Yang, A.; Monkhouse, D. (2001) In vitro and in vivo evaluations of biodegradable implants for hormone replacement therapy: effect of system design and PK-PD relationship. AAPS PharmSciTech 2 (3), E16.

19. Sandler, N.; Salmela, I.; Fallarero, A.; Rosling, A.; Khajeheian, M.; Kolakovic, R.; Genina, N.; Nyman, J.; Vuorela, P. (2014) Towards fabrication of 3D printed medical devices to prevent biofilm formation. Int J. Pharm. 459 (1-2), 62-4.

20. Jones, D. (2007) Steps on the road to personalized medicine. Nat. Rev. Drug Discov. 6 (10), 770-771.

21. Wendt, F. R.; Pathak, G.; Sajantila, A.; Chakraborty, R.; Budowle, B. (2018) Global genetic variation of select opiate metabolism genes in self-reported healthy individuals. Pharmacogenomics J. 18 (2), 281-294.

22. Trenfield, S. J.; Awad, A.; Goyanes, A.; Gaisford, S.; Basit, A. W. (2018) 3D Printing Pharmaceuticals: Drug Development to Frontline Care. Trends Pharmacol. Sci. 39 (5), 440-451.

23. Seitz, H.; Rieder, W.; Irsen, S.; Leukers, B.; Tille, C. (2005) Three-dimensional printing of porous ceramic scaffolds for bone tissue engineering. J. Biomed. Mater. Res. B. Appl. Biomater. 74 (2), 782-8.

24. Melchels, F. P.; Feijen, J.; Grijpma, D. W. (2010) A review on stereolithography and its applications in biomedical engineering. Biomaterials 31 (24), 6121-30.

25. Fina, F.; Goyanes, A.; Madla, C. M.; Awad, A.; Trenfield, S. J.; Kuek, J. M.; Patel, P.; Gaisford, S.; Basit, A. W. (2018) 3D printing of drug-loaded gyroid lattices using selective laser sintering. Int. J. Pharm. 547 (1-2), 44-52.

26. Goyanes, A.; Buanz, A. B.; Hatton, G. B.; Gaisford, S.; Basit, A. W. (2015) 3D printing of modified-release aminosalicylate (4-ASA and 5-ASA) tablets. Eur. J. Pharm. Biopharm. 89, 157-62.

27. Goyanes, A.; Chang, H.; Sedough, D.; Hatton, G. B.; Wang, J.; Buanz, A.; Gaisford, S.; Basit, A. W. (2015) Fabrication of controlled-release budesonide tablets via desktop (FDM) 3D printing. Int. J. Pharm. 496 (2), 414-20.

28. Okwuosa, T. C.; Stefaniak, D.; Arafat, B.; Isreb, A.; Wan, K. W.; Alhnan, M. A. (2016) A Lower Temperature FDM 3D Printing for the Manufacture of Patient-Specific Immediate Release Tablets. Pharm. Res. 33 (11), 2704-12.

29. Pietrzak, K.; Isreb, A.; Alhnan, M. A. (2015) A flexible-dose dispenser for immediate and extended release 3D printed tablets. Eur. J. Pharm. Biopharm. 96, 380-7.

30. Solanki, N. G.; Tahsin, M.; Shah, A. V.; Serajuddin, A. T. M. (2018) Formulation of 3D Printed Tablet for Rapid Drug Release by Fused Deposition Modeling: Screening Polymers for Drug Release, Drug-Polymer Miscibility and Printability. J. Pharm. Sci. 107 (1), 390-401.

31. Di Prima, M.; Coburn, J.; Hwang, D.; Kelly, J.; Khairuzzaman, A.; Ricles, L. (2016) Additively manufactured medical products - the FDA perspective. 3D Print. Med. 2, 1.

32. Kolakovic, R.; Viitala, T.; Ihalainen, P.; Genina, N.; Peltonen, J.; Sandler, N. (2013) Printing technologies in fabrication of drug delivery systems. Expert Opin. Drug Deliv. 10 (12), 1711-23.

33. Planchette, C.; Pichler, H.; Wimmer-Teubenbacher, M.; Gruber, M.; Gruber-Woelfler, H.; Mohr, S.; Tetyczka, C.; Hsiao, W. K.; Paudel, A.; Roblegg, E.; Khinast, J. (2016) Printing medicines as orodispersible dosage forms: Effect of substrate on the printed micro-structure. Int. J. Pharm. 509 (1-2), 518-527.

34. Melendez, P. A.; Kane, K. M.; Ashvar, C. S.; Albrecht, M.; Smith, P. A. (2008) Thermal inkjet application in the preparation of oral dosage forms: dispensing of prednisolone solutions and polymorphic characterization by solid-state spectroscopic techniques. J. Pharm. Sci. 97 (7), 2619-36.

35. Goodall, S.; Chew, N.; Chan, K.; Auriac, D.; Waters, M. J. (2002) Aerosolization of protein solutions using thermal inkjet technology. J. Aerosol. Med. 15 (3), 351-7.

36. Wickstrom, H.; Palo, M.; Rijckaert, K.; Kolakovic, R.; Nyman, J. O.; Maattanen, A.; Ihalainen, P.; Peltonen, J.; Genina, N.; de Beer, T.; Lobmann, K.; Rades, T.; Sandler, N. (2015) Improvement of dissolution rate of indomethacin by inkjet printing. Eur. J. Pharm. Sci. 75, 91-100.

37. Arshad, M. S.; Shahzad, A.; Abbas, N.; AlAsiri, A.; Hussain, A.; Kucuk, I.; Chang, M. W.; Bukhari, N. I.; Ahmad, Z. (2020) Preparation and characterization of indomethacin loaded films by piezoelectric inkjet printing: a personalized medication approach. Pharm. Dev. Technol. 25 (2), 197-205.

38. Vakili, H.; Kolakovic, R.; Genina, N.; Marmion, M.; Salo, H.; Ihalainen, P.; Peltonen, J.; Sandler, N. (2015) Hyperspectral imaging in quality control of inkjet printed personalised dosage forms. Int. J. Pharm. (1-2), 244-9.

39. Genina, N.; Fors, D.; Palo, M.; Peltonen, J.; Sandler, N. (2013) Behavior of printable formulations of loperamide and caffeine on different substrates--effect of print density in inkjet printing. Int. J. Pharm 453 (2), 488-97.

40. Genina, N.; Janssen, E. M.; Breitenbach, A.; Breitkreutz, J.; Sandler, N. (2013) Evaluation of different substrates for inkjet printing of rasagiline mesylate. Eur. J. Pharm. Biopharm. 85 (3 Pt B), 1075-83.

41. Tarcha, P. J.; Verlee, D.; Hui, H. W.; Setesak, J.; Antohe, B.; Radulescu, D.; Wallace, D. (2007) The application of ink-jet technology for the coating and loading of drug-eluting stents. Ann. Biomed. Eng. 35 (10), 1791-9.

42. Boehm, R. D.; Miller, P. R.; Daniels, J.; Stafslien, S.; Narayan, R. J. (2014) Inkjet printing for pharmaceutical applications. Mater. Today 17 (5), 247-252.

43. Genina, N.; Fors, D.; Vakili, H.; Ihalainen, P.; Pohjala, L.; Ehlers, H.; Kassamakov, I.; Haeggstrom, E.; Vuorela, P.; Peltonen, J.; Sandler, N. (2012) Tailoring controlled-release oral dosage forms by combining inkjet and flexographic printing techniques. Eur. J. Pharm. Sci. 47 (3), 615-23.

44. Buanz, A. B.; Saunders, M. H.; Basit, A. W.; Gaisford, S. (2011) Preparation of personalized-dose salbutamol sulphate oral films with thermal ink-jet printing. Pharm. Res. 28 (10), 2386-92.

45. Hoffmann, E. M.; Breitenbach, A.; Breitkreutz, J. (2011) Advances in orodispersible films for drug delivery. Expert Opin. Drug Deliv. 8 (3), 299-316.

46. Singer, A. C.; Shaw, H.; Rhodes, V.; Hart, A. (2016) Review of Antimicrobial Resistance in the Environment and Its Relevance to Environmental Regulators. Front. Microbiol. 7, 1728.

47. Cassini, A.; Högberg, L. D.; Plachouras, D.; Quattrocchi, A.; Hoxha, A.; Simonsen, G. S.; Colomb-Cotinat, M.; Kretzschmar, M. E.; Devleesschauwer, B.; Cecchini, M.; Ouakrim, D. A.; Oliveira, T. C. et al. (2019) Attributable deaths and disability-adjusted life-years caused by infections with antibiotic-resistant bacteria in the EU and the European Economic Area in 2015: a population-level modelling analysis. Lancet Infect. Dis. 19 (1), 56-66.

48. Blair, J. M.; Webber, M. A.; Baylay, A. J.; Ogbolu, D. O.; Piddock, L. J. (2015) Molecular mechanisms of antibiotic resistance. Nat. Rev. Microbiol. 13 (1), 42-51.

49. Flemming, H. C.; Wingender, J. (2010) The biofilm matrix. Nat. Rev. Microbiol. 8 (9), 623-33.

50. Walters, M. C., 3rd; Roe, F.; Bugnicourt, A.; Franklin, M. J.; Stewart, P. S. (2003) Contributions of antibiotic penetration, oxygen limitation, and low metabolic activity to tolerance of Pseudomonas aeruginosa biofilms to ciprofloxacin and tobramycin. Antimicrob. Agents Chemother. 47 (1), 317-23.

51. McConoughey, S. J.; Howlin, R.; Granger, J. F.; Manring, M. M.; Calhoun, J. H.; Shirtliff, M.; Kathju, S.; Stoodley, P. (2014) Biofilms in periprosthetic orthopedic infections. Future Microbiol. 9 (8), 987-1007.

52. Walsh, C.; Wright, G. (2005) Introduction: antibiotic resistance. Chem. Rev. 105 (2), 391-4.

53. Landry, R. M.; An, D.; Hupp, J. T.; Singh, P. K.; Parsek, M. R. (2006) Mucin-Pseudomonas aeruginosa interactions promote biofilm formation and antibiotic resistance. Mol. Microbiol. 59 (1), 142-51.

54. James, G. A.; Swogger, E.; Wolcott, R.; Pulcini, E.; Secor, P.; Sestrich, J.; Costerton, J. W.; Stewart, P. S. (2008) Biofilms in chronic wounds. Wound Repair Regen. 16 (1), 37-44.

55. Zander, Z. K.; Becker, M. L. (2017) Antimicrobial and Antifouling Strategies for Polymeric Medical Devices. ACS Macro Lett. 7 (1), 16-25.

56. Bjarnsholt, T.; Kirketerp-Moller, K.; Jensen, P. O.; Madsen, K. G.; Phipps, R.; Krogfelt, K.; Hoiby, N.; Givskov, M. (2008) Why chronic wounds will not heal: a novel hypothesis. Wound Repair Regen. 16 (1), 2-10.

57. Gjodsbol, K.; Christensen, J. J.; Karlsmark, T.; Jorgensen, B.; Klein, B. M.; Krogfelt, K. A. (2006) Multiple bacterial species reside in chronic wounds: a longitudinal study. Int. Wound J. 3 (3), 225-31.

58. Choong, P. F.; Dowsey, M. M.; Carr, D.; Daffy, J.; Stanley, P. (2007) Risk factors associated with acute hip prosthetic joint infections and outcome of treatment with a rifampinbased regimen. Acta Orthop. 78 (6), 755-65.

59. Moran, G. J.; Krishnadasan, A.; Gorwitz, R. J.; Fosheim, G. E.; McDougal, L. K.; Carey, R. B.; Talan, D. A.; Group, E. M. I. N. S. (2006) Methicillin-resistant S. aureus infections among patients in the emergency department. N. Engl. J. Med. 355 (7), 666-74.

60. Lebeaux, D.; Ghigo, J. M.; Beloin, C. (2014) Biofilm-related infections: bridging the gap between clinical management and fundamental aspects of recalcitrance toward antibiotics. Microbiol. Mol. Biol. Rev. 78 (3), 510-43.

61. Hoiby, N.; Ciofu, O.; Johansen, H. K.; Song, Z. J.; Moser, C.; Jensen, P. O.; Molin, S.; Givskov, M.; Tolker-Nielsen, T.; Bjarnsholt, T. (2011) The clinical impact of bacterial biofilms. Int. J. Oral Sci. 3 (2), 55-65.

62. Wu, H.; Moser, C.; Wang, H. Z.; Hoiby, N.; Song, Z. J. (2015) Strategies for combating bacterial biofilm infections. Int. J. Oral Sci. 7 (1), 1-7.

63. Defoirdt, T. (2017) Quorum-Sensing Systems as Targets for Antivirulence Therapy. Trends Microbiol. 26 (4), 313-328.

64. Givskov, M.; de Nys, R.; Manefield, M.; Gram, L.; Maximilien, R.; Eberl, L.; Molin, S.; Steinberg, P. D.; Kjelleberg, S. (1996) Eukaryotic interference with homoserine lactone-mediated prokaryotic signalling. J. Bacteriol. 178 (22), 6618-22.

65. Fernandez, M.; Corral-Lugo, A.; Krell, T. (2018) The plant compound rosmarinic acid induces a broad quorum sensing response in Pseudomonas aeruginosa PAO1. Environ. Microbiol. 20, 4230-4244

66. Nicol, M.; Alexandre, S.; Luizet, J. B.; Skogman, M.; Jouenne, T.; Salcedo, S. P.; De, E. (2018) Unsaturated Fatty Acids Affect Quorum Sensing Communication System and Inhibit Motility and Biofilm Formation of Acinetobacter baumannii. Int. J. Mol. Sci. 19 (1) 214.

67. Manner, S.; Fallarero, A. (2018) Screening of Natural Product Derivatives Identifies Two Structurally Related Flavonoids as Potent Quorum Sensing Inhibitors against Gram-Negative Bacteria. Int. J. Mol. Sci. 19 (5), 1346.

68. Paharik, A. E.; Parlet, C. P.; Chung, N.; Todd, D. A.; Rodriguez, E. I.; Van Dyke, M. J.; Cech, N. B.; Horswill, A. R. (2017) Coagulase-Negative Staphylococcal Strain Prevents Staphylococcus aureus Colonization and Skin Infection by Blocking Quorum Sensing. Cell Host Microbe. 22 (6), 746-756 e5.

69. Percival, S. L.; Mayer, D.; Kirsner, R. S.; Schultz, G.; Weir, D.; Roy, S.; Alavi, A.; Romanelli, M. (2019) Surfactants: Role in biofilm management and cellular behaviour. Int. Wound J. 16 (3), 753-760.

70. Bellingeri, A.; Falciani, F.; Traspedini, P.; Moscatelli, A.; Russo, A.; Tino, G.; Chiari, P.; Peghetti, A. (2016) Effect of a wound cleansing solution on wound bed preparation and inflammation in chronic wounds: a single-blind RCT. J. Wound Care 25 (3), 160-168.

71. Kiran, G. S.; Sabarathnam, B.; Selvin, J. (2010) Biofilm disruption potential of a glycolipid biosurfactant from marine Brevibacterium casei. FEMS Immunol. Med. Microbiol. 59 (3), 432-8.

72. Banat, I. M.; De Rienzo, M. A.; Quinn, G. A. (2014) Microbial biofilms: biosurfactants as antibiofilm agents. Appl. Microbiol. Biotechnol. 98 (24), 9915-29.

73. Diaz De Rienzo, M. A.; Stevenson, P. S.; Marchant, R.; Banat, I. M. (2016) Pseudomonas aeruginosa biofilm disruption using microbial surfactants. J. Appl. Microbiol. 120 (4), 868-76.

74. Yang, Q.; Schultz, G. S.; Gibson, D. J. (2018) A Surfactant-Based Dressing to Treat and Prevent Acinetobacter baumannii Biofilms. J. Burn Care Res. 39 (5), 766-770.

75. Magill, S. S.; Edwards, J. R.; Bamberg, W.; Beldavs, Z. G.; Dumyati, G.; Kainer, M. A.; Lynfield, R.; Maloney, M.; McAllister-Hollod, L.; Nadle, J.; Ray, S. M.; Thompson, D. L. et al. (2014) Emerging Infections Program Healthcare-Associated, I.; Antimicrobial Use Prevalence Survey, T., Multistate point-prevalence survey of health care-associated infections. N. Engl. J. Med. 370 (13), 1198-208.

76. Pronovost, P.; Needham, D.; Berenholtz, S.; Sinopoli, D.; Chu, H.; Cosgrove, S.; Sexton, B.; Hyzy, R.; Welsh, R.; Roth, G.; Bander, J.; Kepros, J.; Goeschel, C. (2006) An intervention to decrease catheter-related bloodstream infections in the ICU. N. Engl. J. Med. 355 (26), 2725-32.

77. Kurtz, S.; Ong, K.; Lau, E.; Mowat, F.; Halpern, M. (2007) Projections of primary and revision hip and knee arthroplasty in the United States from 2005 to 2030. J. Bone Joint Surg. Am. 89 (4), 780-5.

78. Urish, K. L.; DeMuth, P. W.; Kwan, B. W.; Craft, D. W.; Ma, D.; Haider, H.; Tuan, R. S.; Wood, T. K.; Davis, C. M. (2016) 3rd, Antibiotic-tolerant Staphylococcus aureus Biofilm Persists on Arthroplasty Materials. Clin. Orthop. Relat. Res. 474 (7), 1649-56.

79. Mooney, J. A.; Pridgen, E. M.; Manasherob, R.; Suh, G.; Blackwell, H. E.; Barron, A. E.; Bollyky, P. L.; Goodman, S. B.; Amanatullah, D. F. (2018) Periprosthetic bacterial biofilm and quorum sensing. J. Orthop. Res. 36, 2331-2339.

80. Zimmerli, W.; Lew, P. D.; Waldvogel, F. A. (1984) Pathogenesis of foreign body infection. Evidence for a local granulocyte defect. J. Clin. Invest. 73 (4), 1191-200.

81. Gries, C. M.; Kielian, T. (2017) Staphylococcal Biofilms and Immune Polarization During Prosthetic Joint Infection. J. Am. Acad. Orthop. Surg. 25 Suppl 1, 20-24.

82. Mirza, Y. H.; Tansey, R.; Sukeik, M.; Shaath, M.; Haddad, F. S. (2016) Biofilm and the Role of Antibiotics in the Treatment of Periprosthetic Hip and Knee Joint Infections. (2016) Open Orthop. J. 10, 636-645.

83. Ngo, B. K. D.; Grunlan, M. A. (2017) Protein Resistant Polymeric Biomaterials. ACS Macro Lett. 6 (9), 992-1000.

84. Rodrigues, L. R. (2011) Inhibition of bacterial adhesion on medical devices. Adv. Exp. Med. Biol. 715, 351-67.

85. Asghari, F.; Samiei, M.; Adibkia, K.; Akbarzadeh, A.; Davaran, S. (2017) Biodegradable and biocompatible polymers for tissue engineering application: a review. Artif. Cells Nanomed. Biotechnol. 45 (2), 185-192.

86. Bernard, M.; Jubeli, E.; Pungente, M. D.; Yagoubi, N. (2018) Biocompatibility of polymer-based biomaterials and medical devices - regulations, in vitro screening and risk-management. Biomater. Sci. 6 (8), 2025-2053.

87. P. Pawar, R.; U. Tekale, S.; U. Shisodia, S.; T. Totre, J.; J. Domb, A. (2014) Biomedical Applications of Poly(Lactic Acid). Recent. Pat. Regen. Med. 4 (1), 40-51.

88. Scaffaro, R.; Lopresti, F.; Marino, A.; Nostro, A. (2018) Antimicrobial additives for poly(lactic acid) materials and their applications: current state and perspectives. Appl. Microbiol. Biotechnol. 102 (18), 7739-7756.

89. Wiest, J.; Saedtler, M.; Balk, A.; Merget, B.; Widmer, T.; Bruhn, H.; Raccuglia, M.; Walid, E.; Picard, F.; Stopper, H.; Dekant, W.; Luhmann, T. et al. (2017) Mapping the pharmaceutical design space by amorphous ionic liquid strategies. J. Control. Release 268, 314-322.

90. Gottlieb, H. E.; Kotlyar, V.; Nudelman, A. (1997) NMR chemical shifts of common laboratory solvents as trace impurities. J. Org. Chem. 62 (21), 7512-7515.

91. Moreira, D. N.; Fresno, N.; Pérez-Fernández, R.; Frizzo, C. P.; Goya, P.; Marco, C.; Martins, M. A. P.; Elguero, J. (2015) Brønsted acid–base pairs of drugs as dual ionic liquids: NMR ionicity studies. Tetrahedron 71 (4), 676-685.

92. Zhang, G.; Zhang, L.; Yang, D.; Zhang, N.; He, L.; Du, G.; Lu, Y. (2016) Salt screening and characterization of ciprofloxacin. Acta Crystallogr. B. Struct. Sci. Cryst. Eng. Mater. 72 (Pt 1), 20-8.

93. Reddy, J. S.; Ganesh, S. V.; Nagalapalli, R.; Dandela, R.; Solomon, K. A.; Kumar, K. A.; Goud, N. R.; Nangia, A. (2011) Fluoroquinolone salts with carboxylic acids. J. Pharm. Sci. (8), 3160-76.

94. Paluch, K. J.; McCabe, T.; Muller-Bunz, H.; Corrigan, O. I.; Healy, A. M.; Tajber, L. (2013) Formation and physicochemical properties of crystalline and amorphous salts with different stoichiometries formed between ciprofloxacin and succinic acid. Mol. Pharm. 10 (10), 3640-54.

95. Surov, A. O.; Manin, A. N.; Voronin, A. P.; Drozd, K. V.; Simagina, A. A.; Churakov, A. V.; Perlovich, G. L. (2015) Pharmaceutical salts of ciprofloxacin with dicarboxylic acids. Eur. J. Pharm. Sci. 77, 112-21.

96. Ross, D.; Riley, C. (1990) Aqueous solubilities of some variously substituted quinolone antimicrobials. Int. J. Pharm. 63 (3), 237-250.

97. North, D. S.; Fish, D. N.; Redington, J. J. (1998) Levofloxacin, a second-generation fluoroquinolone. Pharmacotherapy 18 (5), 915-935.

98. Childs, S. L.; Stahly, G. P.; Park, A. (2007) The salt-cocrystal continuum: the influence of crystal structure on ionization state. Mol. Pharm. 4 (3), 323-38.

99. Koeppe, M. O.; Cristofoletti, R.; Fernandes, E. F.; Storpirtis, S.; Junginger, H. E.; Kopp, S.; Midha, K. K.; Shah, V. P.; Stavchansky, S.; Dressman, J. B.; Barends, D. M. (2011) Biowaiver monographs for immediate release solid oral dosage forms: levofloxacin. J. Pharm. Sci. 100 (5), 1628-36.

100. Praptowidodo, V. S. (2005) Influence of swelling on water transport through PVA-based membrane. J. Mol. Struct. 739 (1-3), 207-212.

101. Baker, M. I.; Walsh, S. P.; Schwartz, Z.; Boyan, B. D. (2012) A review of polyvinyl alcohol and its uses in cartilage and orthopedic applications. J. Biomed. Mater. Res. B. Appl. Biomater. 100 (5), 1451-7.

102. Sato, S.; Gondo, D.; Wada, T.; Kanehashi, S.; Nagai, K. (2013) Effects of various liquid organic solvents on solvent-induced crystallization of amorphous poly(lactic acid) film. J. Appl. Polym. Sci. 129 (3), 1607-1617.

103. Rosqvist, E.; Niemela, E.; Frisk, J.; Oblom, H.; Koppolu, R.; Abdelkader, H.; Soto Veliz, D.; Mennillo, M.; Venu, A. P.; Ihalainen, P.; Aubert, M.; Sandler, N. et al. (2020) A low-cost paper-based platform for fast and reliable screening of cellular interactions with materials. J. Mater. Chem. B. 8 (6), 1146-1156.

Supporting information

^{1}H NMR data

Figure S 1 ^{1}H-NMR of SAE195 (400 MHz, DMSO-d$_6$, δ [ppm], J [Hz]) δ 7.15 (t, J = 8.3 Hz, 1H), 6.46 (t, J = 7.9 Hz, 2H), 3.94 (t, J = 6.4 Hz, 2H), 1.69 – 1.62 (m, 2H), 1.44 – 1.35 (m, 2H), 1.31 – 1.25 (m, 4H), 0.87 (dd, J = 9.1, 4.8 Hz, 3H).

Figure S 2 ^{1}H NMR of SAE181 (400 MHz, DMSO-d$_6$, δ [ppm], J [Hz]) δ 7.16 (t, J = 8.3 Hz, 1H), 6.47 (t, J = 7.5 Hz, 2H), 3.94 (t, J = 6.4 Hz, 2H), 1.70 – 1.61 (m, 2H), 1.41 – 1.34 (m, 2H), 1.31 – 1.26 (m, 8H), 0.86 (t, J = 6.8 Hz, 3H).
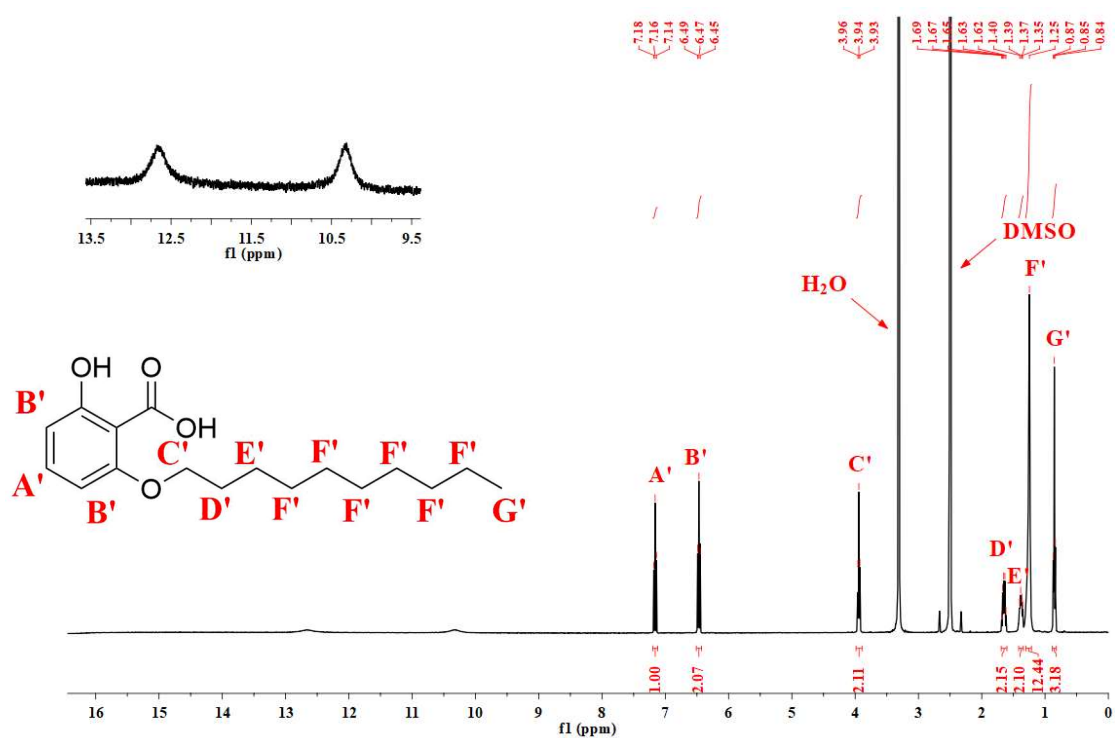
Figure S 3 ^{1}H NMR of SAE180 (400 MHz, DMSO-d$_6$, δ [ppm], J [Hz]) δ 7.16 (t, J = 8.3 Hz, 1H), 6.47 (t, J = 8.2 Hz, 2H), 3.94 (t, J = 6.4 Hz, 2H), 1.69 – 1.60 (m, 2H), 1.42 – 1.34 (m, 2H), 1.31 – 1.23 (m, 12H), 0.85 (t, J = 6.9 Hz, 3H).
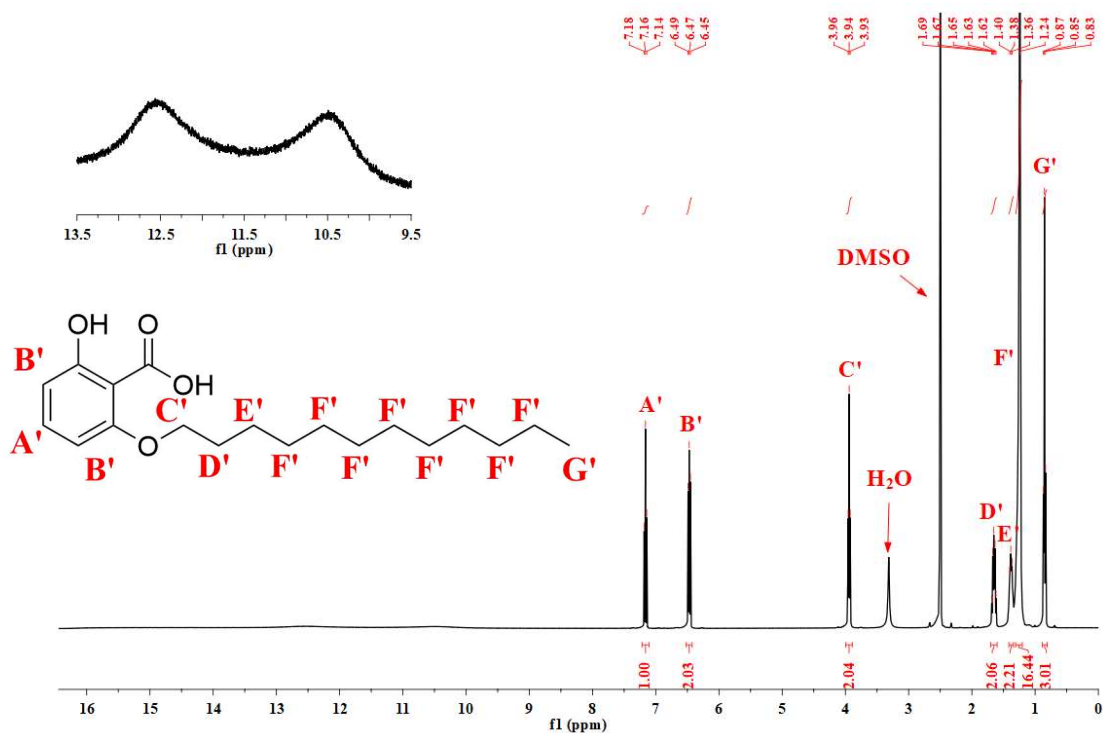
Figure S 4 ^{1}H NMR (400 MHz, DMSO-d$_6$, δ [ppm], J [Hz]) δ 7.16 (t, J = 8.3 Hz, 1H), 6.47 (t, J = 7.0 Hz, 2H), 3.94 (t, J = 6.4 Hz, 2H), 1.70 – 1.60 (m, 2H), 1.43 – 1.33 (m, 2H), 1.31 – 1.20 (m, 16H), 0.85 (t, J = 6.8 Hz, 3H).
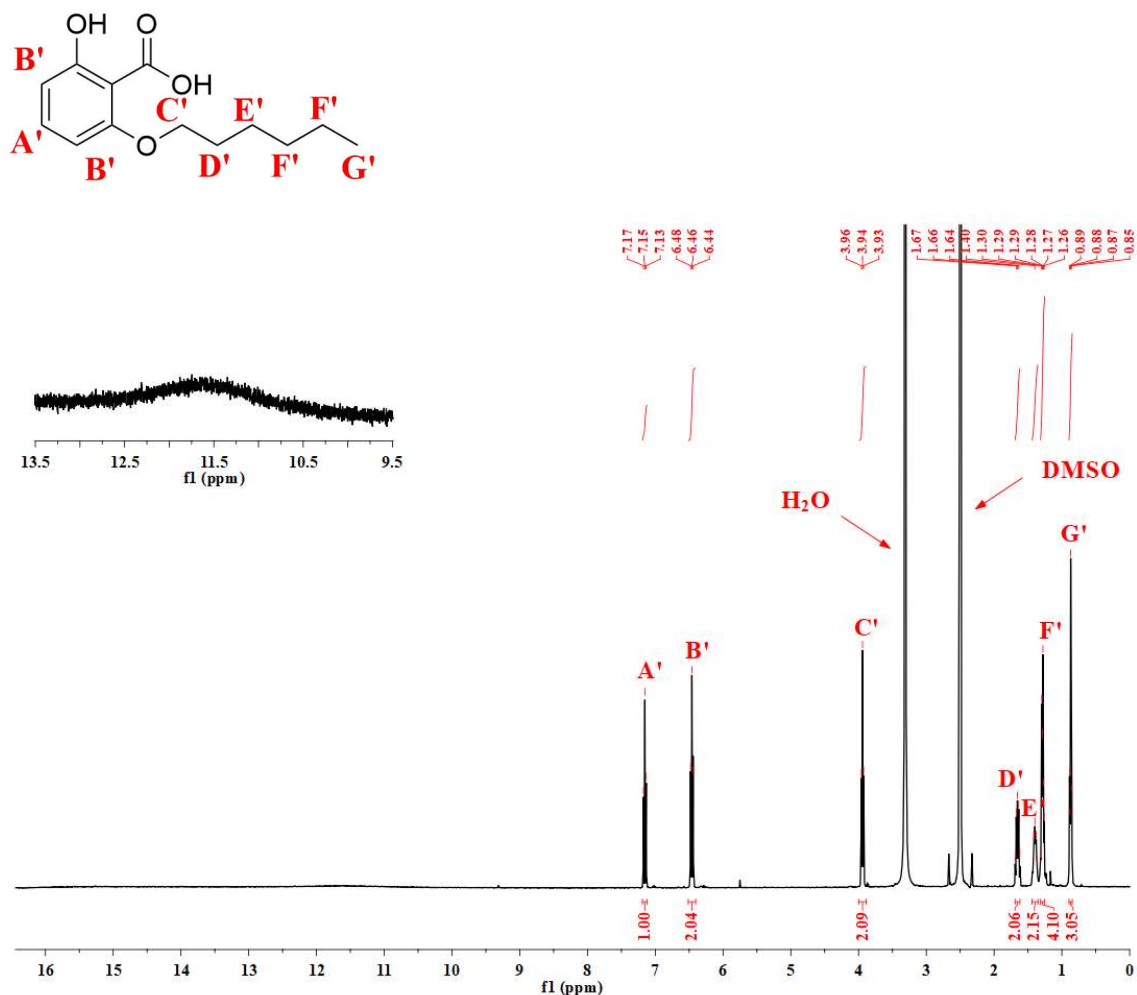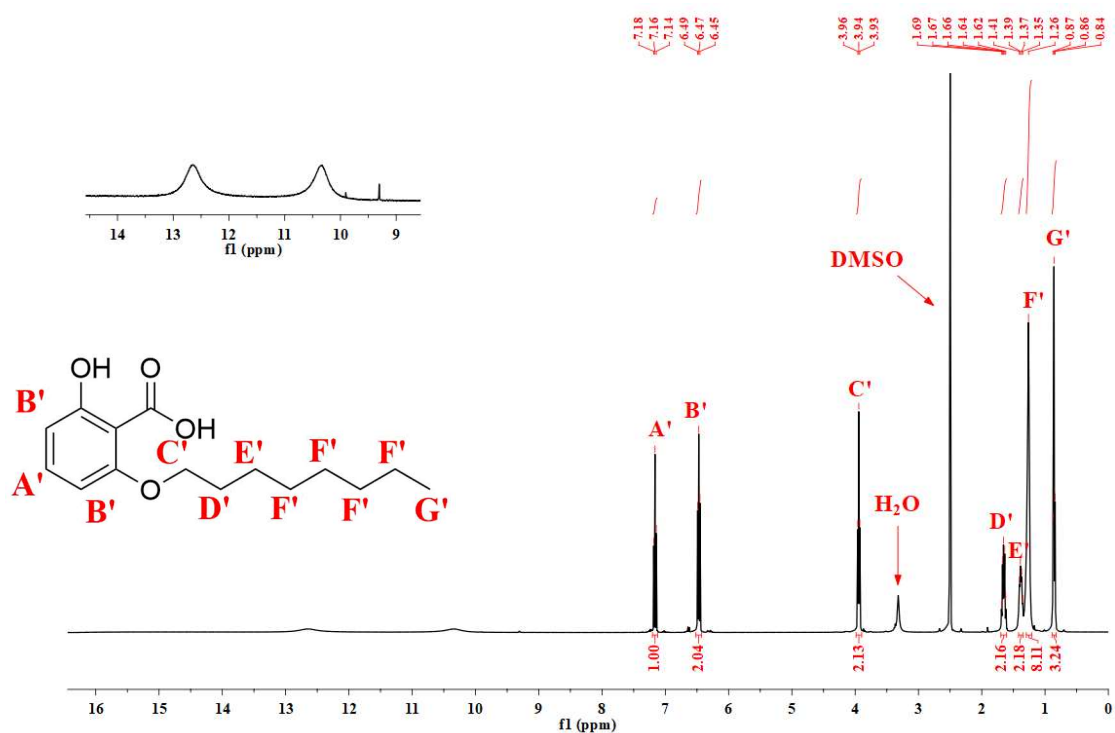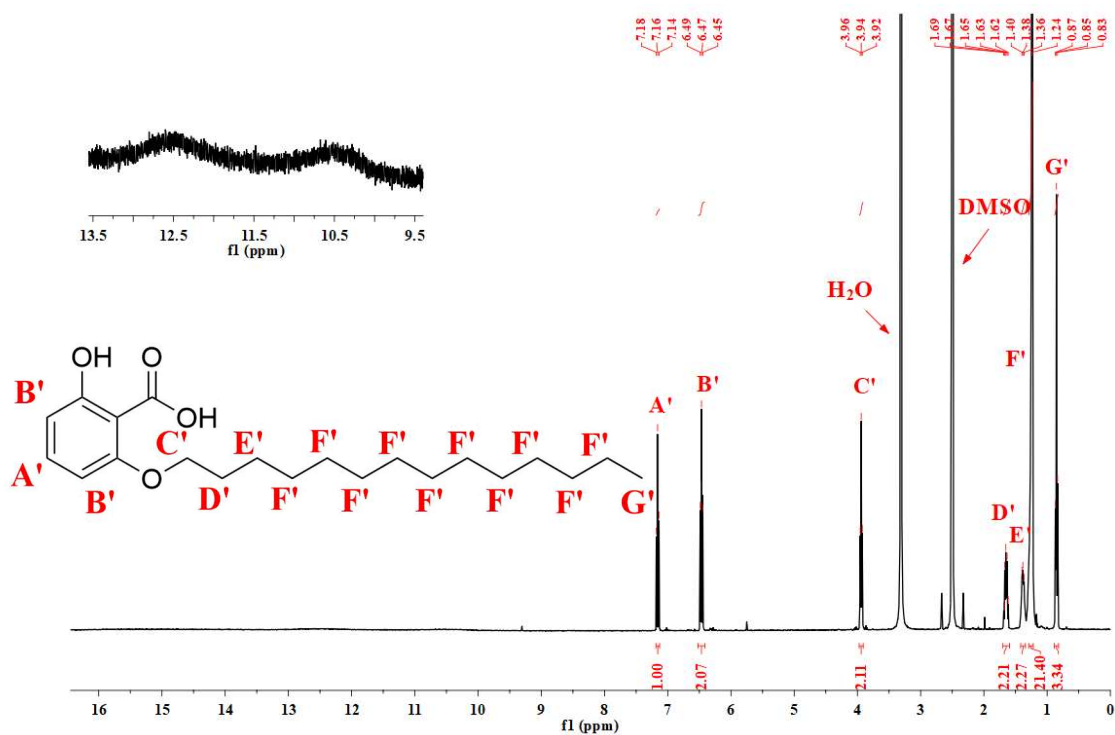

Figure S 5 ^{1}H NMR of SAE197 (400 MHz, DMSO-d$_6$, δ [ppm], J [Hz]) δ 7.16 (t, J = 8.3 Hz, 1H), 6.47 (t, J = 7.9 Hz, 2H), 3.94 (t, J = 6.4 Hz, 2H), 1.70 – 1.60 (m, 2H), 1.42 – 1.34 (m, 2H), 1.31 – 1.20 (m, 20H), 0.85 (t, J = 6.9 Hz, 3H).
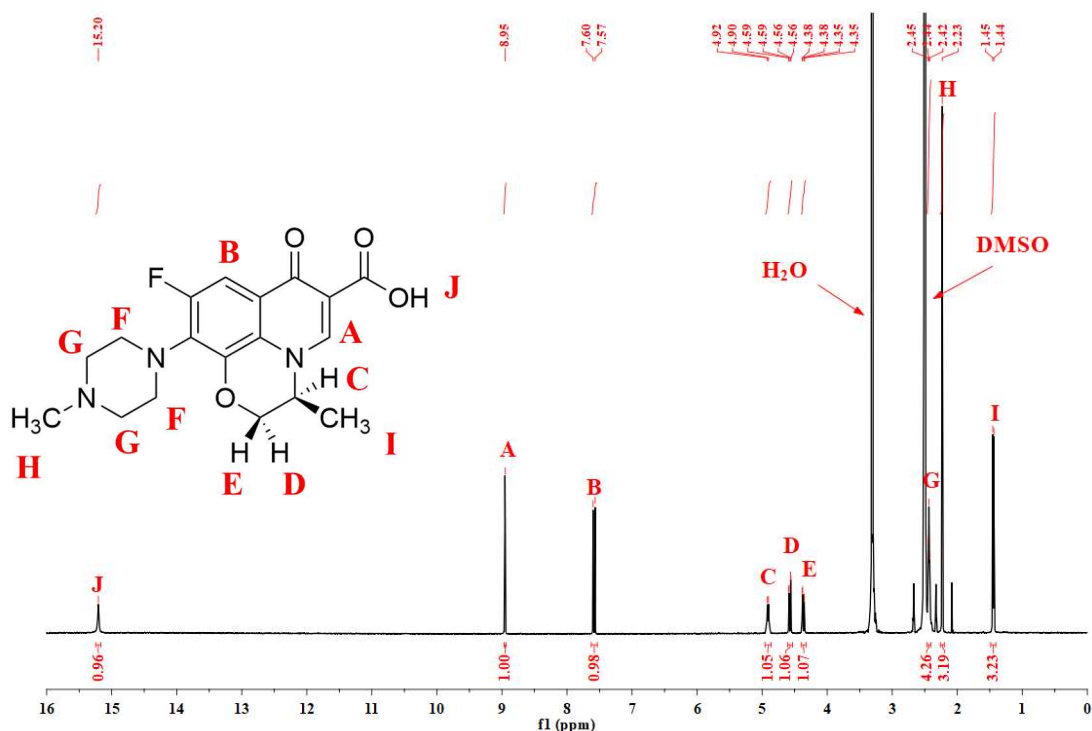
Figure S 6 ¹H NMR of Levofloxacin (400 MHz, DMSO-d₆, δ [ppm], J [Hz]) δ 15.20 (s, 1H), 8.95 (s, 1H), 7.58 (d, J = 12.4 Hz, 1H), 4.91 (d, J = 6.8 Hz, 1H), 4.57 (dd, J = 11.5, 1.7 Hz, 1H), 4.37 (dd, J = 11.5, 2.3 Hz, 1H), 2.44 (t, J = 4.6 Hz, 4H), 2.23 (s, 3H), 1.45 (d, J = 6.8 Hz, 3H).
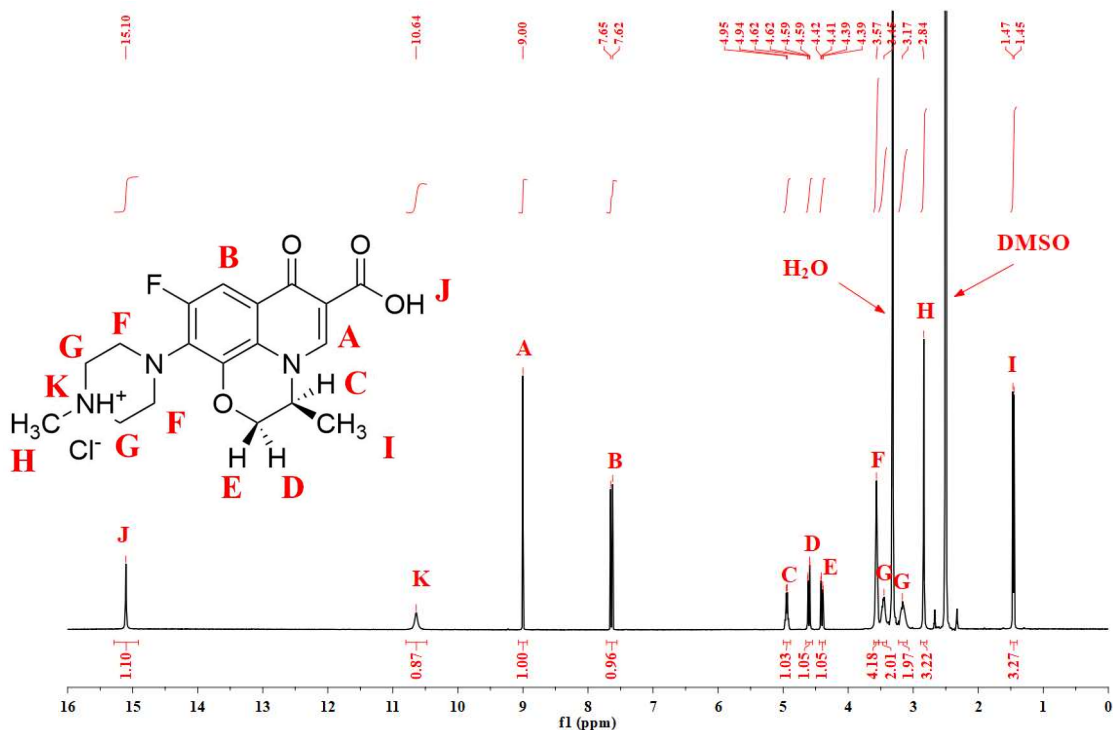
Figure S 7 ¹H NMR of Levofloxacin • HCl • H₂O (400 MHz, DMSO-d₆, δ [ppm], J [Hz]) δ 15.10 (s, 1H), 10.64 (s, 1H), 9.00 (s, 1H), 7.64 (d, J = 12.1 Hz, 1H), 4.94 (d, J = 6.8 Hz, 1H), 4.60 (dd, J = 11.5, 1.6 Hz, 1H), 4.40 (dd, J = 11.4, 2.2 Hz, 1H), 3.60 – 3.53 (m, 4H), 3.51 – 3.41 (m, 2H), 3.21 – 3.10 (m, 2H), 2.84 (s, 3H), 1.46 (d, J = 6.8 Hz, 3H).

Solubility screening

Table S 1 Solubilities of SAE180 and SAE196 in water and different alcohols. Values are shown in mg mL^{-1}.

	DI water	Methanol	Ethanol	Ethanol 70%*	Ethanol 50%*	Ethanol 30%*	Isopropanol
SAE180	5	≥ 50	≥ 50	≥ 50	30	20	50
SAE196	< 1	40	≥ 50	< 1	< 1	< 1	50

* %(v/v)

Table S 2 Solubilities of SAE180 and SAE196 in different organic solvents. Values are shown in mg mL^{-1}.

	Acetone	Dimethyl sulfoxide	Ethyl acetate	Aceto-nitrile	Diethyl ether	n-Hexane
SAE180	≥ 50	≥ 50	≥ 50	≥ 50	≥ 50	≥ 50
SAE196	≥ 50	≥ 50	≥ 50	≥ 50	≥ 50	≥ 50

Nano dispenser batches

Table S 3 Measured single drop size in nL and theoretical calculated values for applied volume in µL, applied drug in µg and drug loading in µg cm^{-2} during nano dispenser print on OTF. 800 droplets were printed in a single print and 1600 droplets in a double print on a total area 800 mm². Values are displayed as geometrical mean ± standard deviation.

	SAE180	SAE180 x2	SAE180 + CIP[a]	SAE180 x2 + CIP[a]	CIP	Control
Drop size nL	73.80 ± 3.54	73.80 ± 3.54	72.48 ± 0.67	72.48 ± 0.67	67.61 ± 2.14	65. 83 ± 1.3
Appl. Volume µL	59.1 ± 2.8	118.1 ± 5.7	58.0 ± 0.5	116.0 ± 1.1	54.1 ± 1.7	52.7 ± 1.0
Appl. drug µg	295.2 ± 14.1	590.4 ± 28.3	289.9 ± 2.7	579.8 ± 5.4	270.4 ± 8.6	-

	SAE180	SAE180 x2	SAE180 + CIP[a]	SAE180 x2 + CIP[a]	CIP	Control
Drug loading **µg cm⁻²**	369 ± 17.6	738 ± 35.4	362.4 ± 3.4	724.8 ± 6.8	338.0 ± 10.8	-

[a] Ciprofloxacin loading is equivalent to CIP column

Table S 4 Measured single drop size in nL and theoretical calculated values for applied volume in µL, applied drug in µg and drug loading in µg cm⁻² during nano dispenser print on PLA scaffolds. 60 droplets were printed in a single print and 120 droplets in a double print on a total area 39 mm². Values are displayed as geometrical mean ± standard deviation.

	SAE180	SAE180 x2	SAE180 + CIP[a]	SAE180 x2 + CIP[a]	CIP	Control
Drop size **nL**	66.81 ± 1.83	66.81 ± 1.83	66.81 ± 1.83	66.81 ± 1.83	66.93 ± 1.45	67.80 ± 2.14
Appl. Volume **µL**	4.01 ± 0.11	8.02 ± 0.22	4.01 ± 0.11	8.02 ± 0.22	4.02 ± 0.09	4.07 ± 0.13
Appl. drug **µg**	20.04 ± 0.55	40.09 ± 1.10	20.04 ± 0.55	40.09 ± 1.10	20.08 ± 0.44	-
Drug loading **µg cm⁻²**	51.34 ± 1.41	102.79 ± 2.82	51.34 ± 1.41	102.79 ± 2.82	51.34 ± 1.41	-

[a] Ciprofloxacin loading is equivalent to CIP column

Zone of Inhibition data

Table S 5 Zone of Inhibition data for nano dispenser printed OTF against *S. aureus* strain JE2. Results are shown as diameter in mm and mean is displayed as geometrical mean ± standard deviation.

Specimen	Inhibition				Reduced growth			
	1	2	3	mean	1	2	3	mean
SAE180	7	6	7	6.7 ± 0.6	14	12	15	13.7 ± 1.5
SAE180 + CIP	5	5	5	5.0 ± 0	14	12	12	12.7 ± 1.2
SAE180 x2	7	7	7	7.0 ± 0	15	15	14	14.7 ± 0.6
SAE180 x2 + CIP	6	6	6	6.0 ± 0	15	14	15	14.7 ± 0.6
CIP	0	0	6	2.0 ± 3.5	11	11	10	10.7 ± 0.6

CIP = ciprofloxacin hydrochloride

Table S 6 Zone of Inhibition data for nano dispenser printed OTF *S. aureus* strain Lac*. Results are shown as diameter in mm and mean is displayed as geometrical mean ± standard deviation.

Specimen	Inhibition				Reduced growth			
	1	2	3	mean	1	2	3	mean
SAE180	6	6	5	5.7 ± 0.6	13	13	13	13 ± 0.0
SAE180 + CIP	6	6	6	6 ± 0.0	12	13	15	13.3 ± 1.5
SAE180 x2	6	6	6	6 ± 0.0	16	17	17	16.7 ± 0.6
SAE180 x2 + CIP	6	6	6	6 ± 0.0	15	16	18	16.3 ± 1.5
CIP	0	0	0	0	10	11	7	9.3 ± 2.1

CIP = ciprofloxacin hydrochloride

Table S 7 Zone of Inhibition data for nano dispenser printed OTF against *S. aureus* strain ST228. Results are shown as diameter in mm and mean is displayed as geometrical mean ± standard deviation.

Specimen	Inhibition				Reduced growth			
	1	2	3	mean	1	2	3	mean
SAE180	6	6	6	6 ± 0.0	11	11	11	11.0 ± 0.0
SAE180 + CIP	5	5	6	5.3 ± 0.6	10	9	12	10.3 ± 1.5
SAE180 x2	6	7	6	6.3 ± 0.6	12	12	14	12.7 ± 1.2
SAE180 x2 + CIP	6	6	6	6 ± 0.0	12	12	13	12.3 ± 0.6
CIP	0	0	0	0 ± 0.0	10	6	6	7.3 ± 2.3

CIP = ciprofloxacin hydrochloride

Table S 8 Zone of Inhibition data for nano dispenser printed PLA scaffolds against *S. aureus* strain JE2. Results are shown as diameter in mm and mean is displayed as geometrical mean ± standard deviation.

Specimen	Inhibition				Reduced growth			
	1	2	3	mean	1	2	3	mean
SAE180	6	6	7	6.3 ± 0.6	8	7	11	8.7 ± 2.1
SAE180 + CIP	6	6	6	6 ± 0.0	13	12	22	15.7 ± 5.5
SAE180 x2	6	6	7	6.3 ± 0.6	8	7	11	8.7 ± 2.1
SAE180 x2 + CIP	6	6	6	6 ± 0.0	15	16	22	17.7 ± 3.8
CIP	6	6	6	6 ± 0.0	11	10	11	10.7 ±.6

CIP = ciprofloxacin hydrochloride

Table S 9 Zone of Inhibition data for nano dispenser printed PLA scaffolds against *S. aureus* strain Lac*. Results are shown as diameter in mm and mean is displayed as geometrical mean ± standard deviation.

Specimen	Inhibition				Reduced growth			
	1	2	3	mean	1	2	3	mean
SAE180	7	6	7	6.7 ± 0.6	12	11	14	12.3 ± 1.5
SAE180 + CIP	6	5	6	5.7 ± 0.6	14	17	18	16.3 ± 2.1
SAE180 x2	8	8	6	7.3 ± 1.2	14	13	15	14.0 ± 1.0
SAE180 x2 + CIP	7	6	6	6.3 ± 0.6	15	13	18	15.3 ± 2.5
CIP	6	6	6	6 ± 0.0	13	16	9	12.7 ± 3.5

CIP = ciprofloxacin hydrochloride

Table S 10 Zone of Inhibition data for nano dispenser printed PLA scaffolds against *S. aureus* strain ST228. Results are shown as diameter in mm and mean is displayed as geometrical mean ± standard deviation.

Specimen	Inhibition				Reduced growth			
	1	2	3	mean	1	2	3	mean
SAE180	7	6	6	6.3 ± 0.6	14	16	8	12.7 ± 4.2
SAE180 + CIP	6	7	6	6.3 ± 0.6	14	15	16	15.0 ± 1.0
SAE180 x2	6	7	6	6.3 ± 0.6	13	15	16	14.7 ± 1.5
SAE180 x2 + CIP	6	6	6	6 ± 0.0	16	15	16	15.7 ± 0.6
CIP	6	9	6	7.0 ± 1.7	0	0	0	0 ± 0.0

CIP = ciprofloxacin hydrochloride

Table S 11 Zone of Inhibition data for controls against *S. aureus* strains JE2, Lac* and ST228. Results are shown as diameter in mm and mean is displayed as geometrical mean ± standard deviation.

Specimen	JE2				Lac*				ST228			
	1	2	3	mean	1	2	3	mean	1	2	3	mean
Vancomycin	18	18	16	17.3 ± 1.2	16	16	17	16.3 ± 0.6	16	15	20	17.0 ± 2.6
OTF control	0	0	0	0 ± 0.0	0	0	0	0 ± 0.0	0	0	0	0 ± 0.0
PLA control	0	0	0	0 ± 0.0	0	0	0	0 ± 0.0	0	0	0	0 ± 0.0

Chapter IV: Pharmaceutical formulation using salt metathesis and 2D/3D printing techniques

Conclusion and outlook

Salt formation is a routinely applied and well-established strategy in the pharmaceutical development of new drug candidates and lead to an estimated proportion of 50% of all marketed solid drug formulations being salts.[1] Fast dissolution rates and increased aqueous solubility often results in a higher bioavailability compared to the parent drug. Ionic liquids are salts with a melting point below 100 °C.[2] Their counterions are often sterically demanding and result in amorphous salts. Their dissolution rate is typically high attributed to their low lattice forces i.e. high energy while the influence on the pH in the aqueous boundary layer is negligible compared to classical salts with small inorganic counterions.[3] Controlling bioavailability as well as release kinetics e.g. immediate release or sustained release by selection of different counterions has already been reported.[4] Herein, solubilization of the drug molecules by complexation in solution is the key parameter driving and maintaining supersaturated states. This finding is very similar to the human body's system of aggregation and micellization for poorly water-soluble, highly lipophilic drugs with amphiphilic bile acids.[5] Investigations for individual drug candidates and adapting natures very own mechanisms to increase bioavailability could potentially lead to very sophisticated drug delivery approaches in the near future. However, salt formation is not applicable for non-ionizable compounds and depends on a sufficient difference between pK_a values of drug and counterion as well as the crystal environment in the resulting salt.[6] Co-crystals have been described as non-ionized alternative to salts demonstrating comparable effects on dissolution rate and apparent solubility.[7] The herein presented anacardic acid derivatives could not be used to prepare salts or co-crystals of fluoroquinolone antibiotics ciprofloxacin, norfloxacin or levofloxacin. While partial ionization was observed for all tested formulations, no metathesis yielded a single crystalline phase, what was considered non-sufficient. However, salt preparation was reported for several fluoroquinolones with small, highly acidic counterions.[8] Retroperspectively, three main reasons were identified for the non-successful salt formation (i) fluoroquinolones with their high melting crystalline structure, low aqueous solubility and zwitterionic nature, (ii) the highly lipophilic, surfactant-likes structure of the anacardic acid derivatives and (iii) the technique of metathesis from solution itself. The latter one being interesting for further investigations on other techniques for metathesis or co-crystal formation. In these lines, fast evaporation, mechanochemical approaches e.g. solid and liquid assisted grinding or co-crystal formation

from slurry could potentially lead to a single crystalline phase in a ionized salt or non-ionized co-crystal.[9-11] However, the salt/co-crystal formation screening should be accompanied by an initial assessment of the potential synergistic antibacterial activity between counterion and antibiotic. While physicochemical properties most likely will be influenced by salt formation with the respective counterion, an increased antibacterial activity or biofilm inhibition in combination strongly relies on the selected antibiotic drug as well as the targeted bacteria. Therefore, including other antibiotics inheriting a basic position such as aminopenicillins, cephalosporins or tetracycline antibiotics could first of all yield synergistic effects and secondly used for the preparation of salts or co-crystals with anacardic acid derivatives.

Novel techniques for drug delivery are tackling the challenges of modern drug discovery, where *in silico* computation, high throughput screening and biological entities yield larger, more lipophilic and in general more complex structures. In this context, 2D/3D printing techniques are on the rise for two decades and already have been commercially available for industrial and private use. Pharmaceutical companies as well as academia is currently investigating the possibilities of this technique to reshape the production and distribution of medication. Moreover, the first 3D printed dosage form was already approved by the FDA paving the way for others to follow.[12] Several studies reported 2D printing as tool to print drugs on diverse matrices i.e. substrates.[13-15] Improving quality management, regulatory aspects and the overall robustness of the printing process could move the batchwise production in the pharmaceutical companies to a decentralized production e.g. in pharmacies. Personalized medicine including dose-adjustment or combination of compatible drugs on a single dosage form could improve therapy effectiveness as well as compliance of the patient. Furthermore, different drugs have been already implemented into polymeric structures using 3D printing techniques.[16] Considering invasive medical devices being a major cause for nosocomial infections, deaths and increasing healthcare costs, printing of implantable medical devices with incorporated antibiotics becomes a favorable strategy.[17] The herein presented 2D/3D printing experiments with one anacardic acid derivative and ciprofloxacin yielded antibacterial oral thin films and polylactic acid specimen. While no physical incompatibilities were observed between ink, drug and matrix, antibacterial properties could be preserved. The tested inkjet and nano dispenser 2D printing techniques were found to be non-linear in volume/dose dispensing with the second one being more inaccurate. In comparison, the solenoid-based valve in the nano dispenser could provide

higher drug loadings while higher dose accuracy was observed for the inkjet printer. Further studies will be necessary to develop and improve this drug printing process.

Conclusively, drug formulation of complex active pharmaceutical ingredients is increasingly demanding under the recent developments. Novel therapeutics and high demands in the healthcare systems require flexible development while minimizing costs. However, quality standards have to be improved wherever possible and at all costs to reduce preventable harm to the patient. In these lines, balancing profit and innovation is key for developing medication, especially when tackling modern challenges such as the antibiotic crisis. However, it is in the hands of the pharmaceutical industry and academia to ensure that the development of new antibiotics and novel strategies for antibiotic treatment continues to be investigated, despite not been financially attractive.

References

1. Stahl, P. H.; Wermuth, C. G., *Handbook of Pharmaceutical Salts: Properties, Selection, and Use*. 2nd Ed. ed.; Wiley-VCH, VHCA: Weinheim, Zurich, 2011.

2. Hough, W. L.; Rogers, R. D.(2007) Ionic Liquids Then and Now: From Solvents to Materials to Active Pharmaceutical Ingredients. B. Chem. Soc. Jpn. 80 (12), 2262-2269.

3. Saedtler, M.; Meinel, L. (2019) Amorphous Ionic Liquid Strategies for Pharmaceutical Application. In: Zhang S. (eds) *Encyclopedia of Ionic Liquids*. Springer, Singapore. https://doi.org/10.1007/978-981-10-6739-6_2-1

4. Wiest, J.; Saedtler, M.; Balk, A.; Merget, B.; Widmer, T.; Bruhn, H.; Raccuglia, M.; Walid, E.; Picard, F.; Stopper, H.; Dekant, W.; Luhmann, T.; Sotriffer, C.; Galli, B.; Holzgrabe, U.; Meinel, L. (2017) Mapping the pharmaceutical design space by amorphous ionic liquid strategies. J. Control. Release 268, 314-322.

5. Wiest, J.; Saedtler, M.; Bottcher, B.; Grune, M.; Reggane, M.; Galli, B.; Holzgrabe, U.; Meinel, L. (2018) Geometrical and Structural Dynamics of Imatinib within Biorelevant Colloids. Mol. Pharm. 15 (10), 4470-4480.

6. Childs, S. L.; Stahly, G. P.; Park, A. (2007) The salt-cocrystal continuum: the influence of crystal structure on ionization state. Mol. Pharm. 4 (3), 323-38.

7. Reggane, M.; Wiest, J.; Saedtler, M.; Harlacher, C.; Gutmann, M.; Zottnick, S. H.; Piechon, P.; Dix, I.; Muller-Buschbaum, K.; Holzgrabe, U.; Meinel, L.; Galli, B. (2018) Bioinspired co-crystals of Imatinib providing enhanced kinetic solubility. Eur. J. Pharm. Biopharm. 128, 290-299.

8. Surov, A. O.; Manin, A. N.; Voronin, A. P.; Drozd, K. V.; Simagina, A. A.; Churakov, A. V.; Perlovich, G. L. (2015) Pharmaceutical salts of ciprofloxacin with dicarboxylic acids. Eur. J. Pharm. Sci. 77, 112-21.

9. Bag, P. P.; Patni, M.; Malla Reddy, C. (2011) A kinetically controlled crystallization process for identifying new co-crystal forms: fast evaporation of solvent from solutions to dryness. CrystEngComm 13 (19), 5650.

10. Shan, N.; Toda, F.; Jones, W. (2002) Mechanochemistry and co-crystal formation: effect of solvent on reaction kinetics. Chem. Commun. (20), 2372-2373.

11. Friščić, T.; Childs, S. L.; Rizvi, S. A. A.; Jones, W. (2009) The role of solvent in mechanochemical and sonochemical cocrystal formation: a solubility-based approach for predicting cocrystallisation outcome. CrystEngComm 11 (3), 418-426.

12. Di Prima, M.; Coburn, J.; Hwang, D.; Kelly, J.; Khairuzzaman, A.; Ricles, L. (2016) Additively manufactured medical products - the FDA perspective. 3D Print Med 2.

13. Melendez, P. A.; Kane, K. M.; Ashvar, C. S.; Albrecht, M.; Smith, P. A. (2008) Thermal inkjet application in the preparation of oral dosage forms: dispensing of prednisolone solutions and polymorphic characterization by solid-state spectroscopic techniques. J. Pharm. Sci. 97 (7), 2619-36.

14. Wickstrom, H.; Palo, M.; Rijckaert, K.; Kolakovic, R.; Nyman, J. O.; Maattanen, A.; Ihalainen, P.; Peltonen, J.; Genina, N.; de Beer, T.; Lobmann, K.; Rades, T.; Sandler, N. (2015) Improvement of dissolution rate of indomethacin by inkjet printing. Eur. J. Pharm. Sci. 75, 91-100.

15. Genina, N.; Fors, D.; Palo, M.; Peltonen, J.; Sandler, N. (2013) Behavior of printable formulations of loperamide and caffeine on different substrates--effect of print density in inkjet printing. Int. J. Pharm. 453 (2), 488-97.

16. Trenfield, S. J.; Awad, A.; Goyanes, A.; Gaisford, S.; Basit, A. W. (2018) 3D Printing Pharmaceuticals: Drug Development to Frontline Care. Trends Pharmacol. Sci. 39 (5), 440-451.

17. Magill, S. S.; Edwards, J. R.; Bamberg, W.; Beldavs, Z. G.; Dumyati, G.; Kainer, M. A.; Lynfield, R.; Maloney, M.; McAllister-Hollod, L.; Nadle, J.; Ray, S. M.; Thompson, D. L.; Wilson, L. E.; Fridkin, S. K. (2014) Emerging Infections Program Healthcare-Associated, I.; Antimicrobial Use Prevalence Survey, T., Multistate point-prevalence survey of health care-associated infections. N. Engl. J. Med. 370 (13), 1198-208.

Abbreviations

2D	two dimensional
3D	three dimensional
AA	Anacardic acid
ABL	Aqueous boundary layer
API	Active Pharmaceutical Ingredient
BHI	Brain heart infusion
CAC	Critical aggregation concentration
CAD	Computer-aided design
CMC	Critical micelle concentration
CVC	Central venous catheter
DI	Deionized
DLS	Dynamic light scattering
DMEM	Dulbecco's Modified Eagle Medium
DMSO	Dimethyl sulfoxide
DOD	Drop on demand
DOSY	Diffusion ordered spectroscopy
DSC	Differential scanning calorimetry
EMA	European Medicines Agency
ESI	Electrospray ionization
FaSSIF	Fasted state simulated intestinal fluid
FCS	Fetal calf serum
FeSSIF	Fed state simulated intestinal fluid
FDA	Food and Drug Administration
FDM	Fused deposition modeling
GA	Ginkgolic acid
GBS	Group B streptococci
GRAS	Generally recognized as safe
GSE	General solubility equation
HAT	Histone acetyl transferase
HBSS	Hanks' balanced salt solution
HPMC	(Hydroxypropyl)methyl cellulose
HPMCAS	(Hydroxypropyl)methyl cellulose acetate succinate
HPLC	High-pressure liquid chromatography
HRMS	High resolution mass spectroscopy

HTS	High throughput screening
IL	Ionic liquid
i.m.	intramuscular
i.v.	intravenous
L	Lecithin
LB	Lysogeny broth
MBIC	Minimal biofilm inhibitory concentration
MEM	Minimal essential medium
MF	Mutant factor
MH	Müller-Hinton-Bouillon
MIC	Minimal inhibitory concentration
MMP	Matrix metalloproteinase
MRSA	Multi-drug resistant staphylococcus aureus
MS	Mass spectrometry
NBE	New biological entity
NCE	New chemical entity
NEAA	Nonessential amino acid
NIR	Near infrared
NMR	Nuclear magnetic resonance
NOESY	Nuclear Overhauser enhancement Spectroscopy
NSAID	Nonsteroidal anti-inflammatory drug
OD	Optical density
OTF	Oral thin film
P_{app}	Apparent permeation coefficient
PBS	Phosphate buffered saline
PDMS	Polydimethylsiloxane
PE	Polyethylene
PEG	Polyethylene glycol
PET	Polyethylene terephthalate
P/S	Penicillin and streptomycin
PGA	Polyglycolic acid
PIJ	Piezoelectric inkjet
PLA	Polylactic acid
PLM	Polarized light microscope
PVC	Polyvinyl chloride
PVP	Polyvinyl pyrrolidine

PTFE	Polytetrafluoroethylene
PWSD	Poorly water-soluble drug
QMS	Quadrupole mass spectrometer
QS	Quorum sensing
rcf	Radial centrifugal force
R&D	Research and development
ROUT	Robust regression and outliner removal
RT	Room temperature
SD	Standard deviation
SLA	Stereolitography
SLS	Selective laser sintering
SSE	Semi-solid extrusion
TC	Taurocholate
TEER	Trans epithelial electric resistance
TIJ	Thermal inkjet
TLC	Thin layer chromatography
TSB	Tryptic soy broth
UV	Ultraviolet
VIS	Visible
VRE	Vancomycin-resistant Enterococci
w/	With
w/o	Without
WST-1	Water soluble tetrazolium salt
XRD	X-ray diffraction
XRPD	X-ray powder diffraction

Curriculum vitae

Personal Details

Name	Marco Saedtler
Date of birth	1988-09-24
Place of birth	Lich, Germany

Professional Experiences

Since 05/2020	Senior Scientist *Merck KGaA, Darmstadt* *Expert for Phys.-Chem. Characterization*
07/2019 – 11/2019	Pharmacist *5K Universum Apotheke, Frankfurt am Main*
04/2019 – 06/2019	Pharmacist *Ohm-Apotheke Nieder-Ohmen, Mücke*
04/2015 – 03/2019	Research assistant at the University of Würzburg *Chair for drug formulation and delivery* *Director Prof. Dr. Dr. Lorenz Meinel*
05/2014-10/2014	Pharmaceutical trainee *Röthelheim Apotheke, Erlangen*
11/2013-04/2014	Pharmaceutical trainee *Boehringer Ingelheim Pharma, Biberach an der Riß* *Department for late stage drug development*

Education

04/2015 – 03/2019	Research assistant at the University of Würzburg *Chair for drug formulation and delivery* *Director Prof. Dr. Dr. Lorenz Meinel*
12/2014	Registration as Pharmacist
10/2009-09/2013	Student of Pharmacy *Friedrich-Alexander-Universität Erlangen-Nürnberg*
09/2005-06/2008	Theo-Koch-Schule, Grünberg
09/1999-06/2005	Gesamtschule Mücke, Mücke

Publications

Saedtler, M., Förtig, N., et al. (2020). "Antibacterial Anacardic Acid Derivatives." ACS Infect. Dis. 6 (7), 1674-1685.

Saedtler, M., Meinel, L. (2019): Amorphous Ionic Liquid Strategies for Pharmaceutical Application, in: Zhang S. (eds), Encyclopedia of Ionic Liquids, Singapore, Springer 2019

Schramm, S., Gunesch, S., et al. (2018). "Investigations into neuroprotectivity, stability, and water solubility of 7-O-cinnamoylsilibinin, its hemisuccinate and dehydro derivatives." Arch. Pharm. Chem. Life Sci. 1-9.

Wiest, J., Saedtler, M., et al. (2018). "Geometrical and Structural Dynamics of Imatinib within Biorelevant Colloids." Mol. Pharm. 15 (10), 4470-4480.

Reggane, M., J. Wiest, et al., (2018). "Bioinspired co-crystals of Imatinib providing enhanced kinetic solubility." Eur. J. Pharm. Biopharm. 128, 290-299.

Huang, G., Drakopoulos, A., et al. (2017). "Cytotoxic properties of the alkaloid rutaecarpine and its oligocyclic derivatives and chemical modifications to enhance water-solubility." Bioorg. Med. Chem. Lett. 27 (21), 4937-4941.

Wiest, J., Saedtler, M., et al. (2017). "Mapping the pharmaceutical design space by amorphous ionic liquid strategies." J. Control. Release. 268, 314-322.

Posters

Saedtler, M. Förtig, N. et al., (2018) "Bioinspired anacardic acid derivatives with antimicrobial and antibiofilm properties" 6th Galenus Workshop, Würzburg

Saedtler, M. Förtig, N. et al., (2018) "Bioinspired anacardic acid derivatives with antimicrobial and antibiofilm properties" Biological Barriers, Saarbrücken

Saedtler, M., Wiest, J. et al., (2017) "In vivo pharmacokinetics of ionic liquids" CRS Local Chapter Germany, Marburg

Acknowledgments

Documentation of authorship

This section contains a list of the individual contribution for each author to the publications reprinted in this thesis. Unpublished manuscripts are handled, accordingly.

P1	**Saedtler M, Meinel L** (2019) Amorphous Ionic Liquid Strategies for Pharmaceutical Application, in: Zhang S. (eds), Encyclopedia of Ionic Liquids, Singapore, Springer 2019		
Author		1	2
Literature analysis and interpretation		x	
Manuscript planning		x	
Manuscript writing		x	
Design of the graphics		x	
Correction of manuscript		x	x
Supervision of Marco Saedtler			x

P2	**Wiest J, Saedtler M, Böttcher B, Grüne M, Reggane M, Galli B, Holzgrabe U, Meinel L** (2018) Geometrical and Structural Dynamics of Imatinib within Biorelevant Colloids. Mol Pharm. 2018 Oct 1;15(10):4470-4480							
Author	1	2	3	4	5	6	7	8
Preparation of imatinib free base	x	x						
DOSY NMR measurements				x				
NOESY NMR measurements	x							
Aggregation assay	x							
Solubility measurements		x						
X-Ray powder diffractometry	x	x						
Dynamic light scattering measurements	x	x						
Cryo-electron microscopy			x					
Study design/concept development	x	x						x
Data analysis and interpretation	x	x			x	x	x	x
Manuscript planning	x						x	x
Manuscript writing	x	x			x	x	x	x
Correction of manuscript	x	x						x
Supervision of Marco Saedtler								x

P3	Saedtler M, Förtig N, Ohlsen K, Faber F, Masota N, Kowalick K, Holzgrabe U, Meinel L (2020) Antibacterial Anacardic Acid Derivatives. ACS Infect. Dis. 2020 June 10;6(7):1674–1685								
Author	**1**	**2**	**3**	**4**	**5**	**6**	**7**	**8**	
Synthesis of compounds	x								
Physicochemical characterization	x								
Permeation assay	x								
Cell proliferation assay	x								
Minimal inhibitory concentration	x	x	x	x	x				
Biofilm-inhibition assay	x	x							
Reverse mutation assay						x			
Galleria mellonella assay	x	x							
Statistical evaluation	x								
Study design/concept development	x	x	x				x	x	
Data analysis and interpretation	x	x	x				x	x	
Manuscript planning	x							x	
Manuscript writing	x	x					x	x	
Correction of manuscript	x	x					x	x	
Supervision of Marco Saedtler								x	

P4	Saedtler M, Förtig N, Ohlsen K, Sahr F, Hussein K, Dachtler M, Holzgrabe U, Meinel L (2020) Pharmaceutical formulation of anacardic acid derivatives utilizing salt metathesis and 2D/3D printing techniques. [unpublished]								
Author	**1**	**2**	**3**	**4**	**5**	**6**	**7**	**8**	
Synthesis of compounds	x								
Salt metathesis	x								
Solid-state characterization	x								
Solubility screening	x								
2D/3D printing	x	x		x	x	x			
X-Ray Powder Diffraction of 2D/3D printed samples	x								
Microscopy of 2D/3D printed samples		x							
HPLC quantification of 2D/3D printed samples		x							
Agar diffusion test	x	x							
Statistical evaluation	x								
Study design/concept development	x	x		x	x	x	x	x	
Data analysis and interpretation	x	x	x				x	x	
Manuscript planning	x							x	
Manuscript writing	x								
Correction of manuscript	x							x	
Supervision of Marco Saedtler								x	

Erklärung zu den Eigenanteilen des Doktoranden sowie der weiteren Doktoranden als Koautoren an Publikationen und Zweitpublikationsrechten bei einer kumulativen Dissertation.

Für alle in dieser kumulativen Dissertation verwendeten Manuskripte liegen die notwendigen Genehmigungen der Verlage ('reprint permission') für die Zweitpublikation vor, außer das betreffende Kapitel ist noch gar nicht publiziert. Dieser Umstand wird einerseits durch die genaue Angabe der Literaturstelle der Erstpublikation auf der ersten Seite des betreffenden Kapitels deutlich gemacht oder die bisherige Nichtveröffentlichung durch den Vermerk „unpublished" oder „nicht veröffentlicht" gekennzeichnet.

Die Mitautoren der in dieser kumulativen Dissertation verwendeten Manuskripte sind sowohl über die Nutzung als auch über die oben angegebenen Eigenanteile informiert.

Die Beiträge der Mitautoren an den Publikationen sind in den vorausgehenden Tabellen aufgeführt.

Prof. Dr. Dr. Lorenz Meinel   Unterschrift

Marco Saedtler   Unterschrift